UNIVERSITY OF CALIFORNIA

Los Angeles

Enhanced liquid rocket injection enabled by additive manufacturing

A dissertation submitted in partial satisfaction

of the requirements for the degree

Doctor of Philosophy in Aerospace Engineering

by

Alex Ross Keller

2024

ABSTRACT OF THE DISSERTATION

Enhanced liquid rocket injection enabled by additive manufacturing

by

Alex Ross Keller

Doctor of Philosophy in Aerospace Engineering

University of California, Los Angeles, 2024

R. Mitchell Spearrin, Chair

Injector design has a significant impact on liquid rocket engine performance because it governs the atomization and mixing of propellants to produce stable combustion over a characteristic length scale. Additive manufacturing (AM) with high-performance metal alloys is revolutionizing combustion device design and development, particularly related to propellant injection. AM injectors can dramatically reduce part counts and implement complex fluid passageways that decrease injector forward pressure-drop, increase combustion stability, and enhance propellant mixing, thereby enabling improved rocket combustor performance and extending mission capabilities. This dissertation focuses on three subtopics of AM injector (coaxial and impinging) design and performance: (1) hydraulics, (2) propellant mixing, and (3) combustion instabilities. A combination of computational and experimental efforts are utilized, which include but are not limited to injector design, fluid dynamics analysis, and experimental hydraulics (cold-flow) and mixing/combustion studies using optical diagnostic techniques. Compiled results demonstrate the promising potential to leverage the flexibility of additive manufacturing to design advanced injector geometries that improve performance and reliability of liquid rocket engines.

The dissertation of Alex Ross Keller has been approved.

Ann Karagozian

Jeff Eldredge

Xiaolin Zhong

R. Mitchell Spearrin, Committee Chair

University of California, Los Angeles

2024

Table of Contents

List of Figures

List of Tables

Acknowledgments

This dissertation is a testament to the exceptional guidance, support, and mentorship I have received throughout both my academic journey and personal life. I would like to begin by expressing my deep gratitude to my advisor, Professor Mitchell Spearrin, for his invaluable counsel and leadership over the past five years. Your passion for research, combined with your gritty work ethic, has been a constant source of inspiration. Through your mentorship, I have gained not only a stronger sense of confidence as a scientist and engineer, but also a better appreciation for the importance of effective scientific writing and communication. Most importantly, you took a chance on me. Joining your lab at UCLA has been an incredible privilege and one of the most rewarding experiences of my life. The knowledge, skills, and opportunities I have gained during my time in graduate school will continue to shape my career, and for that, I will always be grateful. I would also like to thank my thesis committee members, Professor Ann Karagozian, Professor Jeff Eldredge, and Professor Xiaolin Zhong, for their insightful guidance and constructive feedback on this research.

I am a firm believer that you can become a good engineer by being around great engineers. I have had the privilege to be mentored by such people; each of which have also become great friends. Nick Kuenning, you have one of the best engineering brains out of anyone I've ever met and have had such a significant influence on me. You quickly became a leader in the lab and everyone's go-to guy when something needed fixing. I've always admired your sense of urgency to help others, even when your own task list was overflowing. Your remarkable problem-solving ability and extensive knowledge have made you an invaluable resource, not just to me, but to every member of SpearrinLab. Anil Nair, I could not have asked for a better mentor for when I first started graduate school. Coming from a physics background, I initially encountered a steep learning curve when confronted with mechanical and aerospace engineering problems and concepts. My lack of knowledge (and occasional incompetence) was instead met with patience and kindness. The late nights outside in the E4 alley running cold-flow tests with you and Nick, working on the test stand, and conducting hot-fire test campaigns with our RDRE in the Mojave will always stand out as cherished memories from my graduate school experience.

My time at UCLA would not have been nearly as meaningful or enjoyable without the support and camaraderie of my fellow SpearrinLab members. It has been a true pleasure working alongside many members of the SpearrinLab group over the years, but I would like to particularly acknowledge those with whom I worked most closely. Barathan Jeevaretanam, thank you for being a great friend and consistent gym partner. I am extremely fortunate to have had you and Nick along side of me as we all started our PhD journey together. Isabelle Sanders, thank you for your help in getting me started with laser absorption tomography, which later ended up becoming a large portion of my research. More than that, thank you for being a compassionate friend. While we didn't quite get to work on research together, I also want to thank Kevin Schwarm for his humble leadership and joy that he brought to myself and everyone else in the lab. You embody what it means to work hard, but also to have fun while doing it. The lab hasn't quite been the same without you and Isabelle since you both graduated, but I am lucky to have spent most of my time in SpearrinLab with you both around. Ariya Olaee, I greatly admire the enthusiasm you bring to everything

you do, and I've enjoyed watching you mentor younger lab members. I've also appreciated having you as my go-to person for electronic music concerts. I also want to acknowledge Nicolas Minesi for his invaluable guidance during his time as a post-doc in SpearrinLab. Selfishly, I wish you could have stayed for my entire PhD, but I'm certain France has gained an incredible professor in you. Additionally, I want to thank master's students Joel Otomize and Alex Lima, as well as undergraduate researchers Nik Struntz and Blake Spahr, for their computational and experimental contributions to this work.

Much of my graduate work would not have been possible without the financial support from the NASA ESI and Marshall Space Flight Center CAN grants. I am especially grateful to Thomas Teasley for his support of our additively-manufactured injector work and his guidance as our NASA research collaborator. I would also like to thank UCLA facilities, particularly Anthony Redon and Anthony Singleton, for their dependable support and assistance in the UCLA machine shop. My sincere thanks to Amanda Gordillo in the MAE administrative staff for her dedication in procuring the services and hardware necessary for this research, and to Miguel Lozano and Ben Tan of the MAE department for ensuring that 157A ran smoothly during my teaching assistantship. I was fortunate to have had the opportunity to work with Dave Crisalli of Polaris Propulsion, whose expertise was essential in successfully and safely conducting our Mojave hot-fire test campaigns. He is an exceptional engineer, a role model, and an absolute pleasure to work with.

Fabio Bendana, you have been an outstanding mentor, role model, instructor, and friend throughout my career. A significant portion of this dissertation, along with several of my published research papers, owes its higher quality to your meticulous attention to detail. I am constantly inspired by your humility and work ethic, and I have truly enjoyed working alongside you at The Aerospace Corporation over the past few years. Drew Cortopassi, thank you for the incredible opportunity to work as a chemical propulsion intern at The Aerospace Corporation for the past three years. The knowledge and experience I've gained from working with you and Fabio are invaluable, and have profoundly shaped my growth as an engineer. I am also grateful to Vincent Phong for his support on the combustion instability study presented in this thesis. Your assistance with this topic, as well as your contributions to data analysis, were fundamental in that work. Additionally, I want to thank my other colleagues at The Aerospace Corporation—Armando Perezselsky, John DeSain, Tim Wabel, and Dean Kaialau—for their support and expertise in conducting and advising this research.

I have been fascinated by physics and math from a young age, but it wasn't until my junior year of high school that my passion for these subjects—and my future in them—was truly solidified. I am especially grateful to two of my teachers at Red Lion Area High School: David Hively (Calculus) and Ben Smith (Physics). Both of you taught not just with expertise, but with joy, igniting a deep love for learning that has lasted throughout my career. Now, twelve years after taking your classes, I have earned a doctoral degree in Aerospace Engineering—an achievement that I believe was set in motion by your influence.

My academic journey was further shaped by the faculty members of the Physics, Engineering, and Astrophysics departments at Randolph Macon College (RMC). I want to express my heartfelt gratitude to my undergraduate advisor, Professor Rachele Dominguez, who played a pivotal role in my decision to pursue a PhD. You always made time to answer my questions and generously shared your experiences. As a phenomenal instructor, you prepared

me for UCLA's rigorous curriculum, and, more importantly, you helped me believe in my own potential. I cannot thank you enough for your guidance and support; I am certain I wouldn't be where I am today without you. I also want to thank Professor George Spagna for his mentorship and for solidifying my passion for astronomy and astrophysics. Your astrophysics courses remain my favorite classes to this day.

My involvement in organized sports, particularly football, has played a pivotal role in shaping my work ethic and building the confidence needed to overcome adversity. I am deeply grateful for my college football coach, Pedro Arruza, and the entire RMC football program for imparting invaluable life lessons that have shaped my personal growth and equipped me to navigate the challenges of graduate school. The principles that Coach Arruza emphasized–such as 'grit,' 'tenacity,' and 'pound the rock'–were never confined to the football field; they were timeless lessons for life. I will forever be grateful for the profound impact football and Coach Arruza had on shaping both my character and my ability to face challenges with resilience and determination.

A heartfelt thank you to my mother, Denise Keller, whose unwavering support and nurturing guidance have been foundational to my success. Her encouragement and wisdom have given me the confidence to pursue my goals with passion and perseverance. I am endlessly grateful for her love and the strength she has instilled in me. I also want to thank my grandma Theresa, grandpa Craig, great-grandma GG for their consistent love and support of my ambitions throughout my entire life.

I cannot thank my close friends enough for their steadfast support and belief in me. Your faith in my abilities, combined with your friendship and understanding, has been instrumental in making this journey possible. I am truly fortunate to have you all in my life, and I am deeply grateful for the positive impact you've had on me.

To my wonderful life partner, Emily, thank you for being my rock and for your endless support and belief in me. Your love and encouragement have been invaluable in helping me stay focused and motivated throughout this journey, and your presence has made every step more meaningful. I am incredibly fortunate to have you by my side. I love you.

VITA

2014–2018	B.S., Physics, Randolph-Macon College
2020–2022	M.S., Aerospace Engineering, UCLA
2020–2024	Ph.D. Candidate, Aerospace Engineering, UCLA
2022–2024	Chemical Propulsion Intern, The Aerospace Corporation

PEER-REVIEWED PUBLICATIONS

[1] **A.R. Keller**, V.C. Phong, F.A. Bendana, R.M. Spearrin, Combustion instability characteristics of a methane-oxygen shear tri-coaxial rocket injector. In *Journal of Propulsion and Power*. Submitted December 2024 (under review).

[2] **A.R. Keller**, F.A. Bendana, V.C. Phong, R.M. Spearrin, Additively-manufactured shear tri-coaxial rocket injector mixing and combustion characteristics. In *Aerospace Science and Technology*. October 2024. doi: 10.1016/j.ast.2024.109680.

[3] **A.R. Keller**, F.A. Bendana, R.M. Spearrin, Shear Coaxial Methane–Oxygen Injector Mixing and Combustion Examined by Laser Absorption Tomography. In *Journal of Propulsion and Power*. May 2024. doi: 10.2514/1.B39463.

[4] N.M. Kuenning, A.P. Nair, **A.R. Keller**, N.Q. Minesi, E. Ozen, B. Bigler, J. Kriesel, J.W. Bennewitz, J. Burr, S.A. Danczyk, R.M. Spearrin, Multiplexed MHz-rate mid-infrared laser absorption spectroscopy for simultaneous in-chamber CO, CO2, H2O, temperature, and

pressure in a rotating detonation rocket engine. In *Combustion and Flame*. October 2024. doi: 10.1016/j.combustflame.2024.113608.

[5] A.P. Nair, N.Q. Minesi, N.M. Kuenning, **A.R. Keller**, R.M. Spearrin, Optical pressure sensing at MHz rates via collisional line broadening of carbon monoxide: uncertainty quantification in reacting flows. In *Applied Physics B*. March 2023. doi: 10.1007/s00340-023-07985-1.

[6] A.P. Nair, **A.R. Keller**, D.S. Morrow, A.B. Lima, R.M. Spearrin, D.I. Pineda, Hypergolic Continuous Detonation with Space-Storable Propellants and Additively-Manufactured Injector Design. In *Journal of Spacecraft and Rockets*. April 2023. doi: 10.2514/1.A35272.c1.

[7] A.P. Nair, **A.R. Keller**, N.Q. Minesi, D.I. Pineda, R.M. Spearrin, Detonation cell size of liquid hypergolic propellants: Estimation from a non-premixed combustor. In *Proceedings of the Combustion Institute*. July 2022. doi: 10.1016/j.proci.2022.06.015.

CHAPTER 1

Introduction

1.1 Liquid rocket engine injectors

Liquid-bipropellant rocket engines (LREs) operate by injecting liquid (or gaseous) fuel and oxidizer into a combustion chamber, where propellants mix and exothermically react to convert stored chemical energy into useful thermal energy that is then exploited to generate thrust. As illustrated in Fig. 1.1, an LRE *injector* functions as the interface between the propellant feed system and the combustion chamber. The primary roles of an injector in an LRE are to introduce propellants into the combustion chamber in the right proportions, efficiently atomize and mix the propellants, and produce a stable combustion process within a characteristic axial distance and volume. The injector must also ensure that the combustion process is decoupled from the feed system and maintain combustor hardware durability through manageable thermal loading on chamber walls [43]. Achieving these performance characteristics can lead to complex injector designs. An injector plate assembly employed in the Space Shuttle main engine (SSME) is pictured in Fig. 1.2 for reference.

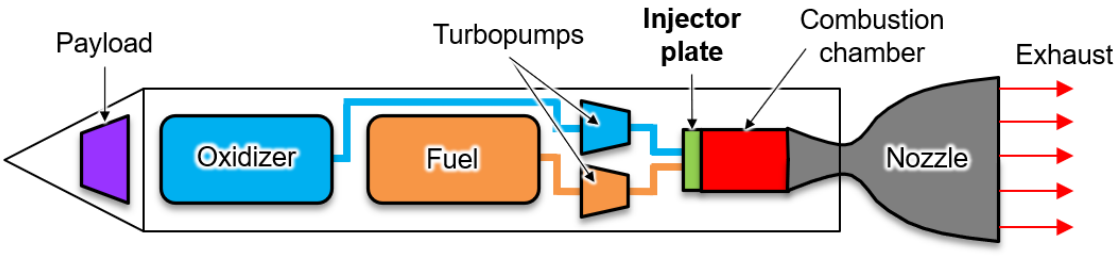

Figure 1.1: Simplified schematic of major components in a liquid bipropellant rocket.

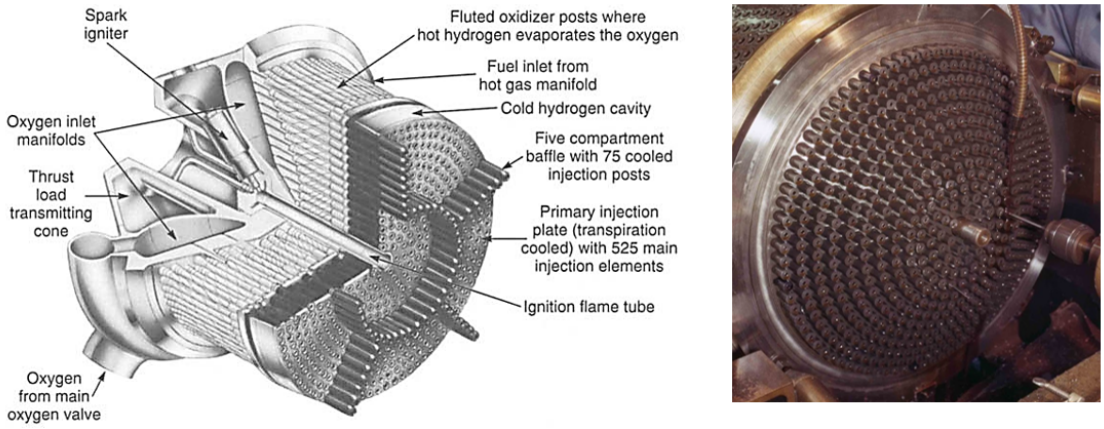

Figure 1.2: Space shuttle main engine (RS-25) injector plate containing hundreds of shear coaxial injector elements. *Left:* Main injector system assembly showing inlet manifolds and baffles (from Ref. [128]). *Right:* Image of injector plate during manufacturing (from NASA.gov).

The performance of a rocket injector can have an acute impact on overall vehicle performance. Used to estimate the maximum achievable velocity change, Δv, the Tsiolkovsky rocket equation (Eqn. 1.1) provides a critical measure of overall vehicle performance in terms of the performance of the propulsion system, as well as the initial and final mass of the vehicle.

$$\Delta v = I_{\text{sp}} g * ln\left(\frac{m_{\text{wet}}}{m_{\text{dry}}}\right) \tag{1.1}$$

Here, specific impulse, or I_{sp} [s], is a common LRE performance parameter used to describe a propulsion system's efficiency of thrust production from a given mass flow rate of propellant, and g is the acceleration due to Earth's gravity (9.81 [m/s$_2$]). m_{wet} [kg] represents the initial total mass of the vehicle, also known as "wet mass", which includes the mass of propellants. Conversely, the final total mass of the vehicle when all propellants have been expended is referred to as the "dry mass", or m_{dry} [kg]. It is evident from Eqn. 1.1 that vehicle performance is enhanced by maximizing I_{sp} and minimizing m_{dry}.

Advancements in injector design, specifically those that enhance mixing and expand operating conditions, enable improved rocket combustor performance thus extending mission capabilities. For example, effective propellant mixing promotes higher I_{sp}, and typically

produces a shorter flame, thereby reducing the required length and mass (m_{dry}) of a rocket combustion chamber. Injectors with minimal hydraulic losses generally require lighter propellant feed system hardware, further reducing m_{dry} which can be traded for payload or mission duration. Injectors that discourage combustion instabilities and maintain high-performance operation over a wide range of conditions are attractive for engines that require deep throttling, which can be used to optimize flight trajectories and reduce aerodynamic stresses on launch vehicles. Therefore, LRE injector design has a significant impact on overall vehicle performance due to its influence in a multitude of different systems and processes including thermal management and feed system operating pressures [54]. The work covered in this dissertation focuses on how advanced injector geometries enabled by additive manufacturing impact the following three topics of LRE operation: (1) combustion and mixing performance, (2) injector-related combustion instabilities, and (3) injector hydraulic performance.

1.1.1 Types of LRE injection schemes

Several types of injector designs have been used for liquid-bipropellant rocket engines, with varying complexity and performance. The appropriate choice of injection scheme is dependent on the specific application and propellants. Some key parameters that must be accounted for when selecting the proper injection scheme are: propellant type (e.g., space-storable, cryogenic, hypergolic) and their phases, mixture ratio, chamber length, chamber pressure, chamber cooling method, throttlability, and reusability [43]. This work focuses on two of the most commonly-used and extensively flight tested injection schemes in LREs: *impinging* and *coaxial* – although other injection schemes (e.g., showerhead, pintle, splash plate, etc.) exist that can be more appropriate for different applications.

A straightforward method of atomizing and mixing propellant jets is by directing two or more separate streams into each other through impingement angles, also known as *impinging*

Vehicle, Engine	Fuel	Oxidizer	Injection scheme
Saturn V, F-1	RP-1	LOX	Impinging (like-doublet)
Saturn V, J-2	LH_2	LOX	Coaxial (shear)
Titan I, first stage	RP-1	LOX	Impinging (like-doublet)
Titan II, first stage	A-50	NTO	Impinging (like-doublet)
Space shuttle, RS-25	RP-1	LOX	Coaxial (shear)
Apollo, lunar ascent	A-50	NTO	Pintle
Ariane 5, Vulcain II	LH_2	LOX	Coaxial (shear)
SpaceX Falcon 9, Merlin	RP-1	LOX	Pintle
SpaceX Starship, Raptor	LCH_4	LOX	Coaxial (swirl)

Table 1.1: Popular rocket engines with their respective liquid bipropellant combinations and injection schemes.

injector elements. Various impinging injection schemes exist (see Fig. 1.3) and are categorized by *like* or *unlike* which refer to propellant matching for impinging jets, and through the number of jets per element (e.g., two jets: *doublet*, three jets: *triplet*, four jets: *quadlet*, and five jets: *pentad*). For example, a simple impinging injection scheme is the *like-doublet*, where two jets of the same propellant collide to form a roughly two-dimensional spray sheet in a plane orthogonal to centerline connecting the two propellant streams as illustrated in Fig. 1.4. These like-doublet elements are typically situated adjacent to other like-doublet elements with the opposite propellant such that the resulting spray sheets of fuel-fuel and oxidizer-oxidizer can form into droplets and mix together via inter-element interaction. Historical uses of the like-doublet impinging injection scheme are the F-1 engine on the Saturn V, and the first stage engines of the Gemini launch vehicle and the Titan I and II.

Coaxial injectors (also known as "concentric-tube elements") have demonstrated high performance and reliability over a wide range of operating conditions due to rapid near-field mixing associated with shear-induced turbulence. Coaxial injectors typically have a high-density inner jet (typically oxidizer) and a low-density outer jet (typically fuel) with different relative velocities. Having an outer jet of fuel mitigates risk of hardware damage resulting from direct contact of the oxidizer with chamber walls. This coaxial injector type is classified into two main sub-categories: *shear coaxial*, where both propellants have outlet velocities that

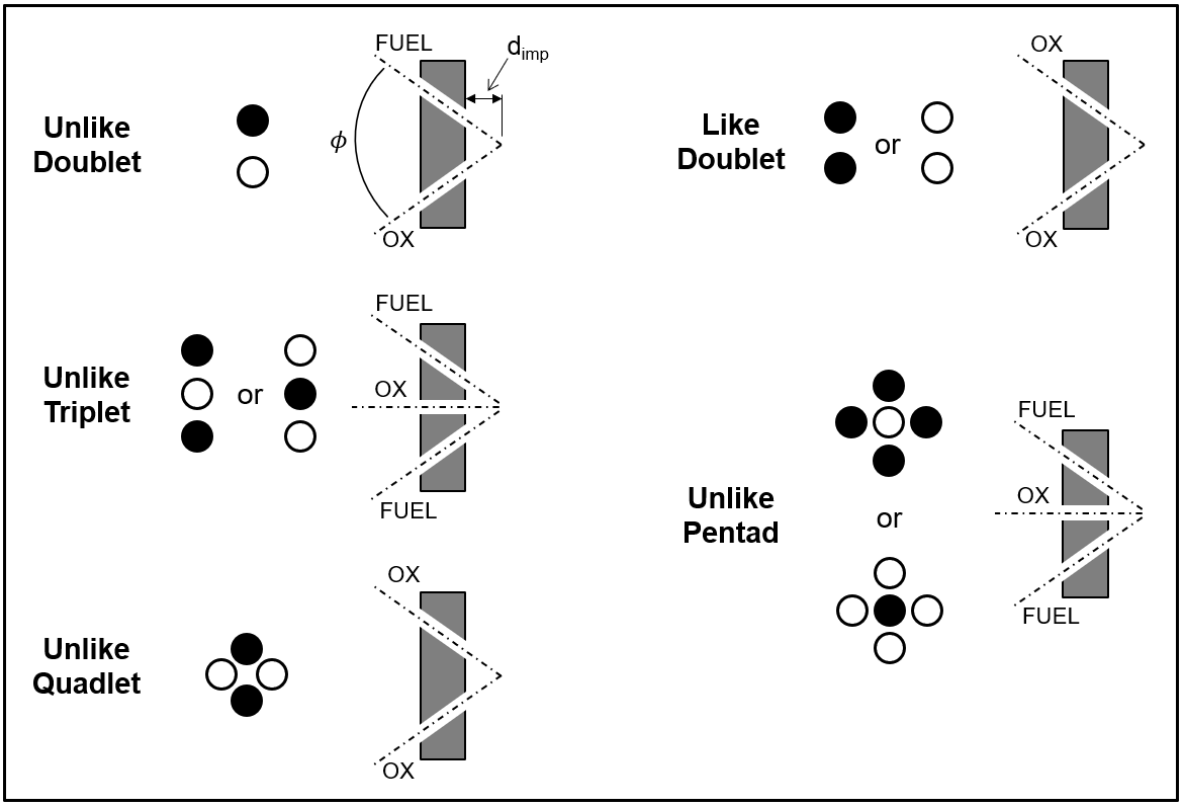

Figure 1.3: Various like and unlike impinging injection schemes with exemplary element configurations shown. ϕ represents the impingement angle, and d_{imp} represents the impingement distance offset from the injection plane.

are axial and co-linear and mixing primarily occurs through shear associated with gradients in axial momentum, and *swirl coaxial*, where the flowpath geometry generates a tangential or angular velocity component in the coaxial streams that adds radial momentum and tangential shear that further enhance mixing. It is noteworthy that shear coaxial injectors have been used in prior liquid rocket engines such as the Space Shuttle Main Engine (SSME) and Vulcain II main stage engine, and are expected to play a role in next-generation methane-oxygen engines that use oxidizer-rich, staged combustion cycles where both propellants may enter the combustion chamber in a gaseous or supercritical state.

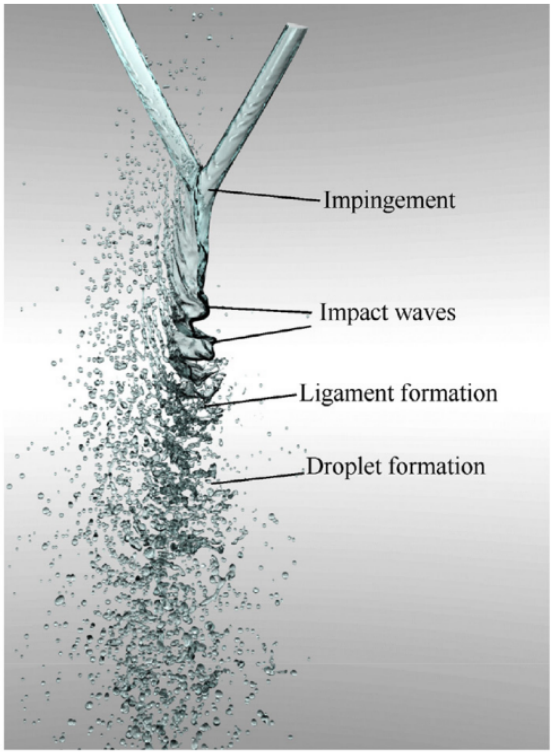

Figure 1.4: High-fidelity numerical simulation rendering of flow-field and atomization of impinging doublet using two liquid water jets. From Ref. [24].

1.1.2 Propellant mixing

Arguably the most important role of the injector in an LRE is to efficiently mix the fuel and the oxidizer. This is accomplished by first breaking up the liquid propellants into small droplets (*atomization*) such that they are quickly converted into a gaseous state (*vaporization*) and then the two fluids are sufficiently blended together in the correct proportions before they exothermically react. Deviations from a perfectly homogeneous mixture, or an off-target propellant mass flow rate ratio will result in a decline in performance. Optimal injector design typically relies on fundamental scaling parameters in order to correctly size the combustion chamber and its injector element configuration.

The atomization, vaporization, and blending processes must be achieved within a characteristic axial length and volume in order to minimize combustion chamber size, which is desirable for reducing a vehicle's dry mass and therefore enabling augmented performance.

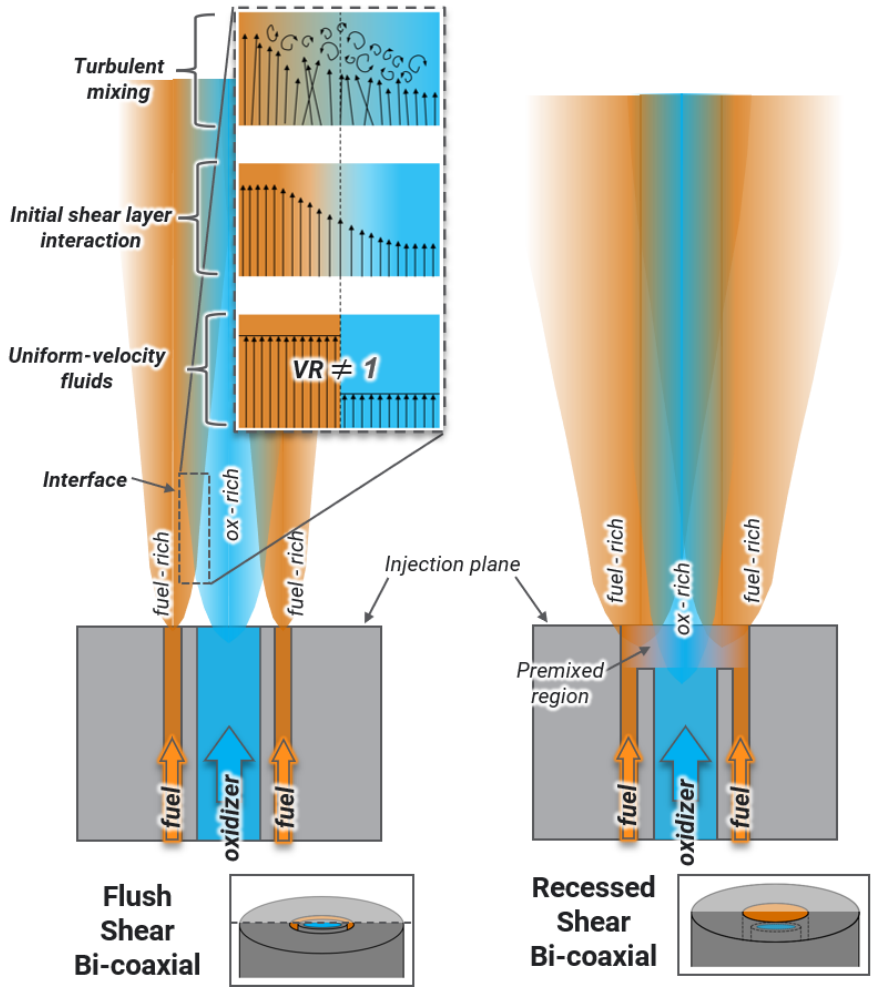

Figure 1.5: Illustration of near-field mixing behavior for shear bi-coaxial injection schemes. *Left:* flush (non-recessed), and *right:* recessed oxidizer post.

To ensure complete mixing and combustion, a minimum adequate chamber size is required, which is contingent upon the "residence time" (t_s) required for several different processes such as propellant injection, atomization, vaporization, mixing, and chemical kinetic rates [53, 54]. Typical "residence time" values range from 0.001 to 0.040 seconds for various types of combustors and propellant combinations [128]. Vaporization is typically the slowest of these processes, and is function of droplet size and therefore heavily dependent on injector design for a given liquid propellant.

A useful one-dimensional scaling metric used for combustion chamber design is *characteristic length* or L^* ("L-star"), which relates combustor size to targeted engine flow conditions,

sonic nozzle throat area, propellant properties, and residence time, as seen here in Eqn. 1.2:

$$L^* = \frac{\dot{m}_{\text{tot}} t_{\text{s}}}{A_{\text{t}} \rho_{\text{avg}}} \tag{1.2}$$

where $\dot{m}$ is the total propellant flow rate [kg/s], t_{s} is the residence time [s], ρ_{avg} is the average density of the combustion products [kg/m^3], and A_{t} is the sonic nozzle throat area [m^2].

A fundamental parameter used to characterize the combustion efficiency, or how well a system converts chemical energy into thermal energy, is called *characteristic velocity* or c^* ("c-star"). The actual c^* value of a system can be measured experimentally (see Eqn. 1.3) and an ideal theoretical value of c^* can be determined as a function of product gas properties (see Eqn. 1.4).

$$c^*_{\text{meas}} = \frac{P_{0,\text{c}} A_{\text{t}}}{\dot{m}_{\text{tot}}} \tag{1.3}$$

$$c^*_{\text{ideal}} = \sqrt{\frac{R_{\text{u}} T_{0,\text{c}}}{M\gamma} \left(\frac{\gamma+1}{2} \right)^{\frac{\gamma+1}{\gamma-1}}} \tag{1.4}$$

Here, these variables correspond to product gas properties: $P_{0,\text{c}}$ represents the chamber stagnation pressure [Pa], $T_{0,\text{c}}$ represents the chamber stagnation temperature [K], M is the molecular weight [kg/kmol], γ is the specific gas constant, and R_{u} is the universal gas constant (8314.5 [J/kmol·K]).

c^* efficiency (η_{c^*}, in Eqn. 1.5) is a direct reflection of how well an injector atomizes and mixes the propellants to the desired mixture ratio [54], and is simply defined by the ratio of the achieved (measured) c^*_{meas} to the ideal theoretical c^*_{ideal}. In modern LREs, c^* efficiencies can reach nearly 100% [54].

$$\eta_{c^*} = \frac{c^*_{\text{meas}}}{c^*_{\text{ideal}}} \tag{1.5}$$

In additional to the design of individual injector elements, the arrangement of elements on the injector face has a significant influence on LRE performance, particularly related to mixing. The relative positions of adjacent elements must be configured in such a way

that improves mixing uniformity from inter-element interaction, and also avoids extreme combustion environments near the chamber walls to ensure hardware survivability [43].

High-thrust output LREs, such as booster-class engines, require higher propellant flow rates, which can be achieved by increasing the per-element flow rates via larger injector element outlet areas (e.g. larger orifices) for a given combustor size and upstream feed system pressure. However, larger injector elements produce wider jets of liquid propellant which slow down the rates of atomization and vaporization and therefore invoke a reduction in vehicle performance by requiring a larger L^* for complete combustion. Alternatively, high propellant flow rates can also be obtained by increasing the total number of elements, or the "element density" on an injector plate. Maximizing element density, while simultaneously minimizing orifice size is generally desired for performance benefits [54], but both of these design parameters are constrained by manufacturing techniques (discussed further in Sec. 1.2.1).

1.1.2.1 Shear coaxial injector mixing

Two important non-dimensional metrics involved in the mixing processes of coaxial jets are the *outer-to-inner* velocity ratio ($VR = u_{\mathrm{o}}/u_{\mathrm{i}}$) and momentum flux ratio ($J = \rho_{\mathrm{o}} u_{\mathrm{o}}^2/\rho_{\mathrm{i}} u_{\mathrm{i}}^2$). VR directly influences the intensity of shear layer interaction between the coaxial jets which relates to the amount of turbulent mixing that occurs, and also determines the length of the inner potential core [109]. J serves as an important factor in turbulent mixing intensity and predicting characteristic mixing length scales, accounting for differences in fluid density in addition to variance in velocity [109]. Off-unity values of VR and J should generally be targeted to enhance shear-induced turbulent mixing between propellant jets. Both ratios are predominantly dependent on injector outlet geometry and the oxidizer-to-fuel ratio ($\mathrm{O/F} = \dot{m}_{\mathrm{GO_2}}/\dot{m}_{\mathrm{GCH_4}}$).

Notably, prior work has shown that recessing the oxidizer post relative to the injection

plane, which introduces a region of pre-mixing prior to the main injection, leads to improved mixing, wider flame expansion, and sometimes augmented combustion efficiency, albeit with such benefits often traded against less desirable combustion stability characteristics [43,67,83,121,125]. Kendrick et al. [67] concluded that a recessed oxidizer post augments the momentum flux ratio by reducing the effective outlet area of the fuel duct, thus accelerating the stream and ultimately enhancing mixing. Quantifying such mixing benefits is important in refining injector design.

Experimental flow-field characterization efforts have utilized numerous optical diagnostic methods to examine mixing in reacting and non-reacting coaxial jets. These optical methods include visible high-speed imaging [101, 118, 134], chemiluminescence of combustion radicals [67, 83, 118, 147], particle image velocimetry (PIV) [17, 119], planar laser induced fluorescence (PLIF) [5, 40, 115, 119, 140], and x-ray fluorescence [12]. An established metric in analyzing the mixing characteristics of coaxial fuel-oxidizer jets is the *stoichiometric mixing length*, L_S [5, 12, 115, 140]. L_S is defined as the axial length between the injection plane and where a stoichiometric interface contour intersects the jet centerline (see Fig. 2.1). Mass entrainment models capturing shear-induced turbulent flux across an interface of the two fluids indicate that stoichiometric mixing lengths of variable-density, non-reacting shear coaxial jets scale with a non-dimensional momentum flux ratio J [140]. This shear coaxial mixing model has been corroborated experimentally using acetone PLIF [5, 115] in non-reacting coaxial jets where conditions are favorable for such measurements. Further studies have found that mixing lengths for reacting shear coaxial flows scale similarly with J, but were found to be larger than their non-reacting counterparts [115]. The non-reacting studies provide critical insight into estimating L_S, but do not measure L_S directly as it would be in a reacting flow since the effects of heat release from combustion need to be accounted for.

Notably, Tacina and Dahm [34, 130] used an equivalence principle method to resolve the differences in mixing lengths values for reacting and non-reacting flows which account for the density changes resulting from exothermic reaction. Considering this equivalence

principle, Schumaker [116] used hydroxl (OH) PLIF imaging to measure mixing lengths in various coaxial flames, but discovered that an additional non-physical scaling factor (specific to the propellants used) was required to reconcile the reacting and non-reacting mixing length values. This disagreement was later determined to be an inherent byproduct of the OH PLIF measurement technique [12]. Recently, Bennewitz et al. [12] employed a novel x-ray fluorescence technique to measure the stoichiometric mixing length of shear coaxial flames and concluded that the Tacina and Dahm [34, 130] equivalence principle does a good job capturing the relation between reactive and non-reacting coaxial jet mixing. A common issue amongst the aforementioned imaging methods is that despite their high spatial resolution capability, they are generally more qualitative with regards to local species concentration. Additional quantitative diagnostics are needed to measure fundamental gas properties and characterize mixing in reacting coaxial flames to obtain a clearer understanding of how mixing and combustion performance is affected by injector geometry. Our research group recently developed and demonstrated a mid-infrared laser absorption tomography (LAT) technique that yields quantitative and spatially-resolved measurements of temperature and species in quasi-axisymmetric reacting flows [10, 11, 113, 143]. The axisymmetry of coaxial flames allows for this LAT method to be adopted as a novel means of evaluating mixing and combustion characteristics of shear coaxial injection schemes.

1.1.2.2 Shear tri-coaxial injector

Coaxial injectors with a third concentric propellant jet (a second annular flowpath), designated here as *tri-coaxial* injectors, have potential to improve mixing by increasing propellant contact surface area and introducing an additional shear-induced propellant mixing layer. A limited number of prior studies have examined this concept. Cai et. al. computationally and experimentally assessed the combustion performance and thermal characteristics of a hydrogen-oxygen tri-coaxial injector design, reporting significant improvements in combustion efficiency compared to a baseline bi-coaxial design along with higher chamber wall temperatures [18].

Ping et. al. found similar results in comparing the combustion characteristics of various shear coaxial injectors using gaseous hydrogen-oxygen, concluding that the propellant contact area is a primary driver of combustion performance as best demonstrated by a tri-coaxial design with the highest measured combustion efficiencies over a wide range of flow rates [60]. Using liquid ethanol and gaseous nitrous oxide, Lee et. al. experimentally evaluated droplet breakup and flame structure of a tri-coaxial injector using hot-wire anemometry and chemiluminescence videography of OH radicals over a range of momentum flux ratios by altering the outermost annular jet velocity [75]. Boualia et. al. used particle image velocimetry (PIV) to characterize velocity in non-reacting flow-fields of several tri-coaxial configurations with varying central jet displacements [17]. A tri-coaxial injector design has also been tested commercially by Snecma for the Vulcain gas generator, with results indicating improved combustion performance, relative to a bi-coaxial design, with significant increases in the obtainable per-element flow rate (up to 20 times higher) [13, 26, 38, 72, 141]. Injectors with high per-element mass flow rates are desirable since they can significantly reduce the number of individual elements required for a combustor.

The first topic of this dissertation (covered in Chapters 2 and 3) is the utilization of optical diagnostic techniques such as LAT and hydroxyl-chemiluminescence to assess and compare mixing and combustion characteristics of both traditionally-manufactured and additively-manufactured coaxial rocket injector designs, including a novel tri-coaxial design

1.1.3 Combustion instabilities

Combustion instabilities have plagued liquid rocket engines (LREs) since their advent and still present serious concerns today for system performance and hardware survivability. Fundamentally described by the Rayleigh criterion [28], combustion instabilities manifest as periodic fluctuations of pressure within a combustor when in phase with heat release

from combustion, and are further influenced by chamber and feed system resonances, as well as propellant injection processes. Fluctuations in chamber pressure can often negatively influence the fluid dynamics of the propellant injection process, thus reducing performance. In more extreme cases, they can increase local heat transfer rates and induce excessive pressure-based vibrations, both of which may damage engine hardware. Despite decades of research, combustion instabilities remain difficult to predict and model because they are unique to each combustion system – highly dependent on injector and combustor geometry, propellant choice, and flow/operating conditions.

Propellant injection systems in LREs inherently experience a large range of thermodynamic and hydrodynamic conditions from transient engine start-up, nominal operation, throttling, and engine shut-down – all of which can excite and sustain instabilities over a wide range of frequencies. While several different classifications of combustion instabilities exist, this work focuses on linear (self-excited) longitudinal instability modes which originate from the inherent noise that arises from injection and combustion processes [129]. Linear longitudinal instability modes are present in most LREs and generally appear sinusoidal in nature. They can manifest as low-frequency chugging, intermediate-frequency feed system coupled buzzing, and/or high-frequency acoustic eigenmodes, all of which are extremely sensitive to LRE injector design [58, 129]. Low-frequency, feed system instability modes (*chugging*) are in the ∼10–400 Hz range, caused by a coupling between the propellant feed system and combustion processes within the chamber, and is heavily influenced by the injection scheme, injector element geometry, and inter-element arrangement. Intermediate-frequency modes (*acoustic* or *buzzing*) are in the ∼400–1000 Hz range, and are linked with structural vibrations, and feed system and chamber acoustics. Lastly, high-frequency modes (*screeching*) are in the >1000 Hz range, and are related to pressure waves from combustion processes and chamber acoustic resonance properties.

For acoustic modes, the physical mechanisms that drive oscillations in volumetric heat release rate are categorized by either *intrinsic* or *injection-coupled* processes. Intrinsic

instabilities are defined by heat release rate fluctuations initiated by chamber acoustic modes from variations in combustion sub-processes that occur after propellant injection (e.g., atomization, vaporization, mixing, chemical kinetics). Said sub-processes determine the phase relationship between the chamber response and the injector response, hence dictating the feedback mechanism of amplification [56]. Intrinsic instabilities are considered to have a negligible effect on propellant injection flow rates [58]. Alternatively, injection-coupled acoustic instabilities occur from the coupling of chamber resonances and oscillatory fluctuations of propellant flow rates from the propellant injection system [56]. Thermoacoustic instabilities are a subclassification where combustion heat release rates become coupled with acoustic pressure waves within the chamber. Low-frequency chugging modes (non-acoustic) are also induced by injection-coupled processes, caused by a coupling of elastic pressure-wave interactions between the propellant feed system and combustor, and sometimes even influenced by vehicle structures [128].

Although in some special cases where the presence of combustion instabilities (typically higher-frequency transverse modes) can enhance propellant mixing and combustion performance, this is not particularly true for low-frequency chugging modes. For example, when an instability invokes an increase in the local chamber pressure on the injection plane, propellant flow rates are briefly reduced. In some situations, combustion products can backflow into propellant manifolds. In these cases of propellant flow rate modulation, there is a characteristic refresh time for propellants to reestablish nominal flow back into the combustion chamber. Due to differences in propellant densities, flow rates, injector outlet geometries, and injection pressure drops, the corresponding propellant refresh times often mismatch. This results in a transient and spatially varying equivalence ratio and total mass flow rate throughout the combustion chamber, ultimately reducing performance. The consequent reduction in flow conditions then invokes a rapid decline in chamber pressure, encouraging propellants to quickly surge back into the chamber, repeating the cycle.

In most cases, combustion instabilities are empirically characterized and minimized during

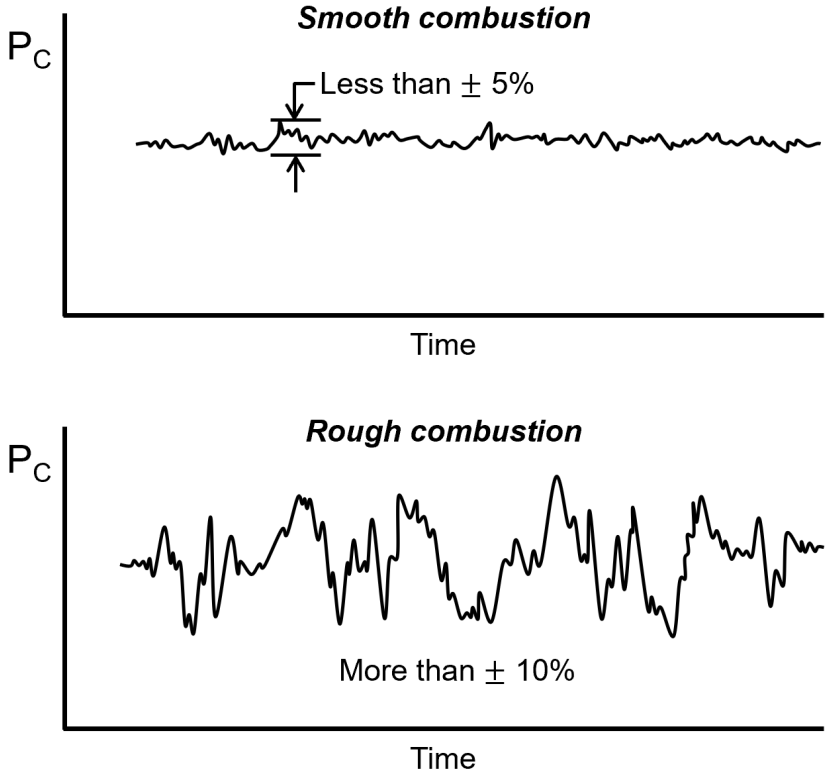

Figure 1.6: Example LRE chamber pressure traces for "smooth" (*top*) and "rough" (*bottom*) combustion.

engine development via hot-fire testing analyses, in which combustion system component and assembly designs are iteratively modified until instabilities are reduced below some predetermined allowable threshold. Classically, "quasi-stable" or "smooth combustion" is achieved when amplitudes of chamber pressure fluctuations do not exceed ±5% of the average chamber pressure, whereas "rough combustion" occurs when these pressure fluctuations exceed ±10% [58]. Fig. 1.6 illustrates example chamber pressure traces for smooth and rough combustion of LRE operation. Beyond limited preliminary design considerations, high-frequency instabilities are traditionally minimized through the use of stabilization methods designed in a highly empirical trial and error manner. These damping devices include baffles or acoustic resonance cavities that can absorb acoustic energy at discrete frequency ranges. Increasing injector stiffness ($\Delta P_{\text{inj}}/P_{\text{C}}$), analogous to increasing the injector's impedance, has proven to be a reliable method of reducing injection-coupled chugging modes. Injector stiffness

is traditionally recommended to be between 15–20% to promote stable combustion [58, 128], although the exact value will be dependent on the system and operational tolerances. While lower stiffness injection systems are desirable for lighter feed systems, they counter an effective combustion instability damping mechanism. Higher injector stiffness therefore requires larger/heavier feed pressurization hardware, and the implementation of damping devices both increase the complexity and overall dry mass of the vehicle, resulting in a decreased payload or mission duration capability for spacecraft and launch vehicles.

Linear instability behavior in combustion systems has been extensively studied, with much of the basic framework being established by Crocco and Cheng [33]. In order to describe chugging behavior in monopropellant LREs, Crocco introduced a simple time lag theory [29], which associates the fluctuations of combustion heat release and chamber pressure via the time lag (or phase shift) τ, between said fluctuations. This time lag is attributed to the sub-processes that must occur prior to complete combustion such as atomization, vaporization, mixing, and chemical kinetics. The classical time lag models were later improved upon by Crocco and Cheng [30–33], Hutt and Rocker [56], and Wenzel and Szuch [146], among others, which extended to high-frequency modes and accounted for parameters such as acoustic effects, damping mechanisms, bi-propellants, and other chamber-injector responses. Casiano [20] provided a detailed explanation of these time lag models and further expanded them for practical application on stability design for LREs, particularly those that employ deep throttling. For a more comprehensive review of combustion instabilities in LREs, the reader is referred to the following compilations edited by Harrje and Reardon [129], Santoro and Anderson [114], and Yang and Anderson [139].

Most research, especially the aforementioned pioneering studies, has been conducted using condensed phase (liquid-liquid or liquid-gas) injection systems due to their frequent use in the majority of space vehicles. Recently, full-flow staged combustion (FFSC) cycle engines, like the SpaceX Raptor engine, have gained traction due to their performance benefits compared to non-staged combustion cycles, and from their less extreme conditions

imposed on turbomachinery compared to oxidizer-rich staged combustion cycles [104]. FFSC cycle engines partially combust each propellant in fuel-rich and oxidizer-rich preburners to drive turbomachinery, ultimately delivering the propellants into the main combustion chamber in a gaseous or supercritical state. Non-condensed phase injection systems avoid many of the complex physical processes associated with liquid injection that can excite high-frequency intrinsic instabilities, such as droplet formation, vaporization, and multi-phase mixing interactions. Previous work done by Lemcherfi et. al. [76] and Pons et. al. [106] investigated the influence of propellant injection temperature on stability in a single-element combustor with staged combustion cycles that used a shear coaxial injector with gaseous methane-oxygen as propellants. It was discovered that higher temperatures of the fuel and oxidizer contributed to higher-frequency modes dominating, while lower injection temperatures prompted low-frequency chugging modes to prevail. Due to the dependence on injector design, additional combustion instability characterization of advanced gas-gas injection systems for next-generation liquid rocket engines is needed.

The second topic of this dissertation (covered in Chapter 4) is an examination of the combustion instability characteristics of a novel, additively-manufactured tri-coaxial methane-oxygen LRE injection scheme.

1.1.4 Injector hydraulics

In liquid rocket injectors, hydraulic performance is most closely associated with injector pressure drop, ΔP_{inj}. The static pressure drop in a liquid injector is associated with the acceleration of liquid propellants through the injector elements and into the combustion chamber. Typical values of injector ΔP_{inj} are on the order of hundreds of psi, or 15–20% of chamber pressure [58] (also known as *injector stiffness*). Injector stiffness (IS) is defined as:

$$\text{IS} \equiv \frac{\Delta P_{\text{inj}}}{P_{\text{c}}} = \frac{P_{\text{feed}} - P_{\text{c}}}{P_{\text{c}}} \tag{1.6}$$

Here, P_c represents the static chamber pressure and P_{feed} is the injector's propellant manifold pressure.

While higher values of ΔP_{inj} are associated with better atomization and improved suppression of combustion instabilities, high ΔP_{inj} is undesirable at the system or vehicle level. Higher ΔP_{inj} requires larger/heavier feed system pressurization hardware, which reduces overall vehicle performance via increased dry mass. Common LRE propulsion systems like gas generator or staged combustion cycles employ turbopumps to pressurize propellants and achieve improved system performance. In said systems, turbopumps rely on combusting propellants in pre-burners or gas generators in order to supply the energy necessary for turbomachinery to pressurize (i.e., do work on) the propellants. Increased propellant pressurization requirements demand greater work output from the turbopumps, thereby reducing the overall propellant efficiency when excess feed pressures are required to meet a given combustion chamber pressure. High ΔP_{inj} can also sometimes produce excessive propellant inlet velocities [53] and negatively affect LRE throttling capabilities [58].

Injector pressure drop, ΔP_{inj}, can be split up into two components:

$$\Delta P_{inj} = \Delta P_{ideal} + \Delta P_{loss} \tag{1.7}$$

Here, ΔP_{ideal} is the ideal pressure differential required to deliver propellants at a given mass flow rate into the combustion chamber, which assumes incompressible, inviscid flow with no energy losses (therefore, total pressure is conserved and no entropy is generated). This pressure differential across injector orifices imparts kinetic energy to the propellant jet, thereby supplying the energy required for efficient atomization and mixing. In contrast, ΔP_{loss} accounts for the hydraulic head losses associated with viscous energy dissipation from inertial (changes in flow direction) and frictional (surface) effects, both of which are contingent upon injector flowpath geometry and surface characteristics. ΔP_{loss} is a metric for quantifying the loss in *total* pressure. Hydraulic losses are undesirable because they reduce the total pressure

across the injector without contributing to the axial momentum of the liquid jet and should therefore be avoided. For impinging injectors, the manifold to orifice geometry is a significant contributor to ΔP_{loss}. The relevant features of orifice geometry include the entrance or inlet to the orifice, the bore diameter, the bore length, as well as the orifice exit profile.

1.1.4.1 Injector hydraulic losses

Liquid propellant flow through an impinging injector flowpath can be approximated as incompressible, fully-developed, steady, viscous flow through a circular pipe with gravitational effects neglected. Characterizing hydraulic losses (ΔP_{loss}) is of great importance to a designer because it informs propellant feed system hardware requirements to achieve specific flow conditions and ultimately influences the total dry mass of the vehicle. The two main contributors to ΔP_{loss} are primarily classified by either *frictional* or *inertial* viscous losses. That is, $\Delta P_{\text{loss}} \approx \Delta P_{\text{fr}} + \Delta P_{\text{inert}}$. Understanding the relative extent at which these two sources affect ΔP_{loss} informs potential injector design modifications that can enable fine tuning of total ΔP_{inj}. Each loss contributor can be predicted given a certain set of flow conditions and an injector geometry by using fairly simple fluid mechanical analyses, and are described in the following sections.

Frictional viscous losses (also known as *major losses*) result from the fluid's internal viscous shear stresses and are influenced by the surface roughness of the pipe walls. Increased wall surface roughness can cause relatively laminar flow to transition to turbulent flow more quickly, accelerating the growth of the boundary layer, and inducing higher wall shear stresses [42]. Consequently, total pressure reduced (ΔP_{loss} increased) via eddy generation and dissipative turbulence within the relatively large boundary layer. The frictional loss component ΔP_{fr} is defined as:

$$\Delta P_{\text{fr}} = f \frac{l}{D} \frac{\rho u^2}{2} \tag{1.8}$$

where f is the dimensionless *Darcy friction factor*, l/D is the flowpath length to diameter

ratio, ρ is the fluid density [kg/m^3], and u is the bulk flow velocity [m/s]. The friction factor for turbulent flow, $f = f(Re_\mathrm{D}, \varepsilon/D)$, is a function of Reynold's number, Re_D, and the *relative roughness*, ε/D. D is the flowpath diameter, and ε is the *equivalent roughness* – a length scale that represents the surface roughness of an irregular surface, defined by the height of a uniform sand-grain surface that would produce the same results as shown in Fig. 1.7. f is traditionally determined via empirical correlations from a Moody chart (Fig. 1.8) by knowing the Re_D and ε/D [89]. While different Moody charts exist for different flow conditions and pipe geometries, the case referenced here corresponds to steady, incompressible, fully-developed, round pipe flow. Recall that Reynolds number is defined as:

$$Re_\mathrm{D} = \frac{\rho u D}{\mu} \tag{1.9}$$

where μ is the dynamic viscosity of the fluid [Pa·s].

The Haaland equation [50], defined below in Eqn. 1.10, enables friction factor to be determined explicitly by approximating the implicit Colebrook–White equation:

$$\frac{1}{\sqrt{f}} = -1.8 \log \left[\left(\frac{\varepsilon/D}{3.7} \right)^{1.11} + \frac{6.9}{Re_\mathrm{D}} \right] \tag{1.10}$$

It should be noted that frictional losses are still present even when walls are smooth ($\varepsilon/D \approx 0$). That is, the Darcy friction factor, f, is non-zero, and can be approximated using the Blasius correlation equation [42]:

$$f = 0.3164 Re_\mathrm{D}^{-0.25} \tag{1.11}$$

For a given set of flow conditions and injector geometry, the expected range of Re_D can be determined, the relative roughness (ε/D) can be found through surface roughness measurements, and f can be estimated via the Moody chart (Fig. 1.8), the Haaland equation (Eqn. 1.10), or the Blasius equation for smooth pipes (Eqn. 1.11). However, careful consideration should be taken since the best achievable accuracy for these methods is around

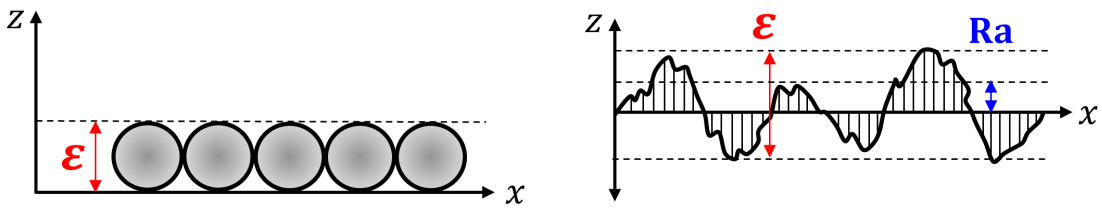

Figure 1.7: (*Left*) Schematic of equivalent sand grain roughness (ε) definition. (*Right*) Schematic of how average surface roughness Ra is defined, relative to ε on a representative surface profile.

10% [42]. Note that the Moody chart and it's associated correlation formulas is generally only valid for $\varepsilon/D \lesssim 0.05$. Due to inherent uncertainties, such as variability in relative roughness and experimental data used to generate the Moody chart, using more than about two significant digits in pipe flow calculations is generally unwarranted.

Alternatively, inertial viscous losses (also known as *minor losses*) are a result of flowpath geometry changes that cause flow to change direction, such as bends, expansions, contractions, or at the entrance (i.e., inlet) or exit (i.e., outlet) of fluid passageways. These momentum changes generate turbulent effects (e.g., flow separation, eddies, and vortices), removing energy from the flow and therefore increasing ΔP_{inj}. The inertial loss component of injector pressure drop, ΔP_{inert}, is defined as:

$$\Delta P_{\text{inert}} = K_{\text{L}} \frac{\rho u^2}{2} = K_{\text{L}} P_{\text{dyn}} \tag{1.12}$$

where K_{L} is an empirically determined constant known as the *loss coefficient*. For typical fluid systems, components such as valves, tees, and elbows are experimentally characterized and assigned a corresponding K_{L} value. In the context of an impinging liquid rocket injector, determining a loss coefficient can be challenging and very design-specific, requiring multi-dimensional analysis. However, an understanding of how general internal flow features and geometry influences K_{L} (and in turn, ΔP_{inert}) is valuable.

Fig. 1.9 illustrates how various flowpath entrance geometries affect K_{L}. Subfigure 1.9a.

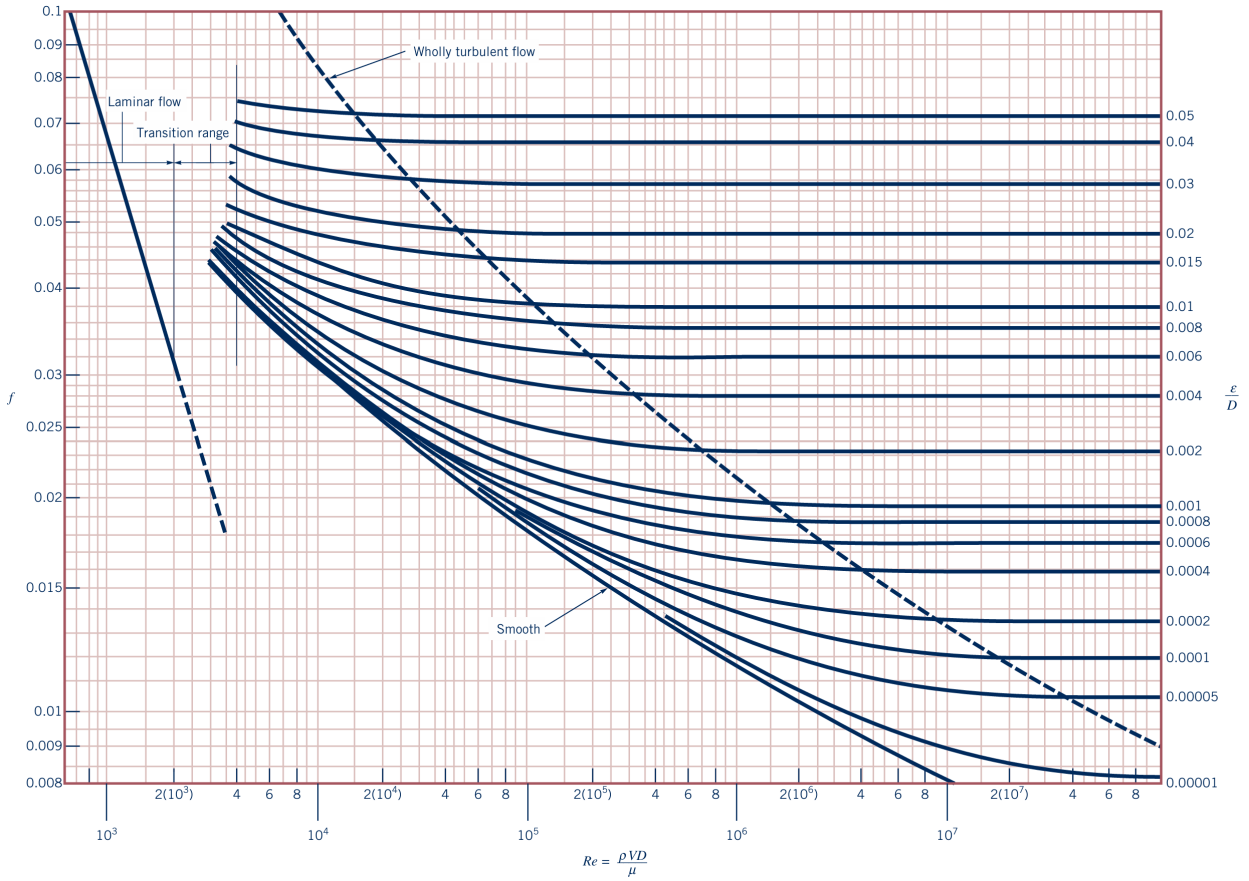

Figure 1.8: Moody chart: Darcy friction factor as a function of Reynolds number and relative roughness for circular pipes. From Ref. [42].

illustrates how sharp corners and sudden changes in flow direction and area can cause flow separation. This phenomena is known as a *vena contracta* effect and contributes directly to total pressure loss [42]. Subfigure 1.9b shows a flow schematic analogous to the entrance to the orifice section of an impinging injector element with sharp flowpath features, like those manufactured using conventional subtractive methods. Here, we can see how the velocity at the "throat" seen at position (2) is greater than that downstream at position (3) from a difference in local flow area. The inertial losses generated at the entrance, in addition to the fluid having to decelerate from position (2) to (3), both contribute to a drop in total pressure (ΔP_{loss}) from viscous dissipation. The bottom left and bottom right schematic in subfigure 1.9a. demonstrate how a rounded ("tapered") entrance can efficiently accelerate

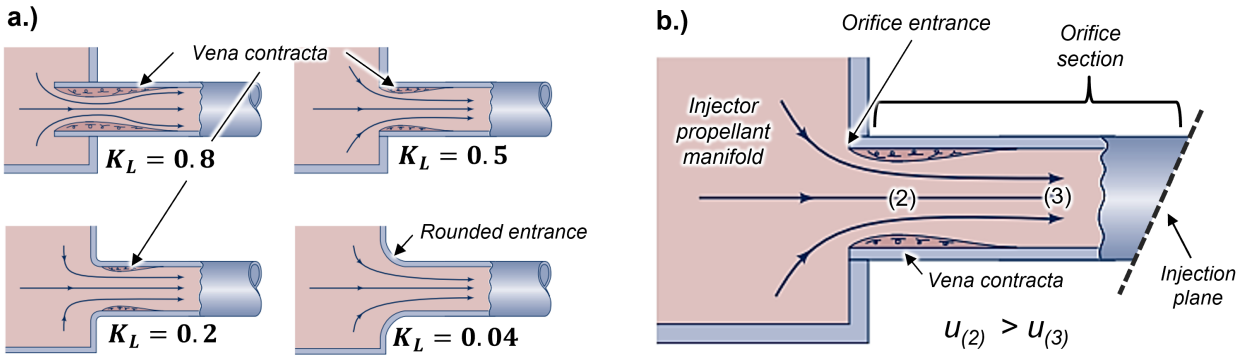

Figure 1.9: (a.) Examples of flowpath entrance geometries and their associated loss coefficients, and (b.) a flowpath schematic with inherent inertial losses relevant to an impinging injector design with sharp flowpath features. Images originally from [42] with labels added.

the flow with significantly reduced inertial losses. Herein lies the primary hydraulic benefit of an impinging injector design with tapered propellant flowpaths – a geometry enabled by additive manufacturing.

1.1.4.2 Hydraulic performance metrics

The *discharge coefficient*, C_{D}, is a key hydraulic performance parameter used to characterize the aggregate hydraulic losses of a fluid passageway. C_{D} may also be thought of as the fraction of effective cross-sectional flow area relative to the actual cross-sectional flow area. C_{D} relates the total injector pressure drop to known flow conditions and injector outlet (orifice) geometry, and is defined as:

$$C_{\mathrm{D}} \equiv \frac{\dot{m}_{\mathrm{meas}}}{\dot{m}_{\mathrm{ideal}}} = \frac{\dot{m}_{\mathrm{meas}}}{A\sqrt{2\rho\Delta P_{\mathrm{inj}}}} \tag{1.13}$$

Here, $\dot{m}_{\mathrm{meas}}$ [kg/s] represents the actual mass flow rate of propellant with density ρ [kg/m^2] through an orifice with a cross-sectional flow area A [m^2], and the total injector pressure drop ΔP_{inj} [Pa] across the measured flowpath. The ΔP_{loss} component of total injector pressure

drop can be determined from C_D by:

$$\Delta P_{loss} = \Delta P_{inj}(1 - C_D^2) \tag{1.14}$$

An ideal flowpath with minimal hydraulic losses would result in a $C_D \approx 1$, resulting in a $\Delta P_{loss} \approx 0$ and thereby conserving total pressure across the injector. A $C_D = 1$ would instead require the fluid to be inviscid.

Orifice discharge coefficients tend to gradually increase with larger orifice diameters, but are also highly sensitive to orifice inlet geometry. Work done by Friant et al [39] in the 1950's characterized injector discharge coefficient for various orifice inlet geometries (e.g., sharp-edged, chamfered, and rounded inlets) fabricated using conventional machining. Burrs located at the orifice inlet were a common manufacturing defect and were also included in Friant's study. Fig. 1.10 illustrates how orifice C_D generally trends with different orifice

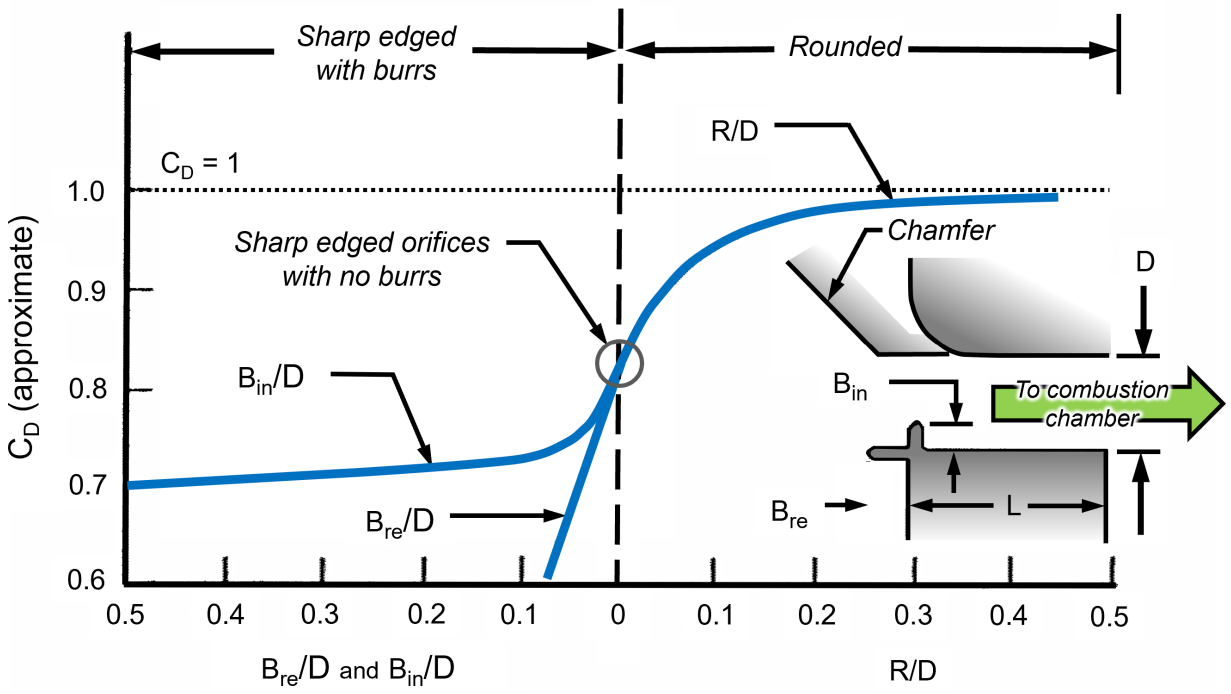

Figure 1.10: Discharge coefficient as a function of orifice inlet geometry. Adapted from Ref. [39].

inlet features and their associated characteristics (figure adapted from [39]). It was shown that rounded orifice entrance profiles with more gradual changes in flow area (higher R/D) achieved the highest C_{D}. In typical LRE impinging injectors, orifice C_{D}'s typically range from 0.50 to 0.92, with the higher end values enabled by smooth bores and rounded orifice inlets [58]. Rounded inlets can be formed using a special contoured mechanical cutting tool, but require direct accessibility for proper fabrication. Such conventional subtractive manufacturing techniques employ fixed tooling geometry and often have restricted tooling accessibility, which can complicate the already process-intensive injector fabrication.

Additionally, the *diodicity* (Di), is defined as a means of characterizing the relative backflow resistance of a flowpath. Diodicity is defined in Eq. 1.15 as the ratio of pressure drop for reverse flow to the required pressure drop in forward flow for the same mass flow rate, or can also be described in terms of forward and reverse discharge coefficients, as seen here:

$$\mathrm{Di} = \left(\frac{\Delta p_{\mathrm{rev}}}{\Delta p_{\mathrm{fwd}}}\right)_{\dot{m}} = \left(\frac{C_{D,\mathrm{fwd}}}{C_{D,\mathrm{rev}}}\right)^2 \tag{1.15}$$

Abrupt changes in liquid propellant flow direction can invoke high local flow velocities, causing liquid propellants to suddenly drop below their vapor pressure and violently expand into their gaseous state, known as *cavitation*. Cavitation is a phenomenon that is generally avoided in LRE component design due to its tendency to negatively influence the hydraulic and mixing performance by altering effective flow passages, and due to its high likelihood of causing hardware damage [58]. Injector flowpath designs that contain gradual changes in flow direction and flow area are desirable to discourage liquid propellant cavitation in addition to other inertial viscous losses, but conventionally-manufactured injectors are limited by traditional subtractive manufacturing techniques. A more in-depth review on the fluid mechanical theories that govern injector hydraulics is covered in Ch. 5.

The third and final topic of this work (covered in Chapters 5 and 6) is an assessment of the hydraulic performance benefits of novel liquid-liquid impinging

rocket injection schemes enabled by additive manufacturing.

1.1.5 Bipropellant selection

Most chemical rockets, especially those used for launch vehicles, use liquid bipropellants (i.e., one fuel and one oxidizer). The propellant combination chosen has a significant impact on overall LRE system performance and individual component design. In addition to performance considerations, LRE designers must also account for the cost, ease of handling, accessibility, and storage requirements when choosing propellants. Liquid propellants include both liquid fuels (hydrogen, RP-1, methane, monomethylhydrazine (MMH), etc.) and liquid oxidizers (oxygen, fluorine, nitric acid, dinitrogen tetroxide (NTO), etc.).

Methane-oxygen has become a particularly attractive liquid bipropellant combination for next-generation launch vehicles. This may be attributed to its high specific impulse, low tendency for thermal decomposition relative to kerosene-fueled systems, and ease of handling and leak management relative to hydrogen due to more moderate cryogenic temperatures and higher molecular weight [99, 128]. Such characteristics, amongst other benefits of methane, lend towards potentially more affordable and reliable re-usable launch systems. Despite these benefits, the design and optimization of liquid methane-oxygen rocket engines are considerably less mature than either kerosene- or hydrogen-fueled systems due to their extensive heritage. This lack of technical maturity motivates fundamental studies of methane-oxygen rocket combustion devices, including injectors, which serve a critical role in overall system performance and stability.

For modern booster-class rocket engines, liquid propellants are generally introduced into a combustion chamber in supercritical state (where liquids appear to behave more like dense gases) [23]. Furthermore, next-gen liquid rocket engines are expected to use staged combustion cycles that implement the use of pre-burners that partially combust their propellants to power turbomachinery prior to injecting them into the main combustion chamber in a gaseous

or supercritical state. As such, further studies on mixing and combustion characteristics of gaseous and supercritical methane and oxygen are needed to provide additional insight to injection design for next generation liquid rocket engines.

1.2 Additive manufacturing

1.2.1 Challenges of conventionally-manufactured injectors

Component manufacturing has traditionally been achieved through *subtractive manufacturing* – an encompassing term for various methods of controlled removal of material (via manual or computer-driven machining) from solid stock to form a final shape. In LREs, injector systems are commonly multi-component assemblies often comprised of several hundred individual injector elements that are later welded or brazed together to form a single injector plate. The design of the upstream feed-system manifold is often very complex and firmly coupled with the injection scheme and inter-element arrangement selection since multiple flowpaths require a single supply source [54]. The injector manifold must be able to provide all injector elements with uniform flow to ensure that targeted local mixture ratios and flow rates are achieved, and therefore demands a large amount of physical space. This manifold volume is known as "dribble volume" which controls the amount of time to prime the system, affects the transient behavior of engine start-up and shut-down, and is often a major source of performance reduction for in-space thrusters with short thrust pulses [54]. Reductions in dribble manifold volume has also been found to improve stability for low-frequency combustion instability modes [54]. Optimizing the multitude of design considerations can be difficult and process-intensive with traditional subtractive manufacturing methods.

The complexity of component design has historically been restricted by the geometry and accessibility of machining tools, which can be limiting for parts that require material to be removed internally such as for propellant flowpaths within an injector element or within the injector manifold. Specific to impinging injectors, orifice geometry and sizing are critical

design parameters that significantly affect propellant flow patterns, discharge coefficients, atomization quality and distribution, local mixing, and rates of local wall heat transfer [128]. Therefore, any manufacturing-related deviations from targeted orifice design (e.g., burrs, non-uniformity, etc.) can drastically impact performance and hardware survivability. LRE impinging injector orifices are traditionally fabricated via milling and drilling techniques. Orifice diameters have ranged from 0.004 in. to 0.75 in. for 1-lb-thrust engine and a booster-class engine, respectively, but typical orifice diameters fall somewhere between 0.015 – 0.080 in [43, 54]. For mixing and combustion performance considerations, small-diameter orifices are typically desired since they improve atomization and reduce vaporization times. However, smaller orifices consequently demand higher element density (number of injector elements per unit injector face area) to achieve higher flow rates and therefore higher thrust. A higher element density is typically desirable for performance considerations, but again is limited by the manufacturing complexity.

1.2.2 Additive manufacturing of metals

Contrary to traditional subtractive manufacturing techniques, *additive manufacturing* (AM) incrementally adds material one layer at a time, typically using a wire or powder feedstock that is melted and fused by a directed energy source until the final targeted part geometry is achieved [52]. AM enables rapid prototyping and testing of complex components, significant reductions in part count and part weight, and elimination of production-process steps. In combination, these benefits can ultimately lower the cost and time required to manufacture, assemble, and mature new component designs. AM technology has rapidly matured over the last decade and is being utilized for its lucrative benefits in a multitude of different industries such as medical, automotive, and aerospace [7]. Advanced metallic "super-alloys" with extremely attractive material properties are constantly being developed for additive manufacturing processes [123, 127, 151]. Furthermore, some modern AM printers also permit monolithic part fabrication that use multiple different metallic alloys, even those with precise

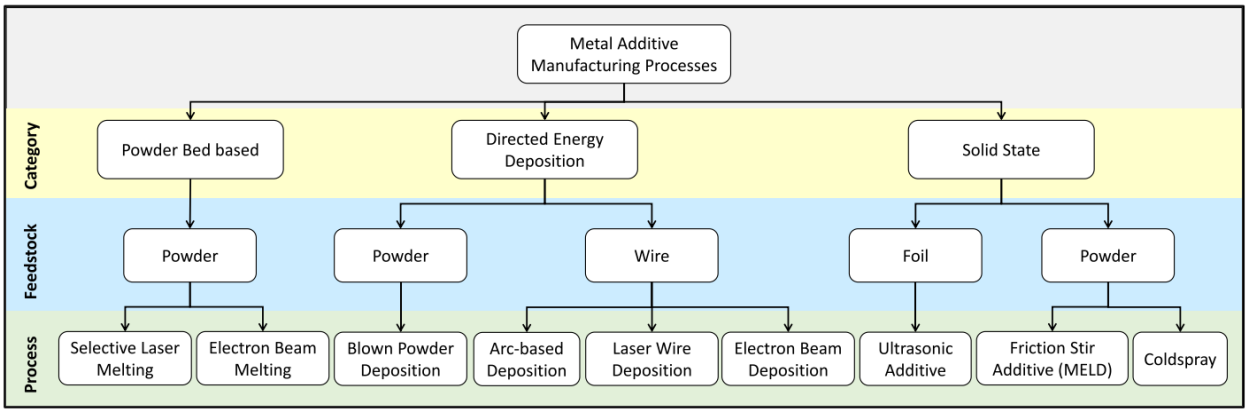

Figure 1.11: Various metal additive manufacturing methods. From Ref. [48].

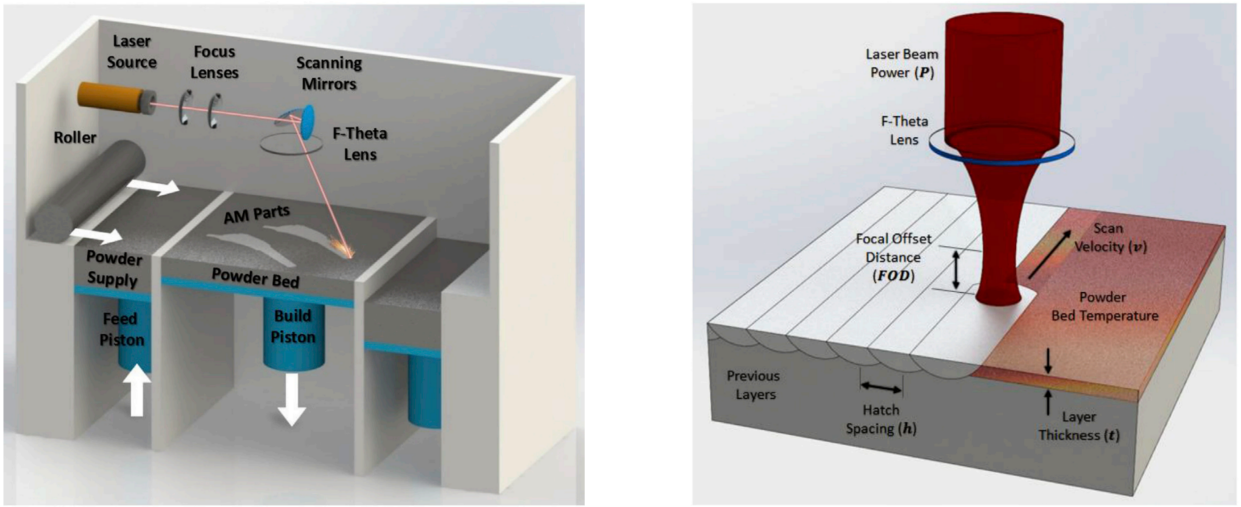

Figure 1.12: (*Left*) Schematic of a typical L-PBF machine. (*Right*) Schematic of the laser and powder bed interface with key operating parameters labeled. Both images from Ref. [120].

gradient-control of alloy mixtures [69, 94, 122].

Several metal additive manufacturing methods exist (see Fig. 1.11) ranging in complexity and application. A brief overview of these methods is highlighted here, but a more comprehensive description of how they operate along with their own inherent advantages and disadvantages can be found in [15, 48, 52, 112]. The type of AM method is chosen for part fabrication is primarily based on resolution requirements, complexity of features, and the scale or size of the part [48]. The most popular AM method in the aerospace industry, and

particularly relevant to this work, is Laser Powder Bed Fusion (L-PBF), which is well-known for producing high-precision, fully dense components [48]. L-PBF is also referred to as other names such as Laser Beam Melting (LBM), Direct Metal Laser Sintering (DMLS), and Selective Laser Melting (SLM). In the L-PBF method (shown in Fig. 1.12), metallic powder feedstock is selectively melted by a focused laser beam, and then rapidly solidifies layer-by-layer into a complete solid part [15]. Typical layer thicknesses for L-PBF range from 20 μm – 100 μm [52], enabling high feature resolution as small as $\sim$0.2 mm ($\sim$0.008 in) [15]. However, even modern state-of-the-art L-PBF technologies are limited by relatively small build volumes, with maximum achievable AM part sizes on the order of $\sim$400 mm, although larger systems are currently being developed [15].

1.2.3 Advantages of additively-manufactured injector design

Additive manufacturing with high-performance metal alloys (e.g., stainless-steel, inconel, titanium, aluminum, copper, etc.) is revolutionizing the design and development of combustion devices [48]. Examples of modern aerospace companies that are currently utilizing metal AM components include: SpaceX, Rocket Lab, Relativity, Boeing, Orbex, Blue Origin, Astra, Aerojet Rocketdyne, Lockheed Martin, and Airbus. Beyond the practical economic and production-rate advantages, AM also provides a more flexible design space, allowing for optimal material distribution and thus reducing the mass of components while maintaining critical mechanical and structural properties. This expanded design freedom from metal AM permits the fabrication of sophisticated three-dimensional geometries, enabling a new means to tailor the fluid dynamics of combustion devices to maximize performance, particularly related to propellant injection.

Additive manufacturing offers a multitude of benefits to LRE injector design and development. AM enables accelerated production of monolithic injector designs, allowing for rapid-prototyping, dramatically reducing part counts and total mass of injection systems, and

Figure 1.13: Additively-manufactured (L-PBF) LRE injectors for a range of thrust classes, printed and hot-fire tested at NASA MSFC. From NASA MSFC.

simplifying/improving interpropellant joint sealing. To date, AM injectors have demonstrated equivalent combustion performance to conventionally-manufactured injectors, and exceptional life-cycle performance over a wide range of LRE thrust classes [8, 44, 48, 49, 95, 96, 131]. AM injectors permit the implementation of complex fluid passageways and orifice profiles that can decrease injector forward pressure-drop, increase element density, enhance propellant mixing, and reduce injector manifold ("dribble") volume [8, 44, 48, 132], many of which can be achieved in a monolithic form. Several examples of additively-manufactured LRE injector designs (fabricated using L-PBF), which were printed and hot-fire tested by NASA MSFC, are pictured in Fig. 1.13.

Despite promising evidence of improved performance, the aforementioned tri-coaxial injector design also adds complexity to the multi-part, process-intensive fabrication of bi-coaxial injector element assemblies using traditional manufacturing methods, which require multiple components to be combined via brazing or welding for each injection element. Multi-element injector geometries, such as those used in a liquid rocket main combustion chamber, can employ up to hundreds of individual elements, with a correspondingly large number of parts with amplified process intensity. Recent works, including from our own research

group, have shown that coaxial injectors can be additively manufactured in a monolithic or single-part form factor, thereby reducing manufacturing complexity and risks associated with manufacturing error [3, 8, 93, 131]. Ahn et. al. experimentally assessed hydraulic and mixing performance of various additively-manufactured bi-coaxial injector elements via cold-flow testing and flow structure imaging, and discovered that despite having a lower discharge coefficient than traditionally-manufactured injectors from inherent AM surface roughness, the AM coaxial injectors demonstrated no significant problems with propellant injector and atomization [3]. Additive manufacturing flexibility further enables the geometrically tailored manifolding required to supply the optimal amount of propellant to each injector element [44, 48, 131]. Manifold design for optimal flow distribution becomes a greater challenge for tri-coaxial injection elements, along with the difficulty of inter-propellant sealing given the additional parallel flowpath. Additive manufacturing has the clear potential to address these complexities and enable the tri-coaxial injector design to realize its benefits.

1.2.4 Challenges of additively-manufactured injector design

Although the constraints of additive manufacturing are fewer in comparison to conventional subtractive manufacturing techniques, AM still has a few inherent challenges. One of the most difficult design restrictions to overcome when designing any additively-manufacturable component is staying within the unsupported overhang angle limit. This critical angle varies for different printing methods and materials, but often range between 30° to 45° with respect to the normal of the printing surface. As an injector's internal flow-path complexity increases in order to achieve desired performance outcomes, creating a design that is printable and structurally robust becomes a more arduous task. Additionally, the removal of residual unsintered powder from internal passageways is usually a necessary, but potentially difficult task within the injector where access is limited. Feature resolution often scales with the build-volume of AM printers. Therefore, achieving sub-mm feature resolution (relevant to injector orifice sizes) for relatively large parts, such as a full-scale high-thrust class injector

plate, is currently difficult, although not impossible. Fortunately, AM technology is still rapidly maturing, enabling the development of high-resolution, large build volume printers [15]. Smaller, current state-of-the-art printers have demonstrated repeatable feature resolution on the order of 0.010" which is expected to be sufficient for advanced AM injector designs. Structural properties of additively-manufactured parts may differ from the solid stock version of the same alloy. AM parts may also be anisotropic from inherent porosity and internal thermal stresses that can lead to crack propagation [15]. However, AM print parameters can be optimized and paired with post-print operations to improve material properties (e.g., heat treatments or hot isostatic pressing), which in some cases, have been shown to exceed those associated with conventional manufacturing techniques [37, 84, 136].

From a hydraulics perspective, the expanded design freedom of additive manufacturing enables flowpath tapering which mitigates the inertial losses generally associated with sharp features within conventionally-manufactured injector geometries. However, the increased surface roughness inherent to AM parts can introduce additional frictional viscous losses, potentially offsetting the hydraulic benefits of geometric optimization. The layer-by-layer manufacturing process creates a "stair-step effect" on sloped surfaces (illustrated in Fig. 1.14), thereby making layer thickness and print angle primary contributors to AM surface roughness. Several other factors that influence AM surface topology are metallic powder distribution, non-uniform melting, thermal effects, and laser scan strategy [27]. Limitations in the ultra-fine control of AM parameters inevitably results in a stochastic surface at small scales. Fig. 1.15 shows images captured by a scanning electron microscope of an AlSi10Mg L-PBF printed surface at various magnifications. The consequences of AM surface roughness are particularly meaningful in the small orifice geometry of impinging injectors, where cross-sectional flow area is minimized and flow velocity is maximized. At scales similar to smaller orifice diameters, AM surface roughness can occupy a finite and spatially-varying fraction of the orifice flow area. This can perturb flow characteristics and potentially shift C_{D}.

Fortunately, many of the aforementioned challenges associated with AM surface roughness

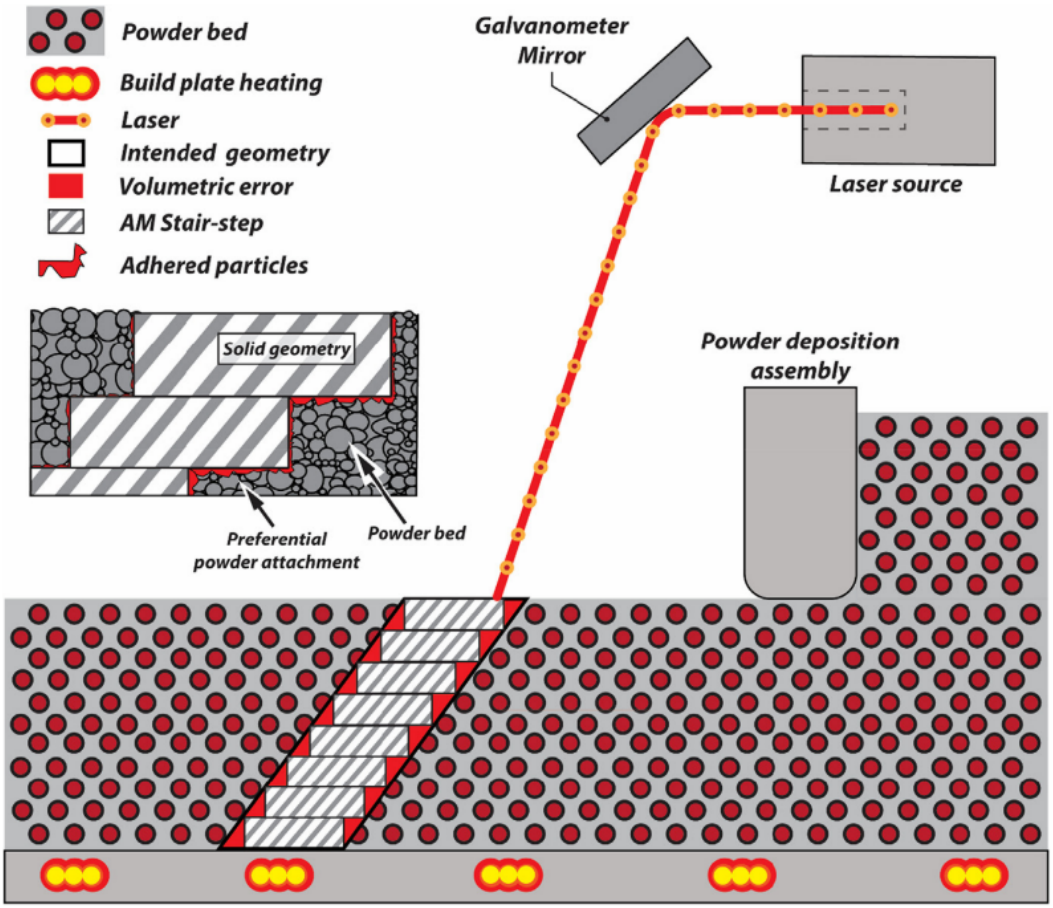

Figure 1.14: Another schematic of the L-PBF AM printing method, highlighting the "stair-step effect" relevant to surface roughness of AM parts. From Ref. [73].

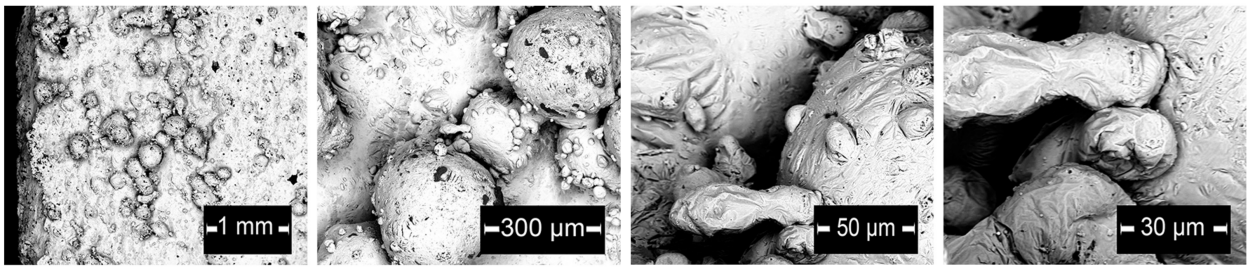

Figure 1.15: Multi-scale surface topology images captured by a scanning electron microscope of a AlSi10Mg part printed using L-PBF. From Ref. [137].

can be overcome by supplementing with post-print traditional subtractive manufacturing processes. For example, AM injector flowpath surface finish can be improved via flow polishing techniques (i.e., flow machining, or *honing*) as demonstrated by our research group in Ref. [97])

or simply through advancements in as-printed surface finish. For injector surfaces that require sealing or o-ring grooves, facing or turning on a lathe or mill may be adopted. Orifice geometries unable to be sufficiently resolved from printing may be formed from conventional or electrical discharge machining (EDM) drilling.

1.3 Scope and organization

This dissertation focuses on how advanced injector geometries enabled by additive manufacturing impact the following three topics of LRE operation: (1) combustion and mixing performance, (2) injector-related combustion instabilities, and (3) injector hydraulic performance. Novel injection schemes with AM-enabled features are investigated and assessed through both computational and experimental efforts, which include but are not limited to: computational fluid dynamics, cold-flow testing, hot-fire testing, laser absorption spectroscopy, and chemiluminescence imaging.

Chapter 2 examines propellant mixing of different LRE injector designs by employing a novel optical diagnostic technique (laser absorption tomography) on coaxial flames. Coaxial mixing length scales are characterized and compared for three shear coaxial injectors with varying oxidizer post recess. Methane and oxygen are used as propellants and combusted in an atmospheric burner. This technique generates quantitative distributions of temperature and carbon-monoxide concentration for a range of axial positions. Planar measurements are compiled to produce two-dimensional, spatially-resolved images of each flame's thermochemical structure. This technique also enables a unique method of directly capturing the stoichiometric mixing length.

Chapter 3 evaluates propellant mixing and combustion characteristics of a novel, monolithic, AM-enabled, methane-oxygen shear *tri-coaxial* injection scheme using two optical diagnostic techniques. First, the laser absorption tomography method described in Chapter 2 is employed to generate images of the thermochemical flame structure under ambient

conditions. Second, hydroxyl-chemiluminescence (OHCL) high-speed videography is used to capture OH* emission in-chamber at pressures up to 69 bar. Following some image processing, additional flame length scales are defined and measured. Combustion efficiency is also determined via characteristic velocity measurements. The compiled AM tri-coaxial injector results obtained from the multiple experimental evaluation techniques are compared to that of a conventionally-manufactured bi-coaxial injection scheme.

In Chapter 4, combustion instabilities are experimentally characterized for the novel tri-coaxial injector design through the employment of multiple diagnostics during hot-fire tests within a single-element high-pressure methane-oxygen combustor. Dynamic pressure within the combustor and the oxidizer feed system is measured using high-speed piezoelectric sensors. Additionally, high-speed OH* chemiluminescence videography captures fluctuations in the spontaneous emission of the excited hydroxyl radical within the combustor. Characteristic frequencies of combustion instability modes are predicted by computational models and also measured directly. Pressure amplitudes corresponding with the characteristic frequencies are also determined, and thermoacoustic coupling between the heat release from combustion and pressure fluctuations are also quantified. Measurements associated with the tri-coaxial injector design were compared to two traditional shear bi-coaxial geometries with and without a recessed central oxidizer post over a range of chamber pressures from 35–69 bar. Supplemental tests were also conducted using hydrogen-oxygen propellants, although methane-oxygen was the main propellant combination.

Chapter 5 focuses on minimizing hydraulic losses in an impinging liquid rocket injector through flowpath tapering enabled by an additively-manufactured design. The increased surface roughness inherent to additive manufacturing was also investigated. Computational fluid dynamics analyses were performed to inform injector design modifications based on a canonical conventionally-manufactured impinging injector. A combination of smooth-wall and rough-wall CFD simulations help distinguish the relative extent of the inertial and frictional viscous effects involved. An experimental testing effort supplemented the CFD analysis.

Based on CFD results, several promising AM tapered injector designs were down-selected for printing. Injectors were cold-flow tested over a range of injector pressure drop, enabling discharge coefficients to be measured to quantify hydraulic losses. Comparisons are made between the down-selected AM designs and the conventionally-manufactured geometries. Experimental results are also compared to CFD predictions.

Chapter 6 further explores the design space offered by additive manufacturing to implement geometric fluidic diodes and tapering features near the injection plane for an impinging injection scheme as a simple means of increasing diodicity, or backflow-resistance. Steady single phase and transient multiphase CFD analyses are conducted on novel injector geometries that characterize forward and reverse flow resistance, as well as backflow recovery behavior.

Lastly, Chapter 7 summarizes the conclusions obtained from this aggregate work and discusses current and future research directions relevant to the performance-enhancing potential of advanced rocket injection schemes enabled by additive manufacturing.

CHAPTER 2

Shear coaxial injector mixing and combustion examined by laser absorption tomography

The contents of this chapter have been published in the ***AIAA Journal of Propulsion and Power*** *under the full title "Shear Coaxial Methane–Oxygen Injector Mixing and Combustion Examined by Laser Absorption Tomography" [65]. Portions of this chapter's contents have also been presented at the* ***Western States Section Combustion Institute Fall 2023 Technical Meeting****, and presented / included in the conference proceedings for the* ***AIAA SciTech Forum, 2024*** *under the title of "Coaxial rocket injector mixing and combustion via mid-infrared laser absorption tomography" [66] and was awarded the* ***Walter R. Lempert Best Student Paper Award in Diagnostics for Fluid Mechanics, Plasma Physics, and Energy Transfer****.*

2.1 Introduction

Methane-oxygen has become an attractive liquid bipropellant combination for next-generation launch vehicles. This may be attributed to its high specific impulse, low tendency for thermal decomposition relative to kerosene fueled systems, and ease of handling and leak-management relative to hydrogen due to more moderate cryogenic temperatures and higher molecular weight [99, 128]. Such characteristics, amongst other benefits of methane, lend towards potentially more affordable and reliable re-usable launch systems. Despite these benefits, the design and optimization of liquid methane-oxygen rocket engines are considerably less mature

than either kerosene- or hydrogen-fueled systems due to their extensive heritage. This lack of technical maturity motivates fundamental studies of methane-oxygen rocket combustion devices, including injectors, which serve a critical role in overall system performance and stability.

Injector design has a significant impact on rocket engine performance because it governs the atomization and mixing of propellants to produce stable combustion within a characteristic axial distance and volume, while also maintaining combustor hardware durability [43]. Advancements in injector design, specifically those that enhance mixing and expand operating conditions, enable improved rocket combustor performance thus extending mission capabilities. For example, effective propellant mixing typically produces a shorter flame, which reduces the required length and mass of a rocket combustion chamber, which can be traded for payload or mission duration. Injectors that discourage combustion instabilities and maintain high-performance operation over a wide range of conditions are attractive for engines that require deep throttling, which can be used to optimize flight trajectories and reduce aerodynamic stresses on launch vehicles.

Several types of injector designs have been used for liquid rocket engines, with varying complexity and performance. Coaxial injectors (also known as "concentric-tube elements") have demonstrated high performance and reliability over a wide range of operating conditions due to rapid near-field mixing associated with shear-induced turbulence. Coaxial injectors typically have a high-density inner jet (typically oxidizer) and a low-density outer jet (typically fuel) with different relative velocities. Having an outer jet of fuel mitigates risk of hardware damage resulting from direct contact of the oxidizer with chamber walls. This coaxial injector type is classified into two main sub-categories: *shear coaxial*, where both propellants have outlet velocities that are axial and co-linear and mixing primarily occurs through shear associated with gradients in axial momentum, and *swirl coaxial*, where the flowpath geometry generates a tangential or angular velocity component in the coaxial streams that adds radial momentum and tangential shear that further enhance mixing. This work described in this

chapter focuses on shear coaxial injectors and their associated mixing characteristics. It is noteworthy that shear coaxial injectors have been used in prior liquid rocket engines such as the Space Shuttle Main Engine (SSME) and Vulcain II main stage engine, and are expected to play a role in next-generation methane-oxygen engines that use oxidizer-rich, staged combustion cycles where both propellants may enter the combustion chamber in a gaseous or supercritical state.

Optimal injector design typically relies on fundamental scaling parameters in order to correctly size the combustion chamber and its injector element configuration. Critical design parameters for shear coaxial injectors include fuel-oxidizer velocity ratio, momentum flux ratio, and the recess length of the oxidizer post, with associated performance metrics including radial diffusion or spread, axial flame length, combustion instability (frequencies and intensity), and characteristic velocity. Here we examine propellant mixing of different injector designs using a novel diagnostic method to measure mixing parameters. Notably, prior work has shown that recessing the oxidizer post relative to the injection plane, which introduces a region of pre-mixing prior to the main injection, leads to improved mixing, wider flame expansion, and sometimes augmented combustion efficiency, albeit with such benefits often traded against less desirable combustion stability characteristics [43, 67, 83, 121, 125]. Kendrick et al. [67] concluded that a recessed oxidizer post augments the momentum flux ratio by reducing the effective outlet area of the fuel duct, thus accelerating the stream and ultimately enhancing mixing. Quantifying such mixing benefits is important in refining injector design.

Experimental flow-field characterization efforts have utilized numerous optical diagnostic methods to examine mixing in reacting and non-reacting coaxial jets. These optical methods include visible high-speed imaging [101, 118, 134], chemiluminescence of combustion radicals [67, 83, 118, 147], particle image velocimetry (PIV) [17, 119], planar laser induced fluorescence (PLIF) [5, 40, 115, 119, 140], and x-ray fluorescence [12]. An established metric in analyzing the mixing characteristics of coaxial fuel-oxidizer jets is the *stoichiometric mixing length*, L_S [5, 12, 115, 140]. L_S is defined as the axial length between the injection plane and where a

stoichiometric interface contour intersects the jet centerline (see Fig. 2.1). Mass entrainment models capturing shear-induced turbulent flux across an interface of the two fluids indicate that stoichiometric mixing lengths of variable-density, non-reacting shear coaxial jets scale with a non-dimensional momentum flux ratio J [140]. This shear coaxial mixing model has been corroborated experimentally using acetone PLIF [5, 115] in non-reacting coaxial jets where conditions are favorable for such measurements. Further studies have found that mixing lengths for reacting shear coaxial flows scale similarly with J, but were found to be larger than their non-reacting counterparts [115]. The non-reacting studies provide critical insight into estimating L_S, but do not measure L_S directly as it would be in a reacting flow since the effects of heat release from combustion need to be accounted.

Notably, Tacina and Dahm [34, 130] used an equivalence principle method to resolve the differences in mixing lengths values for reacting and non-reacting flows which account for the density changes resulting from exothermic reaction. Considering this equivalence principle, Schumaker [116] used hydroxl (OH) PLIF imaging to measure mixing lengths in various coaxial flames, but discovered that an additional non-physical scaling factor (specific to the propellants used) was required to reconcile the reacting and non-reacting mixing length values. This disagreement was later determined to be an inherent byproduct of the OH PLIF measurement technique [12]. Recently, Bennewitz et al. [12] employed a novel x-ray fluorescence technique to measure the stoichiometric mixing length of shear coaxial flames and concluded that the Tacina and Dahm [34, 130] equivalence principle does a good job capturing the relation between reactive and non-reacting coaxial jet mixing. A common issue amongst the aforementioned imaging methods is that despite their high spatial resolution capability, they are generally more qualitative with regards to local species concentration. Additional quantitative diagnostics are needed to measure fundamental gas properties and characterize mixing in reacting coaxial flames to obtain a clearer understanding of how mixing and combustion performance is affected by injector geometry.

Our research group recently developed and demonstrated a mid-infrared laser absorption

tomography (LAT) technique that yields quantitative and spatially-resolved measurements of temperature and species in quasi-axisymmetric reacting flows [10, 11, 113, 143]. The work presented in this chapter focuses on adapting and applying this novel optical diagnostic technique to make planar species and temperature measurements on a single-element, shear coaxial injector flame using gaseous methane and oxygen propellants. The chapter includes a brief theoretical description of relevant mixing parameters as well as the laser absorption spectroscopy method, followed by a description of the experimental test facility and optical hardware interface. The tomographic data processing methods are then described for the quantitative interpretation of measured spectra to obtain species and temperature profiles in the reacting coaxial jet flame. The resulting spatially-resolved measurements are shown to provide valuable quantitative data in a form that can be directly compared to numerical models capturing the reacting fluid mechanics of injector design and the gas-phase kinetics of methane-oxygen combustion. The experimental method allows for alternative mixing length scales to be measured directly and enables a unique approximation of a flame's stoichiometric mixing length. In compiling the results, we evaluate the mixing effects of oxidizer post recess length within the near-field region of a shear coaxial GCH_4-GOX flame, relevant to next-generation liquid rocket injectors.

2.2 Theory

This section offers a brief review of theory to clarify some of the terminology and nomenclature used to describe the mixing characteristics of co-axial jets as well as the spectroscopic methods used to extract measurements of gas properties in the associated flames.

2.2.1 Bi-coaxial mixing

The complexities of the near-field flow structure from the interaction of two coaxial jets are illustrated in Fig. 2.1. The resulting flow-field is comprised of three zones. Zone I is the

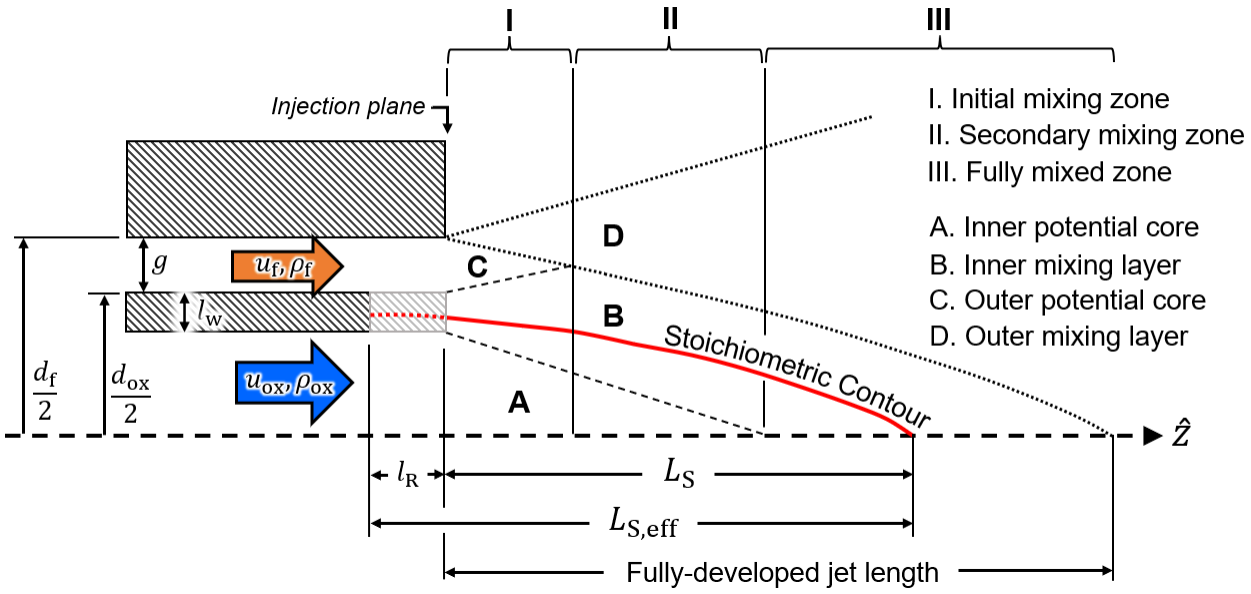

Figure 2.1: Near-field mixing schematic for bi-coaxial jet interaction with relevant dimensions and mixing length scales shown.

initial mixing zone where all jets penetrate the injection plane and is bounded by the end of the shortest potential core (unmixed fluid). This zone consists of the potential cores as well as the inner and outer mixing layers. As the flow progresses and mixes further downstream, the inner and outer potential cores decrease in size, whereas their corresponding mixing layers increase in size. The inner potential core contains only the inner jet fluid and the outer potential core contains only the outer jet fluid. Zone II is the secondary mixing zone where the majority of the mixing occurs via mass and momentum transfer. Zone III is the fully mixed zone which begins at the axial location where the most pronounced potential core finally terminates. Here, the coaxial jet behaves more like a single jet and becomes fully-developed. Injector outlet geometry, propellant properties, and flow conditions all influence the relative lengths of the potential cores.

In this theoretical diagram, g represents the annular gap width, l_w is the annular wall thickness, d_f is the inner diameter of the fuel outlet, d_{ox} is the outer diameter of the oxidizer post, and l_R is the recess depth of the oxidizer post relative to the injection plane, all of

which influence the downstream flow structure. At the interface of different propellant streams (within the inner mixing layer), a stoichiometric contour defines the surface at which stoichiometric diffusive flux conditions are met between the fuel and oxidizer. Recall that the stoichiometric mixing length L_{S} (a characteristic scaling parameter relevant to coaxial jets) is defined as the axial termination distance of the stoichiometric contour as seen in Fig. 2.1. An effective stoichiometric mixing length $L_{\mathrm{S,eff}}$ can be introduced specific to recessed injectors that extends upstream of the injection plane and starts at the outlet of the recessed oxidizer post, which is simply defined as:

$$L_{\mathrm{S,eff}} = L_{\mathrm{S}} + l_{\mathrm{R}} \tag{2.1}$$

where L_{S} is the traditional stoichiometric mixing length and l_{R} is the recessed length of the oxidizer post.

Two key non-dimensional metrics involved in the mixing processes of coaxial jets are the outer-to-inner velocity ratio (VR) and momentum flux ratio (J), and are defined here:

$$VR = \frac{u_{\mathrm{o}}}{u_{\mathrm{i}}} \tag{2.2}$$

$$J = \frac{\rho_{\mathrm{o}} u_{\mathrm{o}}^2}{\rho_{\mathrm{i}} u_{\mathrm{i}}^2} \tag{2.3}$$

The velocity ratio directly influences the intensity of shear layer interaction between the coaxial jets which relates to the amount of turbulent mixing that occurs, and also determines the length of the inner potential core [109]. Momentum flux ratio serves as an important additional factor in turbulent mixing intensity and radial spread, further accounting for differences in fluid density. A well-designed shear coaxial injector element should target off-unity velocity ratio and momentum flux ratio to enhance turbulent mixing between propellant jets.

While the aforementioned parameters and theoretical model provide a framework to

understand coaxial injector mixing, experiments that directly measure mixing length scales are required to validate the relationship between mixing lengths and velocity or momentum ratios for a given fuel-oxidizer combination and injector geometry. In this work, a laser absorption tomography technique is implemented that targets the nascent carbon monoxide (CO) present in coaxial methane-oxygen flames in order to infer a stoichiometric contour from species and temperature measurements to approximate mixing length scales, L_{S}, for coaxial injector geometries with varying oxidizer post recess depth.

2.2.2 Laser absorption tomography

Laser absorption spectroscopy (LAS) is a non-intrusive optical diagnostic technique that exploits the resonance of coherent light with the differences between quantum energy states of specific molecules, typically those with intrinsic dipole moments. LAS permits in-situ, quantitative measurements of species-specific physical gas properties within high-temperature gas flows. A brief overview of the fundamentals of LAS is provided here, while a more comprehensive review can be found in [51].

The change in energy associated with quantum state transitions assigns molecules their unique spectral fingerprints (i.e., lines). For a given spectral absorption line or set of lines, the Beer-Lambert law relates the attenuation of light intensity, or spectral absorbance, $\alpha(\nu)$, to thermochemical gas properties. For a non-uniform flow field, this is expressed as:

$$\begin{aligned} \alpha(\nu) &= -\ln\left(\frac{I_{\mathrm{t}}}{I_0}\right)_{\nu} \\ &= \int_0^L \sum_j P S_j(T(l)) X(l) \phi_j(\nu) \mathrm{d}l \end{aligned} \tag{2.4}$$

Here, I_0 and I_t are the incident and transmitted light intensities, respectively, at a specific wavelength or frequency, ν [cm^{-1}]. L [cm] is the aggregate absorbing path length, and P [atm] is the total pressure. $S_j(T(l))$ [cm^{-2}/atm] is the linestrength of rovibrational transition,

j, which is a function of temperature, $T(l)$ [K]. $X(l)$ is the mole fraction of the absorbing species, and $\phi_j(\nu)$ [cm] is the line-shape function. It should be noted that this expression is a line-of-sight integral over an optical path length with non-uniformity in temperature and species along the spatial dimension l.

For line-of-sight measurements of axisymmetric property distributions, tomographic deconvolution methods can be applied. The practice of utilizing laser absorption spectroscopy in combination with tomography is referred to as *laser absorption tomography* (LAT). Assuming an azimuthally symmetric flow field distribution, a tomographic reconstruction technique known as *onion peeling* can be employed [35]. The line-of-sight and spectrally-integrated absorption area, $A_{\text{proj}}(x)$, can then be related to the radially-resolved form of the integrated spectral absorption coefficient, $K(r)$ [cm^{-2}]. This relationship is described by Eq. 2.5:

$$\begin{aligned} A_{\text{proj}}(x) &= \int_{-\infty}^{\infty} \alpha(\nu)\mathrm{d}\nu \\ &= \int_{0}^{L(x)} K(l)\mathrm{d}l = 2\int_{x}^{R} \frac{K(r)r}{\sqrt{r^2-x^2}}\mathrm{d}r \\ &= \int_{0}^{L(x)} \sum_{j} PS_j(T(r))X(r)\mathrm{d}r \end{aligned} \tag{2.5}$$

In Eq. 2.5, $L(x)$ [cm] is the absorbing path length at position x, from the axis of symmetry. The radial distribution of temperature $T(r)$ and species mole fraction $X(r)$ are embedded in $K(r)$, which can be determined from $A_{\text{proj}}(x)$. As previously stated, this approach assumes an axisymmetric flow field, which is expected in the near-field region of a shear coaxial flame with sufficient time-averaging. A Voigt line shape function is used to fit the measured absorbance, $\alpha(\nu)$, and obtain the projected absorbance area, $A_{\text{proj}}(x)$ [cm^{-1}], thus eliminating the dependence on spectral line shape.

$T(r)$ is obtained by measuring two spectral absorption features of the same species and taking the ratio between the two (radially-resolved) integrated spectral absorption coefficients, $K_1(r)$ and $K_2(r)$. This approach eliminates the dependence on pressure and mole fraction,

such that $T(r)$ can be inferred from an aggregated linestrength ratio, as shown in Eq. 2.6:

$$R(r) = \frac{K_i(r)}{K_j(r)} = \frac{\sum_i S_i(T(r))}{\sum_j S_j(T(r))} = f(T(r)) \tag{2.6}$$

Linestrength values, $S(T(r))$, and their corresponding uncertainties are known for each transition and are obtained from spectroscopic databases (HITRAN [46] and HITEMP [110]). Given the measured temperature distribution found from Eq. 2.6, along with a known pressure, Eq. 2.7 shows that the mole fraction distribution of the absorbing species, $X(r)$, can be determined from the spectral absorption coefficient, $K(r)$:

$$X(r) = \frac{K_1(r)}{\sum_i PS_i(T(r))} = \frac{K_2(r)}{\sum_j PS_j(T(r))} \tag{2.7}$$

This procedure can be carried out across multiple parallel planes over a range of axial lengths, ultimately enabling quantitative two-dimensional imaging of gas properties within the plume of a propulsion-relevant flame [11, 113, 143, 144].

It can be noted that line pairs with a large difference in lower state energy, $\Delta E''$, are desirable for sensitive thermometry, correlating to absorption transitions with very different temperature dependence over the dynamic range of interest. To achieve the desired sensitivity, we examine the linestrength ratio, $R(r)$, for a pair of transitions to ensure that it varies significantly with temperature, T. The specific lines chosen for this study are shown in Fig. 2.2 at a representative combustion condition [11].

Carbon monoxide (CO) is targeted for LAT measurements due to its natural abundance in hydrocarbon flames and strong vibrational absorption in the infrared. CO is abundant in methane-oxygen flames because it is a stable combustion intermediate and precursor to carbon dioxide (CO_2). At fuel-rich conditions, CO is a significant product species. The CO rovibrational transitions that occur in the mid-infrared regime at $\nu = 2008.421$ and 2008.525 cm^{-1} (denoted as *Line A* and *Line B*, respectively) are a well-established line-pair used for

sensitive temperature and species measurements in combustion gases [11, 74, 113, 144]. This CO line-pair avoids cross-species interference with other species present in the gas medium and the linestrength ratio $R(r)$ of these two transitions varies considerably with temperature T, which is related to the pair's large difference in lower state energy $\Delta E''$. This temperature sensitivity can be approximated as:

$$\left|\frac{dR/R}{dT/T}\right| \approx \left(\frac{hc}{k_B}\right)\frac{|\Delta E''|}{T} \tag{2.8}$$

where h [J·s] is Planck's constant, c [cm/s] is the speed of light, and k_B [J/K] is the Boltzmann constant. Eq. 2.8 shows that sensitive thermometry requires line-pairs with a large $\Delta E''$.

Table 2.1 contains important spectroscopic parameters specific to the targeted ro-vibrational transitions of CO, and Fig. 2.2 shows an example absorbance spectra and linestrengths for conditions relevant to the methane-oxygen combustion associated with the coaxial flame experiment.

Table 2.1: Carbon monoxide rovibrational transitions selected for the methane-oxygen combustion experiment. Values are taken from HITEMP 2010 [110].

Line	Transition (ν'',J'')	Frequency [cm^{-1}]	Wavelength [nm]	E'' [cm^{-1}]	$S(T = 296$ K) [$cm^{-1}/(molec \cdot cm^{-2})$]
A	P(2,20)	2008.421	4979.04	5051.74	1.149×10^{-28}
B	P(0,31)	2008.525	4978.78	1901.13	2.669×10^{-22}

2.3 Methods

This section describes the test hardware, optical interface, testing procedure, and data-processing workflow for the shear coaxial combustion experiments using gaseous methane (GCH_4) and gaseous oxygen (GOX) as propellants. Single-element injectors are tested over a set of steady-state flow conditions within an atmospheric burner. Mixing length scales and species/temperature distributions are quantified for a variety of shear coaxial injector designs

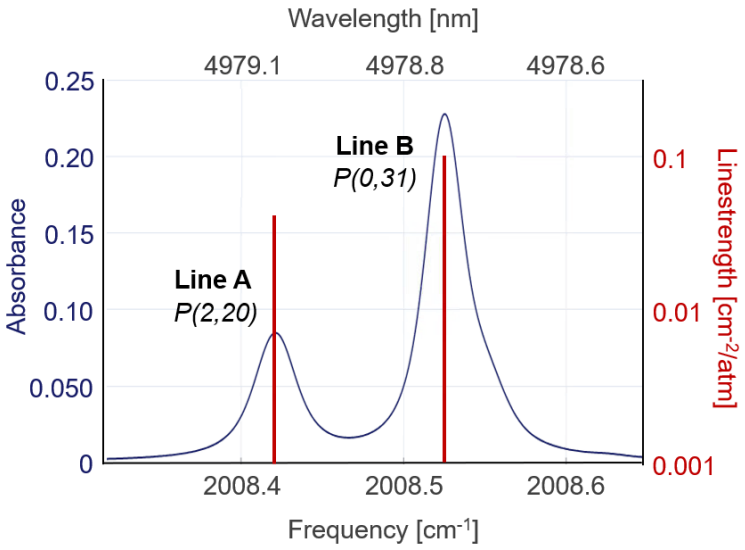

Figure 2.2: Simulated absorbance spectra [45] for relevant ro-vibrational transitions of carbon-monoxide at 3000 K and 1 atm with a pathlength of 0.4 cm.

using the laser absorption tomography technique which targets the CO present within the reacting flow-field.

2.3.1 Test hardware

Three shear coaxial injector designs with various oxidizer post recess depths, denoted A, B, and C, were tested in this study. Injector A was non-recessed and represents the baseline geometry with the oxidizer post flush with the injection plane. Injector B and C have oxidizer posts recessed by 4 mm ($l_R/d_{ox} = 0.7$) and 9.5 mm ($l_R/d_{ox} = 1.7$), respectively. All other critical dimensions, such as the oxidizer post outer diameter d_{ox}, wall thickness l_w, and the fuel annulus outer diameter d_f remain the same, and are specified in Table 2.2 with nomenclature defined in Fig. 2.1. The fuel-to-oxidizer area ratio, AR, is 0.75 for all three coaxial injectors of interest. As shown in Fig. 2.4, a single injector element consists of an oxidizer post and a fuel sleeve, installed inside a housing assembly for testing. Positioned at the injection plane is an N_2 co-flow plate with a total of 432 1/32" diameter holes where coaxial flow of gaseous nitrogen is used to mitigate the effects of entrainment and fuel reacting with the atmospheric

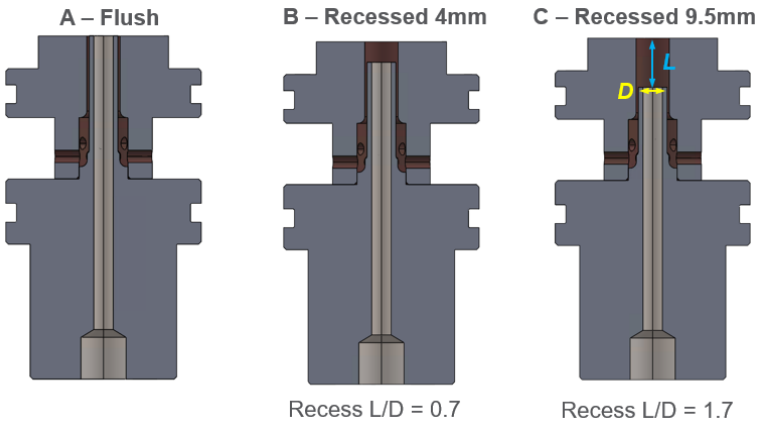

Figure 2.3: The three traditionally-manufactured shear bi-coaxial injectors with variable recess lengths.

oxygen within the near-field region of the flame.

Gaseous methane, oxygen, and nitrogen are supplied at constant flow rates using mass-flow controllers (MKS ALTA 0-200 slm with MKS 647C multi gas controller) at a target oxidizer-to-fuel (O/F) ratio of 3.0 and a target dilution ratio (N/O) of 3.0. O/F is defined by the oxidizer-to-fuel ratio of flow rates as shown in Eq. 2.9, with O/F = 4.0 being the stoichiometric condition for methane-oxygen combustion, and N/O is defined by the nitrogen-to-oxidizer ratio of flow rates as shown in Eq. 2.10.

$$\mathrm{O/F} = \frac{\dot{m}_{\mathrm{ox}}}{\dot{m}_{\mathrm{f}}} \tag{2.9}$$

$$\mathrm{N/O} = \frac{\dot{m}_{N_2}}{\dot{m}_{\mathrm{ox}}} \tag{2.10}$$

Total propellant mass flow rate (0.350 g/s) is defined by the sum of the mass flow rates of the oxidizer (0.265 g/s) and the fuel (0.089 g/s). These flow rates were chosen because they consistently produced a steady, stable, axisymmetric flame at relevant fuel-rich conditions for rocket combustion. Flow conditions were held constant for each test and can be seen in Table 2.3.

Table 2.2: Bi-coaxial injector dimension call-out.

Metric	Value	Units
AR	0.75	
d_{ox}	5.60	[mm]
d_{f}	6.50	[mm]
l_{w}	0.90	[mm]
g	0.45	[mm]
l_{R} (Inj. A)	0	[mm]
l_{R} (Inj. B)	4	[mm]
l_{R} (Inj. C)	9.5	[mm]

Table 2.3: Flow conditions used for each test. Velocity ratio VR and momentum flux ratio J are both defined by fuel-to-oxidizer.

Metric	Value	Units
$\dot{m}_{\mathrm{tot}}$	0.350	[g/s]
$\dot{m}_{\mathrm{ox}}$	0.265	[g/s]
$\dot{m}_{\mathrm{f}}$	0.089	[g/s]
O/F	3.0	
N/O	3.0	
VR	0.86	
J	0.38	

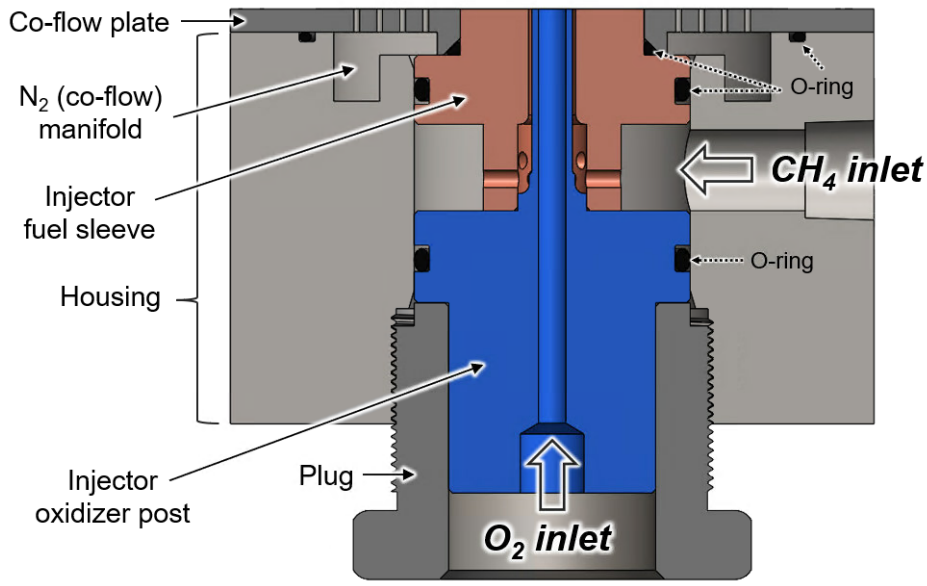

Figure 2.4: Cross-sectional view of the injector housing assembly.

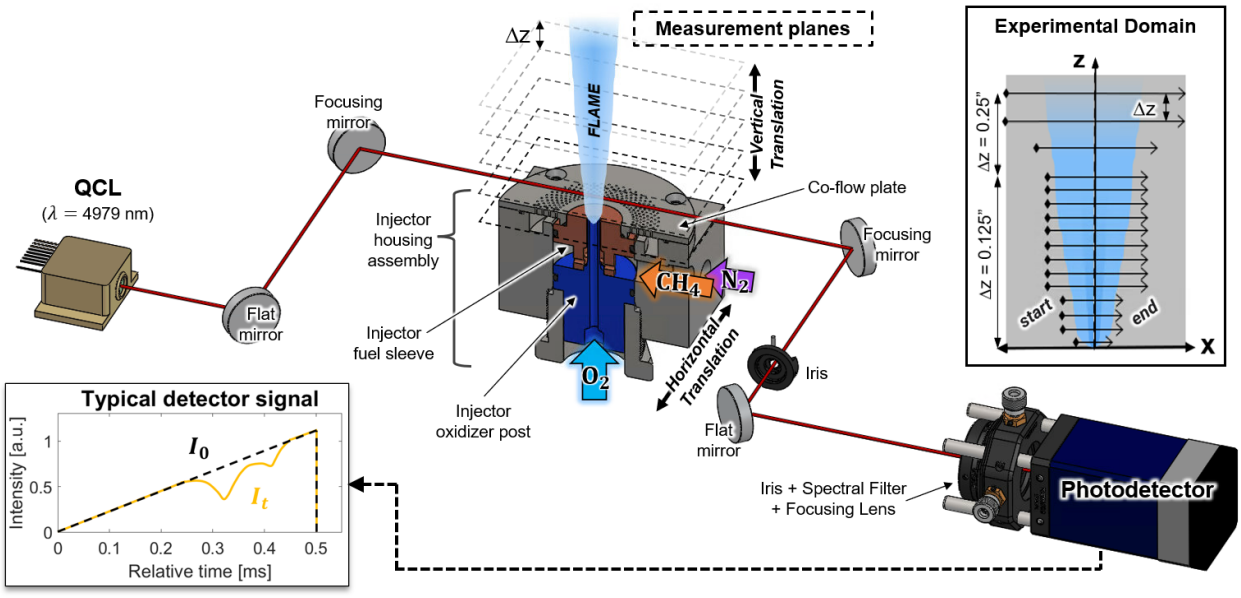

Figure 2.5: Schematic of shear coaxial combustion experiment with optical interface. *Top right*: Two-dimensional experimental domain, and *bottom left*: typical detector intensity signal showing absorption lines.

2.3.2 Optical interface

A schematic of the experimental setup and relevant optical hardware is shown in Fig. 2.5. A quantum cascade laser (QCL) with a wavelength centered near 4979 nm and output power of ∼70 mW was used to target the rovibrational transitions of CO shown in Table 2.1. Spatial resolution in the radial direction was maximized by using a long focal length mirror (f = 250 mm) to reduce the laser's beam waist down to ∼0.5 mm over the region of interest. A second focusing mirror with identical focal length was used to re-collimate the beam. The transmitted laser light passed through two irises and a spectral filter (4960 ± 148 nm) to mitigate emission effects, followed by a CaF_2 plano-convex lens to focus the beam onto a thermo-electrically cooled, DC-coupled photovoltaic (PV) detector (VIGO PVI-4TE-6-1x1).

The injector housing assembly was mounted on a Newport IMS300V 2-DOF motorized translation stage capable of both horizontal and vertical translation at user-specified velocities and positions using a Newport ESP301 motion controller. All optical hardware was fixed to

an optical table and remained stationary during testing. The lower bound of the experimental domain is represented by the injection plane (z $\approx$ 0 mm), while the upper bound of the experimental domain is an axial distance just before entrainment begins to interfere with the measurement, z $\approx$ 57.2 mm.

2.3.3 Experimental procedure

A scanned-wavelength direct absorption spectroscopy method was used to resolve the target absorption transitions, with spatial resolution achieved via translation of the injector rig as mentioned. The wavelength of the QCL was modulated by applying a 2 kHz sawtooth waveform to its injection current. Additionally, the laser was scanned below its lasing threshold to measure and correct for thermal emission, while the background was scaled to the non-absorbing regions to account for beam steering. Data from the PV detector (in the form of raw voltages) was recorded on a Picoscope 4824A oscilloscope at a sample rate of 1 MHz. Propellant and nitrogen flow rates were set on the mass flow controllers and monitored throughout each test run to ensure steady-state operation.

Planar measurements were taken for a total of 16 axial flame heights for each of the three injector geometries. The first 13 planar measurements were recorded with a difference in axial position Δz of $\sim$3.2 mm, whereas the remaining 3 were recorded with a Δz of $\sim$6.4 mm. As a result, the first $\sim$57.2 mm of the flow-field is resolved in two dimensions. Due to the divergent nature of the flame, experimental settings such as translation velocity, horizontal measurement range, test time, and number of averaged scans varied depending on the corresponding height in order to capture quasi-steady radial spatial resolution such that the steep gradients of temperature and CO concentration could be resolved within the near-field region.

The total number of spectral scans per planar measurement was a result of the laser scan rate (2 kHz) and the test or translation time (20 seconds for height slices 1 through

Table 2.4: LAT experimental settings applied to each injector.

z_i	Height [mm]	x_{range} [mm]	v_x [mm/s]	t_m [s]	Total scans	Scans averaged	Δr [mm]
z_1	0	10	0.5	20	40,000	800	0.2
z_2	3.2	20	1.0	20	40,000	400	0.2
z_3	6.4	20	1.0	20	40,000	400	0.2
z_4	9.5	20	1.0	20	40,000	400	0.2
z_5	12.7	40	0.8	50	100,000	500	0.2
z_6	15.9	40	0.8	50	100,000	500	0.2
z_7	19.1	40	0.8	50	100,000	500	0.2
z_8	22.2	40	0.8	50	100,000	500	0.2
z_9	25.4	40	0.8	50	100,000	500	0.2
z_{10}	28.6	40	0.8	50	100,000	500	0.2
z_{11}	31.8	40	0.8	50	100,000	500	0.2
z_{12}	34.9	40	0.8	50	100,000	500	0.2
z_{13}	38.1	40	0.8	50	100,000	500	0.2
z_{14}	44.5	50	1.0	50	100,000	400	0.2
z_{15}	50.8	80	1.6	50	100,000	250	0.2
z_{16}	57.2	80	1.6	50	100,000	250	0.2

4, and 50 seconds for slices 5 through 16). Therefore, a 20 second test resulted in 40,000 total spectral scans and a 50 second test resulted in 100,000 total scans. The absorbance was then calculated via the Beer-Lambert Law (Eq. 2.4) for each scan. Although the near-field region of the flame is approximated to be steady-state, it is actually turbulent on small scales throughout and therefore requires that the absorbance of every few hundred scans be averaged. The number of scans averaged for each slice is dependent on the translation velocity, v_x, and is chosen such that the radial integration, Δr, is 0.2 mm and so that minimal time-dependent variation is observed. We note that the beam size will ultimately limit radial resolution to around 0.5 mm, and thus these methods preserve that resolution. Table 2.4 specifies the horizontal measurement range x_{range}, constant horizontal translation velocity v_x, test duration t_m, number of scans averaged, and the resulting spatial integration in the radial direction Δr for each axial plane z_i.

2.3.4 Spectroscopic data processing

This subsection outlines the procedure involved in converting line-of-sight integrated absorption data to radially-resolved profiles of the integrated spectral absorption coefficient $K(r)$ from a one-dimensional radial inversion scheme. By assuming an axisymmetric flame, temperature and CO mole fraction distributions can be recovered from $K(r)$ at each axial position enabling a two-dimensional flow-field reconstruction of thermochemical properties.

Fig. 2.6 illustrates the main steps of the data processing workflow for planar thermometry measurements at a representative axial position. The measured absorbance $\alpha(\nu)$ was obtained through Eq. 2.4 using the incident and transmitted light intensities. A Voigt line-shape function was least-squares fit to the target lines within the absorbance spectra. The absorbance results were averaged as described (specific to each axial position, denoted in Table 2.4) before calculating the projected absorbance areas, $A_{\text{proj}}(x)$, through Eq. 2.5. As seen in Fig. 2.6, the fractional residuals from Voigt fitting were typically less than $\pm 1.5\%$ for the targeted CO line pair. Motorized translation of the injector test article enabled spatially-resolved measurements, plotted here as a function of distance x from the center axis ($x = 0$ mm). The position x is obtained by multiplying translation stage speed v_x by the time instant.

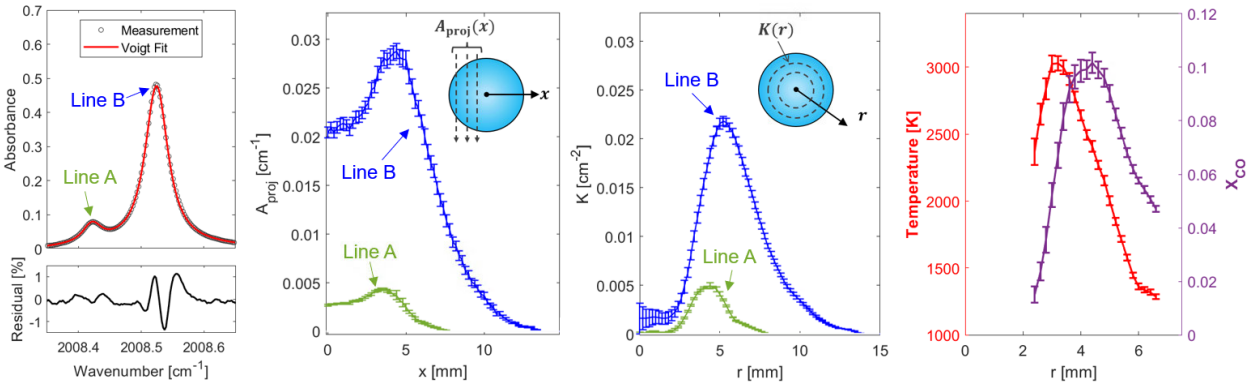

Figure 2.6: LAT data processing workflow for a representative axial position. From *left--to-right*) Measured CO absorbance with a Voigt line-shape fit of averaged scans, A_{proj} *versus* distance x from the center axis of the injector element, radially-resolved $K(r)$ from onion-peeling method, and the resulting temperature and CO mole fraction distributions.

$A_{\text{proj}}(x)$ measurements across the entire flame were mirrored and averaged about the injectors' center axis to verify an axisymmetric flow-field (see Fig. 2 in [11]). Thereafter, a Tikhonov-regularized inversion method [35] (i.e., onion-peeling) was implemented to transform the $A_{\text{proj}}(x)$ distributions into radially-resolved profiles of the integrated absorption coefficient $K(r)$. Temperature was extracted from each radial $K(r)$ value through Eq. 2.6, and subsequently, CO mole fraction was determined from Eq. 2.7 to obtain the complete radially-resolved thermochemical flame structure. The onion-peeling method was chosen over alternative inversion methods, such as 2-pt and 3-pt Abel inversion [35], as it was shown to minimize the need for regularization or smoothing and therefore provided good resolution of the steep gradients of gas properties associated with the reacting coaxial flow-field in this experiment. The total localized uncertainty for each point i in $K(r)$ can be approximated as:

$$\delta K(r_i) = \frac{N_i}{\Delta r}\xi_i \tag{2.11}$$

where N_i is the local error in the projected absorbance area data $A_{\text{proj}}(x)$, Δr is the radial spatial resolution, and ξ_i is the noise coefficient specific to the deconvolution method at data point i. The reader should refer to Appendix A (Sec. 2.5.1) for a more detailed review of the onion-peeling inversion method and the corresponding uncertainty, which is translated to error bars in subsequent plots.

It is important to note a few additional details and assumptions pertaining to LAT data processing. When fitting the spectra, the temperature was first set to a guessed value that aligned with an estimate predicted by chemical equilibrium. The Doppler width $\Delta\nu_D$, collisional width $\Delta\nu_C$, and the projected line-of-sight area $A_{\text{proj}}(x)$ were set as free parameters and solved using the initial temperature estimate. Once $A_{\text{proj}}(x)$ was found, Eq. 2.6 was used to calculate the new temperature value using the aforementioned two-line thermometry technique. An updated Doppler width was determined from this new temperature. These steps were iteratively repeated until a convergence criterion was satisfied, which required the

temperature residual to fall below 0.1 K.

A sufficient signal-to-noise ratio (SNR) on the measured absorbance spectra is required to determine thermochemical properties. Absorbance SNR is dependent on several factors – particularly the mole fraction of CO and the temperature of the CO molecules present in the beam path. As seen in the Beer-Lambert Law (Eq. 2.4), absorbance is directly proportional to mole fraction, as well as each transition's linestrength (which is temperature dependent). The thresholds determined to produce an adequate SNR for confident thermochemical measurements was a CO concentration of 1%, and a minimum CO temperature of 1000 K. Henceforth, results in regions within the measured flow-field that had an insufficient amount CO present, or regions that were too cold, are omitted. As seen in Fig. 2.1, the inner potential core of the flow-field is cold gaseous oxygen, therefore it should be expected that temperature and mole-fraction cannot be measured in the core of the flame.

2.4 Results & Discussion

Quantitative, planar measurements of gas properties were collected for each injector at various axial distances and used to assess how oxidizer post recess depths influence mixing length scales. Data were recorded at 16 different axial positions which captured the first 2.25 inches of the reacting flow-field for each injector. The 16 planar measurements were then combined to create 2D images to depict how temperature and CO mole fraction spatially evolve throughout each flame. Mixing length scales are derived from the data, highlighting mixing characteristics associated with differences in injector design.

2.4.1 Planar thermochemical measurements

Temperature and CO mole fraction radial profiles were measured at varying axial positions along the flame, indicating the reacting flow evolution. Fig. 2.7 displays how temperature and CO concentration evolve in both the radial and axial directions for the non-recessed baseline

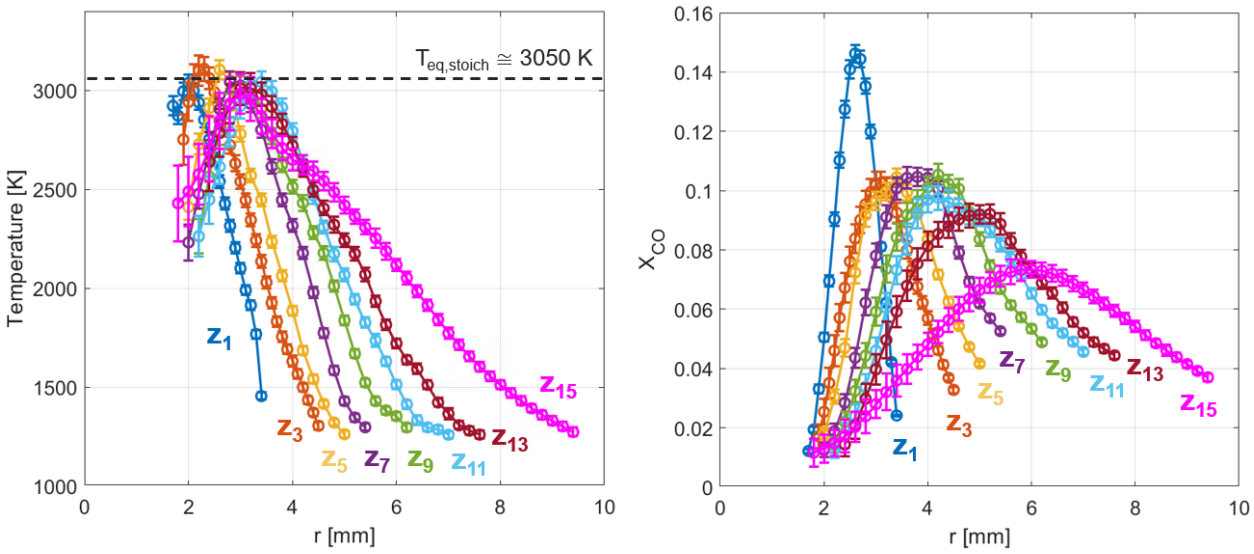

Figure 2.7: Radially-resolved thermochemical results for non-recessed nominal injector A. Temperature (left) and CO mole fraction (right) distribution shown for multiple height slices.

injector (injector A). Note that the center of the axisymmetric flame is denoted by $r = 0$ mm. Recall that temperature and CO mole fraction measurements can only be made when 1) a sufficient amount of CO is present within the flow-field, and 2) the temperature along the line-of-sight is within a specific range where each targeted transition produces a sufficiently high linestrength. Due to the nature of shear coaxial injector elements, an oxidizer-rich (inner potential) core prohibits thermochemical measurements within this narrow region. A shortened oxidizer-rich core is associated with less data missing from the center of the flow-field, and typically indicates enhanced mixing and a reduction in the stoichiometric mixing length.

Variation in combustion temperatures depends on the local ratio between the oxidizer and fuel (O/F ratio). Fig. 2.8 shows how temperature varies with the O/F ratio for methane/oxygen combustion at one atmosphere. Using the NASA Chemical Equilibrium with Applications (CEA) solver [47], the stoichiometric flame temperature for an atmospheric methane/oxygen reaction is predicted to be $T_{\text{eq,stoich}} \simeq 3050$ K, whereas the maximum equilibrium temperature is predicted to be $T_{\text{eq,max}} \simeq 3060$ K at a slightly fuel-rich condition.

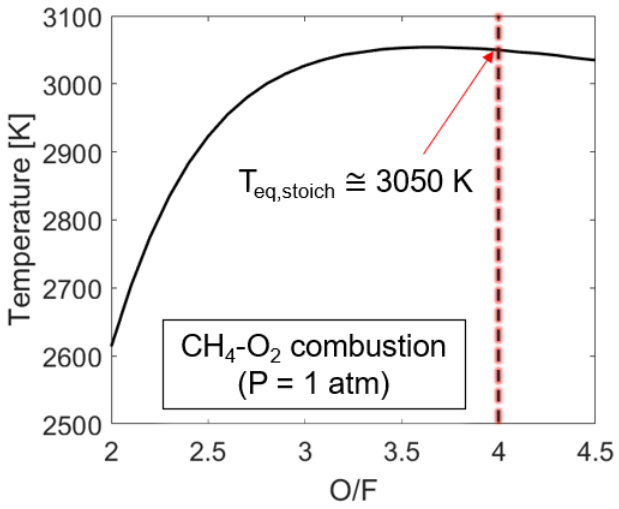

Figure 2.8: Equilibrium temperature *versus* O/F ratio for methane/oxygen combustion at 1 atm. Values determined by NASA Chemical Equilibrium Solver [47].

The stoichiometric temperature is plotted alongside measured temperatures in Fig. 2.7 for reference. Despite the global O/F ratio determined by the pre-established flow conditions (Table 2.3), a steep gradient of O/F fluxes exists within the interface region of the oxidizer and fuel jets. Therefore, the localized O/F ranges from oxidizer-rich (O/F $>$ 4) towards the center of the injector element (r = 0 mm), to fuel-rich (O/F $<$ 4) towards the exterior of the annular fuel gap of the injector element, at longer radial distances. Diffusion and mixing of the combustion products with the relative cold nitrogen co-flow also leads to a reduction in CO mole fraction and temperature at increasing radial position. The stoichiometric condition can be approximated as occurring within near where the coaxial flame temperature peaks. Notably, the predicted value for equilibrium temperature at stoichiometric conditions (at one atmosphere) demonstrates good agreement with the local maxima of the radially-resolved temperature distributions for each axial plane, as depicted in Fig. 2.7.

Planar thermochemical results are compared between the three injectors of interest at four representative axial planes in Fig. 2.9 to highlight differences in each injector's thermochemical spatial evolution. The magnitudes and corresponding radial locations of peak temperature and peak CO mole fraction indicate that oxidizer post recess directly affects the

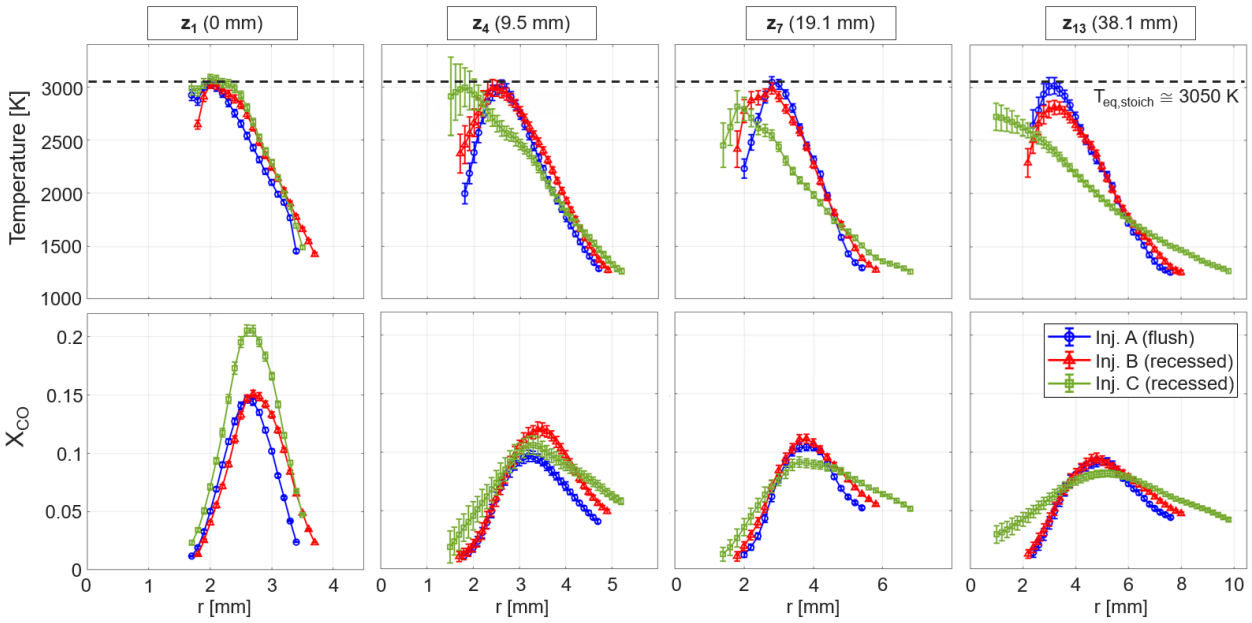

Figure 2.9: Comparison of radially-resolved temperature and CO mole fraction distributions at various axial positions shown for all three injectors.

mixing characteristics of the reacting flow-field. Most noticeably, injector C ($l_R/d_{ox} = 1.7$) demonstrates significantly different temperature and CO mole fraction profiles than those of injectors A and B. At the immediate outlet of the injector (i.e., the injection plane, $z_1 = 0$ mm), the temperature profiles for the three injectors appear very similar and peak values agree well with the predicted equilibrium temperatures. As the reacting flow progresses downstream, the radial position of the peak temperature value for injector C visibly shifts towards the center of the flame (r = 0 mm), whereas injectors A and B share similar peak temperature locations (2 mm < r < 4 mm) within the first 40 mm downstream. Additionally, the magnitude of the peak temperature value begins to decrease further downstream in the flame as recess is increased. This drop in maximum temperature is associated with an increase in radial diffusion of combustion products with the co-flow. This is most obvious for injector C, but is also subtly apparent with injector B at higher axial positions (i.e., z_{13} in Fig. 2.9).

Regarding CO mole fraction profiles, injector C shows a ∼35% higher peak concentration of CO at the injection plane with mole fractions of 0.148, 0.150, and 0.205 for injectors A, B,

and C, respectively. This likely indicates greater combustion progress for injector C associated with greater pre-mixing prior to propellants reaching this first measurement plane. We note that the first measurement plane, while referenced as z = 0 mm datum, spatially integrates the first 0.5 mm of axial height above the burner (associated with the laser beam size). It is notable that significant combustion progress occurs for all injectors within this short distance from the injector face. Injector C further demonstrates a wider radial distribution of CO compared to injectors A and B. However, with greater recess, the magnitudes of the peak CO mole fraction decline at a faster rate as the flow progresses downstream associated with increased radial diffusion with the co-flow and potentially some increased chemical kinetic progress towards carbon dioxide relative to the other injectors. Additional evidence that increased recess yields higher radial diffusion can be clearly seen by the wider radial spread of CO. Mixing length scales such as CO radial mixing and diffusion are quantified and discussed more in depth in Sec. 2.4.3.

2.4.2 Spatially-resolved thermochemical images

Planar measurements from all 16 axial positions were compiled to form two-dimensional images of both temperature and CO mole fraction. Fig. 2.10 shows the thermochemical structure for each each injector considered, with temperature on the left r-z plane of symmetry and CO mole fraction on the right r-z plane. The 2D images are not smoothed to highlight spatial resolution in the axial direction. As previously mentioned, spectroscopic measurements cannot be made within the oxygen-rich core where there is an insufficient amount of CO present, and thus this domain appears as gray in the temperature images (or dark blue in the X_{CO} images).

A flame expansion angle θ, is used to characterize the radial diffusion of the non-premixed coaxial flame driven by turbulent mixing. Here, it is defined by the radial position of the outer boundary where the CO mole fraction is equal to $X_{\mathrm{CO}} = 0.05$ for each axial position

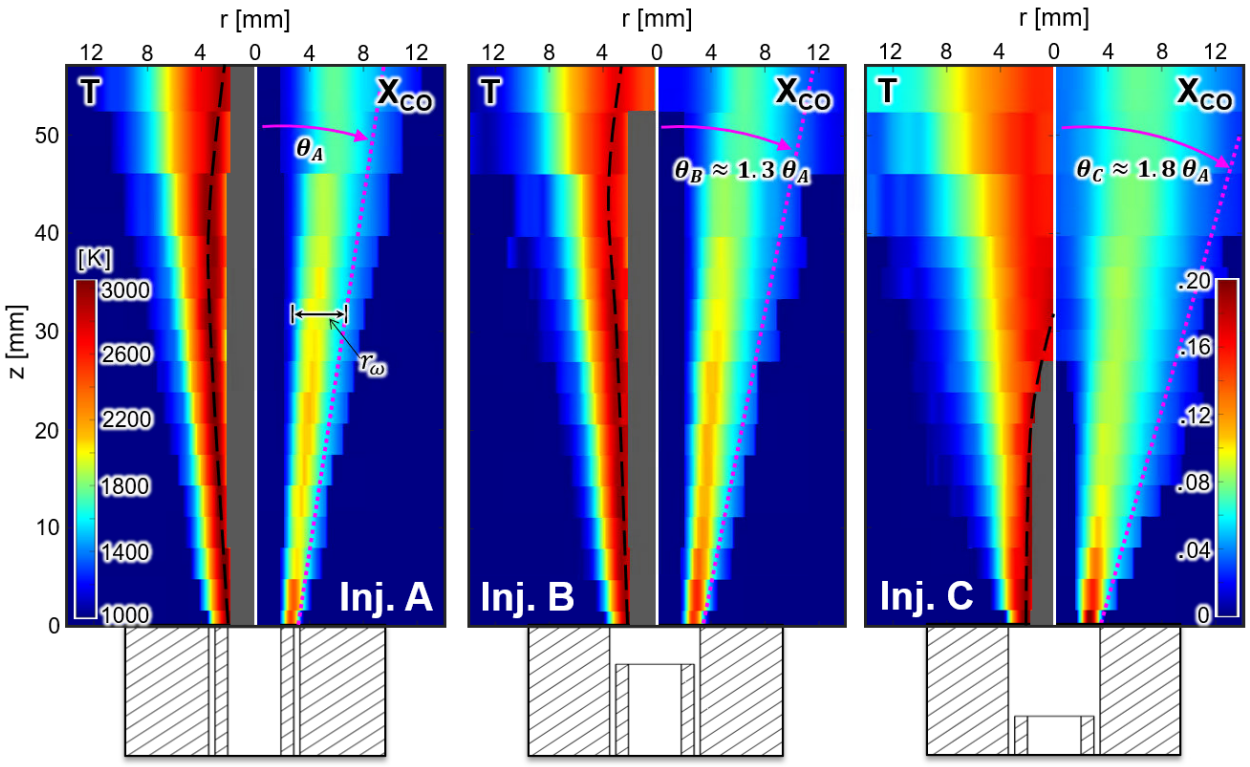

Figure 2.10: Two-dimensional images of thermochemical flow-field reconstruction enabled by laser absorption tomography. Temperature and CO mole fraction contour plots are shown for all three injectors. Inferred stoichiometric contours are outlined by black dashed lines.

within the first inch (∼25 mm) of each flame. This produces a linear trend across the planar measurements at different axial positions and enables an expansion angle to be measured for each flame. Each flame expansion angle value is normalized by the non-recessed injector (θ_{A}) and are specified in Table 2.5 and highlighted in 2.10. Injector B and C had a 30% and 80% larger flame expansion angle compared to the flush injector A. Greater oxidizer post recess demonstrated a wider flame expansion as a result of increased pre-mixing in the recess volume where radial expansion is initially constrained before entering the larger unconstrained co-flow domain.

Despite injectors B and C both being recessed, ($l_{\mathrm{R}}/d_{\mathrm{ox}} = 0.7$ and 1.7, respectively), injector B more closely aligns with the thermochemical distributions of the non-recessed injector (A). Aside from a slight increase in flame expansion, differences between the thermochemical

Table 2.5: Normalized relative flame expansion angles calculated for each injector's flow-field.

Injector	θ/θ_A
A	1
B	1.3
C	1.8

images of injector A and B are subtle. Within the first 30 mm of the flow-field, injector B shows a marginally higher concentration of CO than injector A, ranging from only 3% to 23% higher when comparing corresponding planes. Additionally, injectors A and B have very similar temperature distributions, which is most apparent in the axial evolution of the radial positions of the peak temperatures which remain close to predicted peak equilibrium temperature of this reaction ($T_{eq,stoich} \simeq 3050$ K). Further downstream (z > 30 mm), injector B's peak temperature value begins to decrease below $T_{eq,stoich}$, likely due to the slight increase in radial diffusion from a moderately recessed oxidizer post.

By contrast, injector C's thermochemical structure is distinctly different than that of injectors A and B. At the injection plane, CO mole fraction is significantly higher, indicative of rapid combustion progress in the radially confined recess volume, but then radially diffuses more quickly as the flow progresses downstream. Unlike injector A and B, an acceptable amount of CO and temperature is found in the core of the flame (r = 0 mm) for downstream axial positions of z > ∼30 mm, thus this domain can be resolved in the thermochemical images. Again, the presence of CO in the flame core further upstream for injector C reflects earlier initial mixing and combustion before radial diffusion associated with downstream turbulent mixing.

2.4.3 Mixing length scales

To further compare and quantitatively assess mixing characteristics between each injector, it is of interest to define mixing length scales (in addition and related to the flame expansion angle) based off of the quantitative species and temperature measurements obtained via laser

absorption tomography. Here, we define a *radial mixing width*, r_ω, by finding the total radial domain wherein $X_{\mathrm{CO}} \geq 0.05$ at a given axial position downstream. For example, Fig. 2.7 shows radially-resolved CO mole fraction for Injector A. For height z_{11}, $X_{\mathrm{CO}} \geq 0.05$ from $r = 3.0$ to 6.8 mm; therefore, r_ω at z_{15} is 3.8 mm for Injector A (also illustrated in Fig. 2.10). This radial mixing length scale is similar to the flame brush width, defined quantitatively here by the CO mole fraction profile. r_ω is calculated for each axial position, normalized by the oxidizer post outer diameter ($d_{\mathrm{ox}} = 5.6$ mm), and then plotted in Fig. 2.11. CO radial mixing width is a mixing metric representative of the amount of radial diffusion of CO in a coaxial flame, which accounts for diffusion inward towards the core and outwards towards the co-flow. Larger values of r_ω signify enhanced mixing, which is exhibited with increased injector recess lengths. As an alternative species-diffusion metric, the local X_{CO} maxima for each planar measurement can normalized by the global X_{CO} maximum over the entire flow-field (see Fig. 2.12). As demonstrated, injector C, which has the highest recess length, renders a much steeper reduction in $X_{\mathrm{CO,max}}$ over the length of the flow-field, indicative of increased mixing. Both radial mixing metrics indicate a similar order of mixing between the injector designs.

Lastly, we can examine the stoichiometric contour and mixing length as previously defined, with the associated dependence on oxidizer post recess. In the two-dimensional temperature contour plots presented in Fig. 2.10, the stoichiometric contour of each flame can be outlined by the axial and radial evolution of the maximum temperature throughout the flow-field, and is highlighted by a black dashed line. The radial position of T_{max} is identified for each planar measurement and the resulting stoichiometric contours are illustrated in Fig. 2.13 corresponding to each of the three injectors. As depicted in Fig. 2.1, the stoichiometric contour is expected to collapse back inwards towards the center axis of the coaxial flow, which is fully demonstrated by injector C in Fig. 2.13. Therefore, the effective stoichiometric mixing length for a reacting coaxial flow-field can be directly approximated by using this thermochemical tomography technique if the stoichiometric contour is fully captured. The

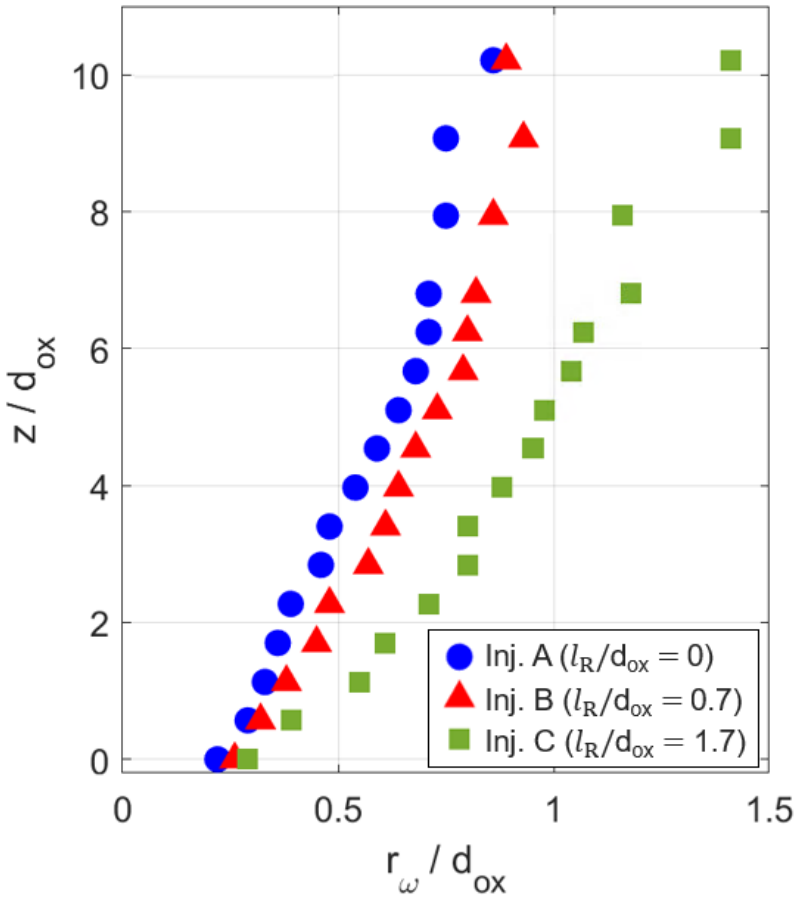

Figure 2.11: Axial length *versus* CO radial mixing length. Both axes are normalized by the oxidizer post outer diameter.

measurement domain of this experiment was restricted to just 57.2 mm due to the entrainment issues seen at higher planar measurements, thus the stoichiometric contours for injectors A and B were not completely obtained. However, the stoichiometric contours for injectors A and B still provide insight as to relative mixing performance over the domain examined, while the stoichiometric contour of injector C appears to be fully captured. As a result, the stoichiometric mixing length for injector C was determined to be approximately 5.7 oxidizer post diameters and its effective stoichiometric mixing length being 7.4 oxidizer post diameters. Notably, the stoichiometric contours of injectors A and B appear quite similar, suggesting the slight oxidizer post recess of injector B does not cause a significant reduction in mixing length scales or expected flame length especially in light of such substantial reduction in flame

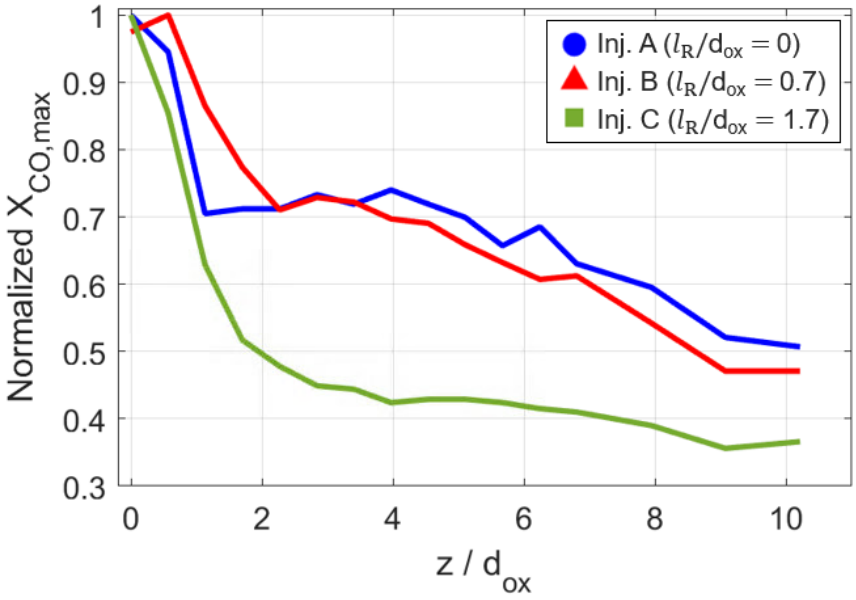

Figure 2.12: Maximum CO mole fraction (normalized by the overall maximum CO mole fraction for each injector) *versus* axial length (normalized by the oxidizer post outer diameter).

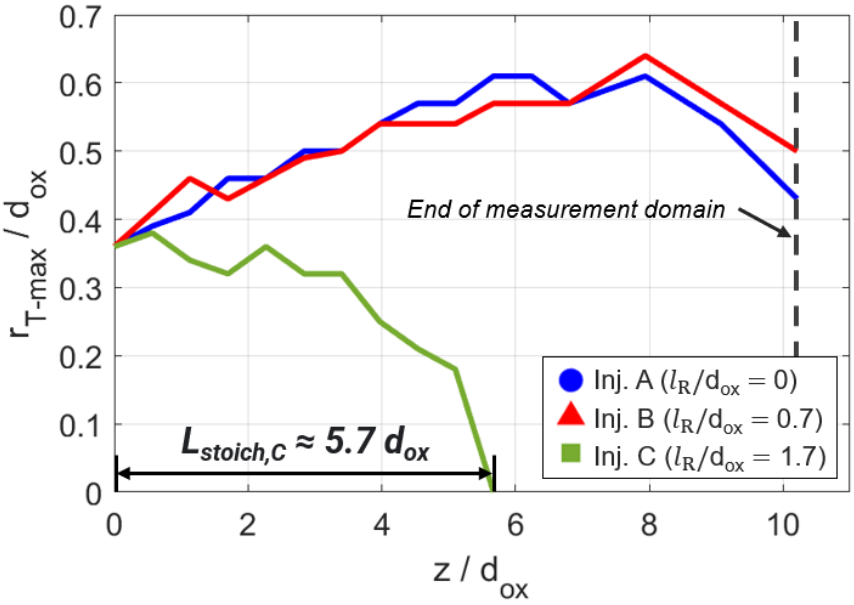

Figure 2.13: Stoichiometric contours that manifest from axial position *versus* radial position of peak temperature for each planar measurement. Both axes are normalized by the oxidizer post outer diameter.

length observed with injector C. This supports the conclusion that a threshold characteristic oxidizer post recess depth is required to induce substantial pre-mixing and overall shortening of the combustion zone. This characteristic value very likely is determined by the recess

depth required for the inner mixing zone to intersect with the fuel path outer boundary before entering the larger combustion volume. Stoichiometric mixing length values are presented in Table 2.6.

Table 2.6: Measured values of each injector's effective stoichiometric mixing length.

Injector	L_S $[d_{ox}]$	l_R $[d_{ox}]$	$L_{S,eff}$ $[d_{ox}]$
A	>10.2	0	>10.2
B	>10.2	0.7	>10.9
C	5.7	1.7	7.4

2.5 Measurement uncertainty

For the quantitative species and temperature measurements, a detailed uncertainty analysis was performed consistent with the prior work of Wei et al. [144]. A Taylor series method of uncertainty propagation from spectral properties (e.g., linestrength) and experimental noise sources was used to estimate potential error within a 95% confidence interval. Uncertainty factors associated with the onion-peeling tomographic deconvolution methods were also calculated by the process outlined in [35] which accounts for the influence of data spacing and the noise from projected absorbance area, and is described in the next section 2.5.1. Total uncertainties for the thermochemical measurements presented here demonstrated a range, with values typically between $\Delta X_{CO} \approx 0.002$–$0.02$ and $\Delta T \approx 30$–200 K, represented by the error bars in Fig. 2.9, with the higher error values appearing closer to the core of the flame or near oxidizer-rich regions.

2.5.1 Onion-peeling uncertainty analysis

The onion-peeling radial deconvolution method has an inherent noise that manifests as a result of the tomographic inversion technique. This section outlines how the noise from the onion-peeling method is determined and accounted for in the uncertainty calculation on the

radially-resolved form of the integrated spectral absorption coefficient $K(r)$ [35].

It is assumed that the line-of-sight projected absorbance area data $A_{\text{proj}}(x)$ are recorded with a narrow beam at equidistant spacing Δr. As a result, the deconvolution method is expressed as a linear operator coefficient D_{ij}, and is independent of data spacing Δr. Each inversion method has its own D_{ij} and only needs to be calculated once. The radially-resolved field distribution $K(r)$ can then be related to the projected field data $A_{\text{proj}}(x)$ by:

$$K(r_i) = \frac{1}{\Delta r} \sum_{j=0}^{\infty} D_{ij} A_{\text{proj}}(x_j) \tag{2.12}$$

where $r_i = i\Delta r$ is the radial distance from the center of the field (r = 0).

The onion-peeling method estimates the field can be represented as concentric homogeneous rings between r_j-$\Delta r/2$ and r_j+$\Delta r/2$ for each data point r_j, resulting in the projection data being:

$$A_{\text{proj}}(x_i) = \Delta r \sum_{j=i}^{\infty} W_{ij} K(r_j) \tag{2.13}$$

where

$$W_{ij} = \begin{cases} 0 & j < i \\ [(2j+1)^2 - 4i^2]^{1/2} & j = i \\ [(2j+1)^2 - 4i^2]^{1/2} - [(2j-1)^2 - 4i^2]^{1/2} & j > i \end{cases} \tag{2.14}$$

Eq. 2.13 is more easily expressed in the deconvolution matrix form as seen in Eq. 2.12 in terms of the linear operator coefficient D_{ij}, therefore:

$$D_{ij} = (W^{-1})_{ij} \tag{2.15}$$

An intrinsic noise coefficient ξ_i (originally seen in Eq. 2.11) of the resulting radially-resolved field distribution is dependent on D_{ij} and is therefore specific to the inversion method being

used. The noise coefficient is determined by:

$$\xi_i = \left(\sum_{j=0}^{\infty} D_{ij}^2 \right)^{1/2} \tag{2.16}$$

Therefore, Eq. 2.11 can be rewritten, and the uncertainty that manifests from the onion-peeling deconvolution method is:

$$\delta K(r_i) = \frac{N_i}{\Delta r} \left(\sum_{j=0}^{\infty} D_{ij}^2 \right)^{1/2} \tag{2.17}$$

where N_i is the local error in the projected absorbance area data $A_{\text{proj}}(x)$ and Δr is the radial spatial resolution.

2.6 Chapter summary

In the study covered in this chapter, a novel optical diagnostic technique was utilized to assess mixing characteristics within the near-field region of various shear coaxial flames using gaseous methane and oxygen. Quantitative, spatially-resolved measurements of temperature and carbon-monoxide mole fraction were directly obtained using laser absorption spectroscopy coupled with tomographic deconvolution methods. Two-dimensional thermochemical property distributions were measured for three shear coaxial injector geometries with oxidizer post recess lengths of $l_{\text{R}}/d_{\text{ox}} = 0$, 0.7, and 1.7 at a similar flow condition. The enhanced mixing effects of a recessed oxidizer post are readily observed in the most recessed ($l_{\text{R}}/d_{\text{ox}} = 1.7$), which showed a wider flame brush, shorter flame length (measured by a stoichiometric contour) and increased radial diffusion of carbon monoxide and temperature – all indicative of enhanced mixing. Although injector B was moderately recessed, its radially-resolved distributions of temperature and CO mole fraction more closely aligned with non-recessed injector A, likely indicating that the modest recess avoids impingement of the inner mixing zone with the

outer diameter of the fuel flow path at the injector face. These finding are consistent with previous studies that have investigated variable recess depths of shear coaxial injectors which indicate that enhanced mixing effects of injector recess are not usually evident until some characteristic recess depth is achieved [67, 121, 148]. To the authors' knowledge, this work demonstrates the first use of laser absorption tomography to assess mixing characteristics of various shear coaxial rocket injector geometries. As such, this work provides quantitative data on methane-oxygen combustion which can be directly compared to numerical simulations of similar injector geometries and associated flames. This experimental approach and diagnostic technique can be extended to other flow conditions and used on a variety of coaxial injector geometries and for different hydrocarbon-based fuels which can inform injector design for liquid rocket engines.

CHAPTER 3

Additively-manufactured shear tri-coaxial rocket injector mixing and combustion characteristics

The contents of this chapter have been published in ***Aerospace Science and Technology*** *under the full title "Additively-manufactured shear tri-coaxial rocket injector mixing and combustion characteristics" [64].*

3.1 Introduction

Additive manufacturing (AM) with high-performance metal alloys is revolutionizing combustion device design and development [48]. AM enables rapid prototyping and testing of complex components, significantly reduces part count, and eliminates production process steps. In combination, these benefits can ultimately lower the cost and time required to introduce and mature new component designs. Beyond such practical advantages, AM also provides a more flexible design space, permitting the fabrication of sophisticated three-dimensional geometries and a new means to tailor fluid dynamics of combustion devices to maximize performance. Liquid-propellant rocket injectors have a particularly high potential for advancement from AM-enabled features. Specifically, additively-manufactured injectors can dramatically reduce part counts and implement complex fluid passageways that decrease injector forward pressure-drop, increase back-flow resistance, and enhance propellant mixing [48, 63, 93, 131].

Modern liquid bipropellant rocket injectors are commonly comprised of a multitude of individual injector elements each responsible for effectively delivering and mixing fuel and

oxidizer streams to facilitate stable combustion over a range of pressures for throttling and within a reasonably short distance to minimize combustor size. Advancements that enhance mixing and expand operating conditions or reduce chamber size are desired to extend mission capabilities. Shear bi-coaxial injectors (two concentric propellant streams) have demonstrated high performance and reliability over a wide range of operating conditions due to rapid near-field mixing associated with shear-induced turbulence. Propellant mixing primarily occurs through axial shear-induced turbulent diffusion resulting from a high-density inner jet (typically oxidizer) and a low-density outer jet (typically fuel) with different relative velocities. These injector elements are typically comprised of a central post and a single coaxial annulus, with each element comprised of multiple parts that must be sealed to prevent inter-propellant mixing before entering the combustion chamber.

Coaxial injectors with a third concentric propellant jet (a second annular flowpath), designated here as *tri-coaxial* injectors, have potential to improve mixing by increasing propellant contact surface area and introducing an additional shear-induced propellant mixing layer. A limited number of prior studies have examined this concept. Cai et. al. computationally and experimentally assessed the combustion performance and thermal characteristics of a hydrogen-oxygen tri-coaxial injector design, reporting significant improvements in combustion efficiency compared to a baseline bi-coaxial design along with higher chamber wall temperatures [18]. Ping et. al. found similar results in comparing the combustion characteristics of various shear coaxial injectors using gaseous hydrogen-oxygen, concluding that the propellant contact area is a primary driver of combustion performance as best demonstrated by a tri-coaxial design with the highest measured combustion efficiencies over a wide range of flow rates [60]. Using liquid ethanol and gaseous nitrous oxide, Lee et. al. experimentally evaluated droplet breakup and flame structure of a tri-coaxial injector using hot-wire anemometry and chemiluminescence videography of OH radicals over a range of momentum flux ratios by altering the outermost annular jet velocity [75]. Boualia et. al. used particle image velocimetry (PIV) to characterize velocity in non-reacting flow-fields of several tri-coaxial

configurations with varying central jet displacements [17]. A tri-coaxial injector design has also been tested commercially by Snecma for the Vulcain gas generator, with results indicating improved combustion performance, relative to a bi-coaxial design, with significant increases in the obtainable per-element flow rate (up to 20 times higher) [13, 26, 38, 72, 141]. Injectors with high per-element mass flow rates are desirable since they can significantly reduce the number of individual elements required for a combustor.

Despite promising evidence of improved performance, the tri-coaxial injector design also adds complexity to the multi-part, process-intensive fabrication of bi-coaxial injector element assemblies using traditional manufacturing methods, which require multiple components to be combined via brazing or welding for each injection element. Multi-element injector geometries, such as those used in a liquid rocket main combustion chamber, can employ up to hundreds of individual elements, with a correspondingly large number of parts with amplified process intensity. Recent works, including from our own research group, have shown that coaxial injectors can be additively manufactured in a monolithic or single-part form factor, thereby reducing manufacturing complexity and risks associated with manufacturing error [3, 8, 93, 131]. Ahn et. al. experimentally assessed hydraulic and mixing performance of various additively-manufactured bi-coaxial injector elements via cold-flow testing and flow structure imaging, and discovered that despite having a lower discharge coefficient than traditionally-manufactured injectors from inherent AM surface roughness, the AM coaxial injectors demonstrated no significant problems with propellant injector and atomization [3]. Additive manufacturing flexibility further enables the geometrically tailored manifolding required to supply the optimal amount of propellant to each injector element [44, 48, 131]. Manifold design for optimal flow distribution becomes a greater challenge for tri-coaxial injection elements, along with the difficulty of inter-propellant sealing given the additional parallel flowpath. Additive manufacturing has the clear potential to address these complexities and enable the tri-coaxial injector design to realize its benefits.

This chapter presents the mixing and combustion characteristics of a monolithic methane-

oxygen shear tri-coaxial injection scheme enabled by additive manufacturing. The bipropellant combination of methane (CH_4) and oxygen (O_2) serves as the focus of this work due to relevance to next-generation liquid-propellant rocket engines. Two combustion experiments were coupled with optical diagnostics to evaluate the theorized mixing enhancements of a single-element shear tri-coaxial rocket injector design compared to a traditionally-manufactured bi-coaxial injection scheme over a range of operating pressures from ambient pressure to approximately 70 bar. The ambient pressure combustion experiment employs a unique laser absorption tomography (LAT) method to attain quantitative and spatially-resolved distributions of temperature and carbon monoxide (CO) mole fraction in the near-field mixing regions. All planar measurements are compiled to produce two-dimensional images of each coaxial injector's thermochemical flame structure. The resulting spatially-resolved thermochemical measurements are shown to provide valuable quantitative data to anchor numerical models capturing the reacting fluid mechanics of injector design and the gas-phase kinetics of methane-oxygen combustion. A second, high-pressure combustion experiment utilizes hydroxyl-chemiluminescence (OHCL) imaging in a single-element combustion chamber to assess flame dynamics and structure from 35 to 69 bar. The OHCL videos (which measure line-of-sight integrated pixel intensity) are time-averaged for each chamber pressure condition and for both injector configurations. Characteristic flame length scales are defined by different spatial scalars recovered from the optical methods. Additional high-pressure combustion tests were conducted to quantify combustion performance via measurements of characteristic velocity (c^*) efficiency. The compiled results indicate mixing augmentation and flow-field structure evolution with a shear tri-coaxial injector geometry enabling combustion performance gains with a monolithic additively manufactured design.

3.2 Methods

This section describes relevant injector design and manufacturing approach, optical diagnostics and experimental methods used to both develop the injector test article and assess mixing and combustion performance.

3.2.1 Coaxial injector design and manufacturing

Key nomenclature and theoretical concepts related to coaxial jet mixing are introduced here to aid the reader in understanding injector design. The generic near-field flow structure from the interaction of two and three coaxial jets is illustrated in top and bottom of Fig. 3.1, respectively. It should be noted that the tri-coaxial injector is depicted as having a *fuel-oxidizer-fuel* coaxial arrangement throughout this paper. As previously covered in Sec. 2.1, the resulting coaxial flow-fields are comprised of three zones. Zone I is the initial mixing zone where all jets penetrate the injection plane and is bounded by the end of the shortest potential core (unmixed fluid). This zone consists of the potential cores as well as the inner and outer mixing layers. As the flow progresses and mixes further downstream, the inner, outer, and intermediate potential cores decrease in size, whereas their corresponding mixing layers increase in size. Zone II is the secondary mixing zone where the majority of the mixing via momentum transfer occurs. Zone III is the fully mixed zone which begins at the axial location where the most pronounced potential core finally terminates. Here, the coaxial jet behaves more like a single jet and becomes fully-developed. Injector outlet geometry, propellant properties, and flow conditions all influence the relative lengths of the potential cores.

At the interface of different propellant streams, a stoichiometric contour defines the surface at which stoichiometric diffusive flux conditions are met between the fuel and oxidizer. Since a second fluid interface mixing layer is introduced by the tri-coaxial jet configuration, a second stoichiometric contour is present. Depending on outlet geometries and flow conditions, the

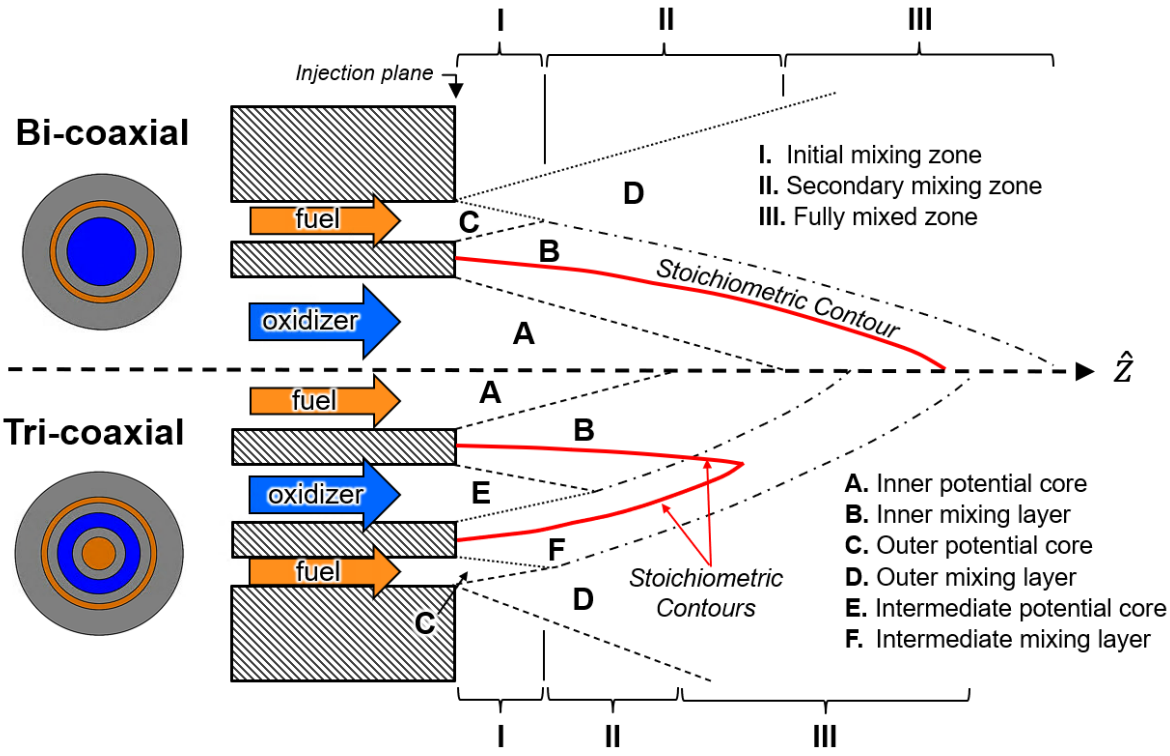

Figure 3.1: Generalized near-field mixing schematic for (*top*) bi-coaxial jet and (*bottom*) tri-coaxial jet fluid interaction.

two stoichiometric contours can converge downstream in zone III as depicted in the bottom half of Fig. 3.1. The axial termination distance of the stoichiometric contour represents a characteristic length scale (i.e., the stoichiometric mixing length, L_{S}) for the turbulent flame. Theoretically, increased turbulent mixing caused by an additional mixing layer permits stoichiometric contours to intersect and terminate further upstream for the tri-coaxial jets, thus enabling a shorter fully-developed jet length and a shorter flame. Two important non-dimensional metrics involved in the mixing processes of coaxial jets are the *outer-to-inner* velocity ratio ($VR = u_{\mathrm{o}}/u_{\mathrm{i}}$) and momentum flux ratio ($J = \rho_{\mathrm{o}} u_{\mathrm{o}}^2/\rho_{\mathrm{i}} u_{\mathrm{i}}^2$). VR directly influences the intensity of shear layer interaction between the coaxial jets which relates to the amount of turbulent mixing that occurs, and also determines the length of the inner potential core [109]. J serves as an important factor in turbulent mixing intensity and predicting characteristic mixing length scales, accounting for differences in fluid density in addition to variance in velocity [109]. Off-unity values of VR and J should generally be targeted to

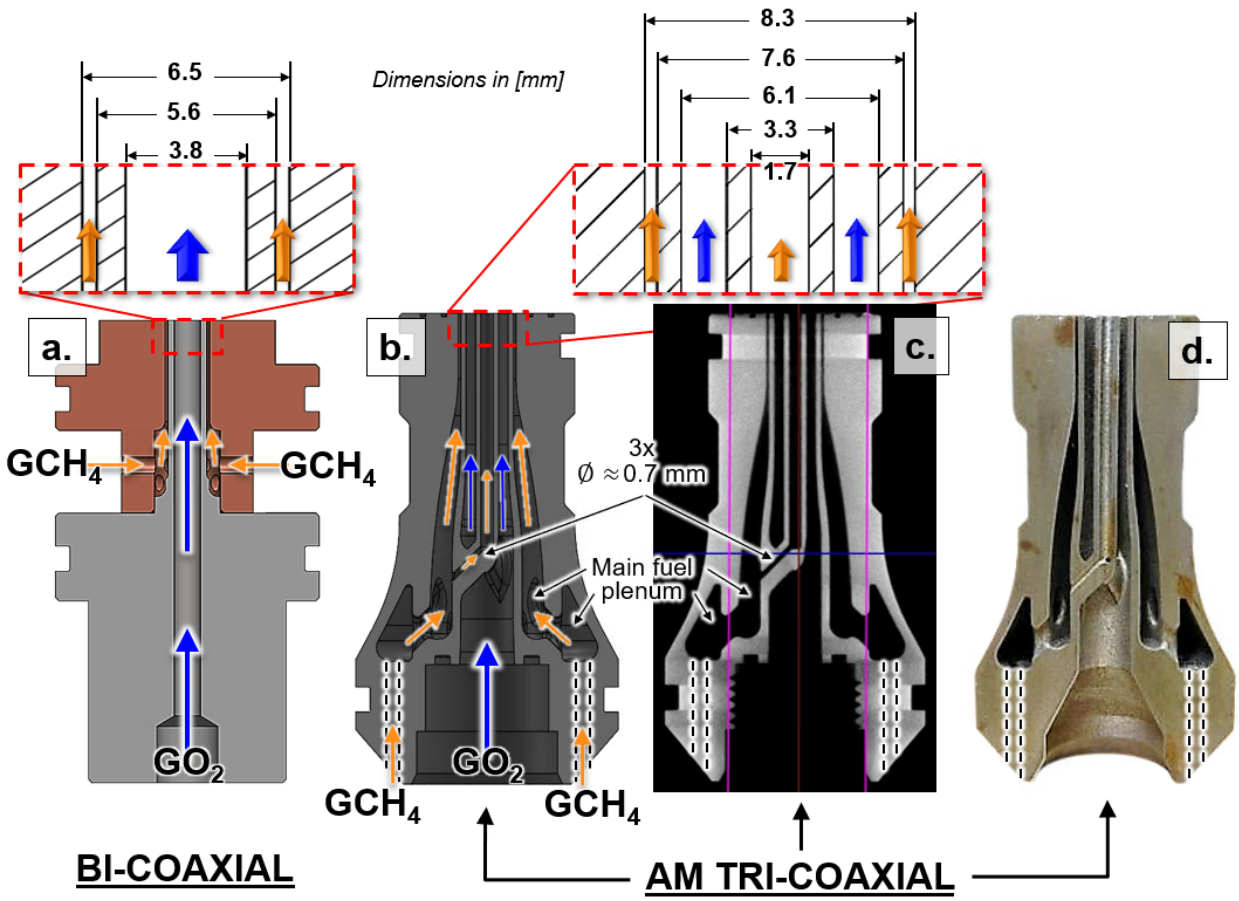

Figure 3.2: Cross-sections of: *a.*) traditionally-manufactured bi-coaxial injector CAD model, *b.*) additively-manufactured tri-coaxial injector CAD model, *c.*) x-ray CT scan of AM tri-coaxial injector, and *d.*) image of *as-printed* AM tri-coaxial injector cross-sectioned by wire-EDM.

enhance shear-induced turbulent mixing between propellant jets. Both ratios are primarily dependent on injector outlet geometry and the oxidizer-to-fuel ratio ($O/F = \dot{m}_{GO_2}/\dot{m}_{GCH_4}$)

Two single-element shear coaxial injector geometries were designed, fabricated and tested in this work: a baseline bi-coaxial design, and an additively-manufactured tri-coaxial design. The shear bi-coaxial injector geometry used in this study was a two-component, conventionally-manufactured assembly consisting of a copper fuel sleeve and stainless steel oxidizer post, with a fuel-to-oxidizer outlet area ratio of approximately 0.75 (see dimensions in Fig. 3.2a).

The tri-coaxial injector was designed to be a single monolithic part adhering to constraints

specific to the printer and material being used such as minimum values of wall-thickness, gap size, and feature size, as well as print angle (see dimensions in Fig. 3.2b). The total fuel-to-oxidizer area ratio was approximately 0.54, while splitting the fuel flow between the center core and outer-most annulus, with a outer-to-inner fuel area ratio of 3.8, achieving off-unity velocity and momentum flux ratios for a targeted oxidizer-to-fuel mass flow ratio (O/F) of 3, a fuel-rich value relevant to methane-oxygen rocket propulsion systems. The single-element tri-coaxial injector design was fabricated as a single part via a laser powder bed fusion (L-PBF) additive-manufacturing process from stainless-steel 17-4 PH (Proto Labs Inc. via GE Concept Laser Mlab R printer) which used a 20 μm layer thickness. Fig. 3.2c shows an image of an x-ray CT scan of AM tri-coaxial injector. Fig. 3.2d shows a cross-section image of the *as-printed* AM tri-coaxial injector cut via wire electrical discharge machining (EDM), revealing the resolved intricate features of internal propellant passageways.

The velocity ratios for the tri-coaxial injector, VR_1 (*oxidizer-to-fuel-center*) and VR_2 (*fuel-outer-to-oxidizer*), were both targeted to be greater than 1 for the O/F ratio of 3 targeted in this experiment. Computational fluid dynamics (CFD) analyses were performed to appropriately size the three channels that connect the main fuel plenum to the central fuel post, resulting in a diameter of 0.7 mm which establishes the desired proportions of fuel mass flow rates through the center fuel post and the outermost fuel annulus. The resultant

Table 3.1: Critical dimensions and fuel-to-oxidizer (total) area ratio, AR, listed for the bi- and tri-coaxial injectors.

Injector	Dimension	Value
Bi-coaxial	$d_{\mathrm{ox,ID}}$	3.8 [mm]
	$d_{\mathrm{ox,OD}}$	5.6 [mm]
	$d_{\mathrm{f,ID}}$	6.5 [mm]
	AR	0.75
AM Tri-coaxial	$d_{\mathrm{f1,ID}}$	1.7 [mm]
	$d_{\mathrm{f1,OD}}$	3.3 [mm]
	$d_{\mathrm{ox,ID}}$	6.1 [mm]
	$d_{\mathrm{ox,OD}}$	7.6 [mm]
	$d_{\mathrm{f2,ID}}$	8.3 [mm]
	AR	0.54

fuel flow percentage split and corresponding outlet areas set the averaged outlet jet velocities, therefore setting the velocity ratios. The CFD cases compared the outlet jet velocities with and without a 1-thou surface roughness condition (relevant to the measured surface roughness of the AM injector) applied to the flowpath walls. These CFD results predict that the surface roughness alters the subsequent fuel jet velocities by <2%. The as-printed dimensions and areas of the relevant AM tri-coaxial injector flowpaths were confirmed via x-ray CT scans and from wire-EDM cross-sections. Minimal post-printing manufacturing included o-ring grooves, sealing surfaces, and removing support material. The total propellant contact surface area is indicative of shear-induced mixing performance and scales with the total inter-propellant perimeter between the fuel and oxidizer outlet geometries. From the addition of a third coaxial flowpath, the AM tri-coaxial injector achieves a total inter-propellant perimeter of ∼10.5 mm, whereas the bi-coaxial has an inter-propellant perimeter of ∼6 mm. Normalized by the propellant outlet areas, this represents an increase in the contact surface perimeter of ∼25%. The design of the AM tri-coaxial injector's outlet geometry was constrained by maintaining off-unity velocity ratios between adjacent propellant jets for the targeted nominal O/F ratio, while also adhering to specific constraints of the AM printer used, particularly the minimum achievable annular gap size of ∼0.35 mm.

3.2.2 Optical diagnostics

Optical diagnostic methods were used for non-intrusive examination of mixing and combustion fields produced by the coaxial injectors. For ambient combustion experiments with full optical access, a novel laser absorption tomography technique was employed for quantitative species and temperature measurements [144]. For high-pressure combustion experiments with more limited optical access, a chemiluminescence imaging method was employed targeting the spontaneous emission of the excited hydroxyl radical (OH*), known as hydroxyl-chemiluminescence (OHCL). Imaging chemiluminescence of OH* near 308 nm is a well-established method to identify heat release zones and flame boundaries in combustion environments by simply

coupling a spectral filter with a high-speed ultra-violet image intensifier and visible camera, and has been used in prior works examining injector mixing [67, 81, 115].

Laser absorption tomography (LAT) enables a more quantitative measurement of species and temperature fields, providing fundamental properties that can be directly compared to results of reacting flow simulations [105]. Notably, flow-field axisymmetry, which can be assumed on a sufficiently time-averaged basis for the axisymmetric injectors studied here, enables inversion via tomographic deconvolution methods (i.e., *onion-peeling*) of line-of-sight spectroscopic measurements across a given transverse plane (from a single view angle) to produce radially-resolved profiles of spectral absorbance that can be used to infer gas properties. Our research group recently developed and demonstrated a mid-infrared LAT technique that yields quantitative and spatially-resolved measurements of temperature and CO mole fraction in quasi-axisymmetric reacting flows [10, 113, 144].

In this work, carbon monoxide (CO) is targeted for LAT measurements due to its natural abundance in hydrocarbon flames. CO is a stable combustion intermediate, a precursor to carbon dioxide (CO_2), and is a significant product species at fuel-rich conditions, typical of hydrocarbon-fueled liquid rockets. CO has very strong vibrational absorption in the mid-infrared. The two targeted CO rovibrational transitions are near 5 μm, specifically at $\nu_A = 2008.421$ cm^{-1} (*Line A*) and $\nu_B = 2008.525$ cm^{-1} (*Line B*), which is a line pair used previously for sensitive thermometry [144]. Additional details on the spectroscopic method integration and optical setups are given in the following sections that describe the respective ambient and high-pressure combustion experiments.

3.2.3 Ambient combustion experiment

The two single-element bi- and AM tri-coaxial injectors were individually tested over a set of steady-state flow conditions in an atmospheric burner. Laser absorption tomography measurements were conducted for each injector design to generate temperature and species

fields in the mixing zone immediately downstream of the injector face. Gaseous oxygen (GO_2) and methane (GCH_4) are supplied at constant flow rates using mass-flow controllers (MKS ALTA 0-200 slm with MKS 647C), which targeted an O/F ratio of 3. Total propellant mass flow rate (0.350 g/s) is defined by the sum of the mass flow rates of the oxidizer (0.265 g/s) and the fuel (0.089 g/s), which were monitored throughout each test run to ensure steady-state operation. A gaseous nitrogen (GN_2) co-flow plate at the injector exit provides a nitrogen-to-oxidizer dilution ratio ($N/O = \dot{m}_{GN_2}/\dot{m}_{GO_2}$) of 3 to mitigate the influence of atmospheric entrainment on the combustion flow-field. Momentum flux and velocity ratios were calculated to be $J = 0.38$ and $VR = 0.86$ for the bi-coaxial, and $J_1 = 2.75$, $J_2 = 0.81$, $VR_1 = 1.19$, and $VR_2 = 1.26$ for the AM tri-coaxial injector.

The same LAT experimental setup, test settings, and data processing methods were used as detailed in Sec. 2.3. A schematic of the experimental setup and relevant optical hardware is shown in Fig. 2.5 with the experimental settings highlighted in Table 2.4.

3.2.4 High-pressure combustion experiment

A second complementary combustion experiment was set up to assess mixing characteristics of the coaxial injectors at higher pressures more relevant to rocket combustor conditions. A brief overview of the single-element combustion chamber is given here, while a more detailed description can be found in [16]. GO_2 and GCH_4 were used as the propellants, and GN_2 was injected co-axially through a co-flow plate to mitigate thermal damage on the inner chamber walls. Three chamber pressures (P_C = 35, 53, and 69 bar) were tested for each injector by altering mass flow rates (metered via choked orifices) and holding O/F and N/O ratios constant at 2.75 and 3.1, respectively, with variations less than 3% across all tests. Conditions for each test are averaged over one second of quasi-steady state operation, which is defined over a test window where chamber pressure is constant within ±2.5%. The total test time lasted five seconds. These conditions were chosen to produce stable combustion relevant to

methane-oxygen rocket combustors and sustain manageable combustion temperatures for hardware integrity.

As show in Fig. 3.3, the combustor included an optical spool section which housed a 2.5 cm thick fused-silica window that was 7.62 cm long and 2.54 cm wide and provided optical access to the injection and mixing zone. The stainless-steel combustor had an ID of 5.08 cm and had an effective length of 26.7 cm before hot combustion gases converged and exited through a water-cooled copper nozzle section. The nozzle throat diameter was measured to be 0.70 cm for each test. Combustion is initiated by a H_2-O_2 spark torch igniter. Static chamber pressure is measured using a Taber 206 pressure transducer and flow rates are metered via choked orifices, Omega PX319 pressure transducers, and K-type thermocouples.

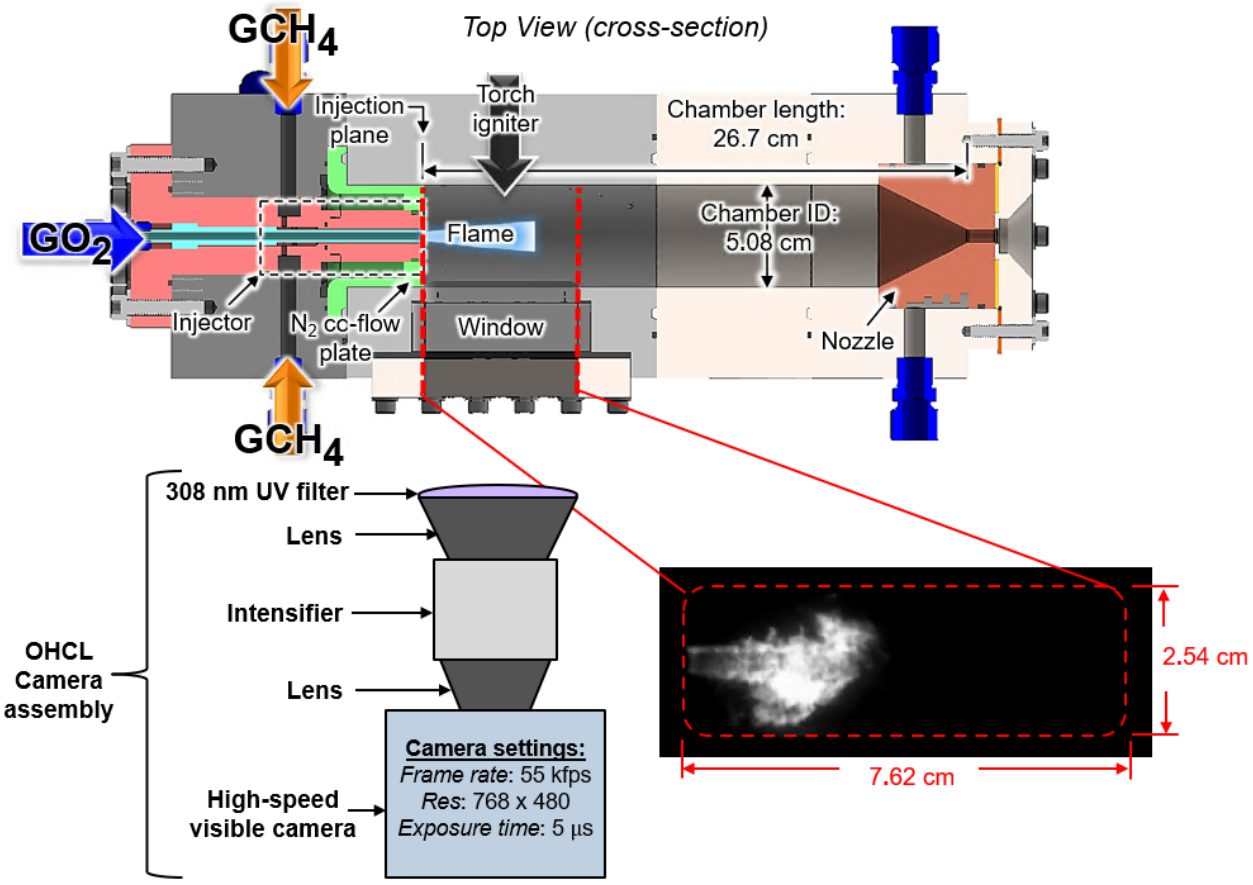

Figure 3.3: Cross-sectioned top-down view of the single-element pressurized combustion chamber assembly shown with exemplary image captured from OHCL videography.

The OH* chemiluminescence (OHCL) videography system consisted of a 308 nm ultraviolet (UV) filter, a UV lens, an intensifier (Invisible Vision UVi model: 2550B-10), and a Phantom high-speed camera to capture OH* emission. During a single hot-fire test, OHCL video is recorded at a frame rate of 55 kfps with a window of 234 x 614 pixels over one second of quasi-steady state operation (verified by chamber pressure traces) to capture the flow-field dynamics and flame structure of each injector for each of the three targeted chamber pressure conditions. This OHCL assembly is offset from the combustor by 40 cm and is centered on the window, resulting in a per-pixel spatial resolution of 0.13 mm. A single frame of the OHCL video for a representative test is shown in the bottom right of Fig. 3.3.

Combustion performance for the two injectors was evaluated via characteristic velocity (c^*) measurements, inferred from chamber pressure, over a similar range of chamber pressures (34-69 bar), denoted later by tests 7–12. To better discern relative performance differences, these c^* measurements were taken with a shortened ($\sim$7.6 cm) combustion chamber section without optical access.

3.3 Results and discussion

Mixing and combustion characteristics were assessed and compared between the additively-manufactured tri-coaxial injector and the conventional bi-coaxial injector via the two aforementioned experiments with integrated optical diagnostic techniques over a wide range of pressures from 1–69 bar.

3.3.1 Species and temperature imaging at 1 bar

In the atmospheric burner, quantitative, spatially-resolved measurements of CO mole fraction and temperature were attained using laser absorption tomography to assess development of the respective reaction zones for each injector. Radially-resolved data were recorded at 16 different axial positions and then compiled to create two-dimensional images (Fig. 3.4) to

depict the thermochemical structure throughout the first 57 mm of each flame. The exhibited spatial domain was constrained by flow-field criteria (a CO mole fraction threshold of 0.01 and a minimum gas temperature of 1000 K) that ensure adequate SNR of the targeted spectral lines for accurate thermochemical measurements. Henceforth, results in regions within the measured flow-field that had an insufficient amount CO present, or regions that were too cold (e.g., oxidizer-rich cores), are omitted.

The temperature field indicates a balance of axial convective transport with radial diffusion of the fuel and oxidizers that define temperature contours. Notably, we can see in Fig. 3.5 that the local temperature maxima for each planar measurement determined by this LAT method show good agreement with the predicted stoichiometric equilibrium temperature $T_{\mathrm{eq,stoich}} \simeq 3050$ K value [47]. The maximum measured temperature occurs at slightly rich conditions, but is of very similar magnitude, $T_{\mathrm{LAT,max}} \simeq 3060$ K. As such, stoichiometric contours can be approximated by the radial position of the maximum temperature across each planar measurement, illustrated by the dark-red regions (and black dashed line) within the temperature contour plots in Fig. 3.4, and by the radial coordinate of the local maxima on the temperature profiles seen in Fig. 3.5. Stoichiometric contours represent the approximate location of the chemical reaction zone (albeit finite) and indicate mixing length scales.

Within the temperature contour plots of Fig. 3.4, the grey regions highlight the oxidizer-enriched regions where insufficient CO is present to make a spectroscopic measurement. For the bi-coaxial injector, the inner potential core (consisting of purely oxidizer) is approximately outlined by this greyed-out region and extends past the measurement domain ($z > 57$ mm). Recall the bi-coaxial near-field mixing schematic depicted in the top of Fig. 3.1; the fully mixed zone begins where the inner (oxidizer-rich) potential core ends, suggesting that the bi-coaxial injector is not fully mixed within the measurement domain. The stoichiometric contour does begin to converge towards the jet centerline, and a simple linear extrapolation suggests that it likely fully converges at an axial distance of 70–80 mm – representing an approximation of the bi-coaxial stoichiometric mixing length.

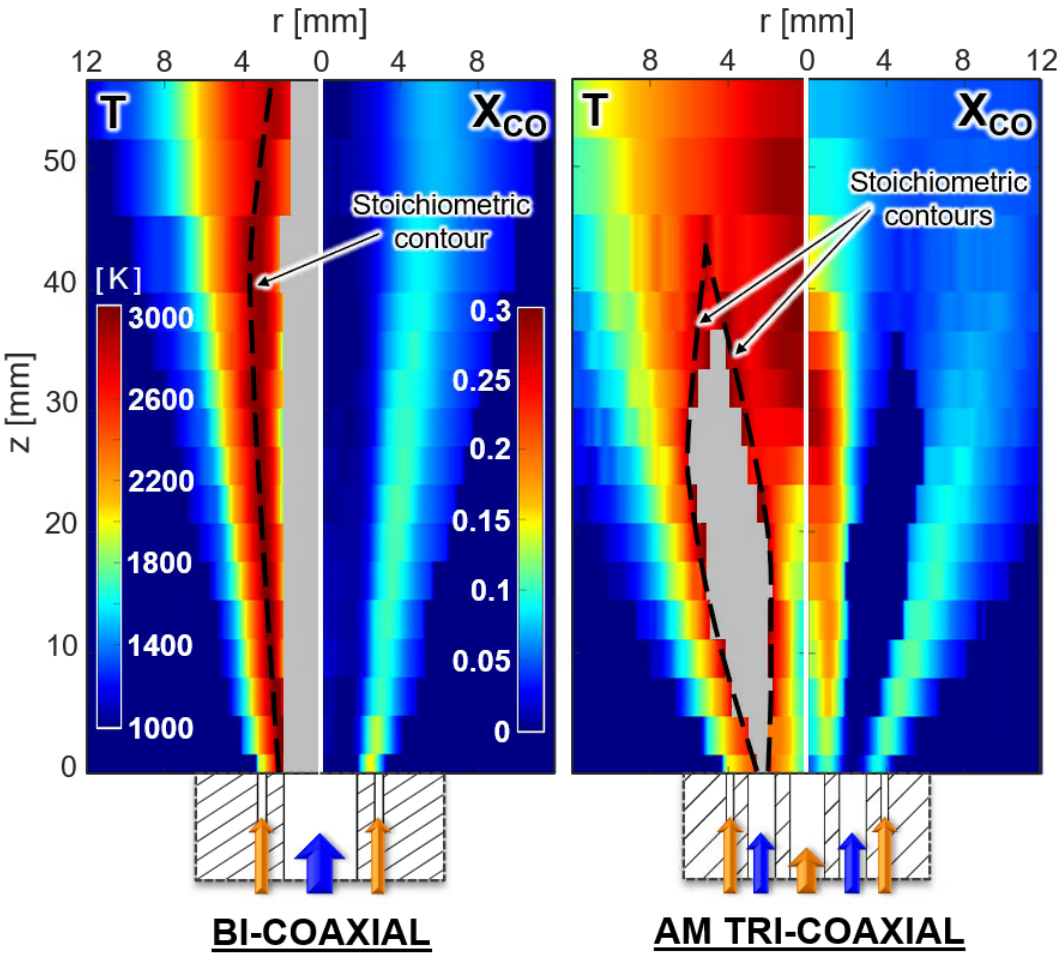

Figure 3.4: LAT-enabled two-dimensional images of radially-resolved temperature and CO mole fraction for the bi-coaxial (*left*) and the AM tri-coaxial (*right*) injectors. Approximate locations of stoichiometric contours are highlighted.

As seen in Fig. 3.4 for the AM tri-coaxial injector, stoichiometric contours are again approximated by the high-temperature regions located on the inner and outer radial bounds of the oxidizer-rich intermediate potential core (greyed-out region), allowing for the locations of the two combustion surfaces to be estimated. The two stoichiometric contours appear to converge at a downstream location of z $\approx$ 43 mm, which represents a tri-coaxial mixing length parameter analogous to the bi-coaxial stoichiometric mixing length. Slightly upstream of the convergence location, the intermediate potential core appears to terminate (z $\approx$ 37 mm), implying that the fully mixed zone begins within the measurement domain. These characteristic mixing and combustion length scales for the AM tri-coaxial injector are roughly

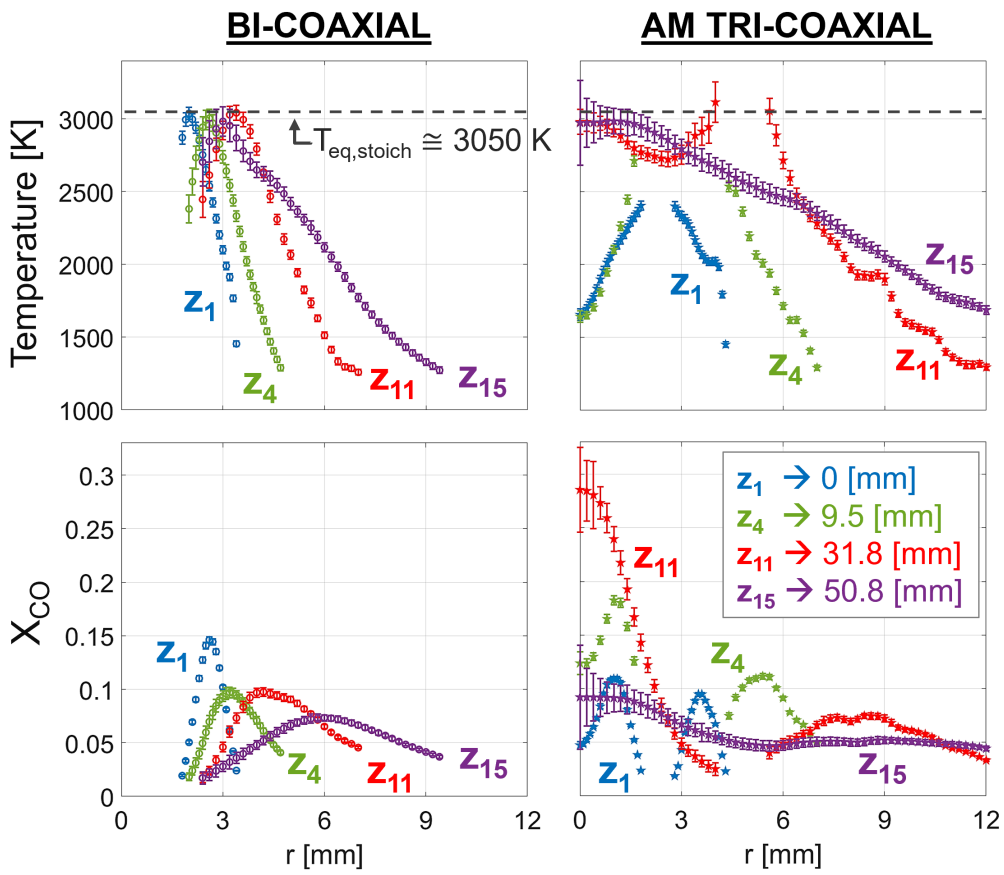

Figure 3.5: Comparison of radially-resolved temperature and CO mole fraction distributions at various axial positions shown for the bi-coaxial and AM tri-coaxial injectors.

half of the magnitude of that observed for the bi-coaxial injector. The *fuel-oxidizer-fuel* arrangement of the AM tri-coaxial injector permits spectroscopic measurements to be recorded within the core of the flame, including the center of the injection plane (r = 0 mm, z = 0 mm) implying that the inner potential core must rapidly collapse.

The respective CO mole fraction distributions for each injector exhibit corroborating features to the temperature fields. For the tri-coaxial injector, the CO mole fraction rapidly rises, peaks, and declines, reaching a higher maximum value (0.285) than that observed for the bi-coaxial injector (0.146), with the peak occurring around z ≈ 32 mm downstream and falling by nearly 80% of the peak value within the next 20 mm of axial distance, suggesting rapid combustion progress and mixing. By contrast, the bi-coaxial injector exhibits a more gradual radial diffusion of CO with axial distance. At the outer-most boundary of the CO

distribution, a flame divergence angle θ, can be used to characterize the radial spread of the flame brush driven by turbulent mixing. Here, θ is defined by the radial position of the outer boundary where $X_{CO} = 0.05$ for each axial position within the first ~25 mm of each flame. This produces a linear trend across the planar measurements at different axial positions and enables a divergence angle to be measured for each flame. Notably, the tri-coaxial flame divergence angle was determined to be 3.1 times that of the bi-coaxial injector.

3.3.2 High-pressure chemiluminescence

The high-pressure single-element combustor was then used to characterize combustion and flame structure of the same injectors (at similar O/F ratios) up to 69 bar using OH* chemiluminescence (tests 1–6). Across the three pressure conditions (P_C = 35, 53, and 69 bar), O/F and N/O ratios were held constant at approximately 2.75 and 3.1, respectively, with variations less than 3% across all tests, and the momentum flux and velocity ratios were calculated to be $J = 0.42 \pm 0.04$ and $VR = 0.91 \pm 0.04$ for the bi-coaxial, and $J_1 = 2.31 \pm 0.15, J_2 = 0.95 \pm 0.05$ and $VR_1 = 1.08 \pm 0.03, VR_2 = 1.38 \pm 0.04$ for the AM tri-coaxial. The velocity ratios are approximately constant due to the fixed O/F ratios, and the momentum flux ratios are nearly constant with changing pressure due to density change of the compressible propellants being more significant than the velocity change. injection pressure drops ranged from 2.8–4.3% P_C for the bi-coaxial injector, and 2.0–3.0% P_C for the AM tri-coaxial.

The OHCL technique measured line-of-sight integrated pixel intensity which was then time-averaged over the 55,000 frames (one second) of quasi-steady state operation for each of the six test conditions, denoted as Tests 1–6. Pixel intensity data is converted to a 0–1 scale via normalization by a single global maximum pixel intensity across all six time-averaged tests. Fig. 3.6 shows contour plots of the normalized line-of-sight pixel intensities for a single frame and the time-averaged data to compare the two injectors at the three targeted chamber

Table 3.2: Averaged flow conditions achieved for each test during 1 second of quasi-steady state operation of the single-element combustor for the high-pressure OHCL experiment.

Test #	1	2	3	4	5	6
Injector	Bi-	Bi-	Bi-	AM Tri-	AM Tri-	AM Tri-
$\dot{m}_{GO_2}$ [g/s]	17.1	26.0	32.0	17.3	25.0	32.0
$\dot{m}_{GCH_4}$ [g/s]	6.1	9.3	12.1	6.2	9.3	12.1
$\dot{m}_{GN_2}$ [g/s]	53.8	79.4	98.7	53.9	79.1	102.0
O/F	2.79	2.80	2.64	2.79	2.69	2.64
N/O	3.15	3.05	3.08	3.12	3.16	3.19
P_C [bar]	35.1	53.2	68.6	34.8	53.3	69.0

pressures. Tests 1 and 4 target $P_C \approx 35$ bar, tests 2 and 5 target $P_C \approx 53$ bar, and tests 3 and 6 target $P_C \approx 69$ bar. Table 3.2 provides the actual flow and chamber conditions achieved for each test. Non-dimensional ratios of velocity (VR) and momentum flux (J) are approximated for each test condition from the chamber pressure, propellant mass flow rates, and injector outlet geometry. Since the tri-coaxial injector has two combustion surfaces instead of one, two values of VR and J are presented for this injector at each chamber pressure (tests 4–6). The width of tri-coaxial flame images are slightly truncated by the limited width of the window (2.54 cm) which is exactly half of the chamber's inner diameter (5.08 cm). All time-averaged images depict each flame to be relatively axisymmetric with slight spatial distortion likely associated with the GN_2 purge entering the chamber radially from the torch igniter. In addition to the atmospheric spatially-resolved thermochemical images from Fig. 3.4, the tri-coaxial flame's divergent behavior is also exhibited here in Fig. 3.6 at higher pressures.

Two characteristic flame length scales are determined by different axial positions bounded by a 0.5 iso-contour profile from the normalized time-averaged OHCL video (see *Avg.* images in Fig. 3.6) to assess key metrics of each injector's in-chamber flame structure. Axial flame length l_f, is bounded by the axial distance between the injection plane and the position of the iso-contour profile furthest downstream. l_f is representative of the approximate length of an injector's reaction zone required for complete combustion which is vital to a designer to appropriately size a combustor. Flame standoff distance l_s, is bounded by the axial distance between the injection plane and the position of the iso-contour profile most upstream. l_s

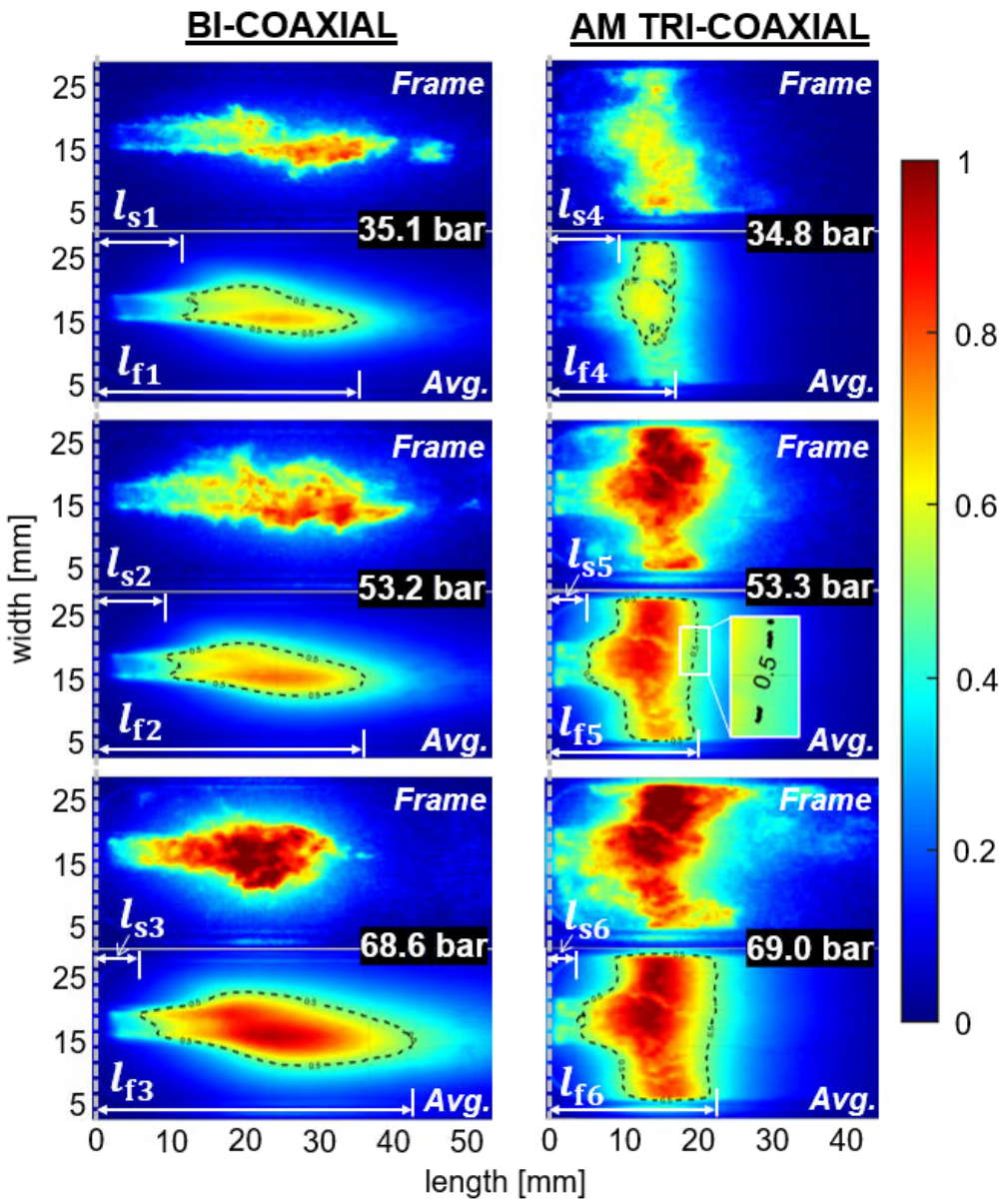

Figure 3.6: Still (*Frame*) and time-averaged (*Avg.*) images from OHCL videography at the high-pressure test conditions. Contour plots depict normalized, line-of-sight pixel intensity and characteristic flame length scales are highlighted.

estimates the proximity of the exothermic reaction zone relative to the injection plane which provides insight into near-field mixing dynamics as well as thermal loading on the injector face.

Fig. 3.7 illustrates how the flame length scales change with increasing chamber pressures for the bi-coaxial and AM tri-coaxial injectors. Axial flame length l_f exhibits an upward trend

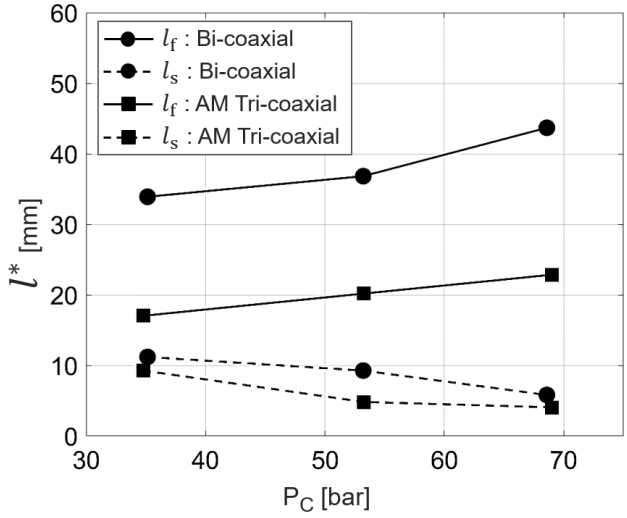

Figure 3.7: Plot of the two characteristic flame length scales (axial flame length l_f, and injector standoff distance l_s) *versus* chamber pressure is shown for both injectors.

with higher chamber pressure for both injectors, which is to be expected due to the increase in total propellant flow rates. On the other hand, injector standoff distance l_s, demonstrates a downward trend with increased chamber pressure for both coaxial injectors. These trends reflect a general increase in the size of the reaction zone and increase in thermal emission with increasing pressures and mass flow rates. Notably, when compared to the bi-coaxial injector, the AM tri-coaxial injector results in a 50%, 45%, and 48% reduction in axial flame length at the three increasing chamber pressure conditions, respectively, while generally exhibiting a smaller reduction in standoff distance, of approximately 31% on average.

A shorter flame, as suggested by smaller values of l_f and l_s, is indicative of improved mixing. However, an l_s that is too short can generate undesirable high heat-fluxes on injector hardware. Proper shear coaxial injector design should aim to enhance mixing by minimizing l_f while simultaneously maintaining a sufficiently long l_s to avoid thermal damage on the injection surface. Visual inspection of the AM tri-coaxial injector face revealed no signs of thermal damage after a combined 160+ seconds of hot-fire tests ranging up to 70 bar in chamber pressure. It should be noted that the broader reaction zones generated by the tri-coaxial injector (in relation to the bi-coaxial injector) requires additional consideration for

protection of the inner combustion chamber side walls. While for these single-element tests, the GN_2 co-flow protected the inner chamber side walls to a degree, multi-element injector configurations may employ separate fuel injector elements for wall cooling or individual co-axial elements at the outer perimeter with different oxidizer-to-fuel area ratios to manage excess heat flux.

3.3.3 Characteristic velocity measurements

Combustion performance was evaluated for the two injectors via characteristic velocity (c^*) measurements for chamber pressures ranging from 34 to 69 bar. Chamber pressure P_C and total propellant flow rate $\dot{m}_{tot}$ were averaged over one second of quasi-steady state operation. The equation for the measured experimental characteristic velocity c^*_{exp} is defined as:

$$c^*_{exp} = \frac{P_C A_t}{\dot{m}_{tot}} \tag{3.1}$$

where A_t is the effective nozzle throat area [m^2]. The ideal theoretical characteristic velocity c^*_{th} is given by:

$$c^*_{th} = \sqrt{\frac{RT_C}{\gamma}\left(\frac{\gamma+1}{2}\right)^{\frac{\gamma+1}{\gamma-1}}} \tag{3.2}$$

Table 3.3: Averaged flow conditions achieved for each test during one second of quasi-steady state operation of the truncated single-element combustor experiment examining characteristic velocity efficiency.

Test #	7	8	9	10	11	12
Injector	Bi-	Bi-	Bi-	AM Tri-	AM Tri-	AM Tri-
$\dot{m}_{GO_2}$ [g/s]	17.7	26.4	33.7	17.7	25.7	33.7
$\dot{m}_{GCH_4}$ [g/s]	6.1	9.2	11.5	6.2	9.1	11.1
$\dot{m}_{GN_2}$ [g/s]	53.2	78.7	100.1	53.2	78.5	97.4
O/F	2.88	2.87	2.94	2.85	2.81	3.03
N/O	3.01	2.98	2.97	3.01	3.05	2.89
P_C [bar]	34.5	52.5	67.9	34.6	53.4	68.8
η_{c^*}	91.8%	93.8%	95.3%	92.0%	96.9%	97.7%

Here, all gas properties specific to the combustion product gas mixture (the gas constant, R [J/kgK], the specific heat ratio, γ, and the chamber temperature, T_C [K]) are determined via NASA chemical equilibrium solver [47] which takes the measured values of chamber pressure and mixture ratios as inputs. The combustion efficiency η_{c^*} is given by:

$$\eta_{c^*} = \frac{c^*_{\text{exp}}}{c^*_{\text{th}}} \tag{3.3}$$

Table 3.3 specifies the range of averaged flow conditions and combustion efficiencies, comparing the bi-coaxial and tri-coaxial combustion performance at different pressures. Both the bi-coaxial and AM tri-coaxial injectors demonstrate improved combustion performance with increasing chamber pressure conditions. When comparing the two injectors at corresponding chamber pressures, the AM tri-coaxial demonstrates higher combustion efficiency at all pressures, with a maximum η_{c^*} of 97.7% compared to 95.3% for the bi-coaxial at the highest pressure condition (∼68–69 bar). It should be noted that at the lowest flow rate condition (test 10), chamber pressure was still increasing for the AM tri-coaxial and therefore did not satisfy the criteria for quasi-steady state operation, likely resulting in a lower combustion efficiency than would have been achieved in steady-state. The increased combustion performance exhibited by the AM tri-coaxial injector is indicative of enhanced mixing driving more complete combustion in the shortened combustion chamber.

3.4 Chapter summary

In summary, a monolithic additively-manufactured shear tri-coaxial rocket injector was designed, fabricated, and tested to examine mixing and combustion characteristics with methane and oxygen relative to a conventional shear bi-coaxial injector. A unique dataset of quantitative temperature and species fields in the mixing region of the injectors was attained using a mid-infrared laser absorption tomography technique in an atmospheric burner.

Stoichiometric contours were defined by tracking peak temperature in the tomographic images, which quantitatively matched well with the stoichiometric equilibrium temperature for GCH_4-GO_2 combustion. Complementary high-pressure combustion experiments were also performed on the same injectors, imaging flame structure via OH* chemiluminescence as a proxy for heat release up to 69 bar. Across the wide range of operating pressures and with multiple diagnostic techniques, the novel tri-coaxial injection scheme was shown to reduce mixing and combustion axial length scales by approximately 50% relative to the bi-coaxial injector at similar conditions. Despite having a modestly shorter flame standoff distance, the AM tri-coaxial injector showed no evidence of thermal damage on its injection surface at any of the tested conditions. High-pressure combustion experiments using a truncated chamber enabled characteristic velocity efficiency measurements, revealing higher performance from the AM tri-coaxial injector compared to the bi-coaxial at comparable flow conditions. The combustion efficiency measurements are consistent with the mixing enhancements from the tri-coaxial injection scheme, and show promise for shortened combustion chamber length and mass. Furthermore, the additive manufacturing approach enabled sophisticated inter-propellant sealing and manifolding in a monolithic form factor that makes a tri-coaxial design practical for fabrication and integration in multi-element rocket combustion devices. More broadly, this work demonstrates the potential to leverage the flexibility of additive manufacturing to design advanced injector geometries that improve mixing and combustion performance, with relevance to next-generation liquid rocket engines. Given the promising results of the tri-coaxial injector design with regards to mixing, future work should be aimed to further evaluate mixing and combustion performance at higher per-element mass flow rates and in multi-element configurations.

CHAPTER 4

Combustion instability characteristics of a methane-oxygen shear tri-coaxial rocket injector

*The contents of this chapter have been submitted to the **AIAA Journal of Propulsion and Power** in December of 2024 under the full title "Combustion instability characteristics of a methane-oxygen shear tri-coaxial rocket injector" (currently under review).*

4.1 Introduction

Combustion instabilities have plagued liquid rocket engines (LREs) since their advent and still present serious concerns today for system performance and hardware survivability. Fundamentally described by the Rayleigh criterion [28], combustion instabilities manifest as periodic fluctuations of pressure within a combustor when in phase with heat release from combustion, and are further influenced by chamber and feed system resonances, as well as propellant injection processes. Fluctuations in chamber pressure can often negatively influence the fluid dynamics of the propellant injection process, thus reducing performance. In more extreme cases, they can increase local heat transfer rates and induce excessive pressure-based vibrations, both of which may damage engine hardware. Despite decades of research, combustion instabilities remain difficult to predict and model because they are unique to each combustion system – highly dependent on injector and combustor geometry, propellant choice, and flow/operating conditions.

Propellant injection systems in LREs inherently experience a large range of thermodynamic

and hydrodynamic conditions from transient engine start-up, nominal operation, throttling, and engine shut-down – all of which can excite and sustain instabilities over a wide range of frequencies. While several different classifications of combustion instabilities exist, this work focuses on linear (self-excited) longitudinal instability modes which originate from the inherent noise that arises from injection and combustion processes [129]. Linear longitudinal instability modes are present in most LREs and generally appear sinusoidal in nature. They can manifest as low-frequency chugging, intermediate-frequency feed system coupled buzzing, and/or high-frequency acoustic eigenmodes, all of which are extremely sensitive to LRE injector design [58,129]. For acoustic modes, the physical mechanisms that drive oscillations in volumetric heat release rate are categorized by either *intrinsic* or *injection-coupled* processes. Intrinsic instabilities are defined by heat release rate fluctuations initiated by chamber acoustic modes from variations in combustion sub-processes that occur after propellant injection (e.g., atomization, vaporization, mixing, chemical kinetics). Said sub-processes determine the phase relationship between the chamber response and the injector response, hence dictating the feedback mechanism of amplification [56]. Intrinsic instabilities are considered to have a negligible effect on propellant injection flow rates [58]. Alternatively, injection-coupled acoustic instabilities occur from the coupling of chamber resonances and oscillatory fluctuations of propellant flow rates from the propellant injection system [56]. Thermoacoustic instabilities are a subclassification where combustion heat release rates become coupled with acoustic pressure waves within the chamber. Low-frequency chugging modes (non-acoustic) are also induced by injection-coupled processes, caused by a coupling of elastic pressure-wave interactions between the propellant feed system and combustor, and sometimes even influenced by vehicle structures [128].

Although in some special cases where the presence of combustion instabilities (typically higher-frequency transverse modes) can enhance propellant mixing and combustion performance, this is not particularly true for low-frequency chugging modes. For example, when an instability invokes an increase in the local chamber pressure on the injection plane, propellant

flow rates are briefly reduced. In some situations, combustion products can backflow into propellant manifolds. In these cases of propellant flow rate modulation, there is a characteristic refresh time for propellants to reestablish nominal flow back into the combustion chamber. Due to differences in propellant densities, flow rates, injector outlet geometries, and injection pressure drops, the corresponding propellant refresh times often mismatch. This results in a transient and spatially varying equivalence ratio and total mass flow rate throughout the combustion chamber, ultimately reducing performance. The consequent reduction in flow conditions then invokes a rapid decline in chamber pressure, encouraging propellants to quickly surge back into the chamber, repeating the cycle.

In most cases, combustion instabilities are empirically characterized and minimized during engine development via hot-fire testing analyses, in which combustion system component and assembly designs are iteratively modified until instabilities are reduced below some predetermined allowable threshold. Classically, "quasi-stable" or "smooth combustion" is achieved when amplitudes of pressure fluctuations do not exceed $\pm 5\%$ of the average chamber pressure [58]. Beyond limited preliminary design considerations, high-frequency instabilities are traditionally minimized through the use of stabilization methods designed in a highly empirical trial and error manner. These damping devices include baffles or acoustic resonance cavities that can absorb acoustic energy at discrete frequency ranges. Increasing injector stiffness ($\Delta P_{\text{inj}}/P_{\text{C}}$), analogous to increasing the injector's impedance, has proven to be a reliable method of reducing injection-coupled chugging modes. Injector stiffness is traditionally recommended to be between 15–20% to promote stable combustion [58, 128], although the exact value will be dependent on the system and operational tolerances. While lower stiffness injection systems are desirable for lighter feed systems, they hinder a lucrative combustion instability damping mechanism. Higher injector stiffness therefore requires larger/heavier feed pressurization hardware, and the implementation of damping devices both increase the complexity and overall dry mass of the vehicle, resulting in a decreased payload or mission duration capability for spacecraft and launch vehicles.

Linear instability behavior in combustion systems has been extensively studied, with much of the basic framework being established by Crocco and Cheng [33]. In order to describe chugging behavior in monopropellant LREs, Crocco introduced a simple time lag theory [29], which associates the fluctuations of combustion heat release and chamber pressure via the time lag (or phase shift) τ, between said fluctuations. This time lag is attributed to the sub-processes that must occur prior to complete combustion such as atomization, vaporization, mixing, and chemical kinetics. The classical time lag models were later improved upon by Crocco and Cheng [30–33], Hutt and Rocker [56], and Wenzel and Szuch [146], among others, which extended to high-frequency modes and accounted for parameters such as acoustic effects, damping mechanisms, bi-propellants, and other chamber-injector responses. Casiano [20] provided a detailed explanation of these time lag models and further expanded them for practical application on stability design for LREs, particularly those that employ deep throttling. For a more comprehensive review of combustion instabilities in LREs, the reader is referred to the following compilations edited by Harrje and Reardon [129], Santoro and Anderson [114], and Yang and Anderson [139].

Coaxial injectors are a common propellant injection scheme for LREs, demonstrating exceptional performance and dependability in rocket engines like the Space Shuttle Main Engine and the Vulcain 2 main stage engine. Best described as "concentric tube elements," coaxial injectors mix the fuel and oxidizer via turbulent shear layer interactions between concentric propellant jets. These injectors generally feature an oxidizer core jet surrounded by an annular jet of fuel with an off-unity velocity ratio. There are two primary types of coaxial injectors. *Shear* coaxial schemes have both propellants enter the chamber co-linearly and mixing largely occurs via differences in axial momentum, whereas *swirl* coaxial schemes invoke a radial and tangential velocity component to one or both of the propellant jets which promotes faster near-field mixing via increased turbulence. Coaxial injector configurations with a recessed oxidizer post are sometimes utilized for their mixing enhancements by which a pre-mixed zone is introduced just prior to the primary injection plane [43]. Several works (most

pertaining to one or more propellants being injected in the liquid phase) have demonstrated the stabilizing effects of a recessed oxidizer post within coaxial injector elements [62,67,83,129,142]. While this is generally true, Lux and Haidn [83] discovered low-frequency chugging modes worsened with a recessed configuration when injection stiffness dropped below 12%, implying that some characteristic injection stiffness must be achieved for recessed shear coaxial injectors to realize stability performance improvements.

A *tri-coaxial* injector implements a third concentric propellant flowpath to the traditional shear bi-coaxial design, aimed to enhance shear-induced turbulent mixing by increasing contact surface area between adjacent propellant jets. The limited number of studies that have investigated a tri-coaxial injector design, including some by our research group, primarily focused on mixing and combustion performance [13, 17, 18, 26, 38, 60, 72, 75, 141]. Notably, our recent work found that a methane-oxygen shear tri-coaxial design can significantly reduce the characteristic mixing length for combustion, enabling a higher characteristic velocity, or c* efficiency, at shorter chamber lengths [64]. However, to the authors' knowledge, there is a lack of prior studies examining the combustion instability characteristics of shear tri-coaxial injection, motivating the current work.

In this work, we examine gaseous and supercritical methane-oxygen combustion instability characteristics of a shear tri-coaxial injection design, with relevance to next-generation liquid rocket engines. Most research, especially the aforementioned pioneering studies, has been conducted using condensed phase (liquid-liquid or liquid-gas) injection systems due to their frequent use in the majority of space vehicles. Recently, full-flow staged combustion (FFSC) cycle engines, like the SpaceX Raptor engine, have gained traction due to their performance benefits compared to non-staged combustion cycles, and from their less extreme conditions imposed on turbomachinery compared to oxidizer-rich staged combustion cycles [104]. FFSC cycle engines partially combust each propellant in fuel-rich and oxidizer-rich preburners to drive turbomachinery, ultimately delivering the propellants into the main combustion chamber in a gaseous or supercritical state. Non-condensed phase injection systems avoid

many of the complex physical processes associated with liquid injection that can excite high-frequency intrinsic instabilities, such as droplet formation, vaporization, and multi-phase mixing interactions. Previous work done by Lemcherfi et. al. [76] and Pons et. al. [106] investigated the influence of propellant injection temperature on stability in a single-element combustor with staged combustion cycles that used a shear coaxial injector with gaseous methane-oxygen as propellants. It was discovered that higher temperatures of the fuel and oxidizer contributed to higher-frequency modes dominating, while lower injection temperatures prompted low-frequency chugging modes to prevail. Despite their simplicity and pragmatic modern applications, the available literature on combustion instability characterization of gas-gas injection systems is scarce, especially those using methane-oxygen with shear coaxial injection schemes, thus further motivating this work.

Here, we investigate the various combustion instability modes associated with the tri-coaxial design, and compare results to baseline bi-coaxial injector designs operating at similar conditions. The tri-coaxial injector design is additively-manufactured (AM) as a monolithic part to overcome challenges with interpropellant sealing, and tested in a high-pressure combustor over a range of pressures at relatively low injector stiffness. In this paper, Sec. 4.2 describes the experimental approach, test hardware, instrumentation, and data analysis methods used to assess instability characteristics. Since full-scale multi-element engine tests are often impractical, single-element tests are conducted in scaled-down combustors as a more cost-efficient way to evaluate relevant intraelement phenomena such as injector fluid dynamics and combustion characteristics.Three total shear coaxial rocket injectors were evaluated in this study: two traditional shear bi-coaxial geometries with and without a recessed oxidizer post and the AM tri-coaxial design. Each injector was individually hot-fire tested using methane-oxygen within a single-element pressurized combustor at chamber pressures ranging from 35–69 bar such that instability behaviors could be captured. Two separate techniques were simultaneously employed to characterize combustion instability behavior for each injector during a hot-fire test. High-speed piezoelectric dynamic pressure

measurements were recorded within the combustor and the oxidizer feed system while high-speed hydroxyl-chemiluminescence (OHCL) videography was recorded to capture fluctuations in the spontaneous emission of the excited hydroxyl radical (OH*). Sec. 4.3 presents the resulting combustion instability data of the three injectors at different operating conditions for methane-oxygen propellants. By calculating power spectral densities across the examined frequency domain, the characteristic frequencies of combustion instability modes were separately determined for the OHCL video data and for the dynamic pressure measurements. While methane-oxygen served as the primary propellant combination for this study, a few supplementary tests were conducted using hydrogen-oxygen propellants (and included here in Sec. 4.4), followed by similar combustion instability results. Sec. 4.5 presents an analysis of the instability results and discusses potential injector-related mechanisms responsible for improved or worsened stability characteristics. Coupling between combustive in-chamber heat release rates (via OHCL video) and pressure fluctuations was determined through magnitude-squared coherence and through normalized cross correlations.

4.2 Methods

4.2.1 Shear coaxial injector design

Three single-element shear coaxial injector geometries were designed, manufactured, and tested in this study – a flush bi-coaxial (served as the baseline design), a nearly identical bi-coaxial with a recessed oxidizer post ($l_\mathrm{r}/d_\mathrm{ox,OD} = 1.7$), and an additively-manufactured tri-coaxial injector. Fig. 4.1 shows these injector geometries with relevant dimensions displayed. The two bi-coaxial designs used in this work were both traditionally-manufactured three-part assemblies consisting of a copper fuel sleeve and stainless steel oxidizer post, each with a fuel-to-oxidizer outlet area ratio of approximately 0.75, yielding an outer-to-inner momentum flux ratio of approximately 0.33 for methane-oxygen at a mass flow ratio ($\mathrm{O/F} = \dot{m}_{\mathrm{GO_2}}/\dot{m}_{\mathrm{GCH_4}}$) value of 2.9, representative of the nominal target test conditions. The actual test conditions

varied and are described further in the results section.

The tri-coaxial injector was designed as a single, monolithic part and fabricated via a laser powder bed fusion (L-PBF) additive-manufacturing process from stainless-steel 17-4 PH (Proto Labs Inc. via GE Concept Laser Mlab R printer) which used a 20 μm layer thickness. The design took into consideration the specific limitations of the printer used, including the smallest possible wall thickness, gap size, feature size, and maximum unsupported print angle. The post-print manufacturing required was minimal, requiring only a few o-ring grooves and sealing surfaces to be machined. The total fuel-to-oxidizer area ratio was approximately 0.54. More information on this AM tri-coaxial design can be found in [64]. The bottom images in Fig. 4.1 depict cross-sections of the AM tri-coaxial injector in a CAD model as well as an x-ray CT scan of the final printed part, revealing the fully-resolved intricate features of the intra-element propellant manifolds. Computational fluid dynamic analyses were conducted to inform intraelement flowpath design. The three channels that connect the main fuel plenum to the central fuel post were appropriately sized to a 0.7 mm diameter to establish the proper fraction of fuel mass flow rates through the center fuel post and the outermost annular flowpath. The total fuel mass flow was split between the center core and outer-most annulus such that off-unity velocity and momentum flux ratios for a similar targeted oxidizer-to-fuel mass flow ratio, O/F = 2.9, a fuel-rich condition pertinent to rocket propulsion systems that use methane-oxygen. Momentum and velocity ratios between the 3 streams varied with test conditions and are described in the results section.

4.2.2 Pressurized single-element combustor experiment

The pressurized single-element combustion chamber assembly and design is summarized here, but more comprehensive documentation can be found in [16]. The combustor assembly was comprised of 5.08 cm thick stainless steel spool sections with an inner diameter of 5.08 cm and had an effective length of 26.7 cm. Hot combustion gases converged and exited through

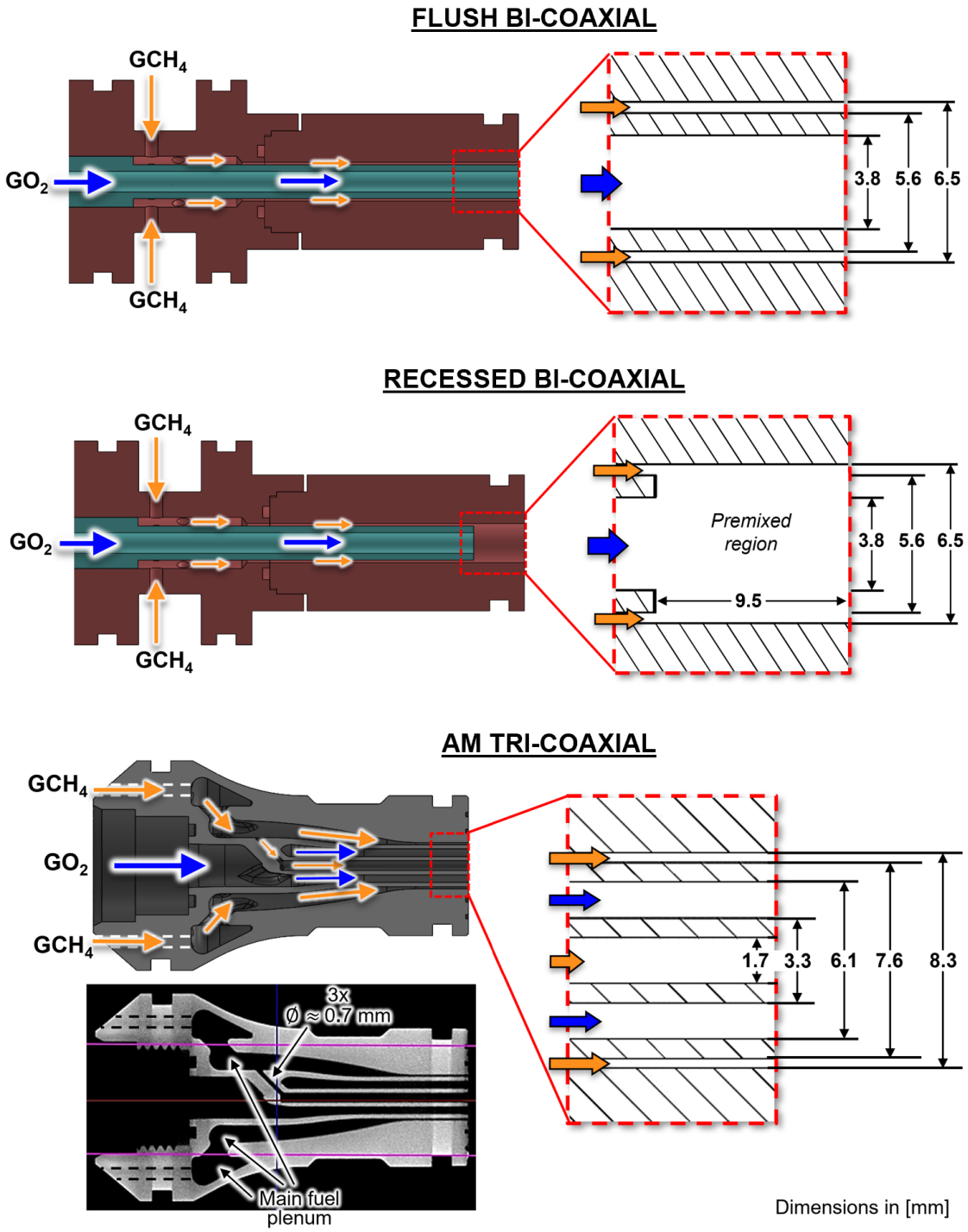

Figure 4.1: Cross-sections of: *top*) traditionally-manufactured flush bi-coaxial injector CAD model, *middle*) traditionally-manufactured recessed bi-coaxial injector CAD model, and *bottom*) additively-manufactured tri-coaxial injector CAD model with an x-ray CT scan of the final printed part.

a water-cooled copper conical nozzle section at the end of the combustor. The nozzle throat diameter was measured before each test and remained constant at 0.70 cm. As seen in Fig. 4.2, the combustor included an optical spool section which housed a 2.5 cm thick fused-silica window that was 7.62 cm long and 2.54 cm wide and provided optical access to the injection and mixing zone.

Combustion was initiated by a H_2-O_2 spark torch igniter, followed by low flow rate propellant injection to ensure main combustion chamber ignition before opening high flow main propellant valves a few seconds later. The primary propellant combination was O_2 and CH_4, while a coaxial co-flow plate injected N_2 near the inner chamber walls to mitigate thermal damage. Three chamber pressures (P_C = 35, 53, and 69 bar) were targeted for each injector by increasing propellant mass flow rates. Static chamber pressure was measured using a Taber 206 pressure transducer and flow rates were metered via choked orifices, Omega PX319 pressure transducers, and K-type thermocouples.

The flow and operating conditions presented throughout this paper are averaged over

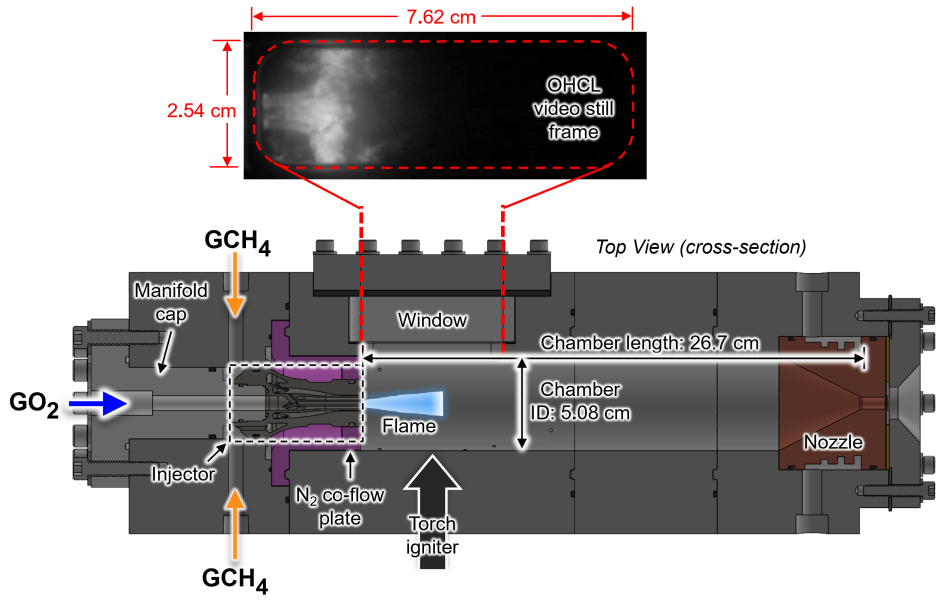

Figure 4.2: Cross-sectioned top-down view of the pressurized single-element combustion chamber assembly shown using the AM tri-coaxial injector with typical still image captured from OHCL videography.

one second of quasi-steady state operation for each test. Here, steady state is defined by maintaining a near constant average chamber pressure, within 2.5%, over a one second test duration. Each test targeted an oxidizer-to-fuel mass flow O/F ratio ($O/F = \dot{m}_{GO_2}/\dot{m}_{GCH_4}$) of 2.9 and a N/O dilution ratio ($N/O = \dot{m}_{GN_2}/\dot{m}_{GO_2}$) of 3.0 with a total test time of five seconds. These conditions were chosen to produce stable combustion relevant to fuel-rich methane-oxygen rocket combustors while sustaining acceptable combustion temperatures for hardware integrity. Although the combustion product gas temperature approached 2200 K, chamber wall temperatures remained below 1150 K from the protective GN_2 layer near the inner chamber walls. Injector stiffnesses for both the fuel and oxidizer flowpaths were low, typically between 2–5%. These low values represent an objective for rocket injector design, but in this case also help promote pressure and thermal oscillations within the combustor which are dampened by the co-flow. It should be noted that the propellant feed system upstream of the combustor's injector housing remained unchanged from test to test. Since choked-flow orifices were used for flow metering of all three fluids, the upstream feed system was decoupled from the combustor. As such, differences in results at a given chamber pressure condition can be well-attributed to changes in injector geometry and assumed independent of any potential flow perturbations from the feed system upstream of the orifices.

4.2.3 Instrumentation

Chamber and oxygen feedline pressures were measured using dynamic pressure sensors (PCB Piezotronics, Model 113B22) with a frequency response up to 500 kHz. For simplicity, this dynamic pressure sensor will be referred to as a *PCB* throughout this paper. Fig. 4.3 shows the PCB sensor positions relative to the combustor assembly. PCB 1 was installed on the oxygen feedline, 33.2 cm upstream of the injector plane. PCB 2 and PCB 3 were installed in the combustion chamber, at axial locations 10.2 cm and 1.0 cm downstream of the injector plane, and azimuthal positions 135° and 105°, respectively. To isolate the combustion chamber PCB sensors from the high heat flux environment, the sensors were offset from the

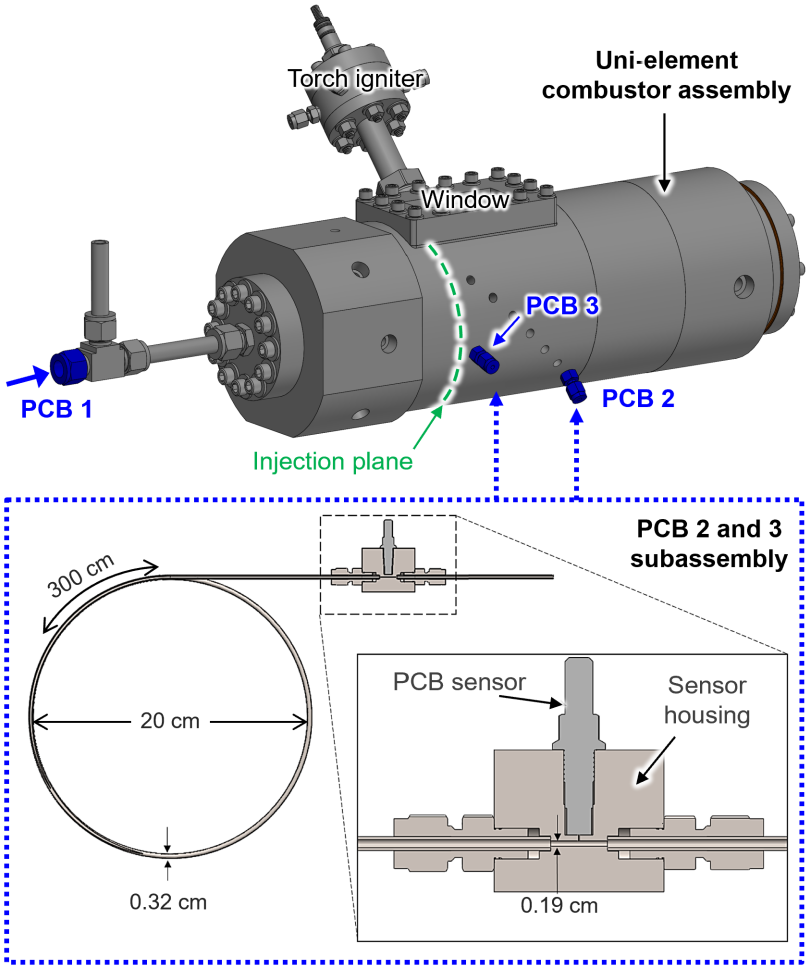

Figure 4.3: PCB dynamic pressure sensor setup and positioning on the single-element combustor.

chamber inner walls with a standoff distance of 76.2 mm, and connected through a 3.175 mm diameter sense line. The PCB sensors were flush mounted to the chamber sense line using a custom designed tee. Cavity resonances from the offset were eliminated by terminating the third branch of the tee to a very long sense line, or semi-infinite tube (L/D $\approx$ 3800), capped at the end. This design leverages viscous dissipation to suppress pressure reflections from the capped end. The PCB sensors were connected to a signal conditioning amplifier (PCB Piezotronics, Model 482C15), which were sampled simultaneously at 250 kHz per channel on a multi-function data acquisition board (National Instruments, Model PXIe-6368). National Instruments LabVIEW software was used to acquire the signals.

OH* chemiluminescence (OHCL) imaging near 308 nm is a common method of identifying heat release zones and flame boundaries in combustion environments by simply coupling a spectral filter with a high-speed ultra-violet image intensifier and visible camera. The method has been used in prior works to assess combustion instability effects on injection dynamics [67, 83]. OHCL videography captured the emitted light from the excited OH combustion radicals associated with the flames produced by each single-element injector, captured via the aforementioned fused-silica window. The OHCL videography system included a 308 nm ultra-violet (UV) filter, a UV lens, an intensifier (Invisible Vision UVi model 2550B-10) to convert UV to amplified visible light, and a Phantom high-speed visible camera (model v2011). OHCL video was recorded over a 234 x 614 pixel window at a frame rate of 55 kfps during the steady-state interval that corresponded to each hot-fire test. A single still frame of the OHCL video is shown in the top of Fig. 4.2 for a representative test. The OHCL videography system was offset from the combustor by 40 cm and was centered on the window, resulting in a per-pixel spatial resolution of approximately 0.13 mm.

4.2.4 Chamber eigenfrequency predictions

The driving mechanism of combustion instability is the coupling between oscillatory energy of combustion and the fluid dynamics of the system. High-frequency acoustic instabilities are defined as chamber pressure oscillations that correspond to the longitudinal and transverse acoustic modes (eigenfrequencies) of the chamber. While analytical solutions for eigenfrequencies are available for constant area, cylindrical ducts with uniform flow, non-uniform effects, such as flow acceleration through the nozzle and instrumentation features at the chamber walls, must be accounted for in practical combustor geometries. These additional features introduce complexities where solutions for the chamber acoustic modes are obtainable only through numerical methods.

Computational aeroacoustics (CAA) simulations were conducted using COMSOL Multi-

physics software. The goals of the CAA analysis were to first predict the eigenfrequencies and their associated mode shapes in the combustion chamber. The results of the analysis were then used to help identify the nature of coupling between the PCB and OHCL signals. Additionally, the CAA results were used as a diagnostic tool to identify both instrumentation noise inherent in the system, or amplitude variations in pressure fluctuations between PCB sensors due to installation effects.

The Pressure Acoustics Frequency Domain interface within COMSOL was used to compute the eigenfrequencies of the combustion chamber. Thermodynamic and mixture properties of the combustion products were simulated using the NASA Chemical Equilibrium with Applications (CEA) program [47]. The target chamber pressure, mixture ratio, and diluent ratio were provided as inputs to CEA to determine the equilibrium temperature of combustion products. The equilibrium temperature was provided as input to COMSOL and was assumed uniform throughout the combustion chamber. The boundary condition at the injector plane was approximated as a solid boundary. The nozzle impedance was approximated as

$$Z = Z_0 \frac{2}{M\left(\gamma - 1\right)} \tag{4.1}$$

where $Z_0 = \rho c$ is the characteristic impedance of the equilibrium gas products and M is the mean flow Mach number. Equation 4.1 is the formulation by LaMarque and Poinsot [70], where the wavelength of fluctuations is large ($\lambda \approx 10L$), compared to the characteristic length of the nozzle. Using the equilibrium conditions output from CEA, the critical frequency to which Eq. 4.1 is applicable is $\approx$ 2kHz.

The sensitivity of the combustion chamber eigenfrequencies to the interior fluid model complexity was determined through multiple simulations of the interior fluid domain. The initial model was the least complex, containing only the length of the chamber with constant cross sectional area between the injector plane to the inlet of the nozzle. Each subsequent simulation included an additional model feature than the previous simulation to observe

the impact of the increased geometric complexity of the feature on the combustion chamber eigenfrequencies. The features added, in order of increasing model complexity, were the convergent nozzle, the window sections along the inner diameter of the combustion chamber, and the torch igniter. All features added after the convergent nozzle did not produce significant changes to the chamber eigenfrequencies below the cut-off frequency of the first tangential mode, up to about 10 kHz.

Resultant mode shapes generated by COMSOL are shown in Fig. 4.4 for the first three longitudinal chamber eigenmodes. For reference, the axial positions of PCB 2 (10.2 cm) and PCB 3 (1.0 cm) are outlined relative to the various node (white) and anti-node (dark blue or dark red) locations for the 1L, 2L, and 3L modes.

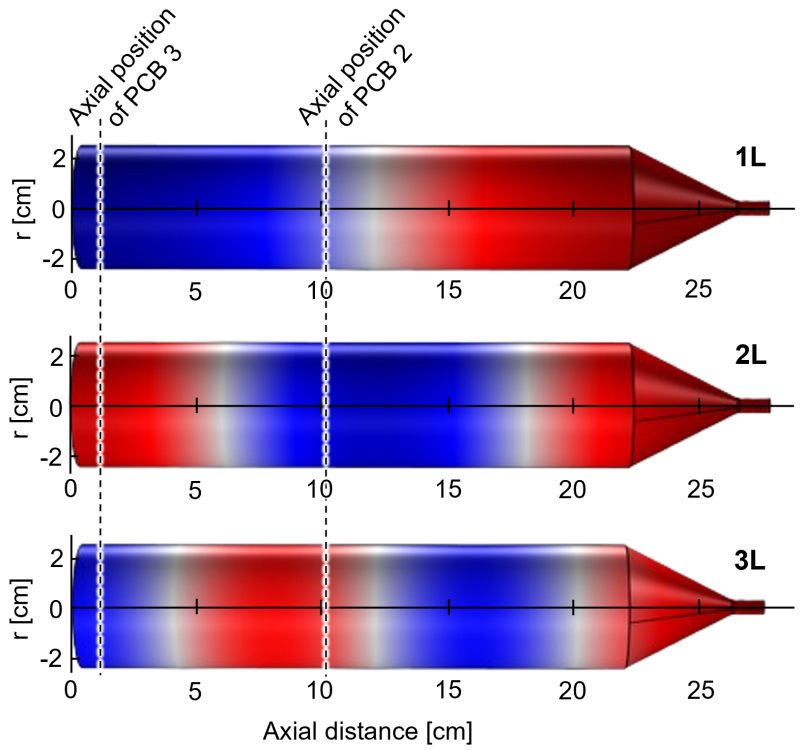

Figure 4.4: Longitudinal chamber mode shapes as predicted by COMSOL for 1L, 2L and 3L, with axial positions of in-chamber PCBs shown.

4.2.5 Experimental data analysis

The top subfigure of Fig. 4.5 details the nominal test sequence in the pressurized single-element rocket injector experiment. Each hot-fire test involved staging of the propellant mass flow rates, and was initiated once ignition of the GH_2-GO_2 torch had been verified. First, propellant combustion was confirmed by a sudden rise in chamber pressure during the low flow stage. Once the required pressure rise was detected, the hot-fire segment proceeded to a high flow stage that delivered propellants at the flow rates required to drive the combustion reaction to reach the desired chamber pressure. All tests were hot-fired with a high flow interval of five seconds to allow the chamber pressure sufficient time to reach steady state. The high-speed videos were continuously recorded with a memory buffer that was triggered to capture the last 1.68 seconds of hot-fire, prior to shutdown. The statistics of the PCB signals were computed over a one second interval during steady state, which was synchronized to the first second of the high-speed video, indicated by the vertical dashed lines in Fig. 4.5.

The power spectral density (PSD) of the PCB signals was used to identify the broadband and tonal frequency content of both feedline and chamber pressure oscillations. The PSDs were computed using a 2^{18}-point Fast Fourier Transform (FFT) of the raw voltage signal. All signals were filtered using a 9^{th} order Butterworth high-pass filter with a 20 Hz corner frequency. The raw voltage signals were corrected for sensitivity and normalized by reference pressure $P_{\text{ref}} = 20\ \mu$Pa. The PCB power spectral density was estimated via Welch's method [145] in Matlab. A few non-physical high-frequency tones were observed throughout the test sequence, both prior and subsequent to the high-flow hot-fire segment. The tones were removed *a posteriori* using spectral subtraction. The noise signal used for subtraction was defined by the PSD of the PCB signals during one second of the low flow segment of hot-fire (see Fig. 4.5).

Heat release rate fluctuations were estimated from the high-speed OHCL videography recorded during hot-fire. Each frame was spatially trimmed to include only the window field of view (7.62 cm x 2.53 cm) to reduce signal contamination due to reflections along the window

port sidewalls and to crop any absence of signal in the border regions of the video recording. The raw pixel amplitude, recorded as a value between 0 to 255, was integrated across the field of view to produce a scalar value of the OHCL for each frame. This was repeated over one second of hot-fire to derive the 55,000-point OHCL time series. A 2^{16}-point FFT was applied to estimate the power spectral density from the OHCL time series. The sensitivity of OHCL power spectral density to both the location and area of the spatially integrated region within the field of view was tested and was found to only scale the broadband spectral amplitude without impacting the fundamental shape or tones of the spectra.

The magnitude-squared coherence was calculated as it provides insight on coupling frequencies between pressure fluctuations and heat release rate. The coherence was computed using

$$\gamma_{xy} = \frac{S_{xy}(f)S^*_{xy}(f)}{S_{xx}(f)S_{yy}(f)} \tag{4.2}$$

where S_{xy} is the cross spectrum of the OHCL and PCB signals, and S_{xx} and S_{yy} are the respective signals' autospectra. The raw PCB signals were resampled at 55 kHz to match the OHCL time series, prior to computing the coherence. The coherence outputs a value between 0 and 1, which indicate weak and strong coupling, respectively, between the PCB and OHCL signals. Strong coupling is indicative of a thermoacoustic instability at the corresponding frequency.

Normalized cross correlations were computed between the OHCL and PCB signals by

$$R_{xy}(t_{\text{delay}}) = \frac{1}{N}\sum_{i=1}^{N} \frac{\left[x(t_i) - \bar{x}\right]\left[y(t_i + t_{\text{delay}}) - \bar{y}\right]}{\sigma_x \sigma_y} \tag{4.3}$$

where x and y are the OHCL and PCB signals, respectively, t_{delay} is the *signal delay time* between the PCB and OHCL signal, i is the time index of the discrete signal, N is the signal length, $\bar{()}$ indicates the signal mean value, and σ is the standard deviation. The signal cross correlations were used to determine coupling and phase shift between heat release and pressure fluctuations of the oxidizer feedline to assess low-frequency injection-coupled

(i.e., chugging) characteristics. Strong coupling would correspond to positive correlation coefficient values close to 1. The delay time was determined by indexing the first positive correlation peak in the time domain and can be interpreted as the response time required for the exothermic combustion process to be influenced by a change in the oxidizer feedline pressure (as detected by PCB 1).

It is notable that the coherence and cross correlations of the pressure and OHCL signals share similarity with the classical Rayleigh Index. While a Rayleigh Index can help describe the amplification of pressure and heat release interactions associated with thermoacoustic instabilities, experimental estimation of this parameter in a complex three-dimensional flow-field, as examined here, is challenging due to limitations in the spatial resolution and dimensionality of diagnostics. Alternative metrics like coherence and cross correlation based on measurements at various chamber locations provide similar insight into coupling characteristics of pressure and heat release for the experiments herein with practical diagnostics. Furthermore, coherence calculations enable a multi-modal distribution of the coupling intensity over a wide frequency domain and the cross correlations quantify the transient phase shift between the heat release and pressure response, and provide a visualization of instability decay behavior.

4.3 Results

4.3.1 Test conditions

For each of the three shear coaxial injector designs investigated in this study, combustion stability characteristics were assessed via hot-fire testing in a pressurized single-element combustion chamber using methane-oxygen propellants. Three chamber pressure conditions (P_C = 35, 53, and 69 bar) were targeted to determine the chamber pressure dependence on stability behavior. Chamber pressures were altered by changing propellant flow rates via setting the upstream pressures of each propellant orifice. O/F and N/O ratios were held constant at approximately 2.9 and 3.0, respectively. Two important non-dimensional

Table 4.1: Test conditions for all single-element CH_4-O_2 combustor tests averaged over one second of steady state operation.

Test	Prop.	Injector	P_C [bar]	$\dot{m}_{ox}$ [g/s]	$\dot{m}_f$ [g/s]	$\dot{m}_{N_2}$ [g/s]	O/F	N/O	$\Delta P_{inj,ox}$ [% P_C]	$\Delta P_{inj,f}$ [% P_C]
6198	CH_4-O_2	Flush Bi	34.9	17.7	6.0	53.7	2.93	3.04	2.7%	2.8%
6234	CH_4-O_2	Recessed Bi	35.6	18.6	6.2	53.8	2.99	2.90	3.0%	1.8%
6219	CH_4-O_2	AM Tri	34.7	18.0	6.1	53.8	2.92	3.00	2.0%	2.0%
6204	CH_4-O_2	Flush Bi	53.0	27.0	9.2	79.3	2.94	2.94	4.1%	3.4%
6233	CH_4-O_2	Recessed Bi	54.2	26.5	9.1	79.7	2.91	3.00	4.2%	2.3%
6223	CH_4-O_2	AM Tri	53.1	25.9	9.2	79.1	2.81	3.06	3.2%	2.5%
6214	CH_4-O_2	Flush Bi	68.4	33.1	12.0	98.7	2.76	2.98	3.9%	4.2%
6231	CH_4-O_2	Recessed Bi	69.6	34.3	11.5	96.1	2.97	2.80	4.8%	3.1%
6229	CH_4-O_2	AM Tri	69.1	33.1	11.9	102.0	2.78	3.08	3.1%	2.6%

metrics involved in the mixing processes of coaxial jets are the *outer-to-inner* velocity ratio ($VR = u_o/u_i$) and momentum flux ratio ($J = \rho_o u_o^2/\rho_i u_i^2$). The momentum flux ratios (J) and velocity ratios (VR) were calculated to be $J = 0.33 \pm 0.03$ and $VR = 0.81 \pm 0.04$ for the flush bi-coaxial, $J = 0.31 \pm 0.01$ and $VR = 0.79 \pm 0.01$ for the recessed bi-coaxial, and $J_1 = 2.62 \pm 0.19$, $J_2 = 1.22 \pm 0.08$ and $VR_1 = 1.15 \pm 0.04$, $VR_2 = 1.28 \pm 0.04$ for the AM tri-coaxial. The velocity ratios are approximately constant due to the fixed O/F ratios, and the momentum flux ratios are nearly constant with changing pressure due to density change of the compressible propellants being more significant than the velocity change. Injection stiffnesses ($\Delta P_{inj}/P_C$) were calculated for each propellant, including the GN_2 co-flow. $\Delta P_{inj,GN_2}/P_C$ was typically 14-19%. Table 4.1 lists the flow conditions achieved and corresponding injection stiffnesses for each of the 9 tests averaged over a one second steady state interval. It should be noted that the injector stiffness was typically a bit lower for the tri-coaxial injector relative to the bi-coaxial injectors at similar flow conditions.

Despite slight deviations in flow conditions and chamber pressures achieved for each test, the calculated equilibrium combustion temperatures were relatively similar ranging between 2010–2175 K for all tests. This resulted in only a +/- 1.5% variation in the speed of sound within the combustion chamber across all tests. As a result, flow condition discrepancies are not expected to significantly affect the chamber eigenmode (i.e., longitudinal) frequencies.

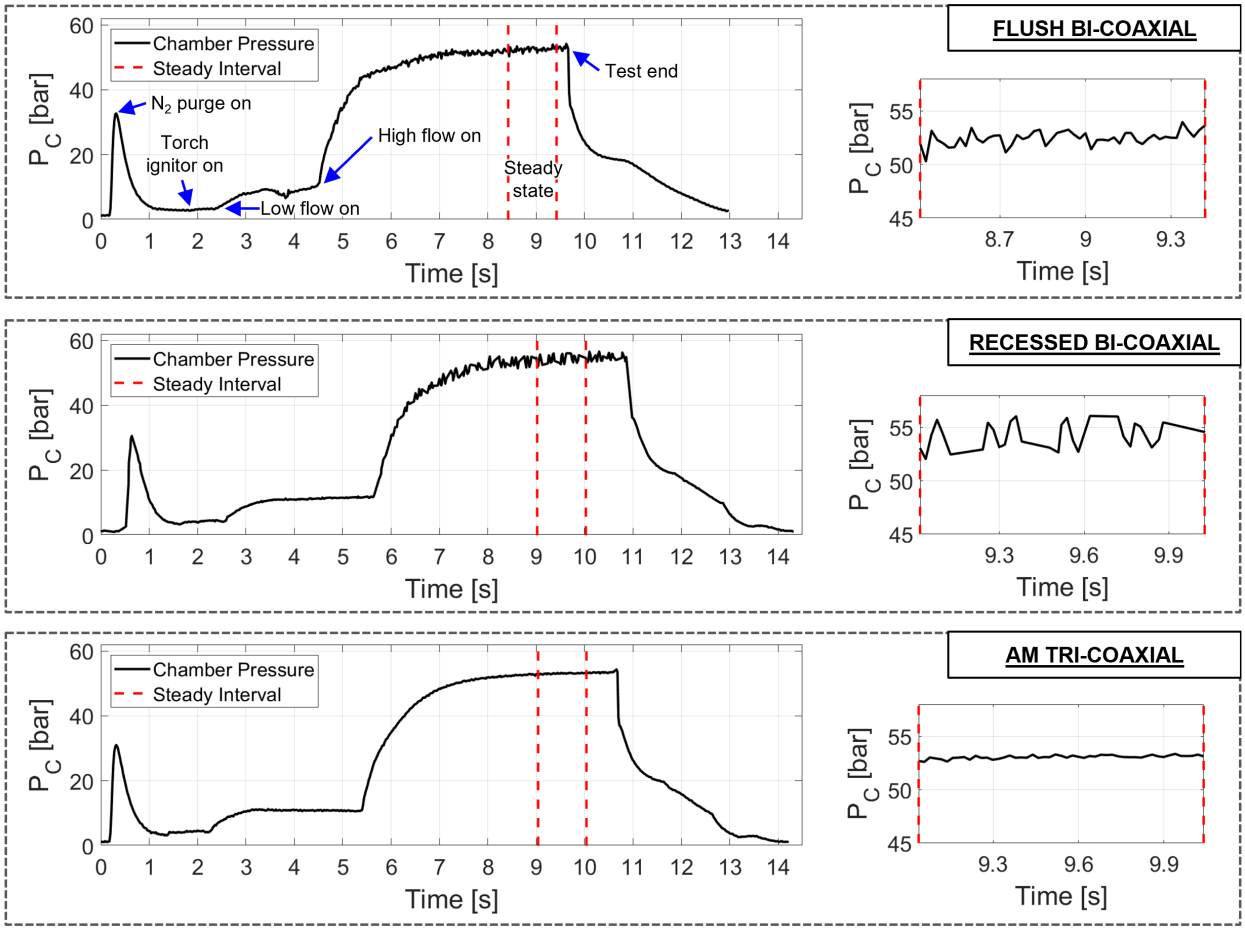

Figure 4.5: Chamber pressure traces for each injector at the 53 bar CH_4-O_2 condition.

Stiffnesses for the fuel and oxidizer varied from 2–5% and generally increased with higher chamber pressures. While injection stiffnesses are traditionally around 15–20% for LREs to operate within sufficient stability margins [58, 128], lower stiffnesses were used in this experiment to encourage the onset of combustion instabilities by reducing the damping effect of high injection pressure drop and the nitrogen co-flow. Low injection stiffnesses were also a result of using gaseous propellants since significantly less viscous losses occur compared to liquids.

As previously mentioned, the GN_2 co-flow was necessary for maintaining acceptable combustor wall temperatures. The injection of the GN_2 into the chamber acted as a constant damping mechanism by absorbing energy from the feedback loop caused by oscillatory heat

release from combustion and reactant injection processes. Due to the relatively high co-flow injection stiffnesses of 14–19%, the GN_2 feed system was only passively involved in instability dynamics. Its influence remained relatively constant from test to test and the trends and results presented here are primarily dependent on injector design and chamber pressure.

The top of Fig. 4.5 illustrates the chamber pressure trace and timing of key test sequence events for a typical hot-fire test. The one second quasi-steady state interval is also highlighted here, with the steady state window magnified off to the right of the figure. The chamber pressure traces for the 53 bar case are shown as a representative comparison between the three shear coaxial injectors. While the absolute pressure transducer used to measure chamber pressure does not possess the necessary bandwidth to resolve pressure fluctuations faster than 50 Hz, the relative amplitudes of the chamber pressure fluctuations are visible and serve as an indication of low-frequency chugging instability behavior. The AM tri-coaxial injector depicts the smoothest pressure trace, indicative of smooth combustion ($\Delta P_{\mathrm{dyn},f} < 5\%\ P_{\mathrm{C}}$), at least within the low frequency domain. In contrast, both bi-coaxial injectors, especially the recessed configuration, show larger changes in pressure indicating some low-frequency chugging effects. These fluctuations can be better quantified with higher bandwidth instrumentation.

4.3.2 Dynamic pressure measurements

The three PCB piezoelectric dynamic pressure sensors recorded high-speed pressure measurements at a sample rate of 250 kHz for each test. PCB 1 was located in the oxidizer feedline just upstream of the combustor oxidizer inlet, while PCB 2 and 3 were positioned at different axial and azimuthal locations in the chamber. Their positioning on the combustor can be seen in Fig. 4.3. It should be mentioned that dynamic pressure measurements were not recorded within the fuel feed system since the oxidizer flow path of a shear coaxial injection element is typically much more susceptible to inciting injection-coupled instabilities from their inherent organ-pipe geometry [129]. Fig. 4.6 depicts the low-frequency chugging instability mode (left

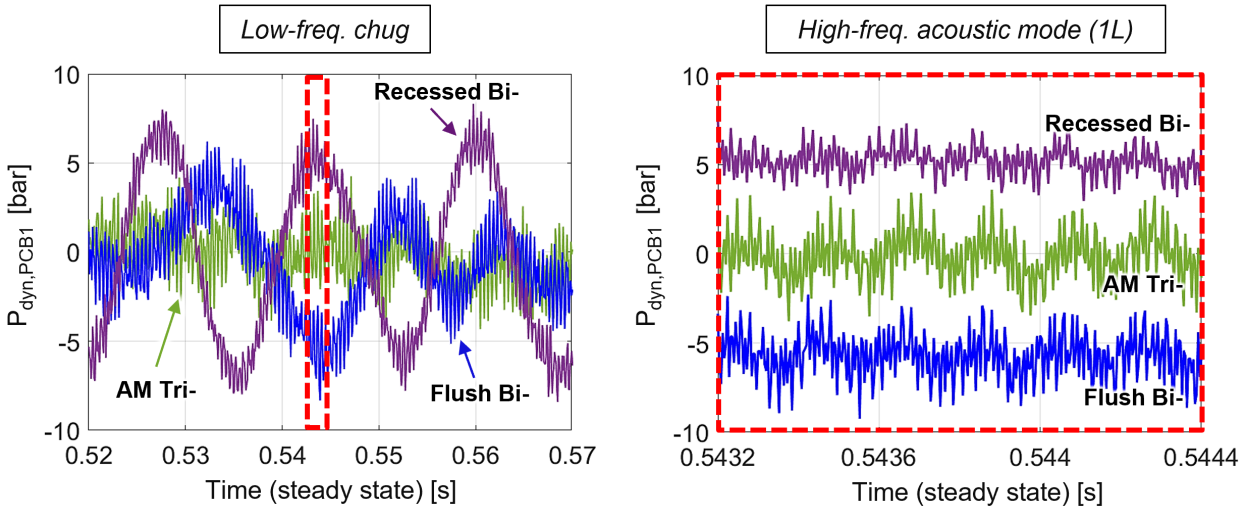

Figure 4.6: Representative raw pressure traces from the oxidizer feedline dynamic pressure sensor (PCB 1) for each injector at the 53 bar CH_4-O_2 test case. Sinusoidal dynamic pressure changes shown for low-frequency chug (*left*) and high-frequency 1L acoustic mode (*right*).

plot) and high-frequency acoustic modes (right plot) from raw pressure traces recorded as voltages by PCB 1 (oxidizer feedline) during a portion of the steady state interval at the 69 bar chamber pressure condition for each of the three injectors. The chugging behavior is illustrated well by high-amplitude sinusoidal pressure traces (left plot of Fig. 4.6) for the two bi-coaxial configurations, whereas the tri-coaxial exhibits negligible low-frequency pressure oscillations. The right subfigure of Fig. 4.6 shows lower-amplitude sinusoidal pressure traces windowed to highlight the 1L acoustic frequencies (1620 Hz for the bi-coaxials, 1720 Hz for the tri-coaxial), with the recessed bi-coaxial appearing slightly lower amplitude that the other two injectors at this condition.

4.3.2.1 Power spectral density

After applying a 20 Hz high-pass filter on the PCB raw voltage traces, power spectral densities (PSD) were determined by first applying an FFT, followed by Welch's method [145], in order to determine how the power of each PCB signal was distributed across the relevant frequency domain. Fig. 4.7 shows the resulting PSD plots for each PCB across all three pressure

Table 4.2: Comparison of COMSOL-predicted and measured combustion chamber eigenfrequencies for CH_4-O_2 tests.

		Bi-coaxials		AM Tri-coaxial	
Mode	Predicted [Hz]	Measured [Hz]	Deviation	Measured [Hz]	Deviation
1L	1890	1620	-14.3%	1720	-9.9%
2L	3766	3230	-14.2%	3410	-10.4%
3L	5603	4800	-14.3%	5280	-6.1%
4L	7351	6410	-12.8%	6840	-7.5%
5L	8924	7680	-13.9%	8450	-5.6%
6L	10354	N/A	–	10070	-2.8%

conditions. Each plot depicts the PSD curves for all three injectors to directly compare the dominant combustion instability frequency modes (represented by pronounced local maxima) that manifest at each PCB. The predicted longitudinal chamber eigenfrequencies are overlaid here for reference. Although chamber eigenfrequencies also predict transverse modes, these fall outside of the examined frequency domain and are therefore ignored in this analysis.

Table 4.2 presents a comparison of the COMSOL-predicted and measured chamber longitudinal eigenfrequencies from 1L to 6L with generally good agreement. The longitudinal mode frequencies were over-predicted by simulation likely from using the equilibrium combustion temperature (determined by NASA CEA), which was higher than the actual combustion temperature considering that heat losses to chamber walls, non-uniformities in gas properties, and bulk flow velocity effects were unaccounted for in this approximation. Over-predicting chamber gas temperature leads to a higher speed of sound, and therefore higher-frequency chamber acoustic modes. Notably, the measured frequencies for the tri-coaxial injector are in somewhat better agreement with predictions.

In Fig. 4.7, a few general trends are readily apparent. For the flush (blue curve) and recessed (purple curve) bi-coaxial injector designs, a dominant ∼60 Hz chugging mode was present across all PCBs for all pressure conditions. The PCB PSD traces for these two bi-coaxial are quite similar across the frequency domain of interest. For the 35 bar and 53 bar tests, the recessed configuration exhibited a marginally higher magnitude (+10%) for the

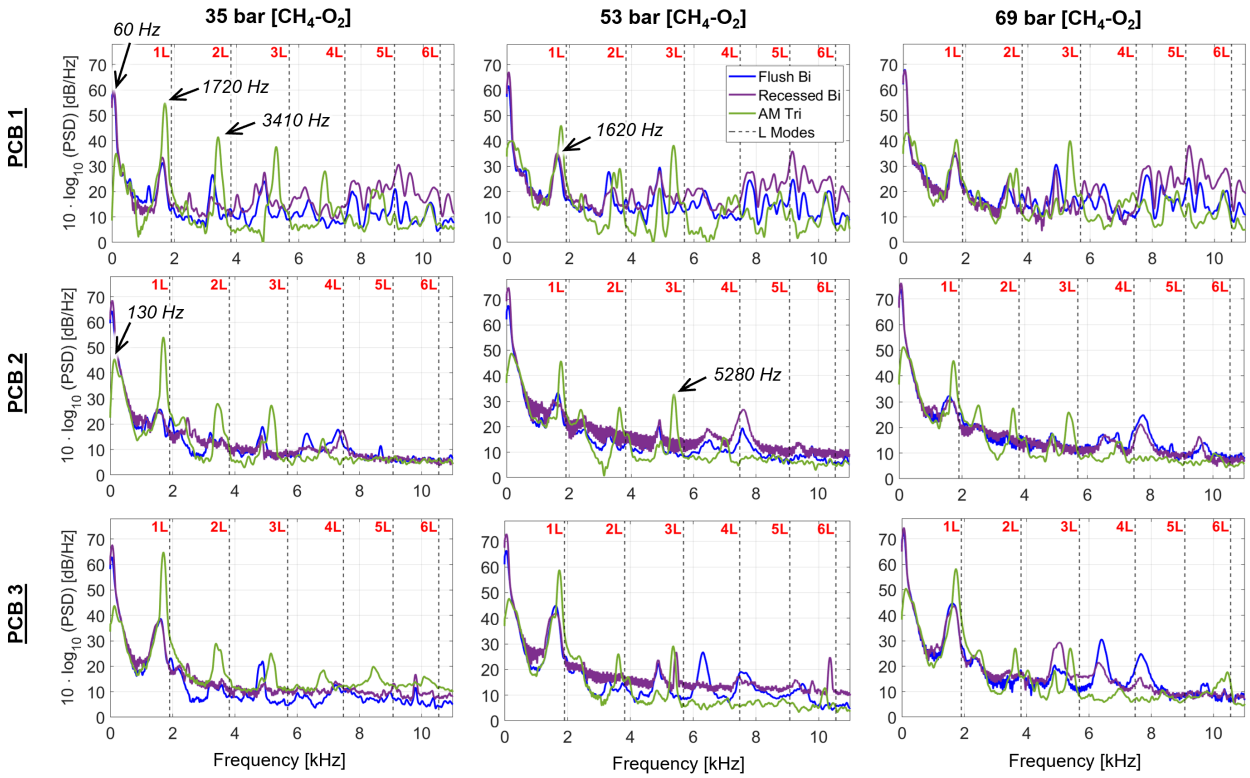

Figure 4.7: Compiled power spectral density plots across the examined frequency domain for each dynamic pressure sensor (PCB) for the 9 CH_4-O_2 test conditions. Each plot compares PSD results for each of the three shear coaxial injector geometries.

60 Hz chugging frequency when compared to the flush bi-coaxial. However, for the 69 bar case, the PSDs of the two bi-coaxial injectors are virtually identical (within 3%), particularly for the low-frequency chugging modes and weaker longitudinal modes. The second most dominant instability mode present for the bi-coaxial injectors was 1620 Hz (near the 1L frequency). No other dominant instability frequencies were consistently present for these injectors.

The tests that used the AM tri-coaxial injector (green curve in Fig. 4.7) demonstrated considerably different instability characteristics than the bi-coaxial designs. First, while a low-frequency chugging mode was still present, it shifted to a higher frequency of ∼130 Hz and was significantly weaker (32–47% less) in magnitude than the bi-coaxial injectors' 60 Hz chugging mode. Additional dominant modes consistently manifested at 1720 Hz, 3410 Hz,

and 5280 Hz, which show good agreement with the predicted longitudinal eigenmodes (1L, 2L, and 3L, respectively) of the chamber. In many test cases, the 1L mode (1720 Hz) was the most pronounced instability for the tri-coaxial injector, and typically more intense than the bi-coaxial injectors. As mentioned, the measured L-mode frequencies for the tri-coaxial injector were closer to the COMSOL-predicted values compared to the bi-coaxial designs.

In Fig. 4.4, the axial location of the two in-chamber pressure sensors (PCB 2 and 3) are displayed to show their positioning relative to the nodes (regions of no pressure fluctuations, shown in grey) and antinodes (regions of large pressure fluctuations, shown in dark blue or dark red) of the primary chamber longitudinal eigenmodes. PCB 3's position (1.0 cm from the injection plane) is generally closer to the antinode regions for all longitudinal modes, whereas PCB 2's position is closer to the middle of the chamber length (10.2 cm from the injection plane) where odd longitudinal (e.g., 1L and 3L) nodes occur. Due to their relative positioning, PCB 3 consistently measures more severe pressure changes at the 1L frequency than PCB 2, as seen in Fig. 4.7. Similarly, PCB 2 and 3 exhibit quite similar magnitudes for the 2L and 3L modes across many of the tests due to their similar positioning relative to the nodes of the two longitudinal chamber eigenmodes.

4.3.3 Chemiluminescence videography

The second method used to characterize combustion instabilities was high-speed videography that recorded 55,000 frames (over one second of steady state operation) of hydroxyl chemiluminescence (OHCL) for each injector and test condition through a window in the chamber. Importantly, this method enabled examination of the coupling between heat release and pressure changes.

4.3.3.1 Oscillatory flame structure

Chronological still images from OHCL video are shown in Fig. 4.8 for each injector at the 53 bar chamber pressure condition. The time increments between each frame were chosen such that each 8-frame sequence captures more than one full period of each injectors' corresponding chugging mode. For example, a signal with a 60 Hz frequency results in a ∼16 ms period. This figure illustrates the effects of the chugging mode instability on flame structure evolution.

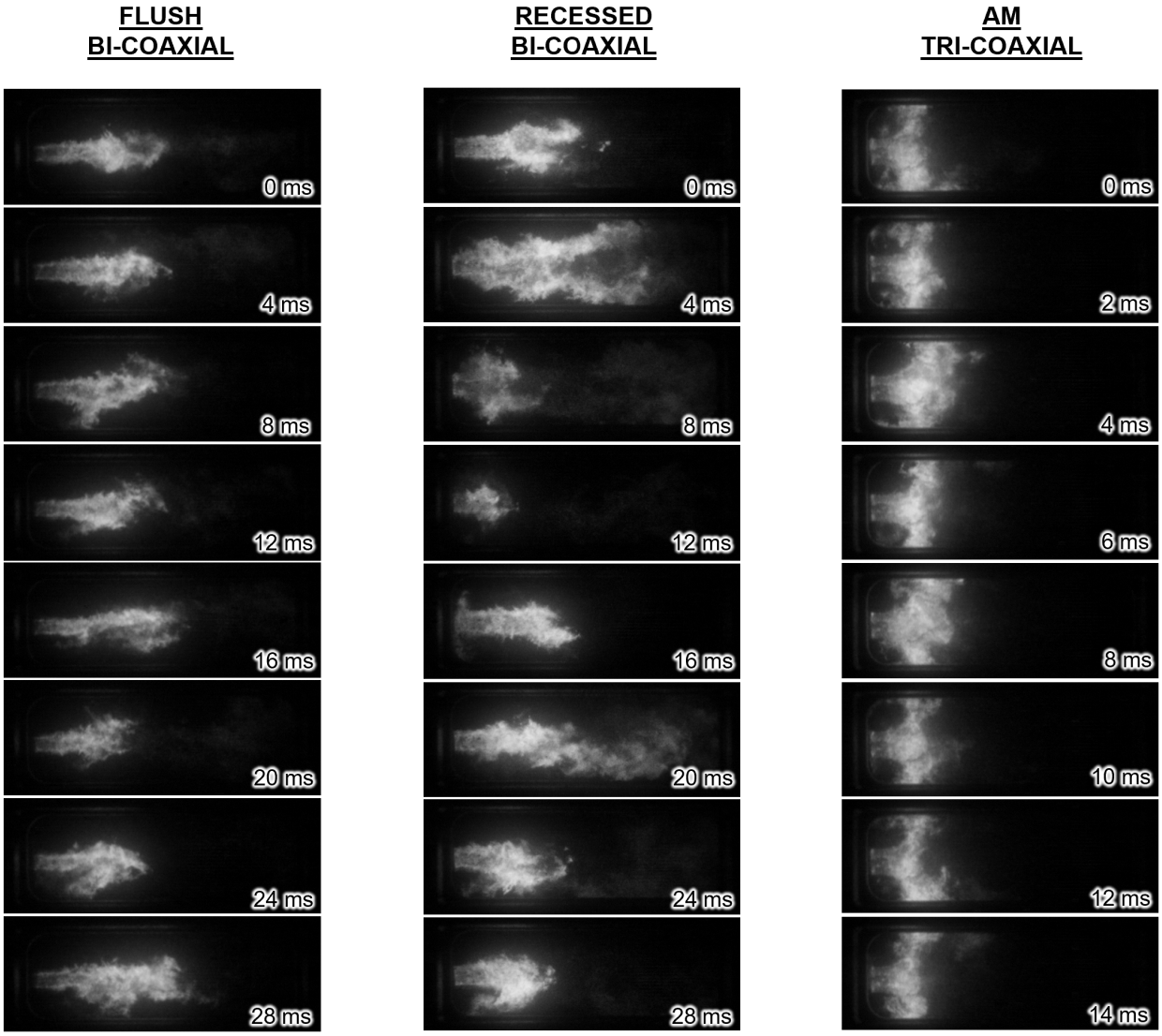

Figure 4.8: Chronological still frames from raw OHCL video depicting CH_4-O_2 flame structure changes from chugging instability for a representative 53 bar test case.

The variation in flame structure over time is seen for both bi-coaxial injectors. Particularly for the recessed configuration, the chugging instability is most noticeable between the 4 ms and 20 ms frames where the flame length is elongated, and truncated at the 8 ms frame. Alternatively, the tri-coaxial exhibits no visible chugging influence on flame structure as the flame length remains relatively unchanged throughout the examined intervals. These trends generally hold true for the entirety of the one second test window for each of the three CH_4-O_2 chamber pressure conditions.

4.3.3.2 Time-averaged flame structure

Pixel intensity data is normalized by a single global maximum pixel intensity across all 9 time-averaged CH_4-O_2 tests. Fig. 4.9 shows contour plots of the normalized line-of-sight

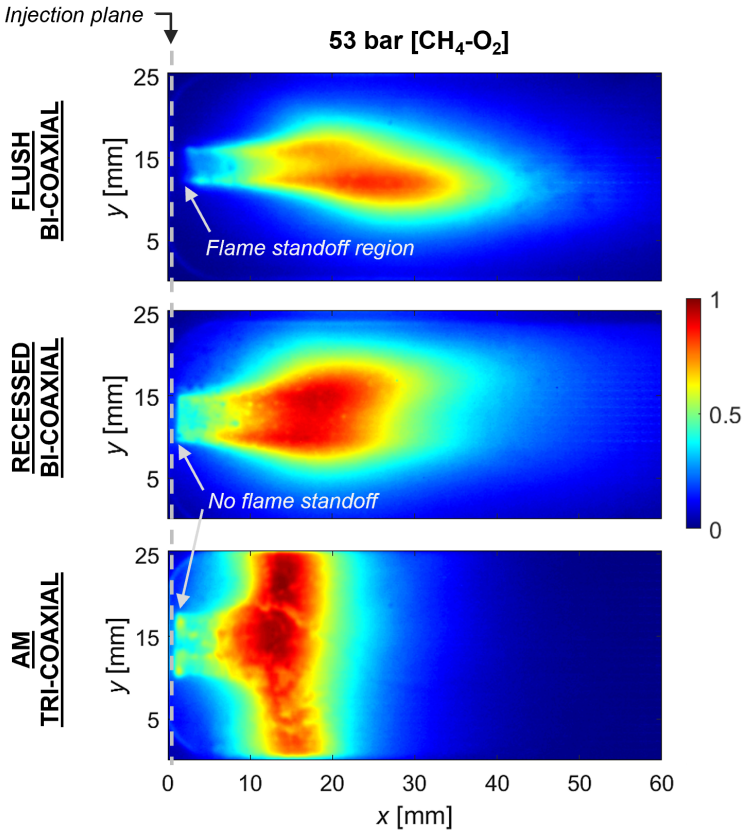

Figure 4.9: Time-averaged images from OHCL video at the 53 bar test condition using CH_4-O_2. Contour plots depict normalized line-of-sight pixel intensity.

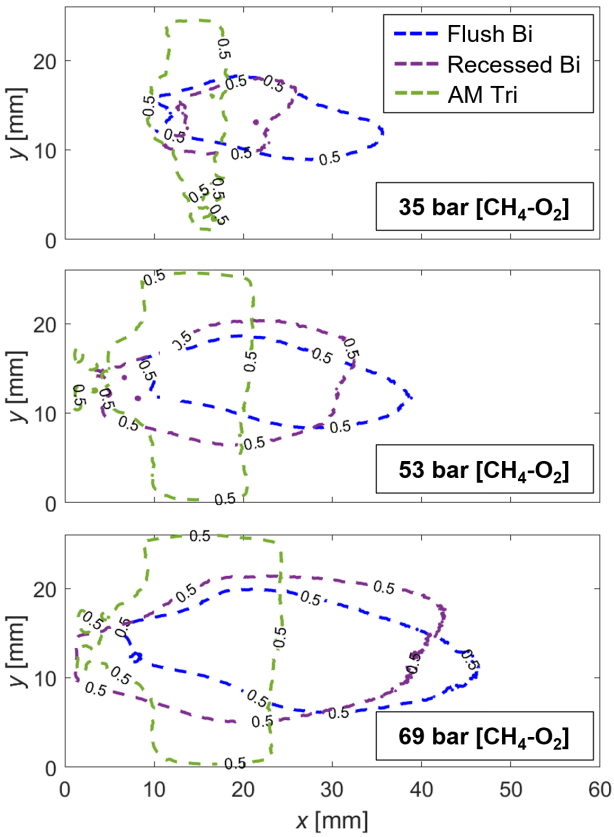

Figure 4.10: Representative time-averaged CH_4-O_2 injector flame structures from normalized OHCL video data using a 0.5 iso-contour profile.

pixel intensities for the time-averaged data to compare the three injectors at a representative chamber pressure condition (53 bar). The recessed injector's flame brush (defined by the width of the exothermic reaction zone at the injection plane) is 41% wider (on average) than that of the flush design. Heat release from combustion is evident directly at the injection plane as a result of the recessed, pre-mixed region just upstream of the injection plane. However, the flush injector shows a visibly cool region immediately downstream of the injection plane where no OH* emission (heat release) is present (highlighted in top subfigure of Fig. 4.9). Some finite axial distance is required for the flush coaxial injector to sufficiently mix its propellants prior to exothermically reacting, whereas the recessed injector's pre-mixed region allows for combustion to occur immediately after (or before) propellants enter the main combustion chamber. This is discussed later in further detail in Sec. 4.5.5 as a likely driver

of injection-coupled instabilities. It should be noted that the width of the tri-coaxial flame images are slightly truncated by the limited width of the window (2.54 cm) which is exactly half of the chamber's inner diameter (5.08 cm).

Furthermore, a 0.5 iso-contour profile was extracted from each normalized and time-averaged flame structure, and is plotted for all three chamber pressure tests in Fig. 4.10. The axial distance between the injection plane and the position of the iso-contour profile furthest downstream serves as a representative flame length metric, l_{f}. l_{f} is reflective of the approximate length of an injector's reaction zone required to achieve complete combustion which is imperative for appropriately sizing a combustor. When compared to the flush bi-coaxial injector, the recessed bi-coaxial and the tri-coaxial result in reduced flame lengths between 8–28% and 46–49%, respectively. A reduction in flame length is indicative of enhanced mixing, best demonstrated by the tri-coaxial design. The increased propellant contact surface area from the addition of the third concentric flowpath facilitates accelerated shear-induced mixing and combustion of the fuel and oxidizer. As the reactants exothermically react further upstream, the energy released rapidly expands the combustion product gas and yields the tri-coaxial's divergent, mushroom-like flame structure seen here.

4.3.3.3 OHCL power spectral density

OHCL power spectral density was calculated over the one second of steady-state operation for each test and is shown in Fig. 4.11. Here, local maxima represent dominant characteristic frequency modes of fluctuating pixel intensity via OH* emission (i.e., heat release) from combustion. The dominant frequencies revealed by the OHCL PSDs show good agreement with some of the characteristic frequencies of pressure changes from the PCB dynamic pressure measurements – indicative of coupling at these corresponding frequencies. Low-frequency chugging modes near 60 Hz were observed for all recessed bi-coaxial tests, and for the flush bi-coaxial at the 69 bar test condition. No low-frequency chugging modes were revealed by

the OHCL PSDs for the tri-coaxial injector. However, the 1L mode (1720 Hz) was captured for the tri-coaxial at the 35 and 53 bar cases, reducing with increasing chamber pressure and flow rates, and was ultimately eliminated for the 69 bar test condition.

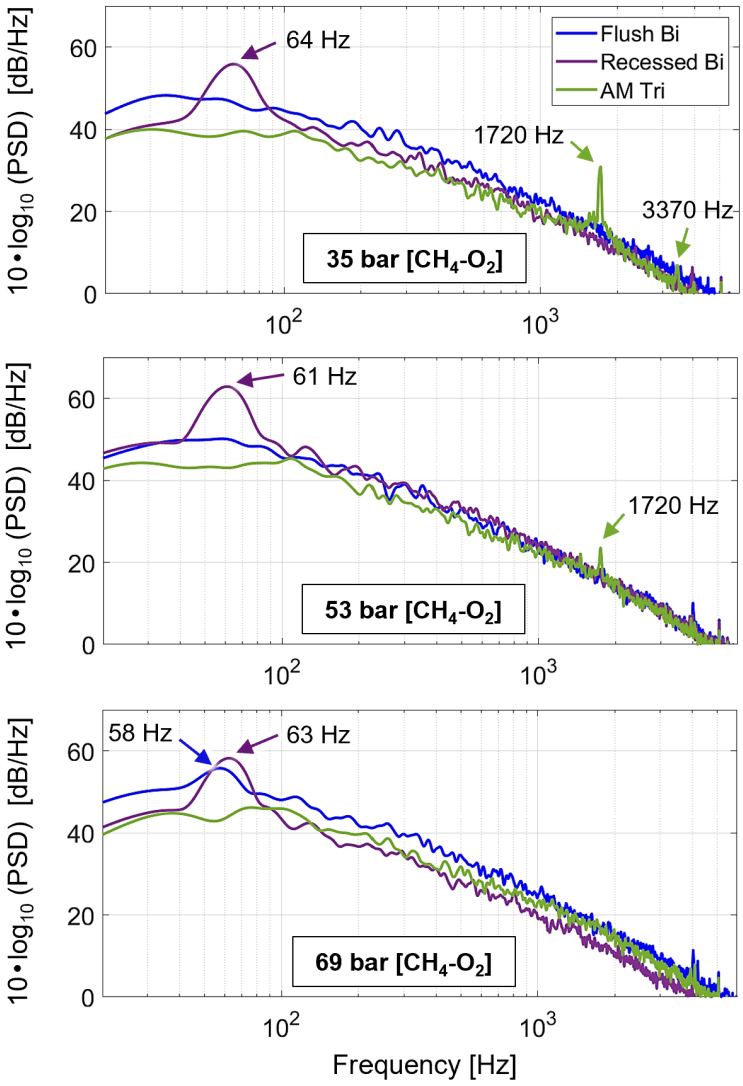

Figure 4.11: Power spectral densities from OHCL video data for each injector across all three chamber pressure conditions using CH_4-O_2. Arrows point to the dominant frequencies of OH* emission intensity fluctuations.

4.4 Supplementary results using H_2-O_2 propellants

While methane-oxygen served as the primary propellant combination for this study, four additional tests were conducted using gaseous hydrogen-oxygen propellants to investigate the influence of propellant choice on the same combustion instability characteristics assessed for CH_4-O_2. In this abbreviated supplementary study, the flush bi-coaxial injector and the AM tri-coaxial injector were tested within the same single-element combustor at chamber pressures of 35 and 53 bar. O/F and N/O ratios were targeted for 6.0 and 4.5, respectively. These particular flow conditions were chosen such that similar combustion temperatures to the CH_4-O_2 tests were achieved and combustor hardware integrity was maintained. Test conditions can be found in Table 4.3.

The experimental procedures, measurements, and data processing methods employed for the aforementioned methane-oxygen tests outline in Sec. 4.2 were identical for these hydrogen-oxygen tests, except for fuel choice and flow conditions. Power spectral densities were calculated for the PCB and OHCL data, revealing characteristic instability modes distributed across the examined frequency domain. COMSOL-predicted chamber eigenfrequencies are presented in Table 4.4 and are compared to the measured values for the two injectors tested.

Power spectral densities were computed and plotted in Fig. 4.12 for the three PCBs across the four H_2-O_2 tests. The trends observed for these hydrogen-oxygen tests were generally similar to the tests using methane-oxygen. The flush bi-coaxial injector again exhibited a dominant low-frequency chugging mode at 60 Hz, followed by a weaker 1L

Table 4.3: Achieved flow conditions for all H_2-O_2 single-element combustor tests averaged over one second of steady state operation.

Test	Prop.	Injector	P_C [bar]	$\dot{m}_{ox}$ [g/s]	$\dot{m}_f$ [g/s]	$\dot{m}_{N_2}$ [g/s]	O/F	N/O	$\Delta P_{inj,ox}$ [% P_C]	$\Delta P_{inj,f}$ [% P_C]
6186	H_2-O_2	Flush Bi	35.1	13.7	2.2	59.7	6.22	4.37	1.7%	3.3%
6189	H_2-O_2	AM Tri	35.1	13.2	2.3	60.3	5.75	4.56	1.4%	1.3%
6187	H_2-O_2	Flush Bi	53.3	19.6	3.3	88.9	5.94	4.54	2.7%	3.3%
6188	H_2-O_2	AM Tri	53.0	19.6	3.3	87.4	5.84	4.46	2.4%	1.5%

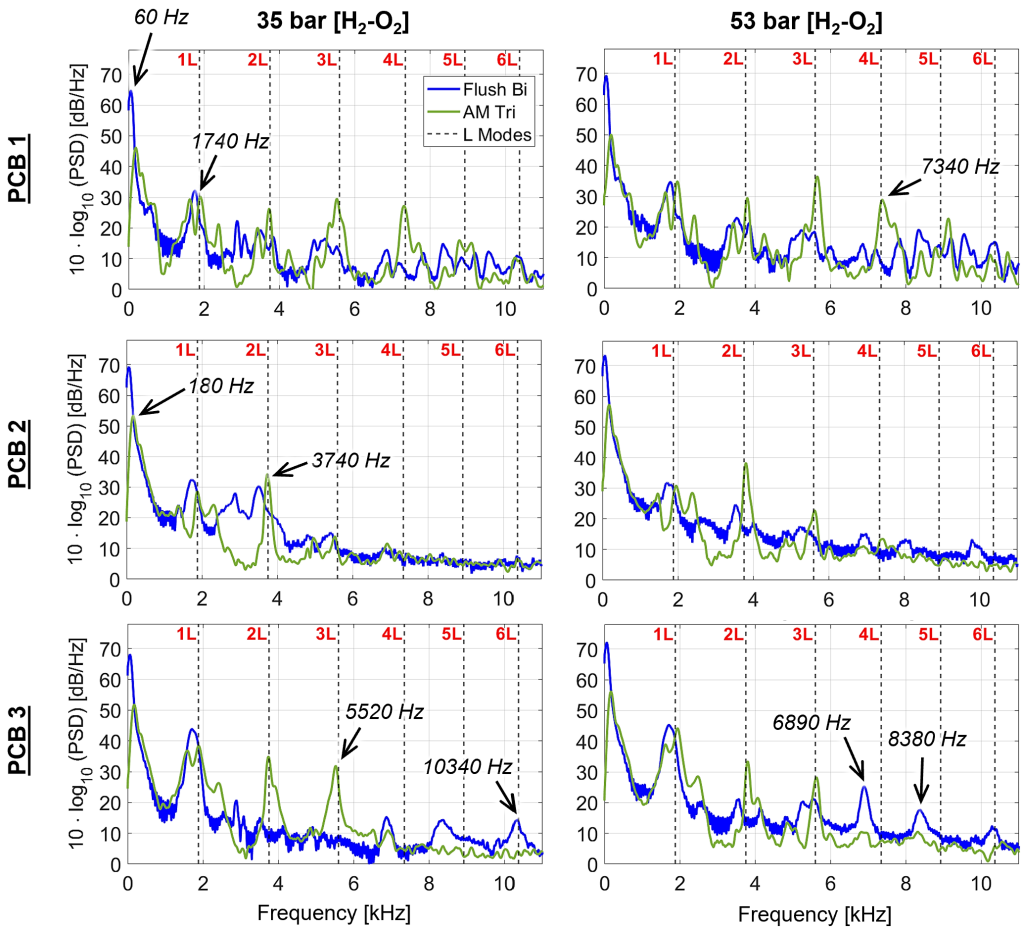

Figure 4.12: Compiled power spectral density plots across the examined frequency domain for each dynamic pressure sensor (PCB) at the four H_2-O_2 test conditions.

tone near 1740 Hz. Unlike the tri-coaxial tests using methane-oxygen where the dominant instability frequency was the 1L acoustic mode, the hydrogen-oxygen tri-coaxial tests instead

Table 4.4: Comparison of COMSOL-predicted and measured combustion chamber eigenfrequencies for H_2-O_2 tests.

		Flush Bi-coaxial		AM Tri-coaxial	
Mode	Predicted [Hz]	Measured [Hz]	Deviation	Measured [Hz]	Deviation
1L	1879	1740	-7.4%	1890	+0.1%
2L	3752	3510	-6.4%	3740	0%
3L	5595	N/A	–	5520	-1.3%
4L	7348	6890	-6.2%	7340	0%
5L	8925	8380	-6.1%	9130	+2.3%
6L	10367	10340	0%	N/A	–

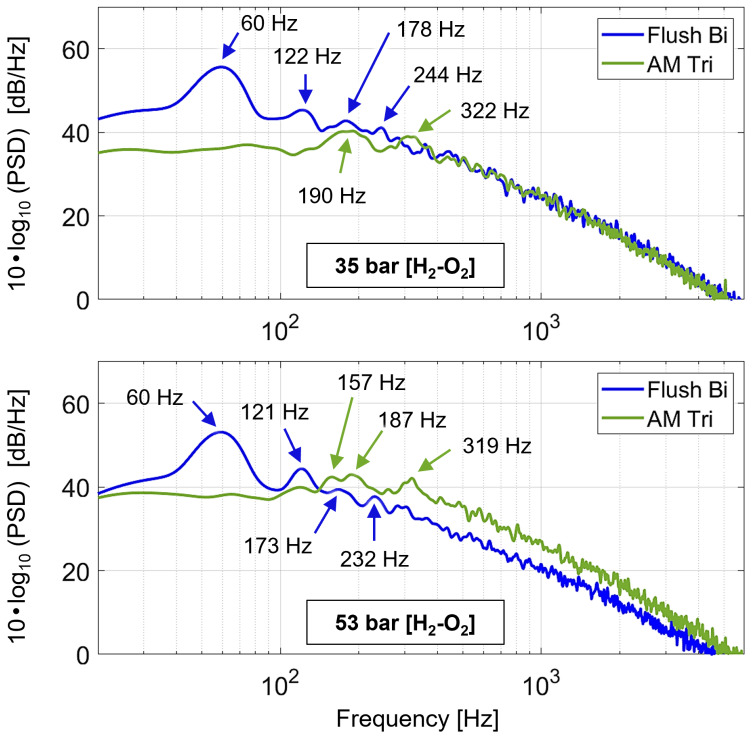

Figure 4.13: Power spectral densities of OHCL video data from H_2-O_2 tests.

demonstrated a dominant chugging frequency near 180 Hz. The 1L, 2L, and 3L acoustic longitudinal modes were present for all three PCB sensors, whereas the 4L mode was only registered by the oxidizer feedline PCB 1. Table 4.4 shows a comparison of the measured longitudinal eigenfrequencies of the two injectors and the COMSOL-predicted values, showing good agreement.

Fig. 4.13 shows the H_2-O_2 OHCL PSDs calculated over the one second of steady-state operation for each test. Local maxima represent characteristic frequencies of fluctuating heat release rates from combustion and show good agreement with the characteristic frequencies measured by the PCB sensors. The OHCL PSDs for the flush bi-coaxial (blue curves) depict a prominent chugging frequency at 60 Hz, with progressively weaker chugging modes present near integer multiples of the dominant 60 Hz mode (e.g., 120, 180, 240, and 320 Hz). The tri-coaxial OHCL PSDs (green curves) also illustrate moderately broadband chugging behavior between ∼150–190 Hz, with a weaker tone present at ∼320 Hz. No high-frequency

acoustic modes are seen in the OHCL PSD plots, suggesting that minimal injection-coupled acoustic instability modes were present since the heat release rates did not fluctuate at high frequencies.

4.5 Discussion and Analysis

Based on the previous results of Sec. 4.3, additional analyses were conducted to better characterize and compare the instability metrics for the different coaxial injectors using a variety of methods. The amplitudes of pressure oscillations over a range of frequencies and conditions were calculated and compared as a primary metric of combustion instability. Coupling behaviors were identified and quantified by calculating coherence and normalized cross correlations between the chemiluminescence signals and the signals from the dynamic pressure sensors. The potential sources and injector-dependent mechanisms that may be responsible for the self-excited combustion instabilities are also discussed.

4.5.1 Amplitudes of pressure fluctuations

Combustion instabilities cause chamber pressure to spatially and temporally fluctuate. These pressure differentials produce non-uniform forces on engine hardware that directly scale with the amplitudes of the pressure changes. Therefore, while characterizing combustion instabilities by their dominant frequency modes is insightful, the amplitudes of pressure changes are more important to the lifecycle and performance of the engine. The root-mean-square (RMS) amplitudes of the dynamic pressure fluctuations, $\Delta P_{\mathrm{dyn},f}$, were quantified for each of the dominant frequency modes across the one second steady interval and are plotted in Fig. 4.14 for the low-frequency chug and high-frequency modes, with the latter typically the 1L acoustic mode. The classical stability threshold of $\Delta P_{\mathrm{dyn},f} < 5\%\ P_{\mathrm{C}}$ that defines "smooth combustion" [58] in rocket combustor operation is overlaid on both plots for reference. In the left subfigure of Fig. 4.14, it can be seen that both bi-coaxial injectors

exceeded the stability threshold for all chamber pressure conditions at the ∼60 Hz chugging mode. At this chugging frequency, the recessed version demonstrated the most extreme chamber pressure fluctuations up to 26% P_C (53 bar case, test 6233), followed by the flush configuration with a maximum $\Delta P_{dyn,chug}$ up to 15% P_C (69 bar case, test 6214).

Notably, the tri-coaxial maintained $\Delta P_{dyn,chug} < 2\%$ P_C for all test conditions. Chamber pressure changes on the order of 1–3% are typically unavoidable in a combustor due to the inherently random nature of turbulent combustion (a stochastic process) [129]. As seen in the right subfigure of Fig. 4.14, the largest chamber pressure change for the tri-coaxial manifested at the 1L mode (1720 Hz) for the 35 bar case and was 12.3% P_C (35 bar case, test 6219) as measured by PCB 3 (in-chamber closest to injection plane). With increasing propellant flow rates, the severity of the $\Delta P_{dyn,1L}$ decreased for the tri-coaxial, notably dropping below the stability threshold for the 53 and 69 bar test conditions but still higher than the bi-coaxial injectors. Results from the high-speed dynamic pressure measurements strongly indicate that the tri-coaxial injection scheme significantly reduces the severity of the chugging instability mode and promotes smooth combustion over a broader range of flow rates compared to the

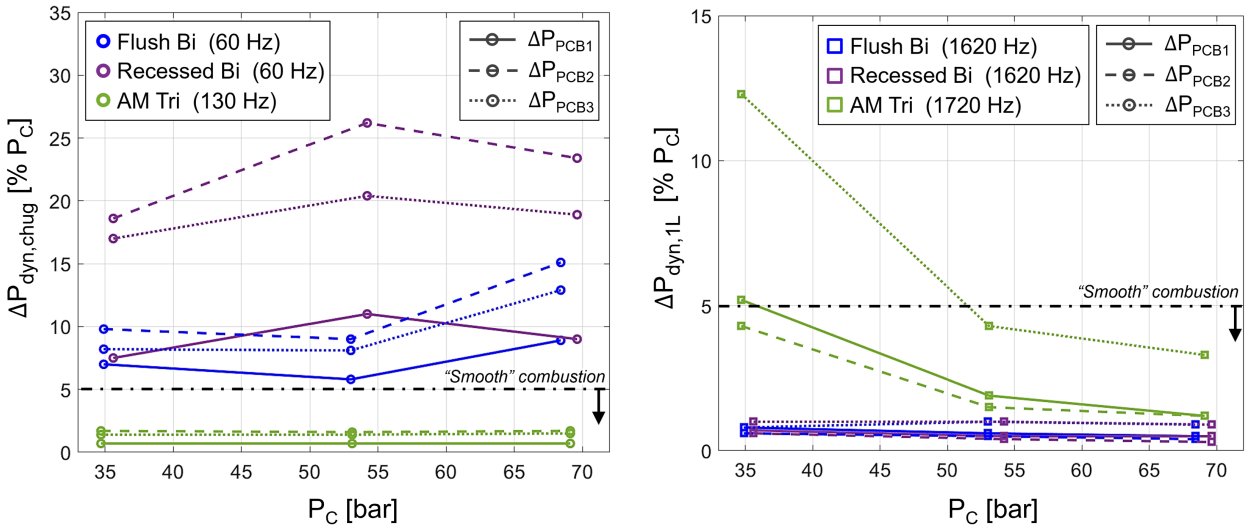

Figure 4.14: RMS chamber pressure fluctuations at the low-frequency chugging modes (*left*) and high-frequency 1L acoustic mode (*right*) shown for each injector across the one second steady state interval for all chamber pressure conditions using CH_4-O_2.

bi-coaxial designs at the conditions tested herein.

4.5.2 Chemiluminescence-pressure coherence

The coupling between the pressure fluctuations (measured by the PCBs) and the heat release rates from combustion (from OHCL measurements) was quantified across the relevant frequency domain by calculating the magnitude-squared coherence, $\gamma_{\text{OHCL-PCB}}$, for these two signals. Magnitude-squared coherence results are plotted in Fig. 4.15 on a 0–1 scale versus

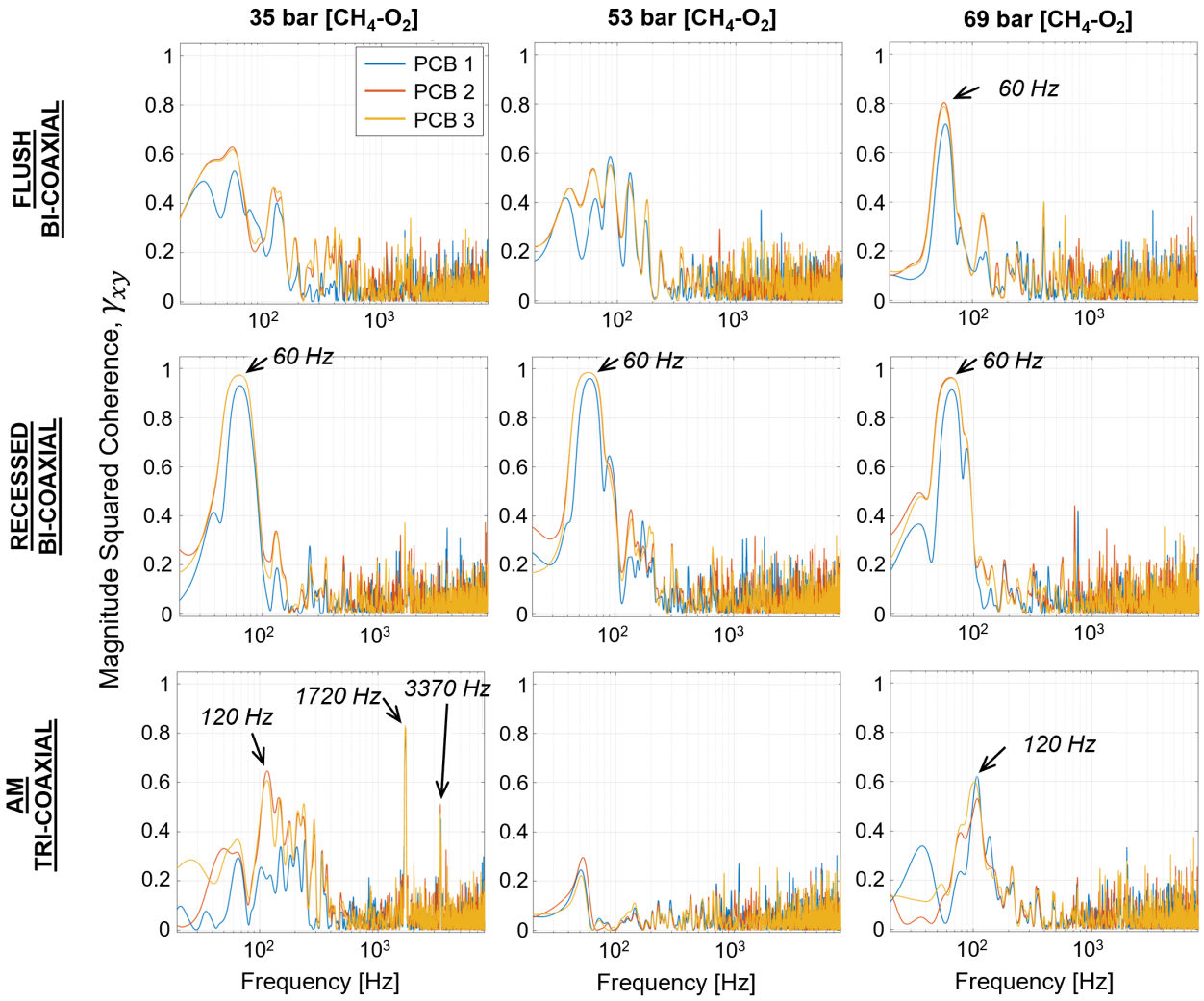

Figure 4.15: Plots of magnitude-squared coherence *versus* frequency to quantify the coupling between OHCL signal and PCB signals for the CH_4-O_2 tests.

frequency for each PCB. Local maxima represent coupling severity between the pressure changes and heat release rates at the corresponding frequency. For a given test, if local maxima are not present at a specific frequency for both the PCB and the OHCL power spectral density plots, a low coherence value should be expected. While the PCB PSDs reveal various peaks that correspond to chug or acoustic modes, not all of these peaks are observed in the OHCL spectra. This implies that the pressure fluctuations in the chamber at those frequencies are not strongly coupled to the injector, hence why they are not present in the OHCL-PCB coherence plots (Fig. 4.15). Coherence values below ∼0.4 were deemed insignificant in this analysis since much of the broadband noise occurred up to this value.

For tests using the recessed bi-coaxial injector, singular pronounced peaks manifested for all three PCBs around the 60 Hz chugging frequency with $\gamma_{\text{OHCL-PCB}}$ values approaching 1, indicative of two signals that are almost perfectly coupled. The flush injector shows strong coupling ($\gamma_{\text{OHCL-PCB}} = 0.8$) at the 60 Hz chugging mode for the highest pressure case only. For the 35 and 53 bar tests, the flush bi-coaxial shows moderate, broadband coherence between frequencies of 40 and 200 Hz. Despite some high-frequency longitudinal modes appearing in the bi-coaxials' PCB PSDs, no pronounced peaks are present at these frequencies in the coherence plots. This implies that the bi-coaxial high-frequency instabilities were purely acoustic from hydrodynamic effects, and not thermoacoustic since heat release rates (indicated by OHCL signals) appear independent of pressure changes at these acoustic frequencies.

The 35 bar test using the tri-coaxial injector depicts broadband coherence up to 400 Hz, while definitive sharp peaks appeared at the 1L and 2L acoustic modes with $\gamma_{\text{OHCL-PCB}}$ values of 0.83 and 0.51, respectively. Injection-coupling at high-frequency acoustic modes is indicative of thermoacoustic instabilities. These two thermoacoustic modes were not observed in the two higher pressure cases. The 53 bar case for the tri-coaxial exhibits no apparent injection-coupling between pressure the heat release oscillations. The highest pressure case (69 bar) demonstrated a moderately broadband coherence peak ($\gamma_{\text{OHCL-PCB}} = 0.61$) centered at 120 Hz.

4.5.3 Normalized cross correlation

Normalized cross correlation, R_{xy}, as defined in section 4.2, was computed and plotted in Fig. 4.16 for signals of PCB 1 and the OHCL video across all tests to assess signal coupling. R_{xy} serves as an additional metric of determining coupling characteristics between heat release and pressure fluctuations. Strong coupling corresponds to high amplitudes with positive R_{xy} values close to 1. Prior to computing R_{xy}, both the OHCL video data and the PCB sensor data were low-pass filtered using 200 Hz as the corner frequency to isolate and assess the low-frequency chugging modes. Consistent with the coherence results, the recessed bi-coaxial injector exhibited a strong cross correlation between heat release and pressure oscillations indicated by the high-amplitude and sinusoidal nature of the R_{xy} plots, which is also demonstrated by the flush bi-coaxial injector at the 69 bar chamber pressure condition. By contrast, the tri-coaxial injector exhibited relatively low amplitude cross correlation and rapid decay across test conditions, further supporting the implicit decoupling of the chugging frequencies. Specifically for the tri-coaxial 53 bar case, both Fig. 4.15 and 4.16 imply independence of heat release and pressure fluctuations at low frequencies.

The signal delay time, t_{delay} [ms], extracted from these plots by taking the positive time value at which the first local maxima of R_{xy} occurs and listed in the bottom left of each plot, can be associated with the response time required for a change in the oxidizer feedline pressure from the PCB location to cause a change in the burning rate within the chamber (as measured by OH* emission intensity). That is, t_{delay} defines the temporal phase shift for the two signals (pressure change at PCB 1 and OH emission from heat release in the chamber) to be perfectly in phase. This physical mechanism assumes the timescales of the chemical reaction kinetics are much shorter than the periods of the chugging frequencies. The differences in signal delay time between the three injectors can then be attributed to the differences in the axial extent of the injectors' combustion zone, which are determined by mixing timescales. Here we can consider a concentrated combustion model [33] where the

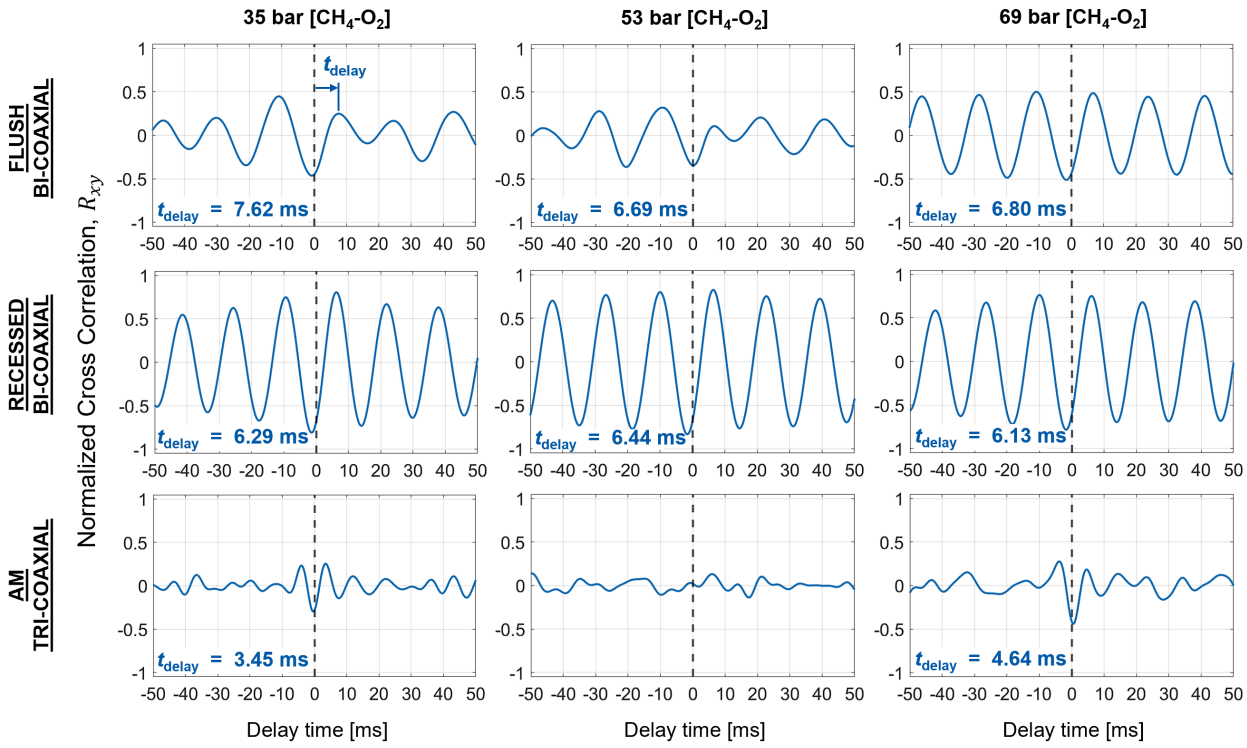

Figure 4.16: Normalized cross correlation is plotted for the PCB1-OHCL signals *versus* time across all CH_4-O_2 test conditions. Resulting signal delay time values are listed at the bottom left of each plot.

exothermic reaction zone of the flame can be approximated as a single axial point within the chamber, such as the average axial length of the iso-contour centers as seen in Fig. 4.10. The resulting local change in chamber pressure from combustion processes would therefore have to travel a shorter distance back upstream to where PCB 1 is located if the axial flame length is shorter, as noted by the higher chug mode frequency and shorter flame length of the tri-coaxial injector. The signal correlation trends in Fig. 4.16 provide supplementary insight in the interpretation of the magnitude squared coherence data (Fig. 4.15). First, the signal time delay between peak-to-peak local maxima in the correlation plots translate directly to the chugging frequency observed for all injectors (Fig. 4.15). The resulting t_{delay} values generally suggest that it is independent of total propellant flow rate and chamber pressure, yet extremely dependent on injector design. Slight variations in t_{delay} were seen with increasing chamber pressure (i.e., increasing flow rates), as the mixing timescales and

axial flame length scales change with pressure as seen in Fig. 4.10.

The decay rates of the peak-to-peak local maxima in Fig. 4.16 indicate dominance in the preferred chugging frequency: a slower or faster decay in the peak-to-peak correlation would translate to a narrow or wider, respective, frequency band of chugging. This is exemplified in Fig. 4.15 by comparison of the flush bi-coaxial test at 69 bar, with the recessed bi-coaxial test case at 35 bar, where the chugging frequency band of the former test case is much narrower than the latter. Finally, lower amplitude peaks in the magnitude-squared coherence were observed at roughly half the chugging frequency (30–40 Hz) for the flush bi-coaxial injector tests at 35 and 53 bar, which can be directly correlated to the peak-to-peak correlation amplitude trends. Observing these two cases in the corresponding subfigures (Fig. 4.16), the local, positive correlation peaks oscillate every other peak. Albeit a small amount, this indicates coupling between the OHCL-PCB signals at roughly half the chugging frequency.

4.5.4 Supplemental H_2-O_2 discussion and analysis

The amplitudes of pressure changes, coherence, and normalized cross correlation results are presented for the supplemental tests using H_2-O_2. As mentioned, only the flush bi-coaxial and tri-coaxial injector were tested using H_2-O_2 propellants at the 35 bar and 53 bar chamber pressure conditions. Some key takeaways are mentioned here, and supporting analyses are presented and discussed further in this subsection. A low-frequency chugging mode prevailed for both the flush bi-coaxial (∼60 Hz) and tri-coaxial (∼180 Hz), although they differed significantly in $\Delta P_{\text{dyn,chug}}$. The flush bi-coaxial was observed to be far less stable when using H_2-O_2 ($\Delta P_{\text{dyn,chug}}$ over 24% P_C), compared to a similar chamber pressure condition with CH_4-O_2 ($\Delta P_{\text{dyn,chug}}$ 10% P_C). Strong injection-coupling was observed at the flush bi-coaxial chugging frequency (∼60 Hz), as well as for higher order harmonics of this frequency (∼120 Hz, ∼180 Hz, and ∼240 Hz).

On the other hand, the tri-coaxial injector's stability improved with H_2-O_2 compared to

Table 4.5: RMS amplitudes of dynamic pressure fluctuations for low-frequency chug and high-frequency 1L instabilities (H_2-O_2 tests).

Parameter [units]	Test 6186	Test 6189	Test 6187	Test 6188
Injector	Flush Bi	AM Tri	Flush Bi	AM Tri
P_C [bar]	35.1	35.1	53.3	53.0
PCB 1 $\Delta P_{dyn,chug}$ [$\%P_C$]	13.3%	1.3%	13.4%	1.3%
PCB 2 $\Delta P_{dyn,chug}$ [$\%P_C$]	24.4%	3.3%	20.3%	3.3%
PCB 3 $\Delta P_{dyn,chug}$ [$\%P_C$]	20.4%	2.7%	17.3%	3.0%
PCB 1 $\Delta P_{dyn,1L}$ [$\%P_C$]	1.3%	1.4%	0.5%	0.9%
PCB 2 $\Delta P_{dyn,1L}$ [$\%P_C$]	1.3%	1.3%	0.5%	0.9%
PCB 3 $\Delta P_{dyn,1L}$ [$\%P_C$]	1.2%	1.2%	1.3%	1.2%

the CH_4-O_2 tests, with a maximum RMS $\Delta P_{dyn,f}$ of 3.3% P_C, therefore achieving "smooth combustion" for both chamber pressure conditions. Acoustic instability modes were comparable between the two injectors, only ranging from $\Delta P_{dyn,1L}$ = 0.5–1.4% P_C for all H_2-O_2 tests. No acoustic modes were captured for either injector in the OHCL PSDs. The root-mean-square amplitudes of the dynamic pressure fluctuations, $\Delta P_{dyn,f}$, were quantified for each of the dominant frequency modes across the one second steady interval and are listed in Table 4.5 for the low-frequency chug and high-frequency modes, respectively. The flush bi-coaxial injector demonstrated severe pressure fluctuations at the 60 Hz chugging mode frequency for both chamber pressure conditions, ranging from 13.3% to 24.4% P_C. While the tri-coaxial injector's most dominant instability mode was the ∼180 Hz chug, the $\Delta P_{dyn,chug}$ was roughly an order of magnitude less than that of the flush bi-coaxial, only ranging from 1.3% to 3.3% P_C. The $\Delta P_{dyn,1L}$ values for both injectors were relatively identical, remaining below 2% P_C. No evidence of thermoacoustic instabilities were observed for any of the H_2-O_2 tests. Notably, the "smooth combustion" requirement of $\Delta P_{dyn,f} < 5\%$ P_C was achieved only by the AM tri-coaxial design for both chamber pressure conditions. The relative magnitudes of $\Delta P_{dyn,f}$ (in units of $\%P_C$) for both injectors generally decreased with increasing flow rates from the 35 bar to the 53 bar test case, indicating that stability could improve with higher propellant flow rates when using hydrogen-oxygen propellants.

To better understand the coupling between the heat release and pressure fluctuations, the

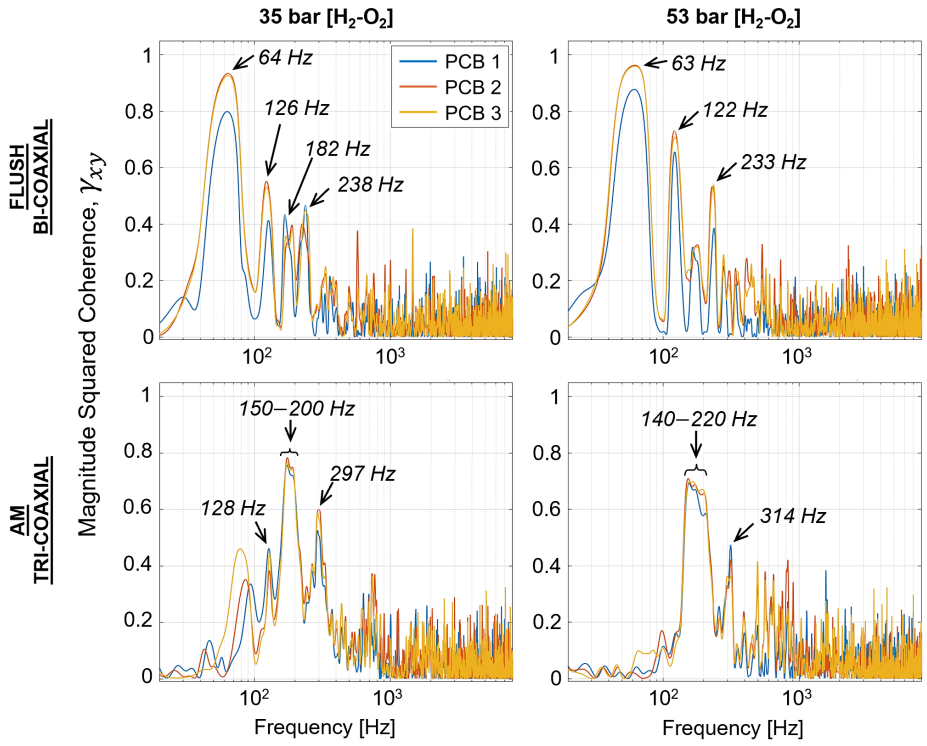

Figure 4.17: Plots of magnitude-squared coherence *versus* frequency to quantify the coupling between OHCL signal and PCB signals for the H_2-O_2 tests.

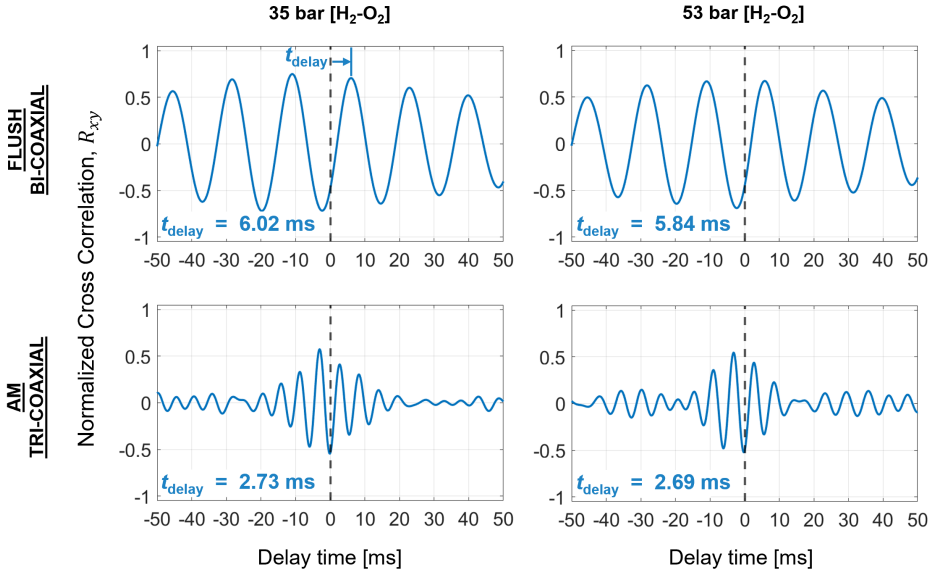

Figure 4.18: Normalized cross correlation is plotted for the PCB1-OHCL signals *versus* time across all four H_2-O_2 test conditions. Resulting signal delay time values for each PCB sensor are listed at the bottom left of each plot.

magnitude-squared coherence, $\gamma_{\text{OHCL-PCB}}$, was calculated for the OHCL-PCB signals. The cyan curves reflect the coherence of the OHCL signal and PCB 1 in the oxidizer feedline, thus specifically representative of injection-coupled instabilities. Fig. 4.17 shows plots of $\gamma_{\text{OHCL-PCB}}$ versus frequency for the four H_2-O_2 test conditions. Here, strong coupling is displayed between heat release and pressure changes for the flush bi-coaxial injector at the ∼60 Hz chugging frequency. Definitive peaks are present, with maximum $\gamma_{\text{OHCL-PCB}}$ values of 0.93 and 0.97 for the 35 and 53 bar tests, respectively, and moderate coupling at integer multiples of this dominant chugging mode up to ∼240 Hz. The AM tri-coaxial coherence plots also show relatively strong coupling near the tri-coaxial injector's chugging frequency of 180 Hz with $\gamma_{\text{OHCL-PCB}}$ reaching values of 0.78 and 0.70 for the 35 and 53 bar tests, respectively.

Lastly, normalized cross correlation, R_{xy}, was calculated for the OHCL signal and PCB 1. This served as an additional method of describing injection-coupling characteristics between heat release and propellant feedline pressure changes, specifically for the low-frequency chugging modes. Fig. 4.18 shows R_{xy} plotted versus time for each of the four H_2-O_2 test conditions. Similar to the methane-oxygen tests, the high-amplitude and steady sinusoidal nature of the R_{xy} plots for the flush bi-coaxial tests is a good representation of strong coupling between in-chamber burning rates and fluctuations in the propellant injection rates. Alternatively, the AM tri-coaxial injector demonstrated significant stability improvements for the injection-coupled chugging instability as seen by the lower R_{xy} amplitudes and rapid peak-to-peak decay rates. While the H_2-O_2 test matrix was quite limited, and quantitative results varied as would be expected, these analyses are supportive of several trends observed for CH_4-O_2 tests, indicating the extensibility of the comparative injector characteristics across propellants.

4.5.5 Injector-dependent instability mechanisms

While combustion instabilities were present to some degree for all hot-fire tests, they varied significantly between the bi-coaxial and tri-coaxial injection schemes. The compiled findings of this combustion instability study strongly suggest that the AM tri-coaxial injector design results in a preference towards intrinsic acoustic instabilities, while significantly weakening or even eliminating injection-coupled instabilities for the higher flow rate conditions tested despite minor changes in injection pressure drops. Recall that intrinsic instabilities are independent of injection rate variations, and are rather only determined by the phasing of burning rate processes and chamber acoustics. On the other hand, both bi-coaxial designs were consistently observed to produce high-amplitude, low-frequency chugging instabilities. Strong injection-coupled instability behavior was evident between cyclic changes in heat release rates and pressure fluctuations across most of the bi-coaxial test conditions. Potential injector-dependent mechanisms that can incite and/or sustain combustion instabilities, relevant to those observed in this work, are discussed below to help understand the differences between injector stability characteristics.

4.5.5.1 Pressure-sensitive elements

Both bi-coaxial injectors, especially the recessed configuration, demonstrated strong injection-coupling instability behavior as the oscillations in feed-system injection rates prevailed as the dominant rate controlling process of instability amplification. Coaxial injectors with a recessed oxidizer post have been observed to have some combustion occur within the recessed, pre-mixed region of the element [85]. Injector elements are considered to be more "pressure-sensitive" when combustion processes in the chamber are significantly dependent on the initial conditions within the element itself [88]. A higher pressure sensitivity results in local in-chamber pressure disturbances to more easily propagate upstream into the injector flowpaths, consequently changing propellant mixing and compressible flow properties, and

ultimately invoking considerable modulations of heat release rates that add to the instability amplification cycle [88].

Substantiated by experimental observations and data recorded in this work (e.g., Sec. 4.3.3.2, Fig. 4.9), a finite amount of combustion is believed to have occurred within the pre-mixed region of the recessed bi-coaxial injector during steady-state operation. The intra-element combustion that precedes main propellant injection into the chamber generates local pressure changes which directly alters injection rates and therefore varies in-chamber heat release rates. By definition, recessed coaxial injector elements are generally more pressure-sensitive than flush injector configurations, and henceforth, are more susceptible to low-frequency injection-coupled (chug) combustion instabilities at low injection stiffnesses, as consistently observed in this study.

4.5.5.2 Vortical flow structures

When coaxial fluid jets (with different momentum flux ratios) mix, vortices are produced from viscous shear layer interactions, leading to an intrinsic hydrodynamic phenomena that spontaneously initiates self-sustained flow oscillations [61, 71]. In cases of high velocity ratio flow, like those employed in practical rocket injectors, these vortices can periodically detach from the main flow, also known as *vortex shedding*. Oscillatory generation of vortical flow structures cause unstable perturbations in the injection flow-field, and are accepted as a potential initiation mechanism of self-excited, injection-coupled combustion instabilities. For example, instabilities are provoked when the oscillatory flow frequency (similarly described by the dimensionless Strouhal number) resembles that of chamber acoustic modes. Experimental and computational studies that have investigated vortex shedding on coaxial injectors concluded that a recessed oxidizer post tends to encourage the generation of high-amplitude flow perturbations and large vortical flow structures that can emanate into the combustion chamber [9, 61, 138].

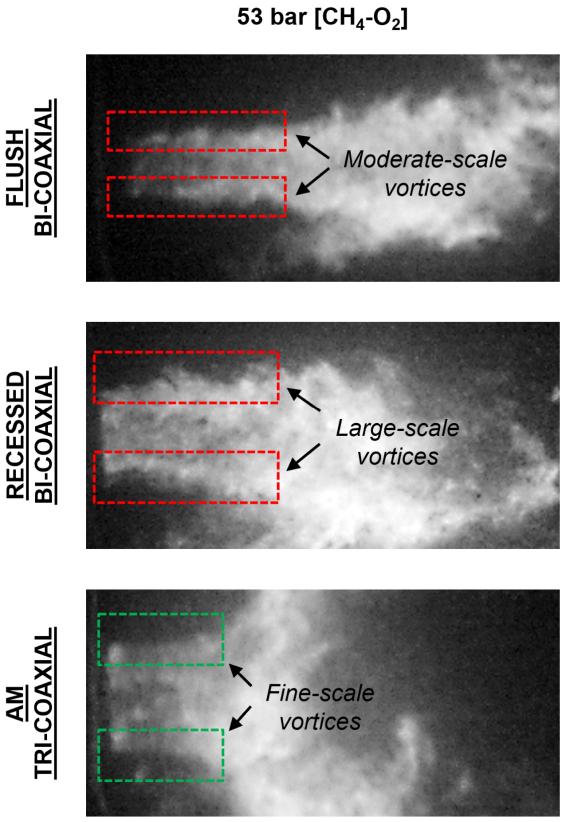

Figure 4.19: Magnified OHCL images depicting vortex shedding tendencies after main injection for each coaxial injector at the 53 bar CH_4-O_2 condition.

While a comprehensive vortex shedding analysis is outside of the scope of this work, qualitative insight can be obtained from flame structure features observed in the OHCL video data. Fig. 4.19 shows magnified OHCL images of the near-field mixing region immediately downstream of the injection plane. The flush and recessed bi-coaxial designs exhibit clear evidence of vortical flow structures within the near-field mixing region immediately downstream of the injection plane. The recessed injector's near-field flow structure regularly contained particularly large wake features, which are on similar scales to that of the injection element's outlet diameter. The same is true for the flush configuration, albeit less severe than the recessed.

Since real flows are not inviscid, and propellant jet Reynolds numbers ranged from $(0.3 - 7.0) \times 10^5$, vortex generation is inevitably present in the injection flow-field to some

degree, which is desirable for improved mixing via induced turbulence at the jet interface layers. However, the tri-coaxial's near-field flow structure routinely resembled quasi-laminar behavior. That is, while vortices were certainly present, they occurred on a scale small enough such that they were not sufficiently visible due to the resolution of the OHCL imaging system. The images displayed here in Fig. 4.19 are representative of behaviors and flow-field features that were consistently observed for each corresponding injector over all 13 test conditions, which includes both propellant combinations. Fig. 4.8 can be referenced for additional frames that further support this claim.

4.5.5.3 Flame-antinode proximity

Injectors with shortened flame lengths (from rapid near-field propellant mixing and combustion) are in general more desirable in rockets (where overall system mass is a concern) since they can shorten the axial length required for the combustion chamber. However, shortened flame lengths can amplify longitudinal acoustic instabilities since a greater portion of the combustion may be concentrated in an antinodal region, causing larger variations in resultant burning (heat release) rates and more work to be produced by the gas [33]. The bi-coaxial flames were on average 2–3 times longer than the tri-coaxial, and therefore extended further away from the longitudinal antinodes, causing relatively weak high-frequency acoustic instabilities with RMS pressure fluctuations remaining under 2% P_C for all tests. In contrast, the tri-coaxial flame was concentrated more closely to the antinodes of the longitudinal eigenmodes (see Fig. 4.9 and relative flame length scales in Sec. 4.3.3.2). This may explain why the RMS amplitudes of the 1L mode pressure fluctuations associated with the tri-coaxial injector were larger than that of the bi-coaxial injectors – particularly for the 35 bar case when the tri-coaxial flame was most confined to the injection plane (antinodal region). As propellant flow rate increased, the tri-coaxial flame extended further downstream in the combustor away from the antinode, and resulted in reduced pressure amplitudes at the longitudinal acoustic frequencies.

4.5.5.4 Mixing influence on stability

The tri-coaxial injector's additional concentric propellant flowpath enhanced rapid near-field and fine-scale turbulent mixing and combustion processes. This enables a more uniform injection mass-flux distribution and energy release rates throughout the chamber from a smoother combustion process, ultimately serving as an intrinsic stability mechanism [58]. Furthermore, the tri-coaxial injector produces a wide, divergent flame shape, unlike the bi-coaxial flames which resemble more of a cylindrical flame structure that extended 2-3 times further downstream in the combustor. The mushroom-like structure of this tri-coaxial flame, well-illustrated by Fig. 4.8, 4.9, and 4.10, typically encompasses the entire inner diameter of the combustor. The stochastic, dissipative nature of enhanced turbulent mixing and combustion acts as an acoustic damping barrier by attenuating sound energy as it propagates through the fluid – an additional inherent stability attribute of the tri-coaxial injection scheme.

4.5.5.5 Organ pipe resonances

The oxidizer post of a shear coaxial injector element contains inherent axial "organ pipe" resonances. Yu et al. [150] conducted variable resonance experiments by continuously changing the effective length of a coaxial injector's oxidizer tube using methane-oxygen propellants. Chia [25], and Morgan and Sokolowki [90] performed similar variable chamber resonance experiments by continuously altering the combustor length during hydrogen-oxygen combustion with a shear coaxial injection scheme. These investigations concluded that injection-coupled acoustic instability behavior is extremely dependent on the relative lengths of the combustor and the oxidizer tube. The organ pipe resonances have long been identified as contributors to self-excited longitudinal combustion instability amplification when these frequencies coincide with chamber acoustic modes [55, 56, 59, 129]. Injector post organ pipe

resonant frequencies can be determined by:

$$f_n = \frac{na}{2l} \quad n = 1, 2, 3, ... \tag{4.4}$$

$$f_n = \frac{na}{4l} \quad n = odd \tag{4.5}$$

where Eqn. 4.4 is for an open-end/open-end pipe, whereas Eqn. 4.5 is for a closed-end/open-end pipe. Here, f_n is the n-th longitudinal mode frequency in Hz, a is the speed of sound of the propellant gas in m/s, and l is the length of the post in meters. When calculating the speed of sound, the temperatures used here were from values measured during testing and found to be between 292–298 K for all gases. The resonant frequencies were characterized for the oxidizer tubes for both bi-coaxial injectors which were approximated as an open-end/open-end pipe.

The lowest resonant frequency of the flush bi-coaxial and the recessed bi-coaxial oxidizer posts were determined to be 865 Hz and 908 Hz, respectively. While these bi-coaxial oxidizer post resonant frequencies are not near any chamber eigenmode frequencies, their odd overtones do resemble the chamber longitudinal modes and could have contributed instability amplifications at these frequencies. Odd overtones correspond to even multiples of the organ pipe frequencies: 1730 Hz, 3460 Hz, 5160 Hz, etc. for the flush bi-coaxial, and 1816 Hz, 3632 Hz, 5448 Hz, etc. for the recessed bi-coaxial. However, all high-frequency acoustic mode pressure oscillations (including the 1L) were insignificant in comparison to the low-frequency chugging for both bi-coaxial injectors, so the influence of the oxidizer post organ-pipe resonances on overall instabilities appears to be relatively negligible in comparison.

On the other hand, the central post of the AM tri-coaxial injector contained the fuel, and due to its geometry, was considered as a closed-end/open-end pipe. For methane, the lowest resonant frequency of the AM tri-coaxial's central fuel post was determined to be 3302 Hz, which is similar to the 2L mode (3410 Hz measured, 3766 Hz predicted). Local maxima consistently appeared at the 2L frequency for the tri-coaxial but their magnitudes were relatively low. For hydrogen, the lowest resonant frequency of the AM tri-coaxial injector was

determined to be 9963 Hz. It is generally difficult to quantify the extent of the influence of the injectors' organ pipe resonances on the chamber acoustic modes. However, corresponding amplitudes of pressure fluctuations (previously discussed in section 4.5.1) at these modes where organ pipe resonances might play a role in chamber pressure changes were relatively minor compared to the alternative frequencies observed. Therefore, all injector organ pipe resonances were considered to have a minor effect on combustion instability amplification for the tests examined in this study.

4.6 Chapter summary

Multiple shear coaxial injector designs were tested within a single-element pressurized combustor experiment at low injector stiffness to characterize and compare self-excited, longitudinal combustion instability behavior. One of these designs was a monolithic shear tri-coaxial injector enabled by additive manufacturing that exhibited exceptional mixing performance. The tri-coaxial injector stability results were compared to two traditionally-manufactured shear bi-coaxial geometries with and without a recessed oxidizer post ($l_r/d_{ox} = 0$ and 1.7, respectively). Combustion chamber pressures ranged from 35–69 bar. Methane-oxygen served as the primary propellant combination at an approximate O/F ratio of 2.9. Two separate techniques were simultaneously employed to characterize combustion instabilities for each injector design during a one-second steady state interval of each hot-fire test. High-speed pressure measurements were recorded within the combustor and the oxidizer feed system using PCB piezoelectric dynamic pressure sensors. RMS amplitudes of pressure changes were determined over the steady-state interval. High-speed chemiluminescence videography was recorded to capture fluctuations in the spontaneous emission of the excited hydroxyl radical, OH*, from each coaxial flame within the combustor. Characteristic frequencies of combustion instability modes were determined for both methods by calculating power spectral densities across the examined frequency domain. The measured high-frequency acoustic modes

showed good agreement with the chamber's COMSOL-predicted eigenfrequencies. Coupling between the heat release from combustion and pressure fluctuations was quantified through magnitude-squared coherence and through normalized cross correlations. Supplementary tests were also conducted using hydrogen-oxygen propellants with the same injectors.

The bi-coaxial injectors, particularly the recessed configuration, demonstrated severe injection-coupling behavior via observed low-frequency chugging modes. At the bi-coaxial chugging frequency of approximately 60 Hz, the flush and recessed injector configurations exhibited RMS dynamic pressure changes upwards of 15% and 26% P_C, respectively. The AM tri-coaxial injector design primarily exhibited intrinsic acoustic instability behavior as suggested by dominant frequencies commonly appearing near the 1L chamber acoustic frequency. Injection-coupled instability behavior was typically inconsequential for the tri-coaxial injector, except for the lowest chamber pressure condition. Effectively no chugging mode was captured for the tri-coaxial, as it maintained low-frequency pressure oscillations under 2% P_C for all test conditions. Notably, the AM tri-coaxial injector consistently promoted a smoother combustion process over a range of flow rates, maintaining RMS amplitudes of pressure fluctuations less than 5% of P_C for two of the three test conditions. Across all tests, the bi-coaxial injector designs exceeded this 5% P_C threshold due to low-frequency chugging. The improved stability performance of the tri-coaxial design is attributed in part to enhanced mixing from the addition of the third concentric flow path and increased shear layer contact area. In addition to a significant flame length reduction, this resulted in more spatially uniform heat release throughout the chamber, negligible vortical flow structure generation, and improved damping of in-chamber pressure disturbances, compared to the bi-coaxial designs.

Future work is expected to involve experimental and computational analyses that further investigate the effects of bi- and tri-coaxial jet mixing on self-excited instability initiation mechanisms (e.g., vortex shedding). The tri-coaxial injector's ability to respond and recover from a finite, high-amplitude instability trigger, such as an in-chamber explosive, should

also be experimentally evaluated. Eventually, tri-coaxial mutli-element testing should be conducted to assess combustion stability characteristics on a larger-scale rocket engine. To the authors' knowledge, this work serves as the first examination of combustion instability characteristics of a shear tri-coaxial rocket injector, and demonstrates the potential of additively-manufacturing to enhance performance of rocket combustion devices.

CHAPTER 5

Minimizing hydraulic losses in additively-manufactured impinging liquid rocket injectors

5.1 Introduction

In liquid rocket engines (LREs), the injector plays a pivotal role in determining propulsion efficiency, with even minor design variations significantly impacting combustion stability and overall performance [58]. LRE injectors function as the interface between the propellant feed system and the combustion chamber, responsible for facilitating the precise delivery, atomization, and mixing of propellants to produce a stable combustion process. A commonly-used method of liquid propellant injection is directing two or more separate liquid streams or jets into each other to induce liquid break-up and mixing through momentum transfer, also known as *impinging* injection. In this work, we focus on the hydraulic efficiency with which such impinging injector elements can introduce propellants with minimal total pressure loss, with potential enhancements and drawbacks associated with additive manufacturing.

In liquid rocket injectors, hydraulic performance is most closely associated with injector pressure drop, ΔP_{inj}, also sometimes called injector stiffness. The static pressure drop in a liquid injector is associated with the acceleration of liquid propellants through the injector elements and into the combustion chamber, and has traditionally been targeted as 15–20% of nominal chamber pressure [58]. While higher values of ΔP_{inj} are associated with better atomization and improved suppression of combustion instabilities, high ΔP_{inj} is undesirable at the system or vehicle level. Higher ΔP_{inj} requires larger/heavier feed system pressurization

hardware, which reduces overall vehicle performance via increased dry mass. High ΔP_{inj} can also sometimes produce excessive propellant inlet velocities [53] and negatively affect LRE throttling capabilities [58].

Injector pressure drop, ΔP_{inj}, can be split up into two components:

$$\Delta P_{\text{inj}} = \Delta P_{\text{ideal}} + \Delta P_{\text{loss}} \tag{5.1}$$

Here, ΔP_{ideal} is the ideal pressure differential required to deliver propellants at a given mass flow rate into the combustion chamber, which assumes incompressible, inviscid flow with no energy losses (therefore, total pressure is conserved and no entropy is generated). This pressure differential across injector orifices imparts kinetic energy to the propellant jet, thereby supplying the energy required for efficient atomization and mixing. In contrast, ΔP_{loss} accounts for the hydraulic head losses associated with viscow dus energy dissipation from inertial (changes in floirection) and frictional (surface) effects, both of which are contingent upon injector flowpath geometry and surface characteristics. ΔP_{loss} is a metric for quantifying the loss in *total* pressure. Hydraulic losses are undesirable because they reduce the total pressure across the injector without contributing to the axial momentum of the liquid jet and should therefore be avoided. For impinging injectors, the manifold to orifice geometry is a significant contributor to ΔP_{loss}. The relevant features of orifice geometry include the entrance or inlet to the orifice, the bore diameter, the bore length, as well as the orifice exit profile. These design features are examined with various metrics for hydraulic losses.

The *discharge coefficient*, C_{D}, is a key hydraulic performance metric used to characterize the aggregate hydraulic losses of a fluid passageway. C_{D} relates the total injector pressure drop to known flow conditions and injector outlet (orifice) geometry, and is defined as:

$$C_{\text{D}} \equiv \frac{\dot{m}_{\text{meas}}}{\dot{m}_{\text{ideal}}} = \frac{\dot{m}_{\text{meas}}}{A\sqrt{2\rho\Delta P_{\text{inj}}}} \tag{5.2}$$

Here, $\dot{m}_{\text{meas}}$ [kg/s] represents the actual mass flow rate of propellant with density ρ [kg/m^2] through an orifice with a cross-sectional flow area A [m^2], and the total injector pressure drop ΔP_{inj} [Pa] across the measured flowpath. The ΔP_{loss} component of total injector pressure drop can be determined from C_{D} by:

$$\Delta P_{\text{loss}} = \Delta P_{\text{inj}}(1 - C_{\text{D}}^2) \tag{5.3}$$

An ideal flowpath with minimal hydraulic losses would result in a $C_{\text{D}} \approx 1$, resulting in a $\Delta P_{\text{loss}} \approx 0$ and thereby conserving total pressure across the injector.

The complexity of component design has historically been restricted by the geometry and accessibility of machining tools, which can be limiting for parts that require material to be removed internally such as for propellant flowpaths within an injector element or within the injector manifold. Specific to impinging injectors, orifice geometry and sizing are critical design parameters that significantly affect propellant flow patterns, discharge coefficients, atomization quality and distribution, and local mixing [128]. LRE impinging injector orifices are traditionally fabricated via milling and drilling techniques. Orifice discharge coefficients tend to gradually increase with larger orifice diameters, but are also highly sensitive to orifice inlet geometry. Work done by Friant et al [39] in the 1950's characterized injector discharge coefficient for various orifice inlet geometries (e.g., sharp-edged, chamfered, and rounded inlets) fabricated using conventional machining. Burrs located at the orifice inlet were a common manufacturing defect and were also included in Friant's study. Fig. 5.1 illustrates how orifice C_{D} generally trends with different orifice inlet features and their associated characteristics (figure adapted from [39]). It was shown that rounded orifice entrance profiles with more gradual changes in flow area (higher R/D) achieved the highest C_{D}. In typical LRE impinging injectors, orifice C_{D}'s typically range from 0.50 to 0.92, with the higher end values enabled by smooth bores and rounded orifice inlets [58]. Rounded inlets can be formed using a special contoured mechanical cutting tool, but require direct accessibility for proper

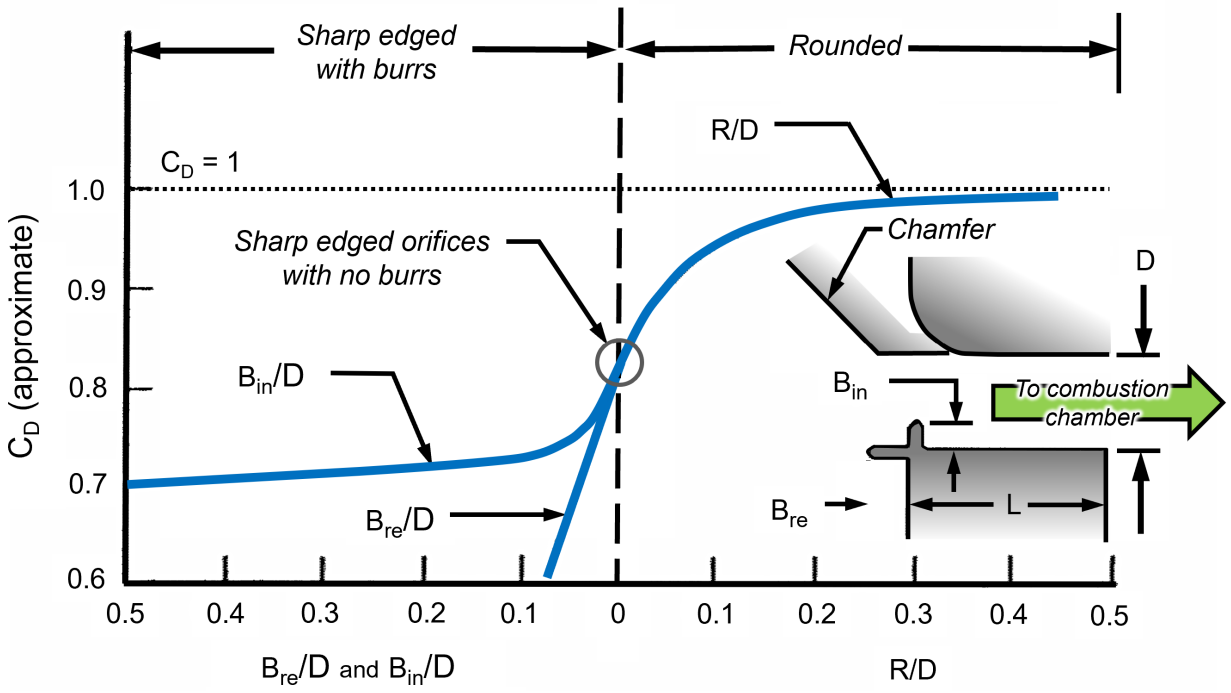

Figure 5.1: Discharge coefficient as a function of orifice inlet geometry. Adapted from Ref. [39].

fabrication. Such conventional subtractive manufacturing techniques employ fixed tooling geometry and often have restricted tooling accessibility, which can complicate the already process-intensive injector fabrication.

The recent maturation of additive manufacturing (AM) with high-performance metal alloys has revolutionized the design and development of modern combustion devices [48]. Beyond the practical economic and production-rate advantages for prototyping, AM also provides more design flexibility, enabling a new means to tailor the fluid dynamics of combustion devices to maximize system performance. There is much potential for LREs to exploit the benefits of AM component design, particularly those related to propellant injection. AM enables accelerated production of monolithic injector designs, allowing for rapid-prototyping, dramatically reducing part counts and total mass of injection systems, and simplifying/improving interpropellant joint sealing. To date, AM injectors have demonstrated equivalent combustion performance to conventionally-manufactured injectors, and exceptional life-cycle performance over a wide range of LRE thrust classes [8, 44, 48, 49, 95, 96, 131]. AM

injectors permit the implementation of complex fluid passageways and orifice profiles that can increase element density, enhance propellant mixing, and reduce injector manifold ("dribble") volume [8, 44, 48, 132]. The most popular AM method in the aerospace industry for metallic parts is Laser Powder Bed Fusion (L-PBF), which is well-known for producing high-precision, fully dense components [48]. In the L-PBF method, metallic powder feedstock is selectively melted by a focused laser beam, and then rapidly solidifies layer-by-layer into a complete solid part [15].

The expanded design freedom of additive manufacturing enables flowpath tapering which mitigates the inertial losses generally associated with sharp features within conventionally-manufactured injector geometries. In this work, LRE impinging injection schemes were designed with AM-enabled flowpath tapering as a means of mitigating the hydraulic inertial losses from the sharp flowpath features associated with conventionally-manufactured injector designs. However, the increased surface roughness inherent to AM parts can introduce additional frictional viscous losses, potentially offsetting the hydraulic benefits of the AM geometric optimization. Average surface roughness for L-PBF parts can range from 0.0002"–0.0025" (5μm–65μm) [124]. For context, the average surface roughness of conventionally-machined metallic surfaces typically ranges from 0.000015"–0.00006". The layer-by-layer manufacturing process creates a "stair-step effect" on sloped surfaces, thereby making layer thickness and print angle primary contributors to AM surface roughness. Several other factors that influence AM surface topology are metallic powder distribution, non-uniform melting, thermal effects, and laser power and scan strategy [27, 124]. Limitations in the ultra-fine control of AM parameters inevitably results in a stochastic surface at small scales. Fig. 5.3 shows images captured by a scanning electron microscope of an AlSi10Mg L-PBF printed surface at various magnifications. The consequences of AM surface roughness are particularly meaningful in the small orifice geometry, where cross-sectional flow area is minimized and flow velocity is maximized. At scales similar to smaller orifice diameters, AM surface roughness can occupy a finite and spatially-varying fraction of the orifice flow area. This can perturb flow

characteristics and potentially shift C_D. The issue of flowpath surface roughness from additive manufacturing can be overcome by supplementing with post-print polishing techniques (i.e., flow machining, or *honing*, to improve flowpath surface finish as demonstrated by our research group in Ref. [97]) or simply through advancements in as-printed surface finish.

Conventional impinging injector design criteria for LREs have been well-understood for decades [43], and the influence of certain injector design features (i.e., orifice geometry) on flow characteristics and hydraulic losses has also been thoroughly examined [1, 43, 68, 77, 78, 80, 107, 108, 111, 126, 133]. However, with the recent emergence of additive-manufacturing, new

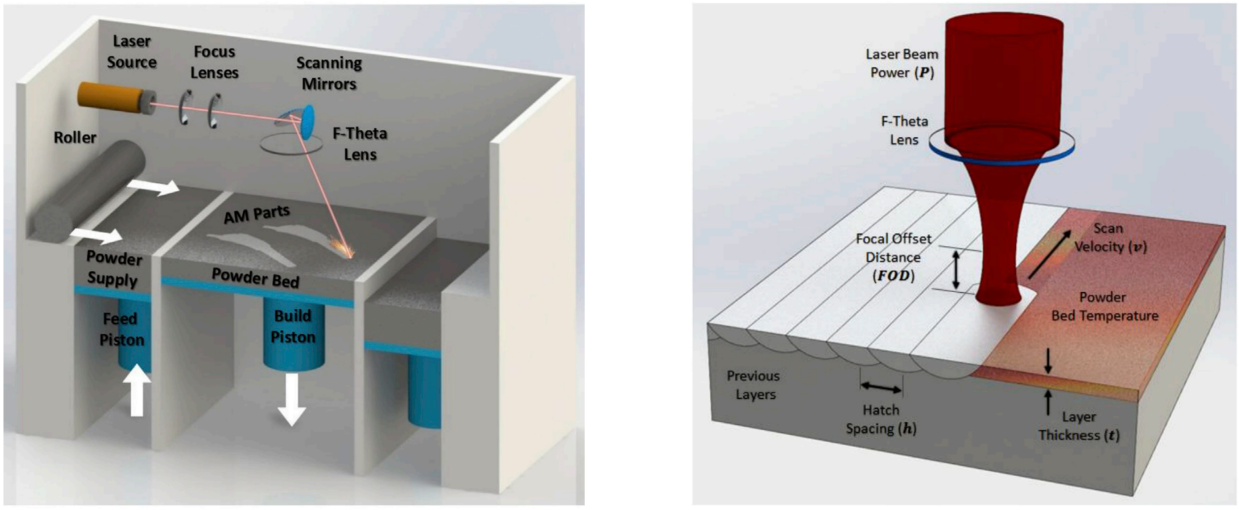

Figure 5.2: (*Left*) Schematic of a typical L-PBF machine. (*Right*) Schematic of the laser and powder bed interface with key operating parameters labeled. Both images from Ref. [120].

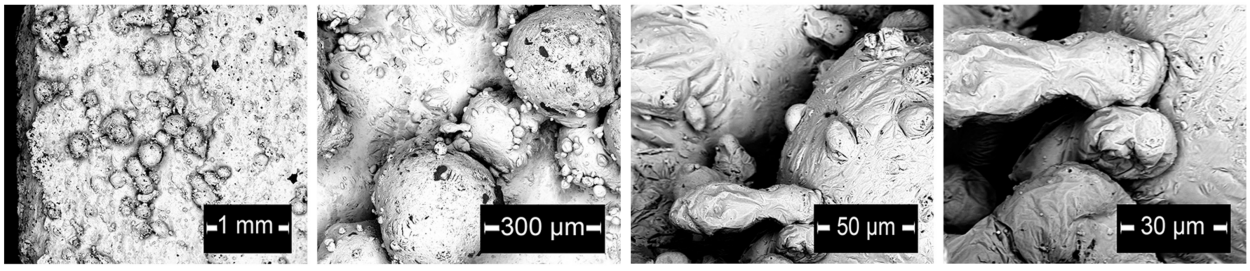

Figure 5.3: Multi-scale surface topology images captured by a scanning electron microscope of a AlSi10Mg part printed using L-PBF. From Ref. [137].

research is required to amend, modify, or validate these pre-established guidelines, particularly those related to injector hydraulics. Despite AM injectors' lucrative benefits and wide use in today's aerospace industry [15, 49, 98, 127, 131], specific research on hydraulic losses in AM liquid injectors is scarcely available in public literature. Morrow [91, 92] used a computational fluid dynamics (CFD) analysis to optimize intraelement flowpaths of a liquid bi-propellant swirl coaxial rocket injector via AM-enabled features that attenuated inertial losses. His CFD simulations demonstrated enhanced hydraulic performance through rounded inlets and tapering, indicated by notable reductions in discharge coefficient. Our research group recently designed, printed, and cold-flow tested a pair of first-generation, additively-manufactured liquid impinging injector with similar tapered flowpath features [97]. Results from cold-flow testing demonstrated that the AM-enabled tapered flowpath could reduce hydraulic losses, and that injector hydraulic performance could be further enhanced with honing. This prior work has motivated a more rigorous examination of the fluid dynamic effects associated with additive manufacturing and opportunities to optimize injector hydraulics.

In this chapter, a coupled computational and experimental study is presented to inform impinging injector design to minimize hydraulic losses through additively-manufactured flowpath geometries and various post-processing techniques. It should be noted that impinging injector orifice diameters have ranged from 0.004"–0.750" for 1-lb-thrust engine and a booster-class engine, respectively, but typical orifice diameters fall somewhere between 0.015"–0.080" [43,54]. For mixing and combustion performance considerations, small-diameter orifices are typically desired since they enhance propellant mixing though improved atomization and reduced vaporization times, as well as enabling higher element density. This provides a pathway for more compact combustor designs with higher efficiency. As such, this work examined impinging injector flowpaths on the lower end of this range, with orifice diameters varying between 0.012" and 0.024". Injector discharge coefficient, C_{D}, served as the primary metric used to characterize the aggregate hydraulic performance. Sec. 5.2 first reviews the relevant fundamental fluid mechanical principles that govern injector pressure drop. Sec. 5.3

then introduces a canonical conventionally-manufactured impinging injector design, and the approach for hydraulic enhancement with modifications that leverage additive manufacturing. The computational analysis framework is outlined in Sec. 5.4, which describes all relevant settings and assumptions applied to the fluid dynamics models. Sec. 5.5 discusses CFD results which provide predictions of C_{D} for various injector flowpath designs and reveal flowpath features that generate high hydraulic losses, informing design modifications. A combination of smooth-wall and rough-wall CFD simulations help distinguish the relative extent of the inertial and frictional viscous effects involved. A select number of designs were additively manufactured for experimental validation, and the associated testing and evaluation is described in Sec. 5.6. The more limited experimental data set included injectors with variations in orifice diameter and flowpath surface roughness. Injector C_{D}'s were experimentally determined via cold-flow testing over a range of injector pressure drops, enabling a comparison between the down-selected AM designs and the baseline conventionally-manufactured injection schemes. Experimental and computational results were also compared and discussed. In sum, this coupled computational and experimental study provides important insights and practical guidelines for manufacturing impinging-style liquid rocket injectors.

5.2 Theory

This section covers an overview of the fundamental fluid mechanical principles and general design philosophies relevant to impinging liquid rocket injection schemes.

5.2.1 Sources of injector pressure drop

For this analysis, liquid propellant flow through an injector flowpath is approximated as incompressible, fully-developed, steady, viscous flow through a circular pipe with gravitational effects neglected. Characterizing hydraulic losses (ΔP_{loss}) is of great importance to a designer because it informs propellant feed system hardware requirements to achieve specific flow

conditions and ultimately influences the total dry mass of the vehicle. The two main contributors to ΔP_{loss} are primarily classified by either *frictional* or *inertial* viscous losses. That is, $\Delta P_{\text{loss}} \approx \Delta P_{\text{fr}} + \Delta P_{\text{inert}}$. Understanding the relative extent at which these two sources affect ΔP_{loss} informs potential injector design modifications that can enable fine tuning of total ΔP_{inj}. Each loss contributor can be predicted given a certain set of flow conditions and an injector geometry by using fairly simple fluid mechanical analyses, and are described in the following sections.

5.2.1.1 Frictional losses

Frictional viscous losses (also known as *major losses*) result from the fluid's internal viscous shear stresses and are influenced by the surface roughness of the pipe walls. Increased wall surface roughness can cause relatively laminar flow to transition to turbulent flow more quickly, accelerating the growth of the boundary layer, and inducing higher wall shear stresses [42]. Consequently, total pressure reduced (ΔP_{loss} increased) via eddy generation and dissipative turbulence within the relatively large boundary layer. The frictional loss component ΔP_{fr} is defined as:

$$\Delta P_{\text{fr}} = f \frac{l}{D} \frac{\rho u^2}{2} \tag{5.4}$$

where f is the dimensionless *Darcy friction factor*, l/D is the flowpath length to diameter ratio, ρ is the fluid density [kg/m^3], and u is the bulk flow velocity [m/s]. The friction factor for turbulent flow, $f = f(Re_{\text{D}}, \varepsilon/D)$, is a function of Reynold's number, Re_{D}, and the *relative roughness*, ε/D. D is the flowpath diameter, and ε is the *equivalent roughness* – a length scale that represents the surface roughness of an irregular surface, defined by the height of a uniform sand-grain surface that would produce the same results as shown in Fig. 5.4. f is traditionally determined via empirical correlations from a Moody chart (Fig. 5.5) by knowing the Re_{D} and ε/D [89]. While different Moody charts exist for different flow conditions and pipe geometries, the case referenced here corresponds to steady, incompressible,

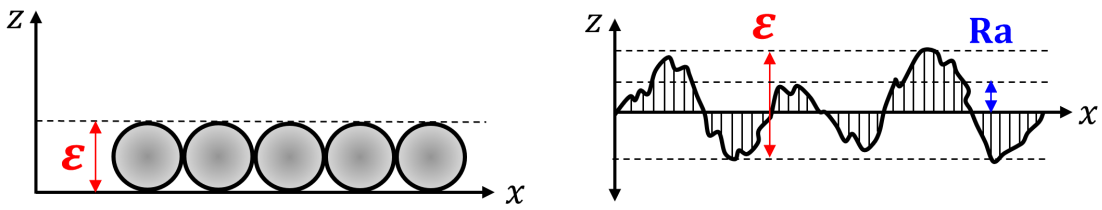

Figure 5.4: (*Left*) Schematic of equivalent sand grain roughness (ε) definition. (*Right*) Schematic of how average surface roughness Ra is defined, relative to ε on a representative surface profile.

fully-developed, round pipe flow. Recall that Reynolds number is defined as:

$$Re_{\mathrm{D}} = \frac{\rho u D}{\mu} \tag{5.5}$$

where μ is the dynamic viscosity of the fluid [Pa·s].

The Haaland equation [50], defined below in Eqn. 5.6, enables friction factor to be determined explicitly by approximating the implicit Colebrook–White equation:

$$\frac{1}{\sqrt{f}} = -1.8 \log\left[\left(\frac{\varepsilon/D}{3.7}\right)^{1.11} + \frac{6.9}{Re_{\mathrm{D}}}\right] \tag{5.6}$$

It should be noted that frictional losses are still present even when walls are smooth ($\varepsilon/D \approx 0$). That is, the Darcy friction factor, f, is non-zero, and can be approximated using the Blasius correlation equation [42]:

$$f = 0.3164 Re_{\mathrm{D}}^{-0.25} \tag{5.7}$$

For a given set of flow conditions and injector geometry, the expected range of Re_{D} can be determined, the relative roughness (ε/D) can be found through surface roughness measurements, and f can be estimated via the Moody chart (Fig. 5.5), the Haaland equation (Eqn. 5.6), or the Blasius equation for smooth pipes (Eqn. 5.7). However, careful consideration should be taken since the best achievable accuracy for these methods is around 10% [42]. Note that the Moody chart and it's associated correlation formulas is generally only valid

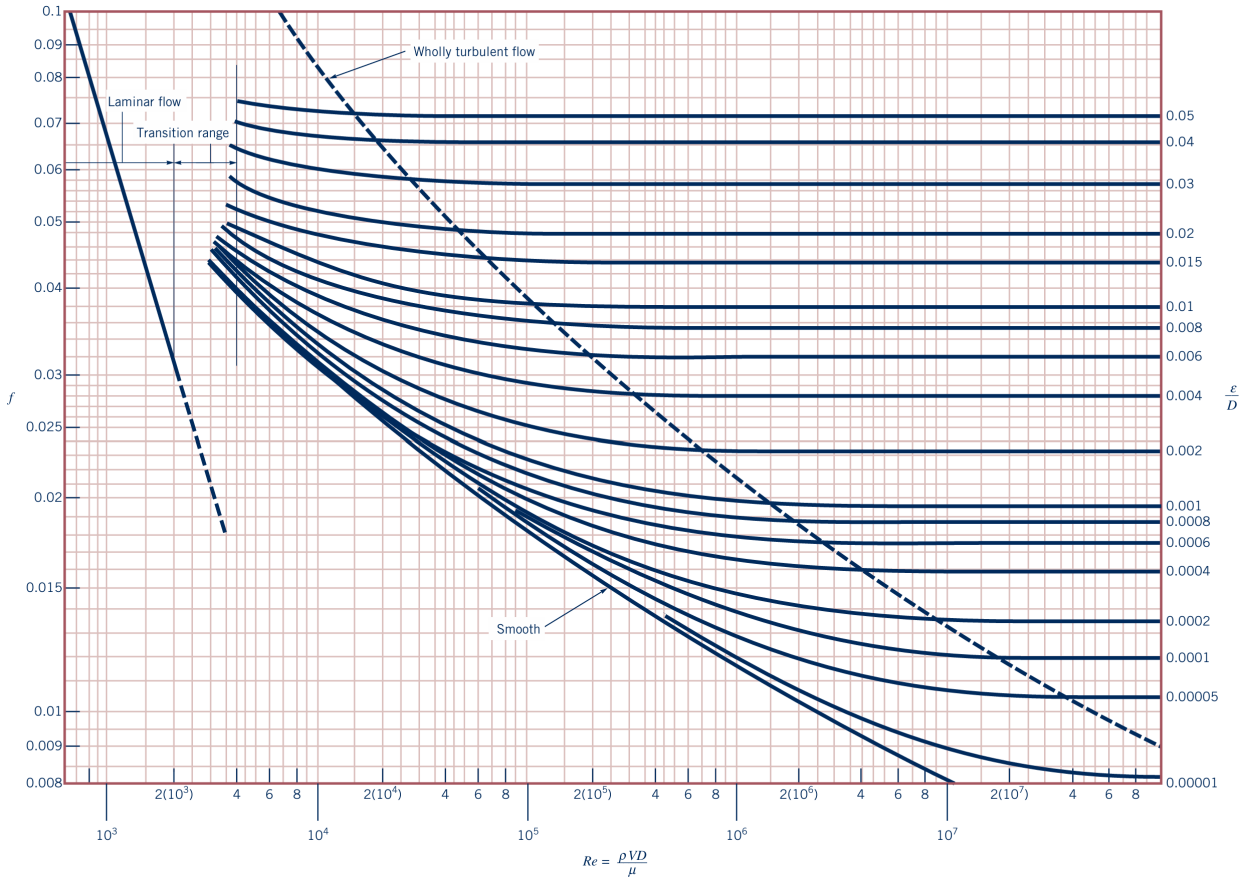

Figure 5.5: Moody chart: Darcy friction factor as a function of Reynolds number and relative roughness for circular pipes. From Ref. [42].

for $\varepsilon/D \lesssim 0.05$. Due to inherent uncertainties, such as variability in relative roughness and experimental data used to generate the Moody chart, using more than about two significant digits in pipe flow calculations is generally unwarranted.

Nonetheless, a good preliminary estimate of the frictional loss component of injector pressure drop can be easily calculated by the designer using Eqn. 5.4. Recall that this ΔP_{fr} calculation assumes a flowpath with a constant circular cross-section. The individual flowpaths that lead up to the orifice in an impinging injector's manifold can generally be approximated as such. When changes in flowpath area are encountered, the designer should separate the different sections of constant cross-section accordingly since ΔP_{fr} is significantly dependent on flowpath diameter and bulk flow velocity. Then the summation of all the

sections' frictional pressure drops can be determined. However, it can be shown that the majority of the frictional pressure drop for an impinging injector typically occurs where the cross-sectional flow area is minimized (i.e., the orifice section just prior to the injection plane) such that the influence on ΔP_{fr} upstream of the orifice section can usually be ignored. That is, $\Delta P_{\text{fr, orf}} \gg \Delta P_{\text{fr,upstr}}$ since ${u_{\text{orf}}}^2 \gg {u_{\text{upstr}}}^2$. This is apparent in Eqn. 5.4 from a simple scaling argument: $\Delta P_{\text{fr}} \propto lu^2/D$. Therefore, the majority of ΔP_{fr} occurs in the orifice section of the injector's flowpath where D in minimized and bulk flow velocity u is maximized. Additionally, we can see that ΔP_{fr} is directly proportional to flowpath length, l, meaning that the length of this orifice section also has a substantial effect on the resultant ΔP_{fr}.

5.2.1.2 Inertial losses

Inertial viscous losses (also known as *minor losses*) are a result of flowpath geometry changes that cause flow to change direction, such as bends, expansions, contractions, or at the entrance (i.e., inlet) or exit (i.e., outlet) of fluid passageways. These momentum changes generate turbulent effects (e.g., flow separation, eddies, and vortices), removing energy from the flow and therefore increasing ΔP_{inj}. The inertial loss component of injector pressure drop, ΔP_{inert}, is defined as:

$$\Delta P_{\text{inert}} = K_{\text{L}} \frac{\rho u^2}{2} = K_{\text{L}} P_{\text{dyn}} \tag{5.8}$$

where K_{L} is an empirically determined constant known as the *loss coefficient*. For typical fluid systems, components such as valves, tees, and elbows are experimentally characterized and assigned a corresponding K_{L} value. In the context of an impinging liquid rocket injector, determining a loss coefficient can be challenging and very design-specific, requiring multi-dimensional analysis. However, an understanding of how general internal flow features and geometry influences K_{L} (and in turn, ΔP_{inert}) is valuable.

Fig. 5.6 illustrates how various flowpath entrance geometries affect K_{L}. Subfigure 5.6a. illustrates how sharp corners and sudden changes in flow direction and area can cause flow

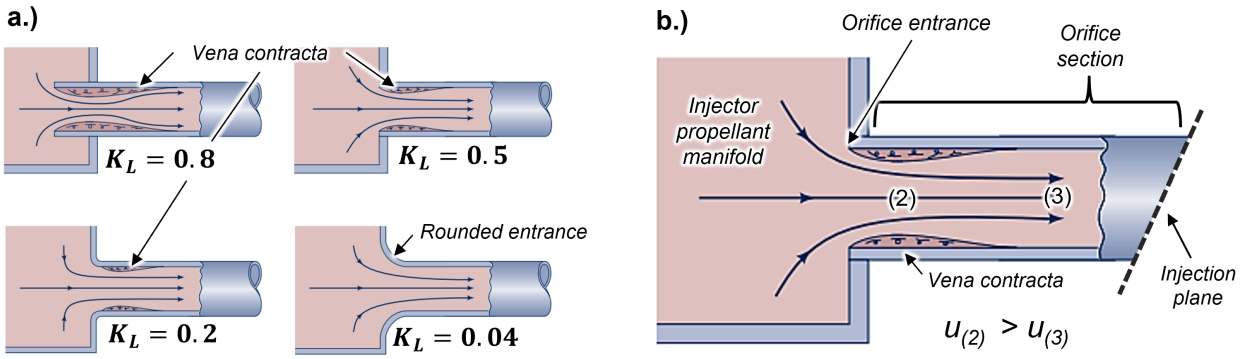

Figure 5.6: (a.) Examples of flowpath entrance geometries and their associated loss coefficients, and (b.) a flowpath schematic with inherent inertial losses relevant to an impinging injector design with sharp flowpath features. Images originally from [42] with labels added.

separation. This phenomena is known as a *vena contracta* effect and contributes directly to total pressure loss [42]. Subfigure 5.6b shows a flow schematic analogous to the entrance to the orifice section of an impinging injector element with sharp flowpath features, like those manufactured using conventional subtractive methods. Here, we can see how the velocity at the "throat" seen at position (2) is greater than that downstream at position (3) from a difference in local flow area. The inertial losses generated at the entrance, in addition to the fluid having to decelerate from position (2) to (3), both contribute to a drop in total pressure (ΔP_{loss}) from viscous dissipation. The bottom left and bottom right schematic in subfigure 5.6a. demonstrate how a rounded ("tapered") entrance can efficiently accelerate the flow with significantly reduced inertial losses. Herein lies the primary hydraulic benefit of an impinging injector design with tapered propellant flowpaths – a geometry enabled by additive manufacturing.

5.2.2 Cavitation

Excessively high ΔP_{inj} and/or abrupt changes in liquid propellant flow direction (from burrs or sharp corners) can invoke high local flow velocities, causing liquid propellants to suddenly drop below their vapor pressure and violently expand into their gaseous state, known as

cavitation. Cavitation is a phenomenon that is generally avoided in LRE component design due to its high likelihood of causing hardware damage [58]. The rapid emergence of gas bubbles within the liquid propellant flow is a highly turbulent event. The increased turbulence in the flow negatively influences the hydraulic and mixing performance via increased viscous dissipation and can alter the effective (wetted) area of fluid passageways. In addition to mitigating inertial losses, injector flowpath designs that contain gradual changes in flow direction and flow area are desirable to discourage liquid propellant cavitation, further motivating AM-enabled tapered flowpath schemes.

5.3 Impinging injector design

5.3.1 General design considerations

While this paper is tailored to enhancing the hydraulic performance of liquid impinging rocket injectors by leveraging an additively-manufactured design, a designer must still adhere to some of the fundamental impinging injector design criteria. A brief overview of established design criteria for liquid-liquid impinging rocket injectors are described here with a focus on orifice geometry design, while more comprehensive descriptions can be found in Refs. [43] and [57]. It should be noted that the impinging injector design criteria described in Refs. [43] and [57] were originally developed with conventional subtractive manufacturing constraints in mind – some of which may no longer be relevant in context of the expanded design flexibility enabled by additive manufacturing.

Several options exist for the number of jets per impinging element (see Fig. 1.3). Whether or not "like" or "unlike" configurations are employed, element orifice geometry selection is of utmost importance. Here, element orifice geometry refers to key features of the entire "orifice section" (highlighted in Fig. 5.6b and Fig. 5.7) of an injector flowpath, such as bore length and diameter, orifice inlet geometry, orifice exit profile, and impingement angle.

Orifice diameters significantly influence many of the critical factors involved in successful, high-performance LRE operation. Typically, a momentum ratio of 1 between the colliding propellant jets is targeted, which is ultimately determined by orifice diameters and impingement angle for a given propellant combination and targeted O/F ratio. Orifice diameters and impingement angle influence atomization (droplet formation) and vaporization rates which greatly affect mixing, combustion performance, and combustion stability. In general, a smaller, faster liquid propellant jet is desired for rapid near-field mixing by producing smaller droplet sizes and higher element density [43]. For a given liquid propellant and range of flow conditions, the total injector outlet area largely determines propellant feed system requirements. From a manufacturing standpoint, high-performing injectors require a reliable fabrication process to properly form orifices to their desired size and impingement orientation within predetermined tolerances. Uniform and accurate orifice diameters are essential for ensuring that spatial uniformity in propellant O/F ratio throughout the combustion chamber which affects overall engine performance and the stability of the combustion process.

5.3.2 Conventionally-manufactured baseline injector

A canonical, subtractively-manufactured impinging doublet injector design (denoted as the *machined injector*) served as the baseline reference for this study. It contains unlike-doublet impinging element pairs each oriented 30° from the normal of the injection plane. The orifice diameters for the fuel and oxidizer flowpaths were 0.0122" and 0.0145", respectively. These orifice sizes are at the lower end of the relevant range and thus serve as a challenge for replication with additive manufacturing. The hydraulic performance of a conventionally-machined injector design is limited by traditional subtractive manufacturing techniques. Such subtractive manufacturing processes, like those used to fabricate this baseline injector plate, include turning and facing on a lathe, 5-axis milling, and drilling. Significant inertial losses are generated by sharp edges and abrupt changes in flow direction – a result of the shape and accessibility of tooling hardware used to form propellant flowpaths. A primary goal of this

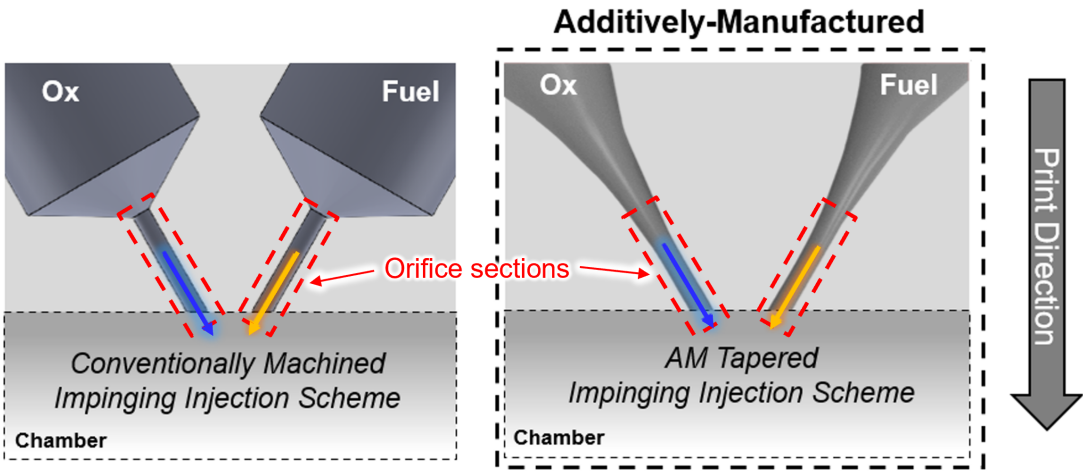

Figure 5.7: CAD cross-sections shown for the conventionally machined (*left*) and AM tapered (*right*) impinging injection schemes.

work is to improve the hydraulic performance of this impinging injector design by minimizing ΔP_{loss} (i.e., increasing C_{D}) via an additively-manufactured design and manufacturing process.

5.3.3 AM tapered flowpath

A modified impinging injector flowpath geometry, enabled by additive manufacturing, was designed with tapered walls (denoted as the *AM tapered* scheme) to minimize the inertial losses inherent to conventionally-machined injectors. Fig. 5.7 shows a cross-sectional flowpath geometry comparison near the injection plane of the conventionally-manufactured (machined) impinging doublet scheme (left subfigure), and a representative impinging doublet scheme that employs the finalized AM tapered flowpath design (right subfigure). The orifice geometry, also denoted "orifice section" is highlighted here. The orifice bore is defined as the straight, cylindrical flow area near the injection plane, and is 0.075" in length for each. The orifice geometries are all oriented at a 30° angle relative to the normal of the injection plane. Since the orifice section contains the smallest flow area, it consequently generates the fastest flow velocities and the highest wall shear stresses. In this work, the design and manufacturing approach largely focuses on modifying and assessing the influence on pressure drop of this crucial portion of the injector. Computational fluid dynamics (CFD) analyses were

conducted to reveal flowpath features that induce inertial viscous losses, which ultimately help inform iterative design modifications. Several different versions of this AM tapered flowpath scheme with orifice diameters ranging from 0.012" to 0.024" were generated and analyzed via computational fluid dynamics tools with comparison to the baseline machined injector. Select designs were eventually down-selected for printing and experimental testing. The CFD analysis framework that informed the design and manufacturing down-selection is outlined in the following section.

5.4 Computational analysis framework

This section outlines a computational analysis methodology as a tool to inform the design of additively-manufactured impinging rocket injectors with enhanced hydraulic performance.

5.4.1 CFD model

CFD analyses were performed in ANSYS Fluent to evaluate hydraulic performance as measured by predicted discharge coefficients between the injector flowpath designs of interest. Discharge coefficient is assumed to be independent of time, so simulations were solved by converging on a steady-state solution. 3-D, single-phase, non-reacting, pressure-based CFD cases were conducted with liquid water selected as the working fluid. Liquid water facilitated model validation by directly comparing CFD-predicted discharge coefficients to those later measured from experimental cold-flow testing with DI water. The viscosity and density of liquid water differs from actual liquid rocket propellants, but this working fluid is a commonly used surrogate for hydraulic and cold-flow testing. The k-ω-SST turbulence model was chosen because of its versatility and accuracy achieved by blending the advantages of the k-ω and k-ϵ models. This hybrid approach enables the effective capture of both boundary layer behavior and freestream effects [87]. Single-phase simulations were found to have negligible differences in results compared to multiphase volume-of-fluid models (i.e., liquid water from

injector discharging into air). Henceforth, single-phase models were selected, which reduced computational costs. Despite the assumptions and corresponding simplifications applied to the model, this CFD approach was considered suitable for sufficiently capturing the relevant fluid mechanics to assess injector hydraulic performance.

The left subfigure in Fig. 5.8 shows a cross-sectioned CAD of a representative AM tapered flowpath. The middle subfigure displays the full corresponding fluid domain modeled in CFD, which is comprised of a single flowpath from manifold inlet to injector outlet (orifice) and a wedge portion of a representative cylindrical chamber. Forward flow through the fluid domain was established by a pressure differential between the inlet and outlet boundary conditions ($\Delta P_{\text{inj}} = P_{\text{inlet}} - P_{\text{out}}$). The outlet boundary condition was assigned to be constant ambient pressure ($P_{\text{out}} = 0$ psig) at the bottom face of the chamber wedge, resulting in $\Delta P_{\text{inj}} = P_{\text{inlet}}$. The inlet boundary condition was assigned a constant feed pressure of a few hundred psig, relevant to conditions later used in cold-flow testing. The resultant ΔP_{inj} range modeled is also consistent with conditions associated with many LREs [58].

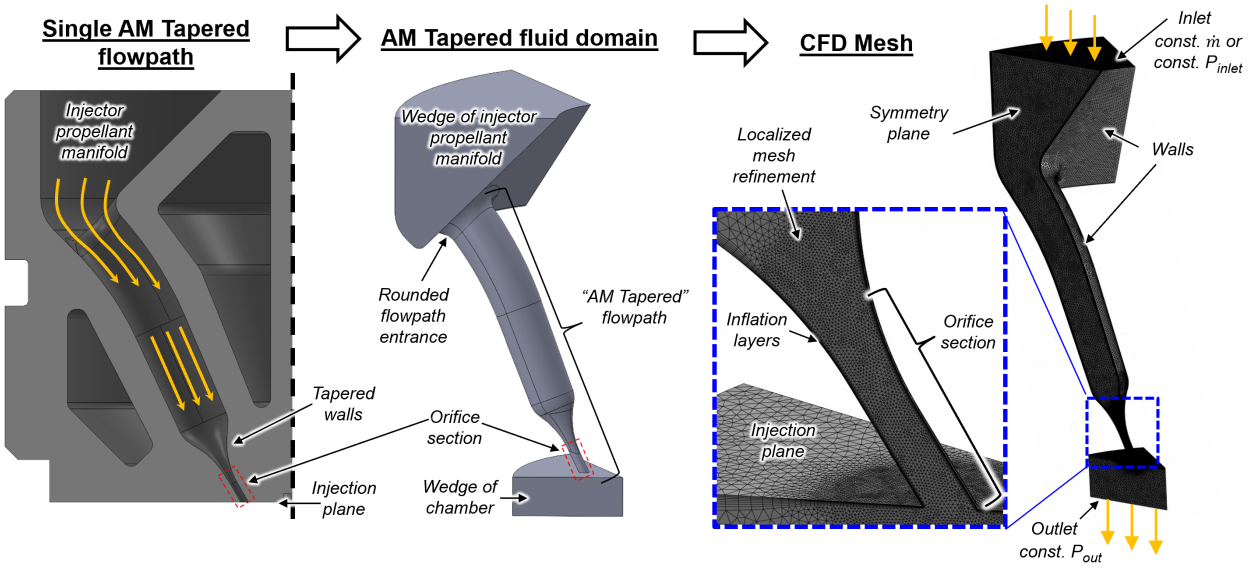

Figure 5.8: (*Left*) Single AM tapered flowpath selected for modeling, (*center*) extracted AM tapered fluid domain, and (*right*) corresponding unstructured tetrahedral CFD mesh using midplane symmetry with boundary conditions shown.

The right subfigure in Fig. 5.8 shows the corresponding CFD mesh with boundary conditions highlighted. Unstructured, tetrahedral meshes of $\sim 2 \times 10^6$ elements were used following a brief mesh study where additional mesh sizes were examined to investigate the influence of mesh resolution on the results. Midplane symmetry was utilized in CFD to further reduce computational times, and was shown to produce similar results to that of a full fluid domain within 1% variability. 8–15 inflation layers (depending on flow conditions) and a no-slip condition were applied to the walls of the mesh. Initially, the model assumed no surface roughness to investigate the influence of flowpath tapering on inertial losses as reflected by the changes in discharge coefficient between the machined and AM tapered flowpath designs. Upon sufficient CFD solution convergence, mass flow rate through the injection plane was extracted from the simulation results. Eqn. 5.2 was then used to determine the CFD-predicted values for discharge coefficient. Across different injector designs, localized mesh sizing and model settings remained unchanged such that comparative results would depend only on changes in flowpath geometry.

5.5 Computational results and discussion

This section presents computational results to characterize hydraulic performance of various impinging injector designs. CFD model predictions inform flowpath design modifications that can minimize hydraulic losses.

5.5.1 Minimizing injector inertial losses

CFD analyses that employed the aforementioned model were conducted to inform iterative design modifications to minimize the inertial losses of impinging injector fluid passageways. Walls were assumed to be smooth ($\varepsilon \approx 0$) to first investigate inertial viscous loss effects inherent to flowpath geometry (recall: Eqn. 5.8, $\Delta P_{\text{inert}} \propto K_{\text{L}}$). While frictional loss effects are still present even when $\varepsilon \approx 0$, the smooth wall assumption initially omits the additional frictional

losses induced from surface roughness. Frictional effects are modeled in subsequent CFD analysis effort using AM-relevant surface roughness values in Sec. 5.5.2. Fig. 5.9 illustrates the varying injector orifice geometry evaluated, starting with the conventionally-manufactured baseline impinging injector design (subfigure 5.9a.), containing a 0.012" diameter orifice with a 30° impingement angle relative to the injection plane normal. A representative constant-pressure boundary condition of 125 psig (862 kPa) was applied to the inlet of the fluid domain. CFD-predicted values of discharge coefficient capture how well flowpath geometry changes influence the overall hydraulic performance. Upon solution convergence, spatially-varying flow parameters like wall shear stress and streamlines of velocity magnitude help identify features that induce high viscous losses, and motivate design changes.

The baseline machined injector resulted in a CFD-predicted discharge coefficient of $C_{\mathrm{D}} = 0.80$. Fig. 5.10 shows contour plots of wall shear stress, with the baseline machined injector in subfigure 5.10a., highlighting the region of maximum wall shear stress (red) caused by the entrance to the orifice section. High localized wall shear stress is indicative of flowpath features that generate high inertial (and frictional) losses from a rapid changes in flow direction and

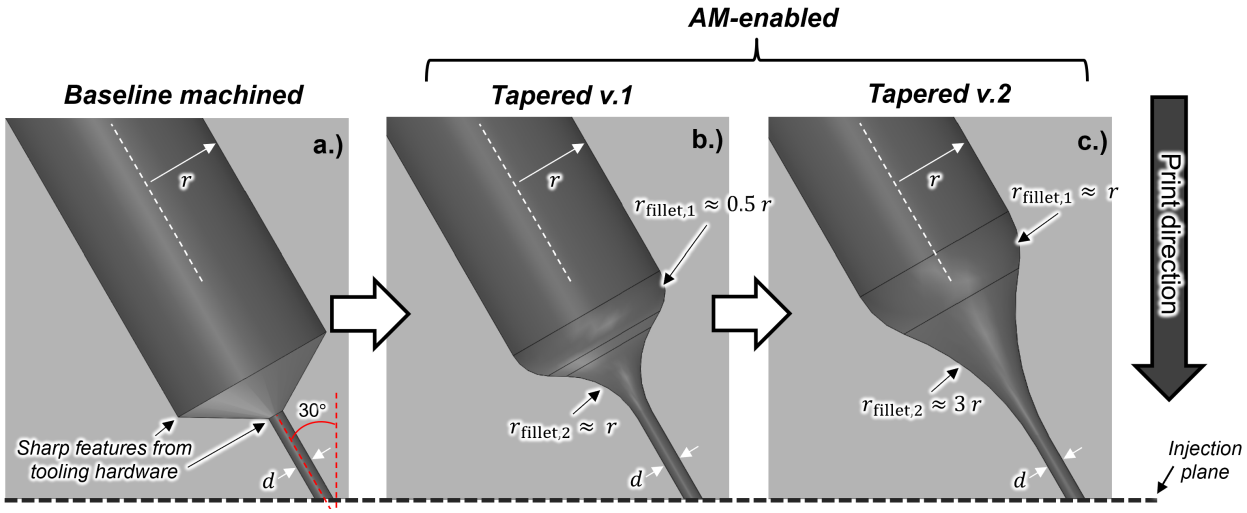

Figure 5.9: CAD cross-sections shown for a single impinging injector design with increased flowpath tapering: baseline conventionally-machined (a.), and AM-enabled with: sub-optimal tapering (b.), and optimal tapering (c.). Shown here, $r = 0.062$" and $d = 0.012$".

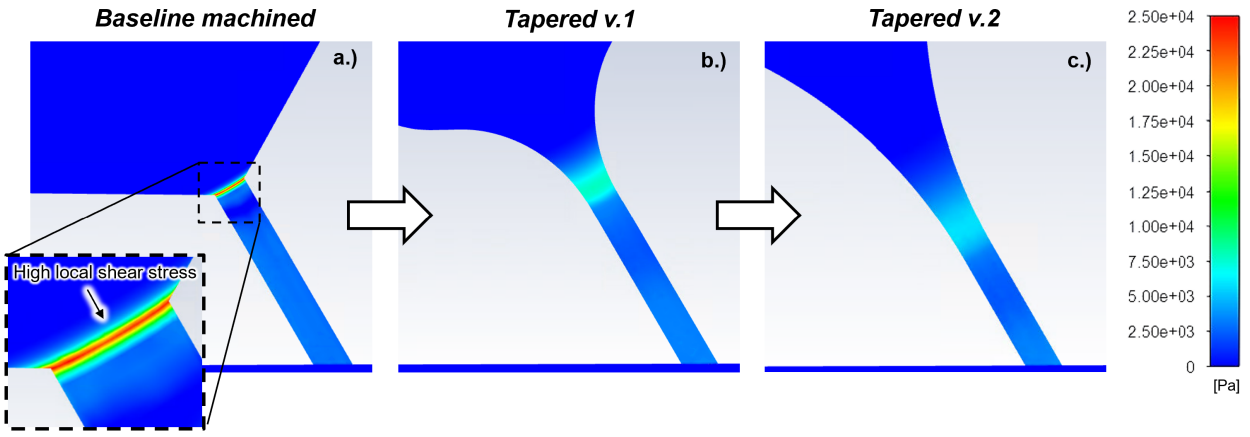

Figure 5.10: CFD-predicted wall shear stress contour plots for a $\Delta P_{\text{inj}} = 125$ psig shown for injector flowpaths. Baseline machined (a.), and AM-enabled with: sub-optimal tapering (b.), and optimal tapering (c.).

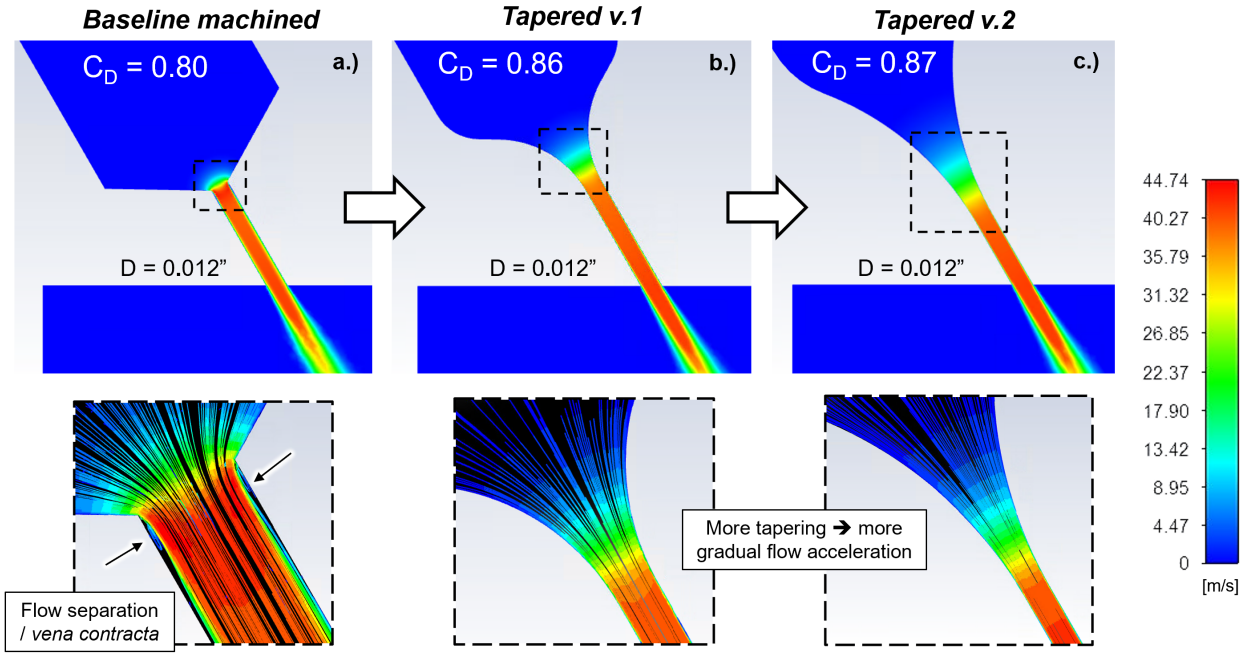

Figure 5.11: CFD-predicted velocity magnitude contour plots for a $\Delta P_{\text{inj}} = 125$ psig shown for injector flowpaths. Baseline machined with *vena contracta* effect highlighted from pathlines scaled by velocity magnitude (a.), and AM-enabled with: sub-optimal tapering (b.), and optimal tapering (c.).

velocity. Fig. 5.11 illustrates the spatial evolution in flow velocity via contour plots of velocity magnitude. The baseline machined injector in subfigure 5.11a. reveals flow separation from

the entrance orifice section causing a visible *vena contracta* effect. The turbulent boundary layer rapidly grows and total pressure is reduced through viscous energy dissipation. The cross-sectional area of the boundary layer, now larger due to the turbulent trip of the sharp orifice entrance, consumes a larger percentage of the total outlet area of the orifice. As such, the effective flow area decreases, reducing the actual mass flow rate delivered by the injector, and is reflected by reductions in C_{D}. The contour plots shown in Fig. 5.10 and 5.11 omit most of the flowpath upstream of the orifice section since the flow is relatively slow ($\sim$100x slower than the bulk flow through the orifice) and is virtually laminar. Considering that the pressure drop from both inertial and frictional effects scale with flow velocity squared ($\Delta P_{\mathrm{loss}} \propto u^2$), it is reasonable to assume that most of the flowpath section upstream of the orifice entrance has a negligible effect on ΔP_{loss}.

Simple adjustments were implemented to the baseline machined flowpath design with the goal of reducing hydraulic losses by adding fillets (rounded corners) where sharp features were located. Subfigures Fig. 5.9b. and Fig. 5.9c. depict two tapered flowpath design examples, v.1 and v.2, respectively. Their upstream flowpath geometry, orifice diameter ($d = 0.012$"), and impingement angle are all identical to the baseline machined design. Fillet features are defined by a radius of curvature, which are normalized by the radius of the upstream flowpath, $r = 0.062$". Subsequent CFD simulations were conducted (using the same boundary conditions) for each design iteration to evaluate their associated discharge coefficients and inform further design improvements.

Contour plots of wall shear stress (Fig. 5.10) and velocity magnitude (Fig. 5.11) illustrate how the gradual changes in flow direction and flow area of the tapered flowpath designs discourage flow separation and reduce wall shear stress, thereby improving C_{D} from 0.80 to 0.87 for the conditions and geometries used herein. Fig. 5.12 illustrates the evolution of wall shear stress *versus* axial position of the orifice bore for each flowpath. The machined injector's sharp orifice entrance induces a large peak wall shear stress, exceeding 25 kPa. In contrast, the tapered schemes reduce and distribute the wall shear stress over a longer distance, reaching

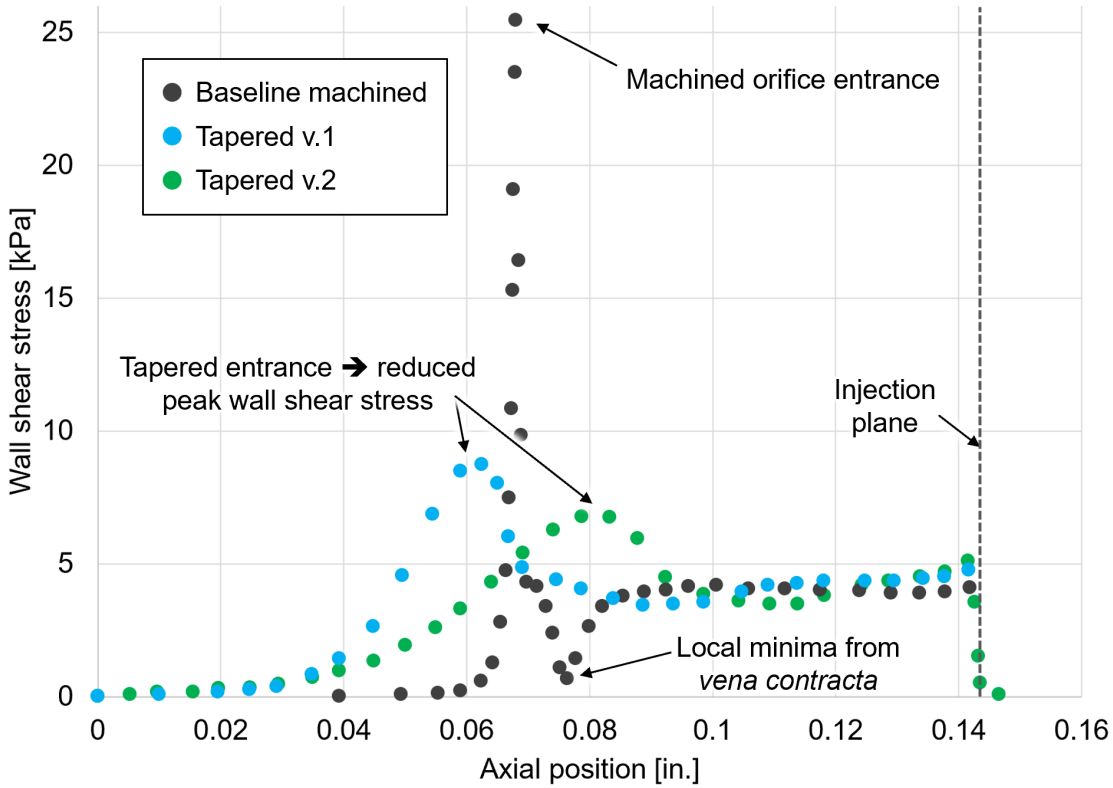

Figure 5.12: CFD-predicted wall shear stress *versus* axial position of orifice bore. Cases shown for a $\Delta P_{\text{inj}} = 125$ psig. Baseline machined, and AM-enabled with: sub-optimal tapering (Tapered v.1), and optimal tapering (Tapered v.2).

lower peak values of 8.7 kPa and 6.8 kPa, for Tapered v.1 and v.2, respectively. Near the exit plane, each injectors' wall shear stress profiles level out to similar values due to sharing identical orifice bore diameters.

Fillet 2, applied to the entrance of the orifice, had the most significant effect on hydraulic performance due to higher local flow velocities relative to those encountered by fillet 1 upstream. Tapered v.2 was down-selected for this work (the *AM Tapered* design) primarily for printability considerations. For example, larger fillet radii allowed for the overhang angle requirement of 45° to be achieved. In general, a designer should select a tapering profile (i.e., fillet radii) that minimizes hydraulic losses for relevant flow conditions, while also adhering to additive manufacturing constraints.

5.5.2 Modeling surface roughness effects

A supplementary CFD study was conducted to evaluate how the added frictional losses from AM-relevant surface roughness offsets the hydraulic performance benefits of a tapered flowpath design. The AM tapered flowpath scheme was modeled with two different orifice diameters (0.017" and 0.022"), each with 4 different flowpath surface finishes, totaling to 8 unique CFD cases. Pertinent to typical L-PBF surface roughnesses (including a smooth wall case for reference), equivalent roughness values of $\varepsilon = 0$, 0.0005", 0.001", and 0.002" were applied to the walls of the fluid domain. Here, similar steady CFD cases were conducted with nearly identical settings as those outlined in the Sec. 5.4.1, albeit with a few key changes. First, the constant pressure inlet boundary condition was replaced with a constant mass flow rate boundary condition of $\dot{m} = 6$ g/s. This value corresponds to a relevant per-element mass flow rate later measured from cold-flow testing. The outlet boundary condition remained at constant ambient pressure. The pressure drop across the flowpath (ΔP_{inj}) was simply calculated by the difference between the outlet pressure and the inlet (feed) pressure, which was extraced from the simulation results upon convergence. Discharge coefficient was calculated from Eqn. 5.2.

Table 5.1 lists key CFD results for each of the cases modeling surface roughness effects. Resultant discharge coefficients are listed for each case. ε/D, bulk flow velocity through the orifice ($\bar{u}_{\text{orifice}} = 41.4$ m/s and 24.6 m/s for 0.017" and 0.022", respectively), and Reynolds number ($\text{Re}_{\text{D}} = 1.78{\times}10^4$ and $1.37{\times}10^4$ for 0.017" and 0.022", respectively) were calculated for each case, such that Darcy friction factor (f) could be estimated. f was calculated using the Blasius correlation (Eqn. 5.7) for the two smooth wall cases, 17-0 and 22-0, whereas the Haaland equation (Eqn. 5.6) was used for the remaining cases. It should be noted that the Haaland equation for calculating friction factor is technically only appropriate for relative roughness values of $\varepsilon/D \lesssim 0.05$, but is still used here for a general estimate of friction factor. Pressure losses due to frictional effects, ΔP_{fr}, were calculated using Eqn. 5.4. Here, the

Table 5.1: CFD-predicted surface roughness effects for the AM tapered flowpath comparing two different orifice sizes and various wall roughness values. Each case targets a per-element mass flow rate of 6 g/s.

D [0.001"]	Case	ε [0.001"]	ε/D	f	ΔP_{inj} [psig]	ΔP_{fr} [psig]	$\Delta P_{\text{inj},+}$ [psig]	$\Delta P_{\text{fr},+}$ [psig]	C_{D}
17	17-0	0	0	0.027	150.3	15.7	–	–	0.90
	17-0.5	0.5	0.03	0.059	170.5	33.9	20.2	18.2	0.85
	17-1	1	0.06	0.079	179.9	45.4	29.6	29.7	0.82
	17-2	2	0.12	0.114	185.4	65.5	35.1	49.8	0.81
22	22-0	0	0	0.029	53.0	4.6	–	–	0.91
	22-0.5	0.5	0.02	0.051	56.4	8.0	3.4	3.4	0.88
	22-1	1	0.05	0.075	59.4	11.8	6.4	7.2	0.85
	22-2	2	0.09	0.098	61.9	15.4	8.9	10.8	0.84

length of the orifice section, l, was approximated as 0.080" although the AM tapered scheme does not have a definitive flowpath entrance feature. ΔP_{inj} represents the CFD-predicted feed pressure differential required to achieve the 6 g/s mass flow rate target of liquid water through a single injector flowpath, and was determined by a surface average from ANSYS Fluent. $\Delta P_{\text{inj},+}$ represents the increase in feed pressure required due to higher viscous losses from the corresponding surface roughness to achieve the same propellant flow rate as a geometrically identical flowpath with smooth walls. In other words, $\Delta P_{\text{inj},+} = \Delta P_{\text{inj},\varepsilon\neq 0} - \Delta P_{\text{inj},\varepsilon=0}$. $\Delta P_{\text{inj},+}$ is important to a designer since it influences changes to propellant feed system requirements. Similarly, $\Delta P_{\text{fr},+}$ is the increase in frictional losses based on the simple calculation from Eqn. 5.4 using the estimated friction factor and flow conditions. In theory, $\Delta P_{\text{inj},+}$ should approximately equal $\Delta P_{\text{fr},+}$ since flowpath geometry and flow velocity are assumed the same, though the former is extracted from CFD application of surface roughness and the latter is derived from the friction factor correlations previously described. $\Delta P_{\text{inj},+}$ and $\Delta P_{\text{fr},+}$ were calculated and compared across the variations in surface roughness evaluated herein. Table 5.1 shows that $\Delta P_{\text{inj},+} \approx \Delta P_{\text{fr},+}$ for cases where $\varepsilon/D \lesssim 0.05$ (where the aforementioned methods for estimating f are valid), indicating that ΔP_{fr} calculations using Eqn. 5.4 show good agreement with CFD-predictions.

5.5.2.1 Critical orifice diameter

While higher flowpath surface roughness consequently raises the feed pressure requirement due to increased frictional viscous losses, the resultant percentage increase ($\Delta P_{\text{inj},+}/\Delta P_{\text{inj}}$) for a larger orifice size is less than that of a smaller orifice. For example, to achieve the targeted mass flow rate of 6 g/s, an average surface roughness of $\varepsilon = 0.001$" on the AM tapered flowpath with a 0.017" diameter orifice (case 17-1) requires an additional ∼20% of feed pressure from surface roughness effects, wheres the same surface roughness on a 0.022" orifice (case 22-1) only requires a ∼12% increase in feed pressure. As seen in Eqn. 5.4, this is a result of the dependence of ΔP_{fr} on the square of flow velocity, u^2, which decreases with increasing orifice diameter for a given per-element flow rate, and also the reduction in ε/D and l/D with increasing diameter, D.

This trend suggests that an AM tapered injector (with reduced inertial losses) may achieve enhanced hydraulic performance despite inherent AM surface roughness if the orifice diameter exceeds a characteristic value. That is, a critical minimum orifice diameter, D_{cr}, exists for an as-printed AM tapered flowpath that can achieve the same discharge coefficient (and therefore equivalent ΔP_{loss}) to that of a conventionally-machined design with the same orifice diameter (and same number of total elements). This depends on the as-printed surface roughness which can be a function of the material, print angle, and printer resolution. An AM flowpath with a diameter greater than D_{cr}, would (in theory) generate less total viscous losses and achieve a higher C_{D}. In contrast, the reduced inertial losses of an AM tapered design would be more offset by the increased frictional losses for an orifice diameter below D_{cr} such that a machined design may be a more appropriate choice in terms of hydraulic performance. It should be noted that this trade-off may be significantly influenced by potential post-processing of as-printed parts that could reduce surface roughness.

D_{cr} is largely dependent on the geometry of the orifice section of the AM flowpath (i.e., entrance geometry, D, ε, l), but is also influenced by the fluid properties (ρ, μ, u). The value

of D_{cr} is also specific to the C_D achieved by the baseline machined injector at a specific flow condition. The actual value of D_{cr} would have to be estimated for a specific injector design and associated manufacturing methods, though the methods here can be similarly employed. For reference, a machined flowpath with smooth walls would result in a CFD-predicted C_D of 0.82 for a 0.017" orifice diameter, which is equal to the C_D predicted for the AM tapered flowpath in case 17-1 (see Table 5.1). As such, the CFD-predicted D_{cr} value would therefore be 0.017" for the AM tapered flowpath with an equivalent roughness of $\varepsilon = 0.001$" at this specific flow condition ($\dot{m} = 6$ g/s). If a honing method is employed on the AM injector, effectively reducing flowpath surface roughness to $\varepsilon \approx 0$, the hydraulic benefits of AM-enabled flowpath tapering may be fully realized (e.g., case 17-0 and 22-0). Knowledge of D_{cr} also informs whether or not post-print honing methods may even be necessary, thus enabling valuable time and cost savings in addition to the proposed hydraulic performance benefits from AM-enabled features with respect to inertial losses.

5.6 Experimental testing and evaluation

To test and corroborate the findings from the CFD study, an experimental effort was conducted to investigate the hydraulic performance of a few AM tapered flowpath designs down-selected for printing. Experimental discharge coefficients of the manufactured designs were quantified through cold-flow testing using liquid water, and compared to CFD-predicted values. Additionally, qualitative insight was gained from evaluating the advantages and shortcomings of AM impinging injector fabrication, as well as various post-print manufacturing methods. Details on the manufacturing processes, test hardware, and testing procedures are described below.

5.6.1 Injector design variations for manufacturing

Five injector designs with the AM tapered flowpath were down-selected for manufacturing, and fabricated as single, monolithic parts via a laser powder bed fusion (L-PBF) additive-manufacturing process. The designs took into consideration the specific limitations of the printer used, including the smallest possible wall thickness, gap size, feature size, and maximum unsupported print angle. The same printing vendor (Proto Labs Inc.) and material (stainless-steel 17-4 PH) was used to manufacture each of the injectors, but with one of two different resolution options. The five AM injectors printed and tested in this study are detailed in Table 5.2 with the machined injector included for reference. The AM tapered flowpaths across the five injectors were effectively identical in geometry, except for differences in cross-sectional area and diameter of the orifice section, and post-print manufacturing processes (which dictated surface finish). These intentional discrepancies in the final injector flowpath geometries enabled an experimental investigation that could test some of the trends observed in the CFD results.

A shortened naming convention, denoted $X.P$, is assigned to the flowpath names for brevity. Here, X is representative of the injector part name (M = machined, L1/L2 = large-scale, S1/S2 = subscale), followed by $.P$ which represents the post-print manufacturing processes (AP = as-printed, D = EDM-drilling, EH = extrude honing, CH = chemical honing). EDM-drilling was used in some cases where the AM printing process resulted in closed or partially-closed orifices and helped ensure a round profile and size uniformity. One of two honing methods was used on some of the injectors, which is a manufacturing technique used to improve flowpath surface finish via controlled material removal. Extrude honing, also known as abrasive flow machining, utilizes an abrasive slurry fluid with high viscosity and gritty particles that are forced through a part with high pressure to erode a surface. Chemical honing, also known as electrochemical honing, instead removes material through a controlled electrochemical reaction between a specialized electrolyte solution and the surface

Table 5.2: Impinging injection schemes down-selected for fabrication and experimental evaluation. Root-mean-square average orifice diameters are listed for each design.

	Flowpath name	D_{RMS} [0.001"]	PPMP
Machined (fuel)	M1	12.2	N/A
Machined (ox)	M2	14.6	N/A
AM Tapered	L1.D	11.6	EDM-drilling
	L2.D.EH	14.5	EDM-drilling, Extrude hone
	S1.AP	15.5	None
	S1.CH	23.7	Chemical hone
	S2.AP	22.5	None

of the metallic part, causing it to dissolve.

Injector orifice characteristics, like area and shape/profile, are targeted by the CAD design submitted for manufacturing, but the as-printed results are ultimately dependent on the AM printer used to fabricate them. Final orifice areas are also determined by which (if any) post-print manufacturing processes are employed. Individual orifice diameters were measured using 0.0005"-increment cylindrical pin gauges and assumed a circular orifice cross-section. The orifice diameters presented in Table 5.2 reflect a root-mean-square average, D_{RMS} across multiple injector elements of the same design.

5.6.1.1 Additive manufacturing with extrude honing

In the first design and manufacturing iteration, the two injectors (L1 and L2) were printed with multiple AM tapered flowpaths. The printer used to fabricate them employed a 0.0012" layer thickness. Upon printing, injectors L1 and L2 were then followed by a standard H900 heat treatment and grit blasting. A 0.0122" orifice diameter was targeted to match the size of the orifice of the machined reference injector. This orifice diameter fell below the hole size limitation (∼0.020") reported by the printing vendor, which resulted in the orifices to be unresolved (closed-up) on the face of the injector plates. EDM-drilling was chosen to form the impinging orifice sections of the L1 and L2 injectors (becoming L1.D and L2.D). The

precision of EDM-drilling also enabled the uniform shaping and sizing of the orifices within tolerance, which is critical to overall injector hydraulics and mixing. Orifice characteristics for each of the manufactured injectors are discussed in more detail in Sec. 5.6.2. Minor post-print machining was required for sealing surfaces and a radial O-ring groove. After EDM-drilling, L2 then underwent abrasive flow machining (via Extrude Hone LLC) to improve flowpath surface finish (finally becoming L2.D.EH), which simultaneously expanded orifice diameters.

5.6.1.2 Additive manufacturing with chemical honing

A subsequent iteration of AM impinging injector design and manufacturing was conducted with notable differences in methods. Here, a higher-resolution printer was utilized that could sufficiently resolve injector orifices of slightly larger diameter, thereby eliminating the expensive/time-consuming EDM-drilling step previously required to form them. A brief printer characterization effort was executed prior to the second design iteration to properly inform printer-specific manufacturing constraints, such as minimum achievable orifice size and surface roughness measurements at various print angles. A higher-resolution printer was selected from ProtoLabs using stainless-steel 17-4 PH, which rendered a 0.0008" layer

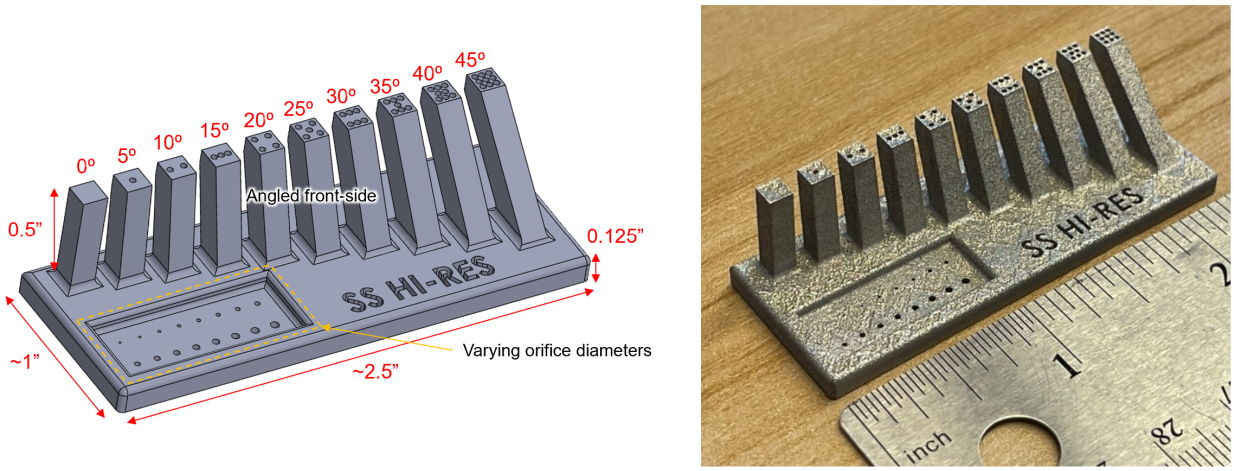

Figure 5.13: *Left:* CAD of AM "tester print" with varying pillar print angles. *Right:* As-printed geometry of AM tester print using ProtoLabs high-resolution stainless-steel 17-4 PH.

thickness (33% less than the previous layer thickness used to manufacture injectors L1 and L2). Fig. 5.13 shows the "tester print" designed and printed for printer characterization. At the time of this writing, a 0.0008" layer thickness is near the highest resolution capable for current commercially-available state-of-the-art L-PBF AM processes [15, 27], although even finer resolutions are expected to be attainable as modern AM technology is still advancing. For this specific printer, the average surface roughness on an AM surface printed 30° relative to the normal of the build plate was measured to be $Ra \approx 320$ μin using a profilometer. Upon inspection, it was discovered that orifices (with a circular cross-section) as small 0.015" in diameter could be resolved with good repeatability. However, orifice diameters were consistently found to be slightly undersized by 0.0015" in diameter relative to the targeted orifice diameter from the CAD file submitted, typical for AM parts due to surface irregularities (roughness) being on a similar sizing scale as these small orifice diameters. If hole undersizing is characterized and repeatable, it can be preemptively accounted for in the design. This also indicated the potential to no longer require the expensive EDM-drilling step previously used in iteration 1 to form the orifice sections that had been closed-up from printing injectors L1 and L2.

In this second design and manufacturing iteration, the higher print resolution option was used to fabricate injectors S1 and S2, both of which also contained multiple AM tapered flowpaths. Fig. 5.14 shows a CAD cross section (left) and an image of one of these AM injectors (right). S1.AP targeted an as-printed orifice diameter of 0.016" (just above the predetermined minimum repeatable orifice diameter), and S2.AP targeted an as-printed orifice diameter of 0.023". To account for the ∼0.0015" diameter undersizing, the injector CADs submitted for printing contained 0.017" and 0.024" diameter orifices, respectively. Minimal post-print machining was required for sealing surfaces and a radial O-ring groove. After visual inspection and orifice diameter measurements, discharge coefficients were experimentally measured via cold-flow testing (discussed in further detail in Sec. 5.6.3). Injector S1 then underwent a chemical honing process (via REM Surface Engineering LLC) to reduce flowpath

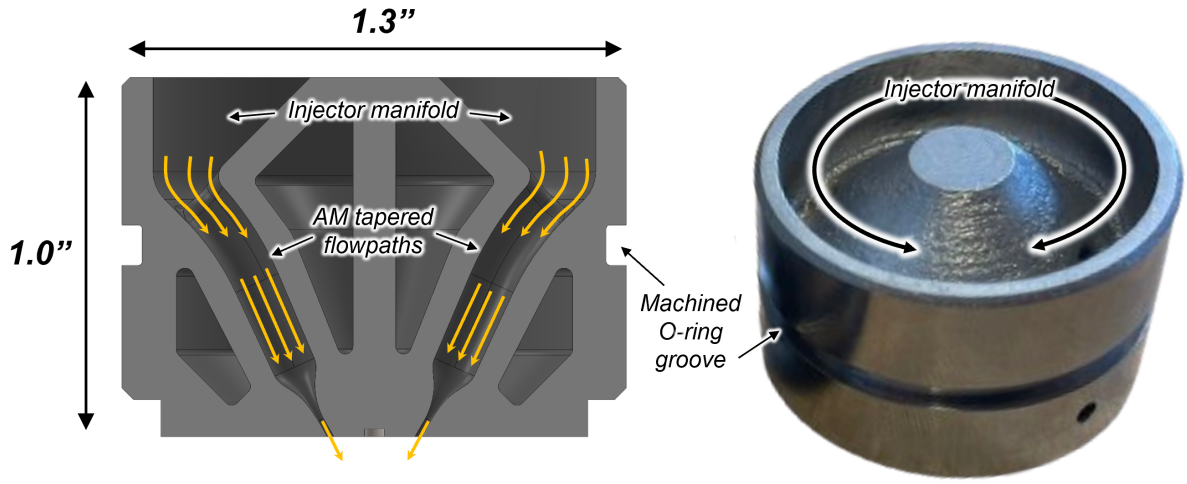

Figure 5.14: (*Left*) CAD cross-section of injector S1 shown with AM tapered flowpaths. (*Right*) Image of AM injector S1.

surface roughness and expand orifice diameters. S1.CH was intended to target a final, post-honing orifice diameter of 0.023" such that hydraulic performance could be experimentally compared to a nearly identical AM tapered flowpath with equal orifice diameter but different flowpath surface roughness (injector S2.AP). Due to minor variance in the measured orifice diameters, the RMS diameter of S1.CH was determined to be 0.0237". While the orifice areas between these two injectors were not identical, they were similar enough to enable an insightful hydraulic performance comparison from cold-flow testing results. It should be noted that in the as-printed CAD files, 0.015" of material was added to any injector surface that required sealing, such that it could be machined off to achieve a proper surface finish.

5.6.2 Orifice characteristics

The size, profile shape, and uniformity of manufactured liquid rocket injector orifice geometry each have a significant impact on the injector's hydraulic performance. The flow-controlling aspects of injector orifice geometry also influences propellant mixing and combustion processes. As such, it is of great importance to verify that injector orifices are properly fabricated within required tolerances through measurement and visual inspection. For each of the 7 fabricated injectors investigated in this study, magnified high-resolution images of their corresponding

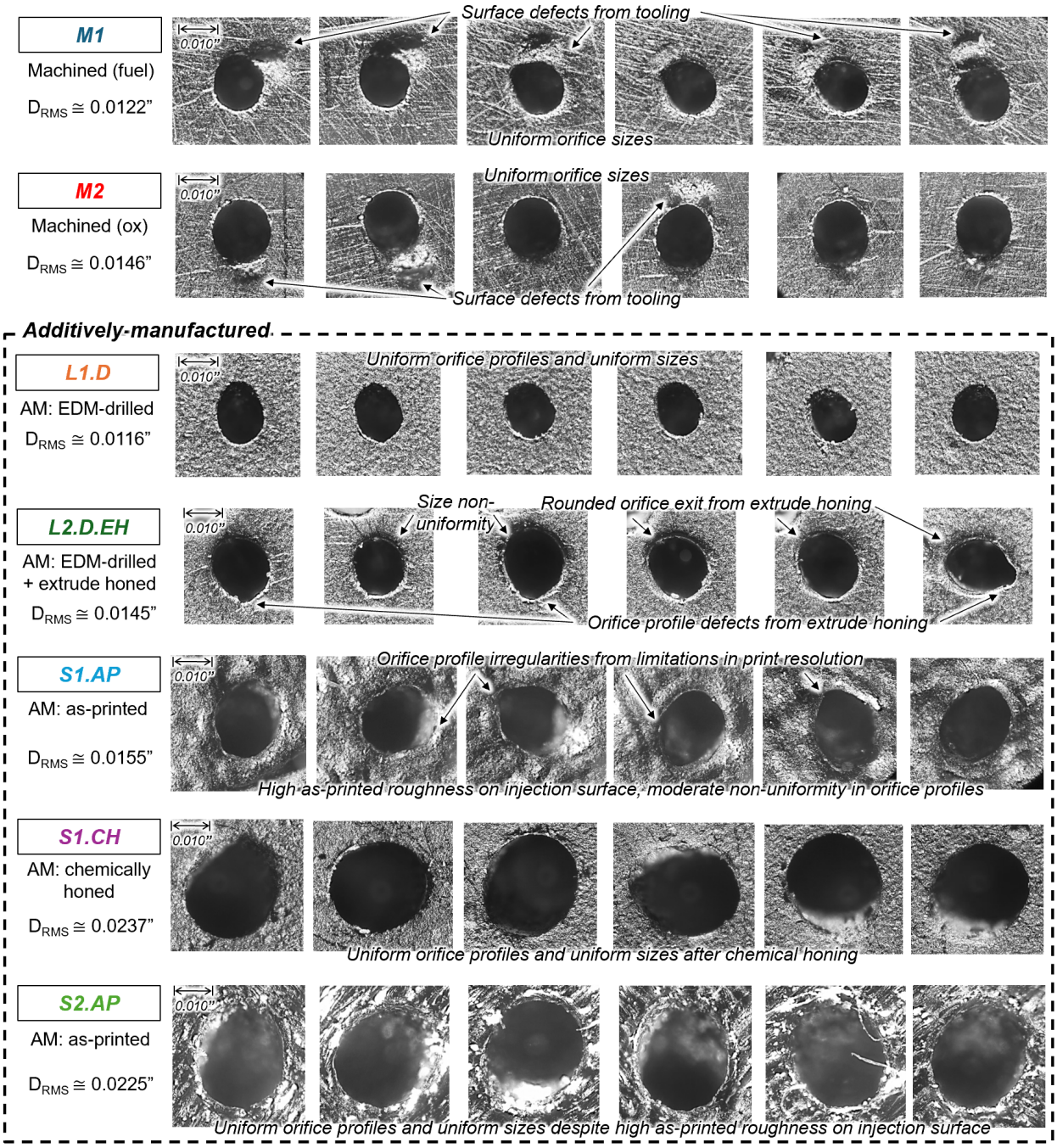

Figure 5.15: Magnified images of 6 orifices for each of the 7 injectors investigated in this study. All images are displayed at the same scale relative to each other with relevant features highlighted.

orifices were captured to inform hydraulic performance assessments. These images also provided valuable qualitative information on orifice fabrication using different manufacturing

processes. Fig. 5.15 displays 6 close-up orifice images per injector with key features highlighted. Here, all orifice images are to scale relative to one another. Due to fixed tooling geometries (e.g., drill bits), the conventionally-machined orifices of M1 and M2 exhibit exceptional orifice uniformity (in size and shape). Surface defects were commonly present on these machined orifices, which can have an adverse effect on liquid propellant jet shape and alignment. There is much greater variability in the additively-manufactured orifices.

The orifices of the additively-manufactured injectors were fabricated from a variety of manufacturing processes (e.g., as-printed, EDM-drilled, extrude/chemical honing), resulting in distinctly different qualities. The EDM-drilled orifices of injector L1.D were consistent in size and shape, with no manufacturing defects visible. In contrast, the extrude honing process that followed EDM-drilling for injector L2.D.EH produced non-uniformity in both size and shape of the orifices. The L2.D.EH orifices ranged in diameter from 0.013"–0.016". Orifice exit profile irregularities (seen highlighted in Fig. 5.15) effectively add to the total flow area by increasing the outlet's wetted perimeter and distorting propellant jet characteristics. Injectors S1.AP and S2.AP are also shown here with as-printed orifices without any post-print manufacturing processes. S1.AP was assigned orifices with diameters near the predetermined minimum achievable orifice size for the printer used. As such, limitations in print resolution formed some irregularities in S1.AP's as-printed orifice profiles – appearing as rounded burr-like features on the orifice exit contours. However, an increase in the targeted orifice diameter showed noticeable improvements in the uniformity and regularity of the as-printed orifices, best demonstrated by injector S2.AP. Notably, the chemically-honed orifices of injector S1.CH were relatively uniform in size and profile shape. While a variety of factors are involved that influence the end result of an orifice, the chemical honing process demonstrated improved precision and quality over the extrude honing method in terms of injector orifice fabrication. As a caveat, it should be noted that these visual inspections only examine the exit of the orifice and while similar features are expected internal to the orifice, a more comprehensive investigation is required to fully evaluate the relative merits of the manufacturing methods.

5.6.3 Cold-flow testing

Hydraulic performance was experimentally assessed by cold-flow testing various impinging injector geometries with liquid water over a range of flow conditions, thereby enabling experimental measurements of injector discharge coefficient. Recall Eqn. 5.2 for measuring discharge coefficient of a particular flowpath. An experimental cold-flow housing assembly was designed and manufactured in-house at UCLA. Pictured in Fig. 5.16, the cold-flow housing facilitated rapid cold-flow testing for each of the injectors. While also capable for reverse flow measurements (discussed more in depth in Ch. 6), only forward flow discharge coefficients were examined for this study. In the forward flow configuration, the bottom cap of the cold-flow housing was removed such that flow was not restricted downstream of the injection plane which may bias results.

A capture-and-weigh method was applied to measure the average mass-flow-rate of water through injector orifices ($\dot{m}$), and each injector's total outlet area (A_{out}) was determined from orifice diameters measured with 0.0005"-increment cylindrical pin gauges. ΔP_{inj} was effectively equal to the feed pressure (psig) since the flow was discharged into ambient air. Feed pressure was measured by a 0-300 psig gauge pressure transducer (Ashcroft model: G27M0210N1300) in the injector manifold positioned at PT port 1 (see Fig. 5.16). The pressure transducer was calibrated before each test. Pressure signals were recorded via a National Instruments NI-9205 DAQ card and National Instruments LabVIEW software. Roughly 15–20 flow-conditions were carried out for each injector with feed pressures that ranged from 25 to 280 psig. Across 7 injectors and all tested cold-flow conditions, the corresponding Reynolds number range was $0.5 \times 10^4 < Re < 3.6 \times 10^4$.

In addition to enabling experimental measurements of discharge coefficients, cold-flow testing also allows for visual inspection of impinging jet behavior for the injector designs of interest. As seen in Fig. 5.17, the as-printed flowpaths of injector S1.AP and S2.AP, and the chemically honed flowpaths of injector S1.CH notably demonstrated a consistent

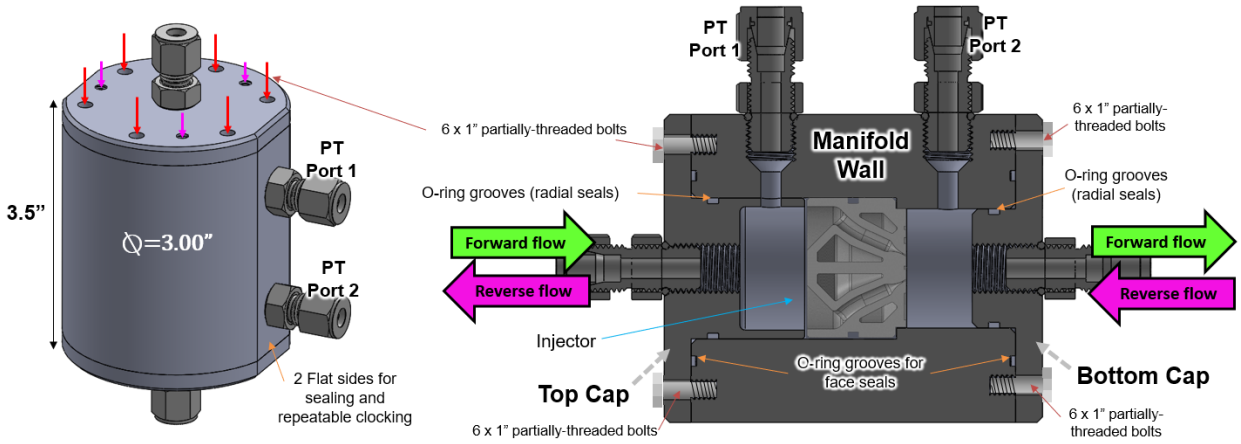

Figure 5.16: (*Left*) Isometric view of the cold-flow housing assembly used for the subscale AM injectors. (*Right*) Cross-section of cold-flow housing assembly CAD with AM tapered injector seated within housing.

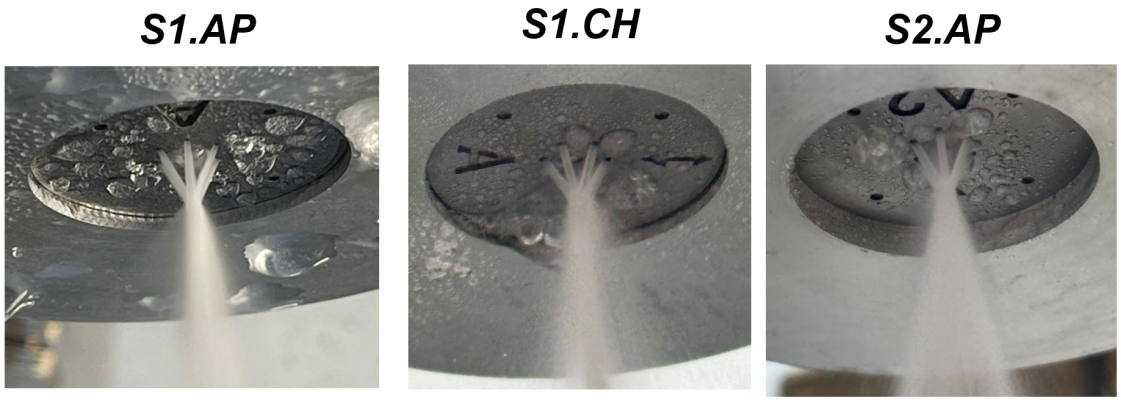

Figure 5.17: Example images of DI water cold-flow tests for different injectors.

impingement angle as indicated by a common jet impingement point. The final coalesced jets were all axial, indicative of no significant misalignment between any individual jets.

5.6.4 Injector discharge coefficients

Fig. 5.18 shows the experimentally-measured values of discharge coefficient (C_{D}) *versus* injector pressure drop (ΔP_{inj}) for all cold-flow tests. Vertical error bars capture the experimental measurement uncertainty, which was determined by a Taylor Series method of error propagation. Sources of measurement error were generally consistent across all cold-flow

tests, such that the trends presented here should still be valid even if the absolute numbers are somewhat biased. It is noted that C_D values beyond 1 are non-physical, which include any positive error bar bounds that extend past $C_D = 1$. Although this testing effort was somewhat limited in the combinations of orifice diameter and manufacturing methods, there are a number of notable observations. C_D results show a minor downward trend with increasing injector pressure drop (thus increasing flow velocity) presumed associated with slightly higher levels of turbulence and associated dissipative losses, but the C_D values are generally similar enough throughout the examined pressure range to be assumed constant. As such, the following C_D values reported and discussed in the text are averages (unless otherwise specified). The smaller of the two machined flowpaths, M1, had lowest discharge coefficient of $C_{D,M1} = 0.75$. With a nearly identical flowpath geometry, but a larger orifice, machined flowpath M2 resulted in a $C_{D,M2} = 0.82$. This is consistent with the orifice size dependence of C_D observed in the smooth wall CFD cases. These two machined injector flowpaths provide reference hydraulic performance values for the AM tapered schemes (L1.D, L2.D.EH, S1.AP, S1.CH, and S2.AP) to be compared.

Injectors M2, L1.D, and S1.AP resulted in very similar C_D distributions across the examined range of injector pressure drop. S1.AP and M2 are similar in orifice size, thus enabling a reasonable comparison between an as-printed AM tapered flowpath, and a conventionally-machined one. S1.AP and M2 yielded very similar C_D values of 0.81 and 0.82, respectively. In other words, S1.AP (AM tapered, as-printed) and M2 (machined) produced roughly the same amount of total viscous losses ($\Delta P_{loss,S1.AP} \approx \Delta P_{loss,M2}$). Recall the definition of critical orifice diameter, D_{cr}, presented earlier in Sec. 5.5.2.1. Here, the friction-dominated total viscous losses of the AM tapered flowpath are roughly equivalent to the inertial-dominated total viscous losses of the machined flowpath with an orifice diameter of D_{cr}. While D_{cr} technically requires an AM flowpath and machined flowpath to have identical orifice diameters and discharge coefficients, this comparison between S1.AP and M2 serves as a general estimate. Hence, cold-flow testing suggests $D_{cr} \approx 0.015$" for this particular injector orifice design. For

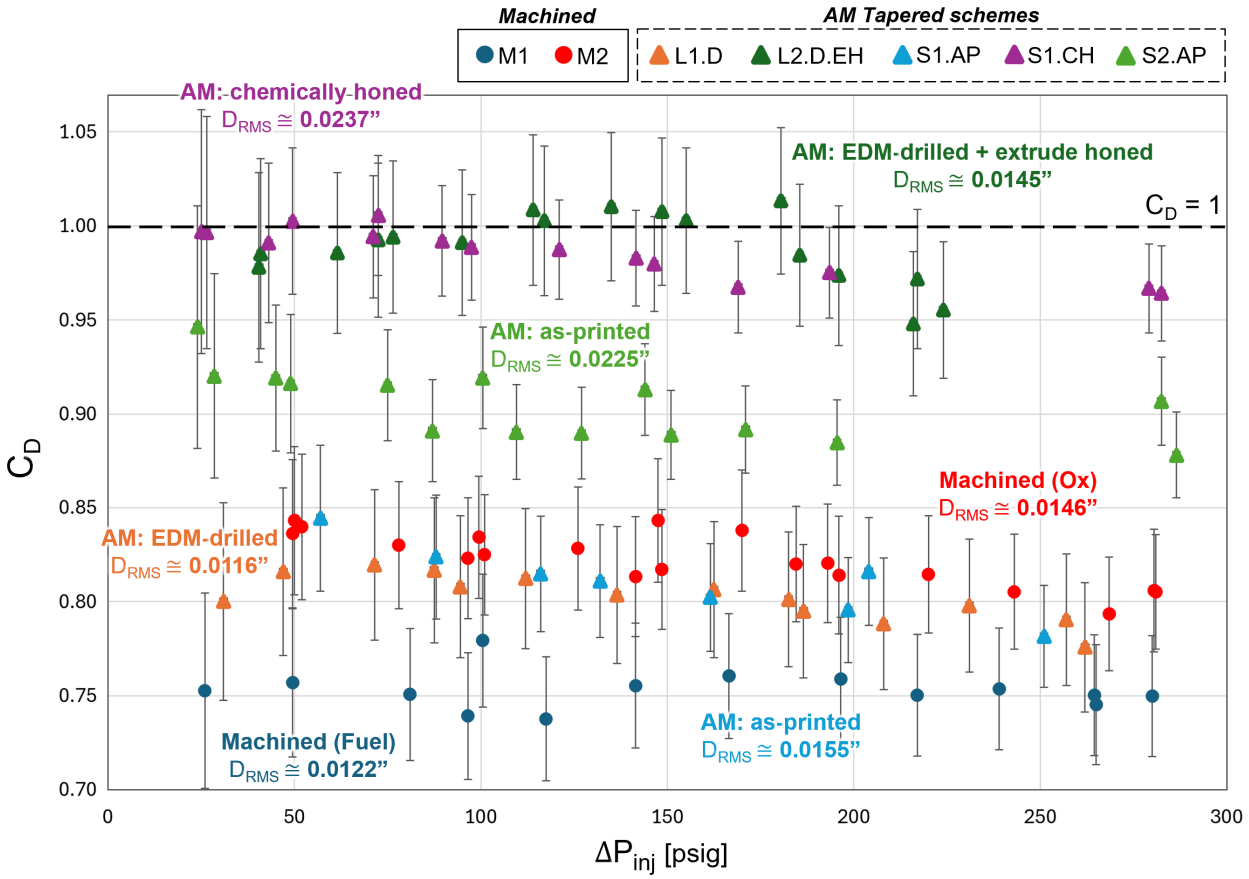

Figure 5.18: Compiled cold-flow results showing discharge coefficient *versus* injector pressure drop.

reference, the CFD-predicted value of D_{cr} was determined to be ≈ 0.017" for the AM tapered with an equivalent roughness of $\varepsilon = 0.001$". More experimental data would be required to more accurately determine D_{cr}, but the implication is that additively-manufacturing orifices of larger than $D \approx 0.02$" has the potential to yield hydraulic benefits even without additional honing processes.

L1.D's orifices were formed from EDM-drilling and resulted in an average diameter ($D_{\text{RMS}} = 0.0116$") close to M1's orifices ($D_{\text{RMS}} = 0.0122$"). Despite being un-honed, L1.D's flowpath tapering achieved a $C_{\text{D,L1.D}} = 0.80$, demonstrating a moderate boost in hydraulic performance of +7% compared to a machined flowpath with a nearly identical orifice size $C_{\text{D,M1}} = 0.75$. Injector S1.AP performed similarly to L1.D, achieving a $C_{\text{D,S1.AP}} = 0.81$. However, the two

AM tapered injectors differ in orifice area and how their orifices were manufactured; S1.AP's as-printed orifices were 1.8x larger in area than L1.D's EDM-drilled orifices. In general, a greater C_D improvement would be expected with this large of an area increase. This discrepancy may be attributed to differences in the two injectors' orifice profiles (previously discussed in Sec. 5.6.2), as well as dissimilar surface finishes on their orifice section walls (i.e., EDM-drilled vs. as-printed). Notably, the second as-printed injector, S2.AP, achieved a $C_{D,S2.AP} = 0.90$ – a 10% increase in C_D from S1.AP simply by expanding the orifice diameter by 0.007" (thereby increasing orifice area by 2.1x).

The two AM tapered injectors that underwent honing processes, L2.D.EH and S1.CH, recorded the highest average discharge coefficients of $C_D = 0.99$. Despite undergoing different methods of honing (L2.D.EH extrude honed, S1.CH chemically honed), and significant differences in orifice area (S1.CH 2.7x larger than L2.D.EH), these two flowpath geometries achieved nearly ideal hydraulic performance. Discharge coefficients approaching 1 is indicative of minimal viscous loss generation from both inertial and frictional sources. However, the non-circularity of the honed orifices (seen pictured in Fig. 5.15) is likely resulting in the orifice areas to be under-approximated and thereby slightly inflating the experimental C_D's. This is particularly true for the extrude honed orifices of L2.D.EH, where orifice exit profile irregularities were typically more severe.

While quantifying post-honed flowpath surface roughness was outside the scope of this work, knowledge of the pre-honed surface roughness can inform an estimation of the post-honed values. The honing processes expanded orifice diameters by 0.0025" and 0.008" (∼0.001" and 0.004" radially) for injectors L2.D.EH and S1.CH, respectively. That is, ∼0.001" and 0.004" of material was removed from the walls of the orifice sections. The pre-honed averaged surface roughness values were measured to be $Ra \approx 320$ μin, implying that height of material removed from the orifice section walls exceeded ∼4x Ra for L2.D.EH and ∼12x Ra for S1.CH. A more in-depth investigation should be conducted that characterizes the surface finish of honed AM flowpaths to better understand how these flow polishing techniques impact

frictional hydraulic losses.

Chemically-honed AM tapered injector S1.CH and as-printed AM tapered injector S2.AP were designed such that they would result in identical orifice diameters of 0.023". The intention was to enable a direct hydraulic performance comparison of two nearly identical AM tapered flowpaths with the same orifice areas, but with different surface finishes of their flowpath walls. Both injectors achieved the targeted orifice diameters within a 0.001" tolerance, but their final RMS orifice diameters were measured to be $D_{\text{RMS,S1.CH}} = 0.0237$" and $D_{\text{RMS,S2.AP}} = 0.0225$". This resulted in a difference in orifice area by roughly 10%, but still makes for a reasonable comparison nonetheless. Notably, the as-printed S2.AP injector achieved a $C_{\text{D,S2.AP}} = 0.90$ without any post-print manufacturing processes required. However, the chemically-honed injector S1.CH with a similar orifice size earned a $C_{\text{D,S1.CH}} = 0.99$. This indicates that: 1) the AM tapered flowpath design effectively mitigates inertial losses as intended, and that the majority of its viscous losses are generated from frictional effects, and 2) honing can fully realize the hydraulic performance benefits of the AM tapered scheme via the mitigation of said frictional losses.

5.6.5 Comparison with computational fluid dynamics predictions

Fig. 5.19 presents a direct comparison between experimental and CFD-predicted values of injector discharge coefficient. Experimental $C_{\text{D,Cold-flow}}$ values (shown here in blue) reflect a $\Delta P_{\text{inj}} \approx 125$ psig, with their corresponding measurement uncertainty range. Each flowpath geometry was simulated using the CFD methodology described in Sec. 5.4.1 with a ΔP_{inj} of 125 psig, first assuming smooth walls ($\varepsilon \approx 0$). Using the same ΔP_{inj} boundary condition, a representative surface roughness of $\varepsilon = 0.001$" was applied to the walls of L1.D, S1.AP, and S2.AP to account for the inherent AM surface roughness associated with the unhoned AM flowpaths. It should be noted that for modeling and analysis purposes, ε was approximated as 0.001", which is ∼3x the measured surface roughness average value ($Ra \approx 320$ μin), although

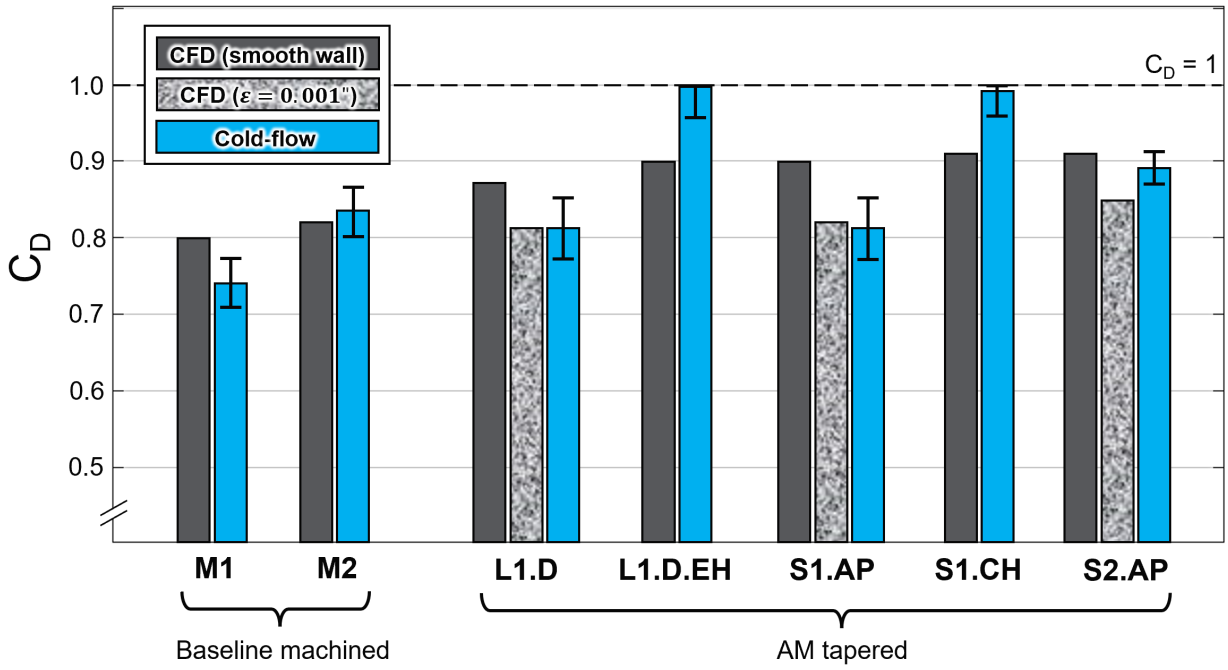

Figure 5.19: Discharge coefficient comparison ($\Delta P_{\text{inj}} \approx 125$ psig.) between cold-flow and CFD-predicted values. Measurement uncertainty shown for cold-flow results.

this factor can be larger [2]. $C_{\text{D,CFD}}$ values are presented for both the smooth and rough wall CFD cases.

In general, there was good agreement between the experimental injector discharge coefficients and computational predictions. The smooth-wall CFD cases only accurately predicted the experimental C_{D} for the machined flowpath M2. The machined flowpath with a smaller orifice, M1, exhibited an experimental C_{D} 8% lower than CFD results. This could be attributed to the presence of fabrication defects (i.e., burrs) within the M1 flowpaths that were visibly inaccessible. For the AM tapered flowpath cases, smooth-wall CFD cases over-predicted C_{D} for the un-honed injectors: L1.D by +7%, S1.AP by +11%, and S2.AP by +2%. This is likely due to the increased frictional losses of AM surface roughness not being accounted for. CFD simulations modestly under-predicted C_{D} for the two honed injectors by −10% for L2.D.EH and −8% for S1.CH. Notably, when an AM-relevant surface roughness of $\varepsilon = 0.001$" was applied to the walls of the model, CFD predictions closely matched with cold-flow results.

Here, computational results (with surface roughness) deviated from measured cold-flow values by 0%, +1%, and −4% for L1.D, S1.AP, and S2.AP, respectively.

While the CFD-predicted C_{D} values presented in this work were not consistently accurate to experimental measurements, the relative trends show reasonable agreement. It should be noted that CFD software tools rely on the use of wall functions and/or turbulence models that are often anchored by empirical correlations. CFD results can therefore vary significantly between which turbulence models are employed, especially when simulating turbulent flow over rough surfaces [102]. The stochastic nature of AM surface topology further convolutes the accuracy of such models. Over recent years, new CFD strategies and turbulence models have been introduced that better capture flow properties over additively-manufactured rough surfaces [41, 86]. All considered, the sensitivity of injector C_{D} on flowpath design and surface characteristics makes experimental characterization important to ensure proper flow conditions are achieved within a propulsion system and as a means of validating computational predictions.

5.7 Chapter summary

Hydraulic losses across a liquid rocket injector are undesirable, and are largely dependent on injector flowpath design and surface characteristics. The expanded design freedom of additive manufacturing enables flowpath tapering which mitigates the inertial losses generally associated with sharp features within conventionally-manufactured injector geometries. However, the increased surface roughness inherent to AM parts can introduce additional frictional viscous losses, potentially offsetting the hydraulic benefits of the AM tapered scheme. In this chapter, a computational fluid dynamics analysis was presented that informed injector design modifications, which started with a canonical conventionally-manufactured impinging injector plate. Initial smooth-wall steady CFD models exhibited how AM-enabled flowpath tapering, particularly applied to the orifice inlet, can significantly improve injector C_{D} (roughly +10%

for the injectors modeled herein) by mitigating inertial viscous losses. Further computational analyses were conducted that captured surface roughness effects using AM-relevant as-printed surface finishes. It was shown that the increase in frictional viscous losses from AM surface roughness can, in some cases, offset the hydraulic benefits of a tapered flowpath design. However, for a given ΔP_{inj}, reductions in flowpath surface roughness and marginally larger orifice diameter exhibited notable improvements in C_{D}, as predicted by the CFD model.

Several promising AM tapered injector designs were down-selected for printing that ranged in orifice diameter and flowpath surface roughness. While some injectors were tested in their as-printed state, others underwent post-print manufacturing processes, such as EDM-drilling of orifices, and/or one of two honing (flow machining) methods. Final orifice diameter and flowpath surface finish were determined by which of these processes were employed. Orifice characteristics were evaluated visually through magnified images, which provided valuable qualitative insight into orifice geometry features that may influence flow behavior. Each AM injector, as well as the baseline conventionally-manufactured injector, was cold-flow tested over a range of injector pressure drop to experimentally characterize discharge coefficients. Liquid water served as a liquid propellant surrogate.

This experimental investigation revealed trends that corroborated the CFD results despite its limited scope. Firstly, CFD simulations using a relatively simple steady, single-phase model were generally a good predictor of injector C_{D}. Similar C_{D} values were measured between the machined and un-honed AM tapered injectors for orifice diameters between $\sim$0.012" and $\sim$0.016". This suggests that the reduced inertial losses enabled by the tapered flowpath were in fact offset by increased frictional losses of a similar magnitude from the rough AM walls. Notably, the two AM tapered injectors that underwent a post-print honing process achieved experimental C_{D}'s of ≈ 1, suggesting a significant benefit. The need for post-print polishing techniques may be alleviated as AM technology continues to progress and as-printed surface finishes improve. Based on current metal printing technology and associated resolution, additively-manufactured liquid injector orifices of larger than $D \approx 0.020$" have the

potential to yield hydraulic benefits even without additional honing processes. In sum, this work has demonstrated that additive manufacturing can be leveraged to minimize impinging liquid rocket injector hydraulic losses through a combination of optimized flowpath tapering to mitigate inertial losses and post-print honing to mitigate friction losses. The broader implication of this work is that LRE propulsion systems with higher system efficiency may be achieved by incorporating the aforementioned design approach outlined in this chapter, thereby facilitating enhanced mission capabilities or payload capacity for spacecraft and launch vehicles. These design strategies have significant potential for application in other combustion devices, such as additively-manufactured (AM) combustion chambers featuring regenerative cooling channels. In such systems, arrays of relatively long fluid channels reside within the combustion chamber walls, circulating liquid propellant to manage thermal loads. This AM-enabled design and manufacturing methodology supports efficient heat transfer optimization while minimizing pressure loss, offering a cost-effective approach to enhancing thermal management, an area of potential future work.

CHAPTER 6

High-diodicity impinging injector design for rocket propulsion enabled by additive manufacturing

*The contents of this chapter have been presented / included in the conference proceedings for the **AIAA SciTech Forum, 2022** under the title of "High-diodicity impinging injector design for rocket propulsion enabled by additive manufacturing" [63].*

6.1 Introduction

Combustion instabilities (CIs) are common in liquid rocket engines and present concerns for system performance and hardware survivability. Such instabilities often present as periodic, high-pressure impulses within a combustor that can negatively influence the fluid dynamics of the propellant injection process - in some cases leading to backflow of combustion products into the propellant manifolds. In more extreme cases, CIs can increase local heat transfer rates and induce excessive pressure-based vibrations, both of which may destroy engine hardware. Backflow caused by combustion instabilities or from detonations within a combustor induces a decline in combustion efficiency due to poor mixing from differences in propellant densities, flow-rates, and orifice geometry, thus causing the corresponding propellant refresh times to often mismatch. This leads to a transient and spatially varying equivalence ratio throughout the combustion chamber, which can negatively impact performance. Specific injector designs have a characteristic resistance to feed system coupling and recovery time (related to backflow) that depends on injector geometry and stiffness (the ratio of the pressure drop across the

injector to the pressure in the combustion chamber) [43]. For traditional combustion-based rocket engines, the injector stiffness is typically ∼15-20% in order to mitigate the performance-reducing effects of combustion instabilities [43]. CIs are traditionally dealt with through the use of stabilization methods such as acoustic baffles or increasing injector stiffness (higher injector ΔP). Increased injector stiffness requires larger (heavier) feed pressurization systems, and the implementation of acoustic baffles both increase the overall dry mass of the vehicle, resulting in a decreased payload or mission duration capability for spacecraft and launch vehicles.

An ongoing goal in improving rocket engine performance is the development of low pressure-loss injectors which are also robust against combustion instabilities and the associated feed-system coupling. An approach which allows for the simultaneous fulfillment of these requirements is the implementation of an injector geometry to resist reverse flow without hindering forward flow. Some recent efforts have explored geometric modifications to impinging injector schemes to enhance backflow resistance and recovery characteristics by angling injector elements relative to the direction of a transverse pressure/shock wave [21]. This angling resulted in only minimal performance improvements due to difficulty in predicting the direction of the wave propagation and a rise in potentially harmful cavitation near the injection plane. The tapering of injector orifices led to noticeably faster propellant recovery times, which is speculated to be the result of the product gases having a larger volume to fill and expand, thus decreasing its pressure [21]. In this work, we examine the potential of additive manufacturing to enable impinging injection designs that provide enhanced backflow resistance or diodicity.

Aside from the production-rate and possible economic benefits, additive manufacturing (AM) provides opportunity to re-imagine combustion device design in the absence of conventional manufacturing constraints, and to more closely couple design with physics-based analysis. AM enables complex three-dimensional geometries and provides a new means for tailoring the fluid dynamics of combustion systems, particularly injection. For example, AM permits the fabrication of sophisticated propellant passageways within an injector's manifold,

which encourage gradual changes in both flow area and direction. These geometric alterations in the flow paths mitigate flow separation and minimize viscous losses, ultimately decreasing the forward pressure drop across the injector [92]. In this work, the design space permitted by additive manufacturing is explored to create low forward pressure-loss impinging injection schemes that hinder propellant backflow. We investigate the implementation of a "fluidic diode" feature as a means of backflow prevention for a representative liquid bi-propellant impinging doublet. Steady single-phase and transient multi-phase CFD models are utilized to quantify backflow resistance and assess forward-flow recovery, respectively. Initial cold-flow results for select printed injectors are also presented, with a discussion of relative performance and future work.

6.2 Methods

6.2.1 Diodicity

Design efforts are driven by computational fluid dynamics analysis, and quantitatively characterized through calculating injector discharge coefficient, C_{D}, a key metric used to assess hydraulic performance, defined as:

$$C_D = \frac{\dot{m}}{A\sqrt{2\rho\Delta p}} \tag{6.1}$$

Here, $\dot{m}$ represents the mass flow rate of propellant with density ρ through an orifice with a cross-sectional flow area A, and a pressure drop Δp across the orifice.

Additionally, we calculate the diodicity of each injector as a means of characterizing its relative backflow resistance. Diodicity, Di, is defined in Eq. 6.2 as the ratio of pressure drop for reverse flow to the required pressure drop in forward flow for the same mass flow rate. This can be modeled by flipping the inlet and outlet boundary conditions in the CFD model, and calculating the discharge coefficient in the reverse direction. Diodicity can also

be described in terms of forward and reverse discharge coefficients, as also seen in Eq. 6.2:

$$\mathrm{Di} = \left(\frac{\Delta p_{\mathrm{rev}}}{\Delta p_{\mathrm{fwd}}}\right)_{\dot{m}} = \left(\frac{C_{D,\mathrm{fwd}}}{C_{D,\mathrm{rev}}}\right)^2 \tag{6.2}$$

6.2.2 Design of a fluidic diode

Here we introduce an AM-enabled, backflow-resistant flow-path geometry termed a "fluidic diode" [132]. Analogous to an electrical diode, which allows electric current to flow in a single forward direction while impeding flow in the opposite direction, this fluidic diode feature serves as a means of resisting the backflow of combustion gases up into the propellant manifold. Implemented slightly upstream of the propellant injector face, this feature is intended to perform similar to a Tesla valve [100] in which the geometry of the flow path provides for low resistance in the forward direction but induces high resistance in the reverse direction (see Fig. 6.1).

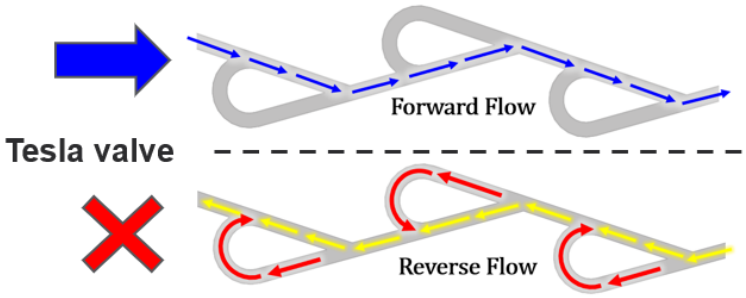

Figure 6.1: Tesla valve flow behavior with low-resistance in forward direction (top) and high-resistance in reverse direction (bottom).

The flow path geometry of a Tesla valve promotes flow losses in the reverse direction from abrupt momentum changes, vorticity generation, and an adverse pressure gradient [135]. The fluidic diode developed in this work will combine the hydraulic benefits of "tapering" the injector element, demonstrated to be efficient in Ref. [22, 97], and the redirection of flow in the reverse direction similar to a Tesla valve.

Implementing these proposed diode features in a real rocket injector using conventional

subtractive manufacturing techniques is impractical and thus leverages the unique capability of AM. However, the fluidic diode design is still constrained by two primary factors: 1) metal AM printability considerations such as sub-mm feature resolution and overhang angles [48] and 2) structural integrity of the injector. For example, the implementation of a fluidic diode cavity near the injection face can cause reductions in minimum wall-thickness between the unlike-doublet flow paths, and between adjacent doublet pairs. Furthermore, printed materials show a reduction in strength when sample thickness is below some characteristic value (dependent on material and AM fabrication process) due to increased porosity [36]. Therefore, the size, shape, and position of the fluidic diode must be taken into consideration throughout the design process.

A coupled CFD-design trade study was performed to examine how various fluidic diode geometries influence net diodicity. Parameters such as diode size, revolution angle, and number of diodes in series were examined (see Fig. 6.2). Orifice outlet diameter was held constant. A secondary design step involved integration of the various designs in the impinging doublet configuration with a 60° impingement angle, see Fig. 6.3. Based on relative diodicity results from steady-state simulations and feasibility assessment for manufacturing and structural integrity, a down-selected fluidic diode design was further analyzed with regards to transient response and compared to tapered impingement design without the diode feature. The analysis framework is discussed in the following subsections.

6.2.3 Steady-state CFD model

Discharge coefficients and diodicities are determined using steady, single-phase, three-dimensional computational fluid dynamics (CFD) analysis performed on the fluid domain of a single injection element for various impinging-doublet designs. Due to the injector's radial symmetry, a wedge-shaped slice of the injector's fluid domain was utilized. Unstructured, tetrahedral meshes of $\sim 5 \times 10^5$ elements were used (see Fig. 6.4) following a brief mesh study

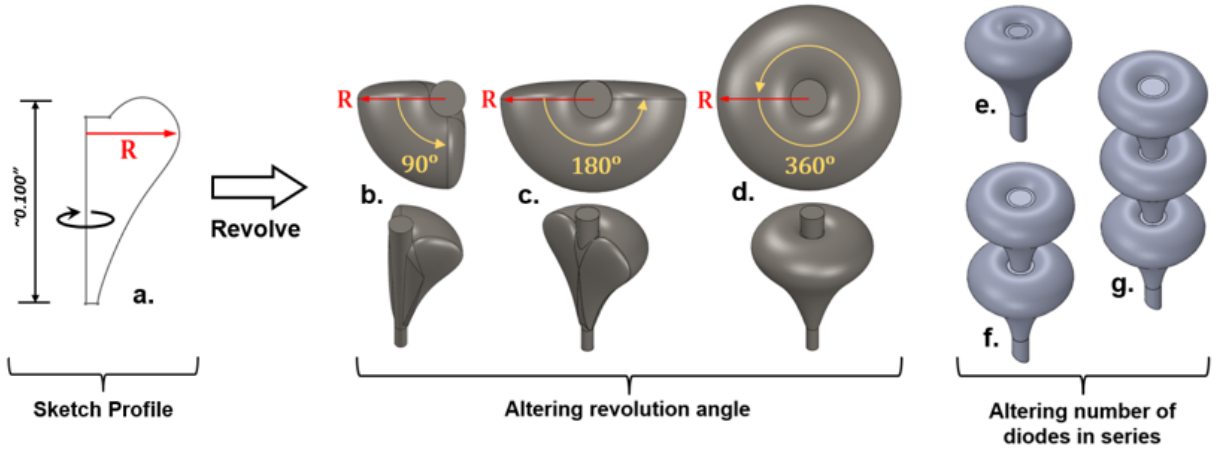

Figure 6.2: a.) 2D sketch profile used to create a diode feature then revolved around at some desired angle. Top and isometric views of diode revolution angles of b.) 90°, c.) 180°, d.) 360°. The variation in the number of diodes in series is shown for e.) one, f.) two, and g.) three diodes.

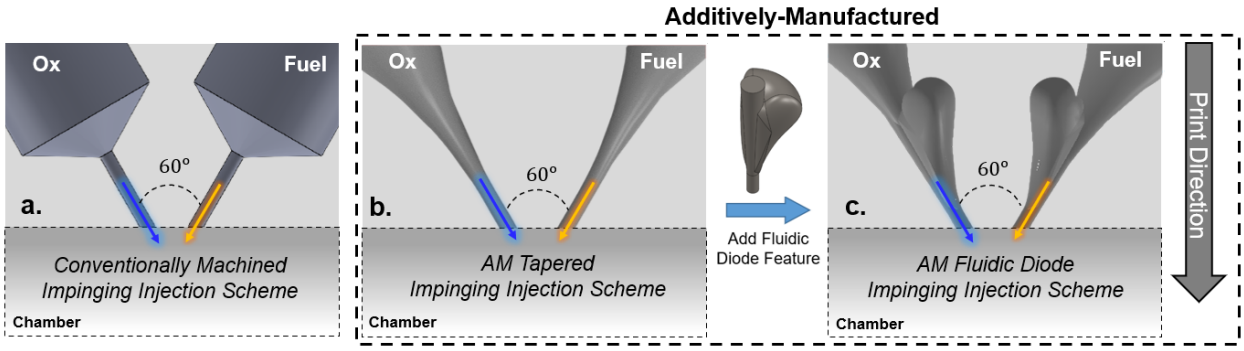

Figure 6.3: Cross-sections of a.) conventional impinging injection scheme using subtractive manufacturing, b.) AM-enabled tapered impinging injection scheme, c.) the same tapered injection scheme as b. but with an example of implemented 90° fluidic diode of radius $R = 0.050$ in.

where additional mesh sizes were examined to investigate the dependence of the results on mesh resolution. A no-slip boundary condition was applied to the injector walls, which also assume no surface roughness. An SST-k-ω turbulence model was applied and liquid water was used as the working fluid. The feed pressure was set to 300 psig at the inlet, and 0 psig at the outlet for forward flow. The pressure boundary conditions were then flipped to assess reverse-flow behavior. Cross-sectional flow area, fluid density, and pressure drop are all held

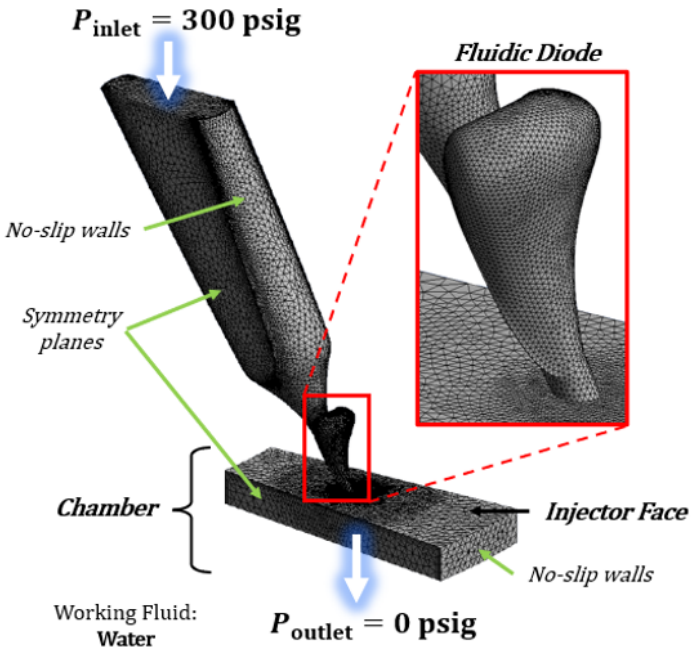

Figure 6.4: Unstructured, tetrahedral mesh of a wedge-shaped symmetric slice of the chamber and the injector's fluid domain with an implemented 90° fluidic diode feature of radius $R = 0.050$ in. Boundary conditions shown are for the single-phase steady CFD cases.

constant for each case and CFD results provide the propellant mass flow rate that passes through the injection plane. Equations 5.2 and 6.2 are then applied to quantify relative hydraulic performance.

6.2.4 Transient back-flow recovery model

A more complex CFD model was used to examine transient fluid behavior associated with a chamber pressure impulse for a smaller subset of injector designs. This model assessed the transient backflow (or flow-rate change) and interaction of liquid propellant and high pressure combustion gas within an injector element when subject to a prescribed sharp increase and decay of pressure at the injector face. Simulations were run for three different injector stiffness values: 20%, 50%, and 150%. Injector stiffness (IS) is defined as:

$$\mathrm{IS} \equiv \frac{\Delta p}{p_c} = \frac{p_{in} - p_c}{p_c} \tag{6.3}$$

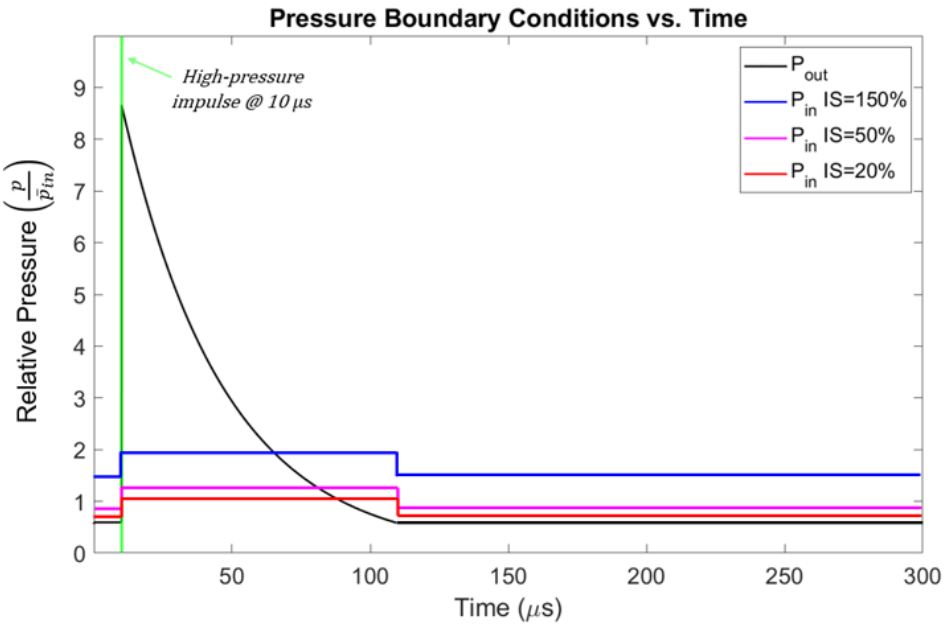

Figure 6.5: Relative pressure *versus* time plots for transient boundary conditions applied to the outlet and inlet.

The steady-state pressure drop across the injector is denoted by Δp, whereas p_c represents the steady-state chamber pressure and p_{in} is the inlet pressure.

Here, we use a pressure-based solver in ANSYS Fluent and employ an unsteady multiphase VOF (volume of fluid) model using liquid water and air as the propellant and combustion gas, respectively. Stiffness values are varied by altering the inlet pressure while the nominal chamber pressure and the peak pressure of the impulse are held constant. The transient simulation is initialized by first executing a steady case (similar to that of the steady state diodicity cases) with the initial boundary conditions used to establish nominal forward flow rates, which is what would be seen prior to applying the high-pressure impulse. Additionally, a rudimentary step-function is applied to the inlet pressure to mimic the responsive increase in manifold pressure (simulated to be an increase of ∼30% relative to the initial inlet pressure) caused by gases displacing incompressible liquid propellant within the manifold. A similar manifold pressure variation is measured by researchers at Purdue in Ref. [21]. As seen in Fig. 6.5, a time-varying outlet boundary condition is set at $t = 10$ µs to mimic the pressure

profile of an impulsive, high-pressure wave traversing an injector orifice and assumes the shape of an exponential decay function [21, 79, 103]. A time-step size of 1×10^{-7} seconds was found to be sufficient for a converged solution with 20 iterations per time-step. Time-step sizes smaller than this showed minimal changes in the results for the flow conditions and geometry used in this study.

6.3 Results

6.3.1 Steady diodicity results

Discharge coefficients and diodicities given by the CFD simulations for the various injector designs are shown in Table 6.1. The diodicity of the baseline conventionally machined injector is 1.17, which was shown to increase to 1.68 (+44%) for a tapered injector enabled by AM. With the introduction of various fluidic diode designs, the diodicity increases substantially to a range of 2.72 to 3.01 (upwards of +157% with respect to the baseline injector). Increasing the revolution angle of the diode resulted in increased forward and reverse discharge coefficients, but ultimately decreased the diodicity of the injector element slightly. Increasing the number of sequential diodes indicated a decrease in both forward and reverse discharge coefficients,

Injector Element Scheme	$C_{\mathbf{D,fwd}}$	$C_{\mathbf{D,rev}}$	**Di**	**Change in Di relative to Baseline**
Baseline	0.77	0.72	1.17	N/A
AM Tapered	0.92	0.71	1.68	+44%
90° Diode ($R = 0.050$")	0.92	0.54	2.90	+148%
180° Diode ($R = 0.050$")	0.94	0.57	2.72	+132%
360° Diode ($R = 0.050$")	0.94	0.56	2.82	+141%
90° Diode ($R = 0.060$")	0.92	0.53	3.01	+157%
Two 360° Diodes ($R = 0.050$")	0.90	0.52	3.00	+156%
Three 360° Diodes ($R = 0.050$")	0.88	0.51	2.98	+155%

Table 6.1: Forward and reverse discharge coefficients for the various injector element schemes as well as their corresponding diodicity values. Down-selected fluidic diode highlighted in **bold**.

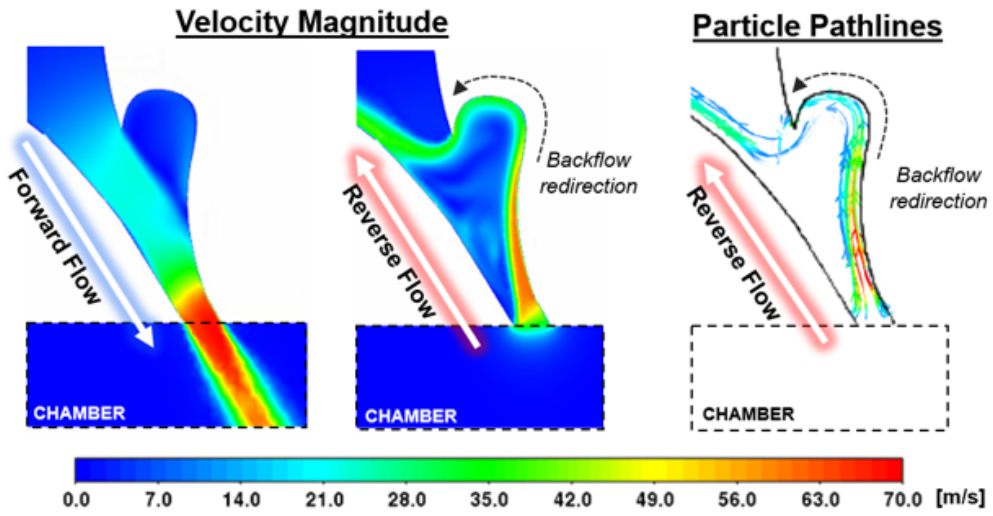

Figure 6.6: Velocity contour plots of the oxidizer injector manifold with the 90° fluidic diode feature for forward flow (left) and reverse flow (middle), and particle pathlines colored by velocity magnitude for reverse flow (right).

but without a significant enhancement to diodicity. Increasing the radius of the diode 20% from 0.050" to 0.060" showed a minimal improvement to diodicity. Therefore, the 90° version of the single diode feature is chosen to be used for the transient backflow recovery simulation due to its high diodicity and its feasibility in being fabricated with AM, fulfilling wall-thickness and overhang angle requirements.

Fig. 6.6 shows a velocity contour plot of the fluid behavior of forward and reverse flow, and particle pathlines colored by velocity magnitude for the reverse flow case for the 90° diode feature. The fluidic diode appears to create negligible impediment to the flow in the forward direction, which yields no change in the forward discharge coefficient. On the other hand, in the reverse flow direction, fluid tends to preferentially fill the fluidic diode's reservoir and become redirected before undergoing a very sharp turn to enter the manifold inlet. This reverse flow redirection is likely responsible for the significant decline in the reverse discharge coefficient and thus an auspicious improvement in backflow resistance.

6.3.2 Experimental validation

To date, our research group has printed and cold-flow tested some of the unlike impinging-doublet liquid bi-propellant injector designs. This includes both the baseline conventionally manufactured injector and the tapered AM injector, which was additively-manufactured using a laser powder bed fusion (L-PBF) process out of stainless steel. The tapered AM injector was cold-flow tested before and after an abrasive extrude honing process, intended to reduce surface roughness. Experimental cold-flow results are shown in Table 6.2 and compared to CFD results. The tapering of the internal flowpaths (even before honing) improves the forward C_{D} (as predicted by CFD) for both the fuel and oxidizer flow-paths relative to the baseline conventionally-manufactured injector. Moreover, significant improvement in the forward C_{D} is displayed after the AM injector undergoes the abrasive flow machining (honing) process. CFD results closely align with cold-flow testing for the fuel lines of both injectors, however CFD analysis seems to over-predict the forward C_{D} for both injectors' oxidizer lines. Despite the disagreement in absolute values, CFD was still able to accurately model the relative changes in flow behavior and thus served as a useful tool to assess relative hydraulic performance. Cold-flow results validate the hydraulic performance benefits of AM-enabled tapered flow-paths, and in conjunction with the post-printing honing process, the AM tapered injector exhibits a 21.5% and 23.4% increase in forward C_{D} for the fuel and oxidizer lines, respectively.

Metric	**Baseline Injector**		**AM Tapered Injector**			
	CFD	Cold Flow	CFD	Cold Flow (un-honed)	Cold Flow (honed)	% Difference after honing relative to Baseline
$C_{\mathrm{D,fwd,fu}}$	0.80	0.79	0.91	0.87	0.96	+21.5%
$C_{\mathrm{D,fwd,ox}}$	0.77	0.64	0.92	0.69	0.79	+23.4%

Table 6.2: CFD and cold-flow results showing the forward discharge coefficients of the oxidizer and fuel lines of the conventionally-machined baseline injector and the additively-manufactured tapered injector.

6.3.3 Transient backflow recovery results

Transient analysis was focused on mass flow rate changes (recovery) associated with a prescribed pressure pulse reflective of a chamber instability. Here, flow-rate recovery timescales represent figures of merit relevant to mitigating the negative effects of injector backflow on engine performance. From time-resolved mass flow rate through the injection plane, we can determine the *refill time* - the amount of time it takes from the instant of back flow occurring (when forward mass flow rate through injector face approaches zero, denoted by t_0), until the forward flow of propellant is reestablished into the combustion chamber (when forward mass flow rate becomes positive again, denoted by t_{fwd}), as seen in Equation 6.4.

$$t_{\text{refill}} = t_{\text{fwd}} - t_0 \tag{6.4}$$

Additionally, we calculate the total amount of propellant mass vs. time by integrating the liquid mass flow rate through the injection orifice with respect to time, starting at the instant

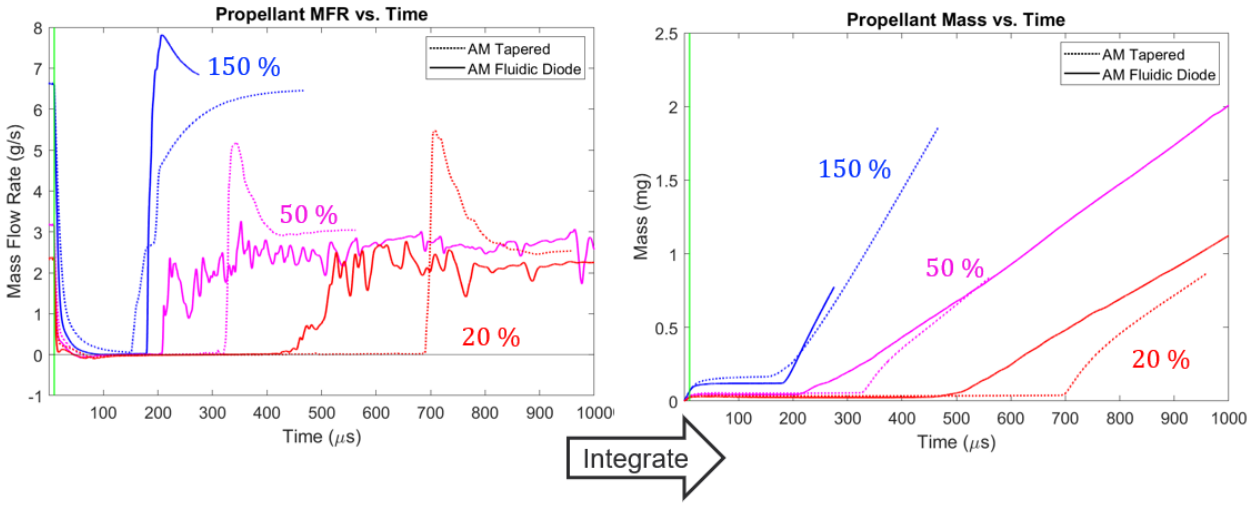

Figure 6.7: (Left) Propellant mass flow rate vs. time (left), and total propellant mass vs. time (right) are plotted for three different injector stiffness values (150%, 50%, and 20%) with the AM Tapered injector geometry (dotted curves) and the AM Fluidic Diode geometry (solid curves).

Injector Stiffness	AM Tapered	AM Fluidic Diode	Difference with Fluidic Diode
150%	141 μs	169 μs	19.8% slower
50%	315 μs	199 μs	36.8% faster
20%	681 μs	415 μs	39.1% faster

Table 6.3: Refill times for the AM Tapered and AM Fluidic Diode injectors at three different injector stiffness values (150%, 50%, and 20%).

of backflow. We show the transient mass flow rate response of two injector geometries for three conditions of stiffness (reflecting a range of feed pressures) in Fig. 6.7a and Fig. 6.7b. At a high injector stiffness (i.e., 150%), the baseline and fluidic diode injector elements show a similar recovery response. However, as injector stiffness begins to decrease, the fluidic diode demonstrates a clear performance advantage as forward propellant flow rates are reestablished appreciably sooner. For injector stiffnesses of 50% and 20%, the fluidic diode permits refill times 36.8% and 39.1% sooner than the AM tapered injector, respectively.

6.4 Discussion

The aforementioned combination of CFD simulations and experimental cold-flow testing reveal some key takeaways regarding potential benefits of AM-enabled non-traditional injector geometries for enhanced hydraulics and diodicity with impingement injection. Gradual tapering of traditional fluid paths is shown to offer a meaningful increase in forward discharge coefficient ($\sim$20%), implying lower pressure losses, which were shown to be realizable after printing and cold-flow testing. The addition a fluidic diode feature on the tapered propellant passageways was further shown to significantly increase diodicity by as much as $\sim$150% compared to a conventionally-machined baseline injector case. However, the addition of multiple fluidic diodes in series exhibited marginal benefit over a single diode feature. Moreover, a fluidic diode feature that was revolved 360° around the circumference of the injector element offered no apparent benefit compared to a well-positioned 90° diode feature. This is likely associated with the impingement angle of the injector element and associated bias in inlet

flow direction (entering the diode) for reverse flow. Diode feature revolution beyond 90° also presents more difficulty in reconciling feasible printing angles. Lastly, we note that based on a subset of transient cases, the diodicity determined from steady-state analysis appears to correlate with shortened flow-rate recovery times, but this is only pronounced at lower injector stiffness.

The observations mentioned above provide design insight for impingement injection with AM, but some shortcomings in the current CFD models should be noted. The models currently do not account for thermodynamics or chemical kinetics as would be associated with combustion, nor a realistic response in the manifold pressure as product gases fill the injector element. The models also do not account for surface roughness. These aspects of the model were omitted due to uncertainties, limitations in accessible computational resources and/or diminishing return on complexity. While the models lacked some sophistication, we do not expect such added elements to meaningfully alter the observed trends. It can be noted that the transient multiphase CFD model used to assess backflow recovery behavior was qualitatively validated by simulating experiments recently performed at Purdue University by Celebi et al. [21], exhibiting good agreement.

Although the constraints of additive manufacturing are fewer in comparison to conventional subtractive manufacturing techniques, they must be accounted for throughout the design process. One of the most difficult design restrictions to overcome when designing any additively-manufacturable component is staying within the overhang angle limit. This critical angle varies for different printing methods and materials, but often range between 30° to 45° with respect to the normal of the printing surface. As the injector's internal flow-path complexity increases in order to achieve desired hydraulic performance outcomes, creating a design that is printable and structurally robust becomes a more arduous task. For example, an increase in the overall size of the diode may have an increased benefit in both diodicity and recovery behavior and will be explored further in future work. However, the designer must then account for the reduction in wall-thicknesses and spacing between doublets and their

adjacent element pairs by positioning the diode cavity accordingly. As such, minimal AM wall thicknesses may limit design features like element density and diode size. Some other challenges of additive manufacturing (i.e., surface roughness and sub-mm feature resolution) can be overcome by supplementing AM with post-printing processes such electrical discharge machining (EDM) and abrasive flow machining (honing), as demonstrated in [97].

6.5 Chapter summary

This work explored the design space offered by additive manufacturing to implement geometric fluidic diode and tapering features near the injection plane for an impinging unlike doublet as a simple means of increasing diodicity. Steady single phase and transient multiphase CFD analyses demonstrate promising results: a fluidic diode feature added to a realistic injector geometry yields a favorable increase in diodicity and a quicker response time to re-establish forward propellant flow. Tapering also exhibits a decrease in forward pressure loss without meaningfully reducing backflow resistance.

CHAPTER 7

Conclusions and future work

In this thesis, advanced injection schemes enabled by additive manufacturing were examined to enhance the performance of liquid rocket engines. Three primary topics of injection-related liquid rocket engine performance were investigated: (1) propellant mixing, (2) combustion instabilities, and (3) injector hydraulics.

In Chapter 2, laser absorption tomography (LAT) was utilized to assess mixing characteristics of various shear coaxial rocket injector geometries. Methane and oxygen were used as propellants and combusted in an atmospheric burner. Quantitative, spatially-resolved distributions of temperature and carbon-monoxide mole fraction were compiled to produce two-dimensional, spatially-resolved images of each flame's thermochemical structure. Coaxial mixing length scales were characterized and compared for three shear coaxial injectors with varying oxidizer post recess. This technique also enabled a unique method of directly capturing the stoichiometric mixing length. The enhanced mixing effects of a recessed oxidizer post were evident in the most recessed injector, which showed a wider flame brush, shorter flame length and increased radial diffusion of carbon monoxide and temperature – all indicative of enhanced mixing. This work provides quantitative data on methane-oxygen combustion which can be directly compared to numerical simulations of similar injector geometries and associated flames. This experimental approach and diagnostic technique can be extended to other flow conditions and used on a variety of coaxial injector geometries and for different hydrocarbon-based fuels which can inform injector design for liquid rocket engines.

In Chapter 3, a monolithic shear tri-coaxial injection scheme, enabled by additive manu-

facturing, was designed and fabricated to enhance propellant mixing. Mixing and combustion characteristics of this tri-coaxial design were assessed experimentally from 1–69 bar by employing the aforementioned LAT technique established in Ch. 2, in addition to OH* chemiluminescence imaging. Methane and oxygen were used as propellants. At similar pressures and oxidizer-to-fuel ratios, the tri-coaxial injector design was shown to enhance mixing and combustion progress, reducing characteristic mixing length scales and achieving improved combustion performance relative to more conventional bi-coaxial designs. Despite enhanced mixing, the tri-coaxial design exhibits more limited reduction in flame standoff distance from the injector face, suggesting that increased heat flux to the injector face can be managed. The tri-coaxial injector highlights the potential to leverage additive manufacturing to enhance performance and simplify the fabrication of liquid-propellant rocket engines.

In Chapter 4, the novel enhanced-mixing AM tri-coaxial design from Ch. 3 was experimentally tested in a single-element high-pressure combustor to characterize combustion instabilities. Here, both high-speed dynamic pressure measurements and high-speed OH* chemiluminescence videography were captured to characterize combustion instabilities during methane-oxygen hot-fire tests. Characteristic frequencies of combustion instability modes, RMS pressure amplitudes corresponding with those characteristic frequencies, and coupling between the heat release from combustion and pressure fluctuations were determined. Measurements associated with the tri-coaxial injector design were compared to two traditional shear bi-coaxial geometries with and without a recessed central oxidizer post over a range of chamber pressures from 35–69 bar. The compiled findings from this chapter indicate that the enhanced-mixing tri-coaxial injector design has a relative resistance to injection-coupled instabilities over a range of flow conditions and may enable improved combustion performance for next-generation liquid rocket engines.

In Chapter 5, a coupled computational and experimental study was conducted towards minimizing hydraulic losses in impinging liquid rocket injectors via geometric optimization enabled by additively-manufacturing. The increased surface roughness inherent to AM parts

was also investigated. Computational fluid dynamics analyses were conducted to inform injector design modifications using a canonical conventionally-manufactured impinging injector as baseline reference. Select injector designs were down-selected for additive manufacturing, followed by an experimental testing effort. Experimental injector discharge coefficients (C_{D}) were determined through a series of cold-flow testing for both the conventionally-manufactured and additively-manufactured impinging injector designs. Results indicate that additively-manufactured liquid injector orifices larger than $D \approx 0.020$" have the potential to yield hydraulic benefits (as-printed) despite high surface roughness associated with AM parts. Notably, the hydraulic benefits of geometric optimization, or flow tapering, enabled by AM, could be more fully realized after post-print polishing (honing) techniques, achieving experimental C_{D}'s ≈ 1. This work demonstrated that additive manufacturing can be leveraged to minimize impinging liquid rocket injector hydraulic losses through a combination of optimized flowpath tapering to mitigate inertial losses and post-print honing to mitigate friction losses.

In Chapter 6, the additively-manufactured low forward pressure-drop impinging injectors examined in Ch. 5 were modified with additional AM-enabled features that increased relative back-flow resistance (diodicity). Steady, single-phase CFD analyses were conducted to assess the hydraulic characteristics of fluidic diode features in a liquid bi-propellant impinging doublet-type injector configuration. A design trade study was conducted that determined an effective fluidic diode feature to be implemented within the injector elements, constrained by practical considerations for additive manufacturing. Noteworthy increases in diodicity are achieved within the constraints of producibility relative to conventional designs. A complimentary transient, multiphase CFD model was then used to evaluate propellant backflow behavior when subject to a high-pressure impulse within a downstream chamber. Results suggest that the diodicity is a relevant predictor of transient back-flow recovery performance as injector stiffness decreases.

In sum, the compiled results of this thesis demonstrate the promising potential to leverage

the flexibility of additive manufacturing to design advanced injector geometries that improve performance and reliability of liquid rocket engines.

7.1 Current and future research directions

7.1.1 Experimental investigation of the fluidic diode

A preliminary experimental study involved testing the fluidic diode analysis work covered in Ch. 6. Recall that diodicity, our backflow resistance metric, is simply defined as $C^2_{\mathrm{D,fwd}}/C^2_{\mathrm{D,rev}}$ for a given mass flow rate. Diodicity was predicted by running both forward-flow and reverse-flow steady CFD analyses which determined $C_{\mathrm{D,fwd}}$ and $C_{\mathrm{D,rev}}$, respectively. As such, three fluidic diode designs (FD1, FD2, and FD3) were additively-manufactured with the same printer, resolution, and material (ProtoLabs high-resolution stainless steel 17-4 PH) as injectors S1 and S2 from Ch. 5. Each of the three diode injectors contained one 90°-revolved fluidic diode feature placed approximately 0.030" upstream of each orifice. FD1 and FD2 contained 50-thou (0.050") diodes, whereas FD3 contained 70-thou (0.070") diodes. This length scale refers to the maximum radial dimension of the revolved diode profile, and can be seen pictured in Fig. 6.2. FD1 and FD3 were originally manufactured with 0.0155" as-printed orifices, which would later be chemically honed to final RMS orifice diameters of 0.0236" and 0.0235", respectively. On the other hand, FD2 contained 0.0230"-diameter as-printed orifices,

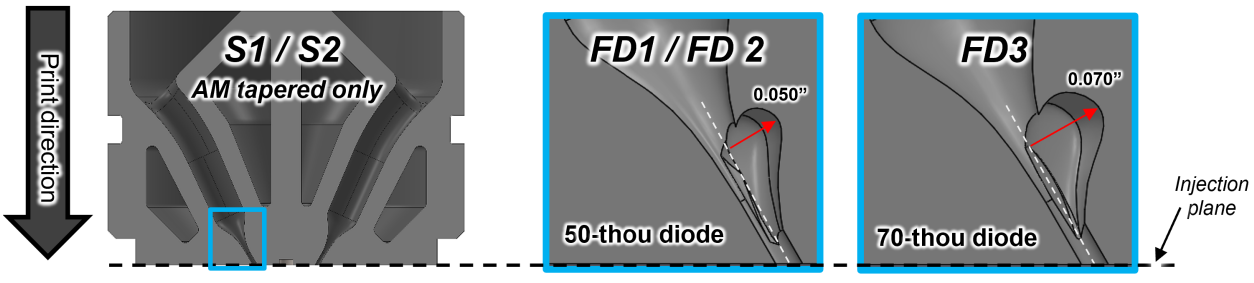

Figure 7.1: CAD cross-sections of: (*left*) AM tapered only impinging injector, (*middle*) 50-thou and (*right*) 70-thou 90°-revolved fluidic diode implemented on AM tapered flowpath.

and did not undergo any honing processes. Fig. 7.1 illustrates how the diode features were implemented on the AM tapered flowpath. Steady, smooth-wall CFD analyses predicted diodicities of 2-3 for these designs.

Similar to Ch. 5, select AM injector designs were cold-flow tested with liquid water, which includes the three diode injectors, as well as AM tapered only injectors S1 and S2. As previously seen in Fig. 5.16, the cold-flow housing assembly was capable of both forward and reverse flow measurements, thereby enabling experimental measurements of $C_{\mathrm{D,fwd}}$, $C_{\mathrm{D,rev}}$, and thus Di. Here, each injector was cold-flow tested in forward and reverse flow directions after each manufacturing process step, starting with their as-printed configurations (denoted with $.AP$). Next, each injector had approximately 0.005" of material removed from their injection surface though a sanding operation on a lathe. This improved the surface finish of each injection plane by polishing the stochastic surface features on the as-printed injection plane. Orifice diameters were measured with 0.0005"-increment pin gauges before and after sanding, with no change in diameter observed. A second iteration of cold-flow testing was conducted on the sanded injectors (denoted with $.S$) to investigate the influence of injection plane surface finish on diodicity. Lastly, injectors S1, FD1, and FD3 were chemically honed (denoted with $.CH$), and then underwent a final iteration of cold-flow testing.

Fig. 7.2 shows preliminary cold-flow diodicity results for each of the 5 injectors throughout different phases of manufacturing. Here, results are presented for a mass flow rate condition of $\dot{m} \approx 3.7$ g/s (per element). AM tapered only injectors S1.AP and S2.AP (in their as-printed state) achieved a poor Di of 1.09 and 1.13, respectively. Upon sanding their injection surface, each injector jumped roughly 20% in Di. The diodicities of the as-printed configurations of diode injectors FD1.AP, FD2.AP, and FD3.AP did not vary much, with Di only ranging between 1.15 and 1.33 despite containing different diode features and different orifice sizes. This was a small improvement compared to the AM tapered only injectors and approximately 60% lower than CFD-predictions. A sanded injection plane similarly improved the net diodicity of these three diode injectors, achieving diodicities of 1.41 to 1.50, an improvement

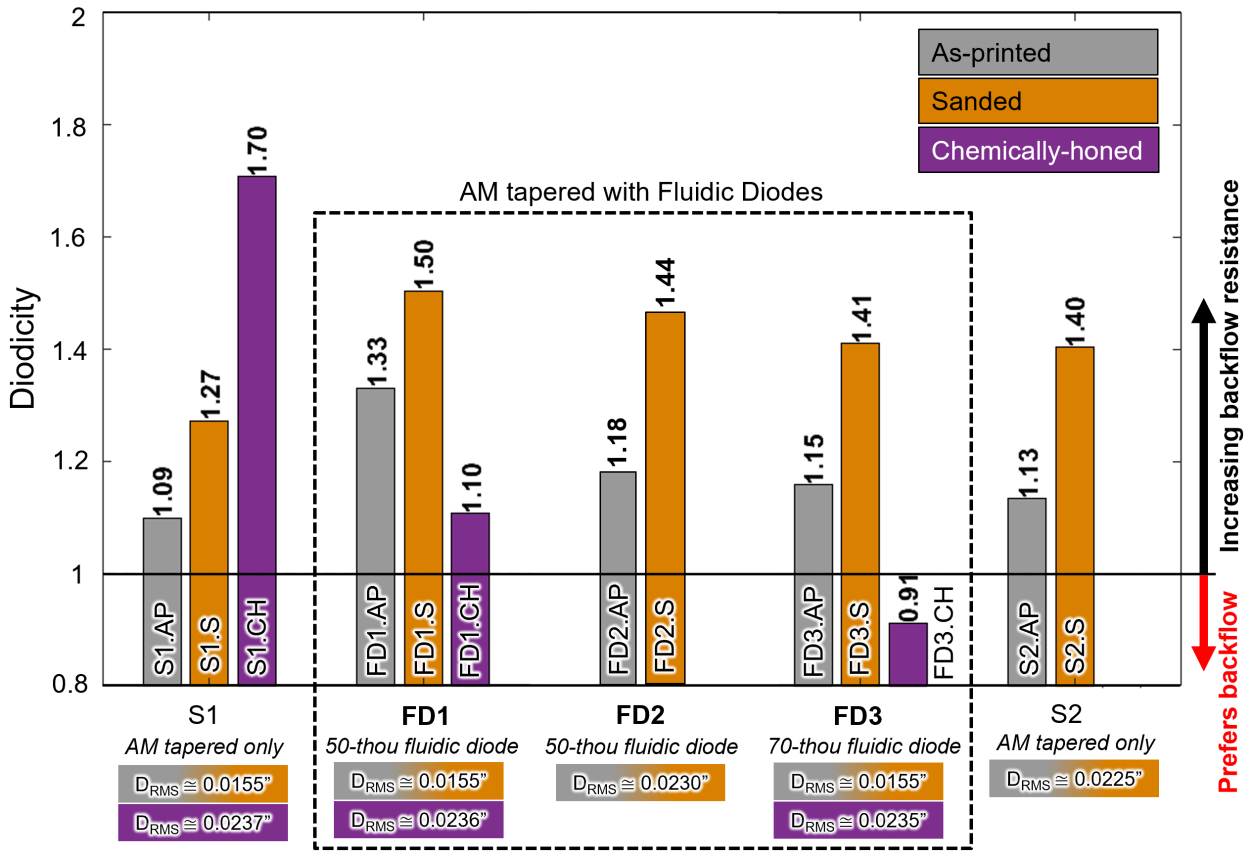

Figure 7.2: Preliminary diodicity results from cold-flow testing various AM tapered only and AM tapered with fluidic diodes. Results pertain to $\dot{m} \approx 3.7$ g/s (per element).

over injectors S1.S and S2.S but still ∼50% lower than CFD predictions. Lower experimental diodicity values are in part due to $C_{\mathrm{D,fwd}}$ being over-predicted since the additional losses from increased surface roughness were unaccounted for in the CFD models.

Notably, after injector S1 was chemically honed, thereby significantly improving its $C_{\mathrm{D,fwd}}$, a diodicity of 1.70 was achieved by S1.CH despite not containing a fluidic diode. Such was not the case for the honed fluidic diode injectors. Experimental diodicities for injectors FD1.CH and FD3.CH were significantly reduced to $Di = 1.10$ and 0.91, respectively. It was discovered that the honed diode injectors produced non-cylindrical liquid jets and contained severely non-circular orifice exit profiles. Fig. 7.3 shows comparison images of orifice exit profiles and the associated cold-flow jet behavior of two AM tapered reference injectors (no diode) and the

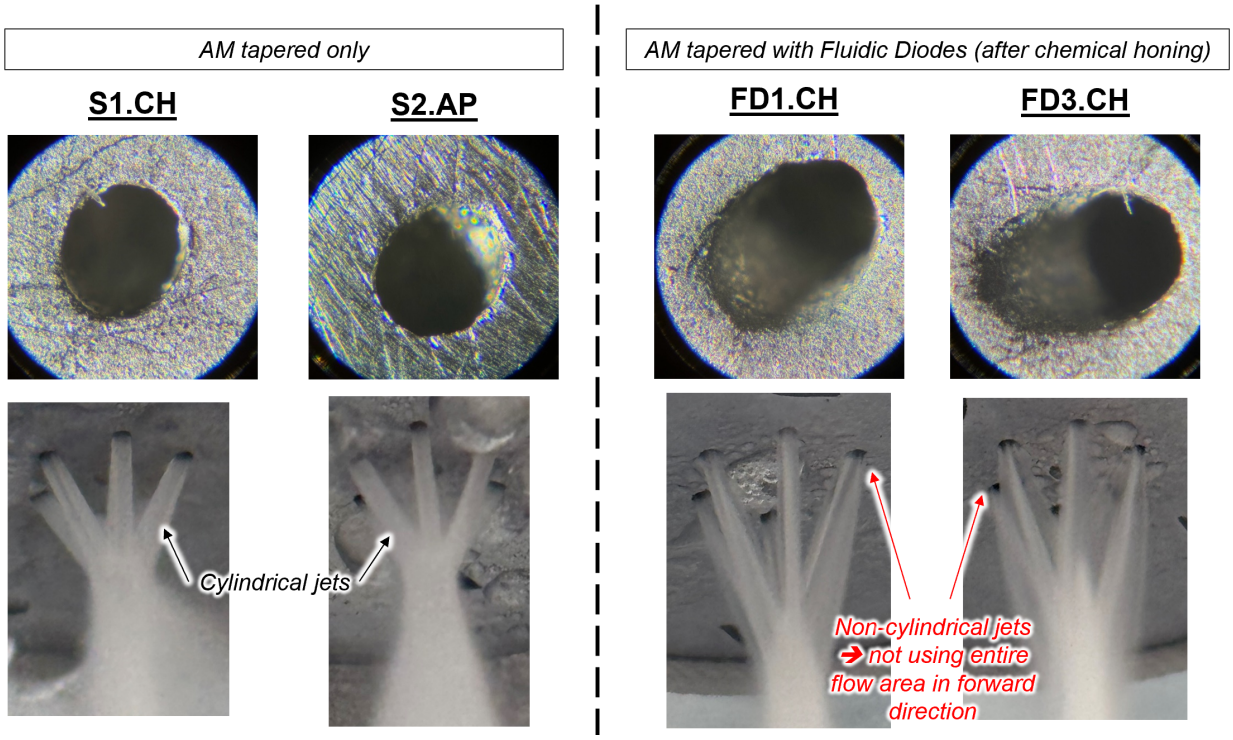

Figure 7.3: Orifice exit profiles and their associated cold-flow jet behaviors shown for two AM tapered only injectors (*left*), and the two honed fluidic diode injectors (*right*).

two honed diode injectors. The honed (S1.CH) and as-printed (S2.AP) flowpaths of the 'AM tapered only' injectors demonstrate nominal jet behavior with cylindrical jets and a common impingement location. In contrast, the presence of the diode feature appears to have caused non-uniform material removal throughout the orifice geometry. This ultimately reduced the wetted flow area in the forward direction (reducing $C_{\mathrm{D,fwd}}$), while also creating a large orifice entrance on the injection plane which increased $C_{\mathrm{D,rev}}$. A wire-EDM cross-section of injector FD3.CH is shown in Fig. 7.4 to help visualize the diode injectors' honed orifice geometry. While orifice areas were likely underestimated as a result of the non-circularity of the orifices, diodicity is independent of flow area and thus diodicity trends are still expected to be valid.

In this limited experimental study, an additively-manufactured fluidic diode injector design achieved a maximum diodicity of approximately 1.50 – roughly 50% lower than smooth-wall CFD predictions. Limiting issues included the AM surface roughness reducing $C_{\mathrm{D,fwd}}$, and

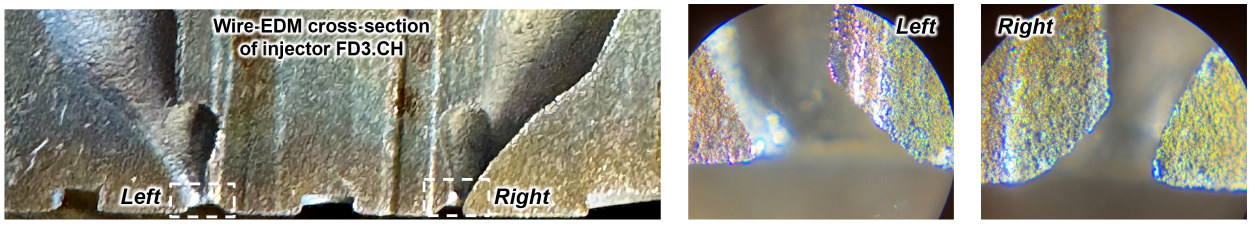

Figure 7.4: Wire-EDM cross-section of honed fluidic diode injector FD3.CH with magnified images of the orifice geometries shown.

a honing operation (intended to address the former issue) that adversely distorted orifice geometry and flow characteristics. The purpose of a fluidic diode positioned on an impinging injector flowpath is to induce additional inertial viscous losses in the reverse flow direction, while having a negligible effect on forward flow. In theory, if injector geometries were manufactured more closely to the ideal geometries simulated in CFD, higher experimental diodicities should be possible. Future computational and experimental design studies may be conducted to optimize the diode feature for additive manufacturing. Alternative methods of improving orifice geometry surface finish without negatively influencing forward flow characteristics may also be investigated. Notably, the honed "AM tapered only" injector S1.CH achieved an experimental diodicity of 1.70 – a 13% improvement over the best diode injector. This demonstrates the potential for impinging injectors with AM-enabled flowpath tapering to achieve high backflow resistance without the added design or manufacturing complexity associated with fluidic diode features. Additionally, the transient backflow recovery behavior of AM tapered flowpaths with and without fluidic diode features should be experimentally evaluated to provide more valuable insight into practical liquid rocket injector operation with respect to chamber instabilities.

7.1.2 Advanced coaxial injection enabled by additive manufacturing

Additional coaxial injector design concepts with attributes that are known to enhance mixing, but are complicated (or infeasible) to generate via traditional manufacturing present additional

opportunities for future research. Fig. 7.5 shows a comparison of the traditional bi-coaxial injection schemes on the left, with some preliminary design examples of alternative shear coaxial schemes on the right enabled by additive manufactured, which includes the tri-coaxial design. Pictured here, the *petaled* coaxial scheme represents an example of AM-enabled design features that increase inter-propellant contact surface area (as demonstrated by the tri-coaxial). For a given pair of total propellant outlet areas (fuel and oxidizer), petaled injector outlet profiles aim to improve mixing by increasing the total contact surface area (which scales directly with the shared perimeter between adjacent coaxial jets) while maintaining the same amount of cross-sectional flow area on an injector face. Additionally, *chevron* nozzles include triangular sawtooth-like serrations on the outlet edge of a coaxial nozzle as a modern means of reducing turbofan engine noise by inducing vorticity in the shear layer and significantly increasing rapid near-field mixing [4, 19]. Similar mixing enhancements are expected to be

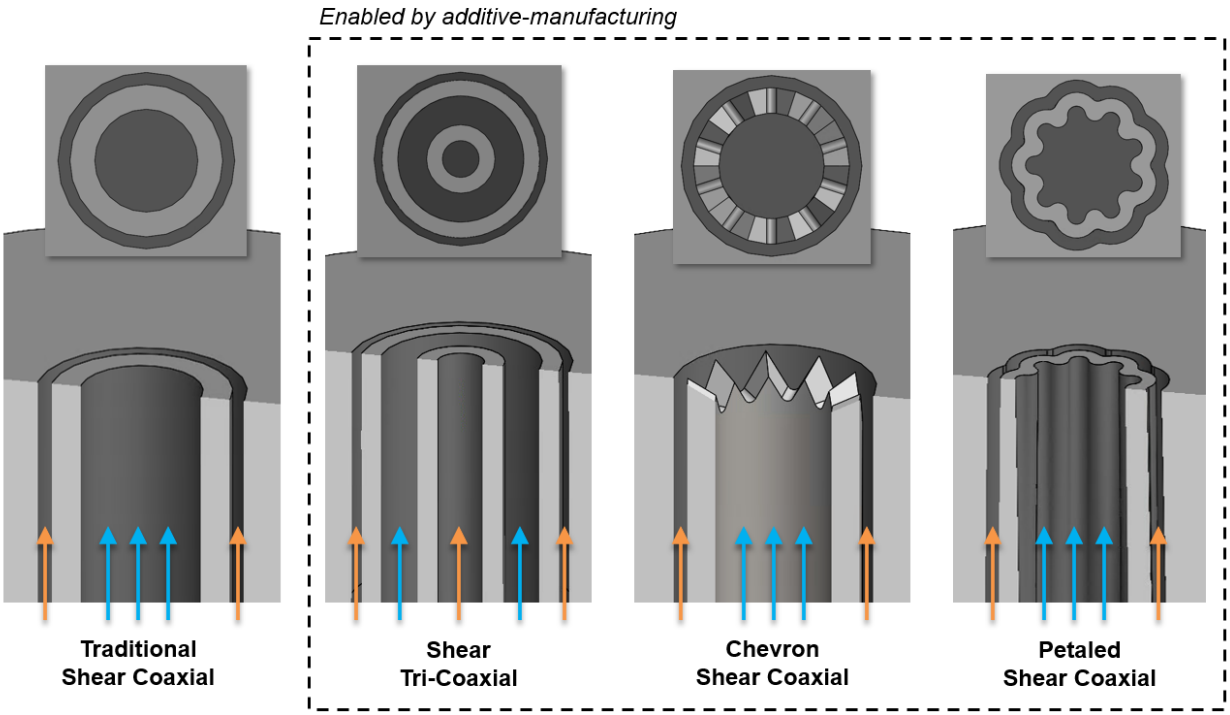

Figure 7.5: A comparison of a traditional shear bi-coaxial injector and various novel high contact surface area and chevron shear coaxial injection schemes enabled by additive-manufacturing.

observed on an additively-manufactured shear coaxial oxidizer post outlet with a chevron-like pattern (seen pictured in Fig. 7.5). AM coaxial injectors with combinations of these design features implemented may compound the enhanced-mixing effects.

7.1.3 Additional experimental evaluations of the tri-coaxial injector

Coaxial injection schemes are expected to play a role in next-generation methane-oxygen launch vehicles that use staged combustion cycles. The work presented in Chapters 3 and 4 demonstrated the performance-enhancing potential of the AM tri-coaxial injector in regards to propellant mixing and combustion stability, which may be utilized in such engines. While these findings are promising, the associated experiments were only conducted with a singular tri-coaxial injection element in a scaled-down single-element combustor. The relative positioning of injection elements on a multi-element injector plate largely influences inter-element mixing, injected mass-flux and heat release distributions and associated heat flux on chamber walls. To understand how the tri-coaxial injection scheme would perform in these larger-scale engines, multi-element injector studies with respect to combustion performance and stability characteristics are required.

Chapter 4 provided valuable insight on linear (spontaneous), longitudinal combustion instabilities for the tri-coaxial for discrete flow conditions and chamber pressures. In addition to multi-element studies, combustion stability behaviors of the tri-coaxial injector must be further characterized. The work on linear instabilities can be expanded upon in several ways. Longer duration tests may be conducted with a continuous ramp-up and/or ramp-down of mass flow rate (and chamber pressure) to simulate start-up and shut-down transients of practical LRE operation and throttling. The tri-coaxial injector's response to transverse instability modes, which typically become more of a concern in combustors as chamber diameter increases, should also be investigated. The dynamic stability of the tri-coaxial injector must also be evaluated, which describes the recovery behavior of an engine system

from common non-linear (induced, or triggered) combustion instabilities. An in-chamber explosive or inert gas-pulse can serve as options for artificial instability triggers during combustor operation.

7.1.4 AM injector designs for rotating detonation rocket engines

A rotating detonation rocket engine (RDRE) is a unique rocket engine architecture theorized to generate higher specific impulse compared to conventional constant pressure liquid rocket engines. RDREs operate by sustaining one or more circumferentially-propagating detonation waves within an annular combustor yielding a pressure gain during combustion [82]. At the time of this writing, RDREs have not yet been demonstrated to outperform their constant pressure counterparts. This is commonly attributed to be in part a result of injection-related issues such as propellant backflow and poor mixing [131]. A comprehensive review on the design optimization of AM RDRE injectors was completed by Teasley et al at NASA MSFC and can be found in Ref. [131]. A common practice to circumvent the issue of backflow consists in increasing the injector stiffness to values that often exceed 100% [6, 14, 97, 117, 149], which as previously mentioned, has a negative impact on overall vehicle performance. As such, RDRE injectors have a particularly high-potential for advancement via high diodicity injector design enabled by additively-manufacturing, which may finally enable the promising performance enhancements of RDREs to be realized.

REFERENCES

[1] Hareth Maher Abd, Omar Rafae Alomar, and Ibrahim Atiya Mohamed. Effects of varying orifice diameter and reynolds number on discharge coefficient and wall pressure. *Flow Measurement and Instrumentation*, 65:219–226, 2019.

[2] Thomas Adams, Christopher Grant, and Heather Watson. A simple algorithm to relate measured surface roughness to equivalent sand-grain roughness. *International Journal of Mechanical Engineering and Mechatronics*, 1:66–71, 2012.

[3] J Ahn, K Ahn, and H Y Lim. Injection Properties According to the Inner Shape of Metal Additive Layer Manufactured Coaxial Injectors. *Journal of Applied Fluid Mechanics*, 15(4), 2022.

[4] K. Ahuja and W. Brown. *Shear flow control by mechanical tabs*. 1989.

[5] S. Alexander Schumaker and James F. Driscoll. Mixing properties of coaxial jets with large velocity ratios and large inverse density ratios. *Physics of Fluids*, 24(5), 2012.

[6] Wesly S. Anderson and Stephen D. Heister. Response of a liquid jet in a multiple detonation driven crossflow. *AIAA Aerospace Sciences Meeting, 2018*, (210059), 2018.

[7] David Appleyard. Powering up on powder technology. *Metal Powder Report*, 70(6):285–289, 2015.

[8] ArianeGroup. 3D Printing for Ariane 6 Propulsion Module. *Electro Optical Systems: Success Story Aerospace*, 2017.

[9] Wolfgang Armbruster, Justin Hardi, and Michael Oschwald. Impact of shear-coaxial injector hydrodynamics on high-frequency combustion instabilities in a representative cryogenic rocket engine. *International Journal of Spray and Combustion Dynamics*, 14:118–130, 3 2022.

[10] F. A. Bendana, I. C. Sanders, N. G. Stacy, and R. M. Spearrin. Localized characteristic velocity (c*) for rocket combustion analysis based on gas temperature and composition via laser absorption spectroscopy. *Measurement Science and Technology*, 32(12), 2021.

[11] Fabio A. Bendana, Isabelle C. Sanders, Josue J. Castillo, China G. Hagström, Daniel I. Pineda, and R. Mitchell Spearrin. In-situ thermochemical analysis of hybrid rocket fuel oxidation via laser absorption tomography of CO, CO2, and H2O. *Experiments in Fluids*, 61(9):190, sep 2020.

[12] John W. Bennewitz, S. Alexander Schumaker, Christopher F. Lietz, and Alan L. Kastengren. Scaling of oxygen-methane reacting coaxial jets using x-ray fluorescence to measure mixture fraction. *Proceedings of the Combustion Institute*, 38(4):6365–6374, 2021.

[13] J. Berque, M. Sion, and J. L. Thomas. Tricoaxial Injector Technology Development. *35th Joint Propulsion Conference and Exhibit*, (c), 1999.

[14] Blaine R. Bigler, Jason R. Burr, John W. Bennewitz, Stephen Danczyk, and William A. Hargus. Rotating Detonation Rocket Engine Scaling using Variable Annular Width Geometries. In *AIAA Propulsion and Energy 2021 ForumForum*, 2021.

[15] Byron Blakey-Milner, Paul Gradl, Glen Snedden, Michael Brooks, Jean Pitot, Elena Lopez, Martin Leary, Filippo Berto, and Anton du Plessis. Metal additive manufacturing in aerospace: A review. *Materials and Design*, 209:110008, 2021.

[16] Christopher D. Bolszo, Cory A. Adams, Ethan A. Barbour, James H. Morehart, and Andrew C. Cortopassi. Development of a pressurized, single-element rocket injector experiment. *2018 Joint Propulsion Conference*, pages 1–10, 2018.

[17] Hassan Boualia, Ammar Hidouri, Mouldi Chrigui, and Jean Charles Sautet. Experimental Investigation of Central Jet Displacements on the Turbulence and Gas Dynamics of a Coaxial Burner. *Applied Thermal Engineering*, 116:303–315, 2017.

[18] Guobiao Cai, Mao Li, Yushan Gao, and Ping Jin. Simulation and Experiment Research for a Hydrogen-Rich/Oxygen-Rich Shear Tricoaxial Gas-Gas Injector. *AIAA/ASME/SAE/ASEE 46th Joint Propulsion Conference and Exhibit*, (July), 2010.

[19] Bryan Callender, Ephraim Gutmark, and Steve Martens. Near-field investigation of chevron nozzle mechanisms. *AIAA journal*, 46(1):36–45, 2008.

[20] Matthew J Casiano. *Extensions to the Time Lag Models for Practical Application to Rocket Engine Stability Design*. Ph.D. thesis, The Pennsylvania State University, 2010.

[21] H. F. Celebi, D. Lim, K. J. Dille, and S. D. Heister. Response of Angled and Tapered Liquid Injectors to Passing Detonation Fronts at High Operating Pressures. *Shock Waves*, 2021.

[22] H. F. Celebi, D. Lim, K. J. Dille, and S.D. Heister. Response of angled and tapered liquid injectors to passing detonation fronts at high operating pressures. *Shock Waves*, 2021.

[23] Bruce Chehroudi. Recent experimental efforts on high-pressure supercritical injection for liquid rockets and their implications. *International Journal of Aerospace Engineering*, 2012.

[24] Xiaodong CHEN and Vigor YANG. Recent advances in physical understanding and quantitative prediction of impinging-jet dynamics and atomization. *Chinese Journal of Aeronautics*, 32(1):45–57, 2019.

[25] W-S Chia. *A Study of Organ-Pipe Combustion Oscillations of Premixed Gases in a Combustor with Variable Length at Atmospheric Pressure*. Ph.D. thesis, California Institute of Tech., 1969.

[26] J. N. Chopinet, F. Lassoudière, C. Fiorentino, P. Alliot, S. Guedron, Ph Supié, and C. Bonhomme. Results of the Vulcain X Technological Demonstration. *62nd International Astronautical Congress 2011, IAC 2011*, 8(August):6289–6298, 2011.

[27] Sohini Chowdhury, N. Yadaiah, Chander Prakash, Seeram Ramakrishna, Saurav Dixit, Lovi Raj Gupta, and Dharam Buddhi. Laser powder bed fusion: a state-of-the-art review of the technology, materials, properties defects, and numerical modelling. *Journal of Materials Research and Technology*, 20:2109–2172, 2022.

[28] Boa-Teh Chu. Stability of systems containing a heat source - the rayleigh criterion. Technical Report NACA RM 56D27, National Advisory Committee for Aeronautics, 1956.

[29] L. Crocco. Aspects of combustion stability in liquid propellant rocket motors part i: Fundamentals. low frequency instability with monopropellants. *Journal of the American Rocket Society*, 21:163–178, 11 1951.

[30] L. Crocco. Aspects of combustion stability in liquid propellant rocket motors part ii: Low frequency instability with bipropellants. high frequency instability. *Journal of the American Rocket Society*, 22 (No. 1):7–16, 1 1952.

[31] Luigi Crocco and Sin Cheng. High-frequency combustion instability in rocket motor with concentrated combustion. *Journal of the American Rocket Society*, 23:301–313, 9 1953.

[32] Luigi Crocco and Sin Cheng. High frequency combustion instability in rockets with distributed combustion. *Symposium (International) on Combustion*, 4(1):865–880, 1953. Fourth Symposium (International) on Combustion.

[33] Luigi Crocco and Sin Cheng. *Theory of Combustion Instability in Liquid Propellant Rocket Motors*. Butterworths Scientific Publications, 1956.

[34] Werner J.A. Dahm. Effects of heat release on turbulent shear flows. Part 2. Turbulent mixing layers and the equivalence principle. *Journal of Fluid Mechanics*, 540:1–19, 2005.

[35] Cameron J Dasch. One-dimensional tomography: a comparison of Abel, onion-peeling, and filtered backprojection methods. *Applied Optics*, 31(8):1146, 1992.

[36] Gabriel Demeneghi, Baxter Barnes, Paul Gradl, Jason R. Mayeur, and Kavan Hazeli. Size effects on microstructure and mechanical properties of additively manufactured copper–chromium–niobium alloy. *Materials Science and Engineering A*, 820:141511, 2021.

[37] Hossein Eskandari Sabzi. Powder bed fusion additive layer manufacturing of titanium alloys. *Materials Science and Technology*, 35(8):875–890, 2019.

[38] A Fournet, J M Lonchard, J L Thomas, and Fort Lauderdale. Technological demonstration for Low Cost Gas Generator. *AIAA 2004-4006 40th AIAA Joint Propulsion Conference and Exhibit*, (July):1–11, 2004.

[39] D. R. Friant, H. J. Kircher, and R. Youngquist. Discharge coefficients for common orifice forms. Technical Report DS-140, Reaction Motors Inc., 1954.

[40] Clifford E. Frieler and Grétar Tryggvason. Vortex structure and dynamics in the near field of a coaxial jet. *Journal of Fluid Mechanics*, 241(32):371–402, 1992.

[41] Himani Garg, Lei Wang, Guillaume Sahut, and Christer Fureby. Large eddy simulations of fully developed turbulent flows over additively manufactured rough surfaces. *Physics of Fluids*, 35(4), 2023.

[42] Philip M Gerhart, Andrew L Gerhart, and John I Hochstein. *Munson, Young and Okiishi's Fundamentals of Fluid Mechanics*. John Wiley & Sons, 2016.

[43] G. S. Gill and W. H. Nurick. Liquid Rocket Engine Injectors. Technical Report NASA-SP-8089, National Aeronautics and Space Administration, 1976.

[44] Nicholas Gloria, Wade Bassett, Ian Vorbach, James Kolano, Akshay Gupta, Alexander Kaplan, Ian Rall, Nicholas Folz, and Shane Dirks. Performance of a Small-Orifice Rocket Injector Utilizing Additive Manufacturing. *AIAA Propulsion and Energy Forum and Exposition, 2019*, (August):1–23, 2019.

[45] Christopher S. Goldenstein, Victor A. Miller, R. Mitchell Spearrin, and Christopher L. Strand. SpectraPlot.com: Integrated spectroscopic modeling of atomic and molecular gases. *Journal of Quantitative Spectroscopy and Radiative Transfer*, 200:249–257, 2017.

[46] I.E. Gordon, L.S. Rothman, C. Hill, R.V. Kochanov, Y. Tan, P.F. Bernath, M. Birk, V. Boudon, A. Campargue, K.V. Chance, B.J. Drouin, J.-M. Flaud, R.R. Gamache, J.T. Hodges, D. Jacquemart, V.I. Perevalov, A. Perrin, K.P. Shine, M.-A.H. Smith, J. Tennyson, G.C. Toon, H. Tran, V.G. Tyuterev, A. Barbe, A.G. Császár, V.M. Devi, T. Furtenbacher, J.J. Harrison, J.-M. Hartmann, A. Jolly, T.J. Johnson, T. Karman, I. Kleiner, A.A. Kyuberis, J. Loos, O.M. Lyulin, S.T. Massie, S.N. Mikhailenko, N. Moazzen-Ahmadi, H.S.P. Müller, O.V. Naumenko, A.V. Nikitin, O.L. Polyansky, M. Rey, M. Rotger, S.W. Sharpe, K. Sung, E. Starikova, S.A. Tashkun, J. Vander Auwera, G. Wagner, J. Wilzewski, P. Wcisło, S. Yu, and E.J. Zak. The HITRAN2016 molecular spectroscopic database. *Journal of Quantitative Spectroscopy and Radiative Transfer*, 203:3–69, dec 2017.

[47] S Gordon and B. J. Mcbride. NASA CEARUN rev4, 2020. https://cearun.grc.nasa.gov/.

[48] Paul R Gradl, Sandy E Greene, Christopher Protz, Brad Bullard, and James Buzzell. Additive Manufacturing of Liquid Rocket Engine Combustion Devices: A Summary of Process Developments and Hot-Fire Testing Results. In *2018 Joint Propulsion Conference*, AIAA Propulsion and Energy Forum, Reston, Virginia, jul 2018.

[49] Paul R. Gradl, Thomas Teasley, Chris Protz, Colton Katsarelis, and Po Chen. Process Development and Hot-fire Testing of Additively Manufactured NASA HR-1 for Liquid Rocket Engine Applications. *AIAA Propulsion and Energy Forum, 2021*, pages 1–23, 2021.

[50] Skjalg E Haaland. *Simple and explicit formulas for the friction factor in turbulent pipe flow*. The American Society of Mechanical Engineers (ASME), 1983.

[51] R.K. Hanson, R.M. Spearrin, and C.S. Goldenstein. *Spectroscopy and Optical Diagnostics for Gases*. Springer International Publishing, Switzerland, 2016.

[52] Dirk Herzog, Vanessa Seyda, Eric Wycisk, and Claus Emmelmann. Acta Materialia Additive manufacturing of metals. *Acta Materialia*, 117:371–392, 2016.

[53] Philip G Hill and Carl R Peterson. *Mechanics and Thermodynamics of Propulsion*. Addison-Wesley Publishing Co, Reading, MA, 2nd edition, 1992.

[54] David H. Huang and Dieter K. Huzel. Design of Thrust Chambers and Other Combustion Devices. In *Modern Engineering for Design of Liquid-Propellant Rocket Engines*, Progress in Astronautics and Aeronautics, pages 67–134. American Institute of Aeronautics and Astronautics, 1992.

[55] James R. Hulka and Gregg W. Jones. Performance and stability analyses of rocket thrust chambers with oxygen/methane propellants. In *46th AIAA/ASME/SAE/ASEE Joint Propulsion Conference*, 2010.

[56] J. J. Hutt and M. Rocker. High-frequency injection-coupled combustion instability. In V. Yang and W. E. Anderson, editors, *Liquid Rocket Engine Combustion Instability*, volume 169, chapter 12, pages 345–355. AIAA Progress in Astronautics and Aeronautics, 1995.

[57] Dieter K Huzel and David H Huang. Design of liquid propellant rocket engines. Technical Report No. NASA-SP-125, National Aeronautics and Space Administration, 1967.

[58] Dieter K. Huzel and David H. Huang. *Modern Engineering for Design of Liquid-Propellant Rocket Engines*. American Institute of Aeronautics and Astronautics, 1992.

[59] R J Jensen and H C Dodson. Lox/hydrocarbon combustion instability investigation. Technical report, NASA Lewis Research Center, 1989.

[60] Ping Jin, Mao Li, and Guobiao Cai. Experimental study of hydrogen-rich/oxygen-rich gas-gas injectors. *Chinese Journal of Aeronautics*, 26(5):1164–1172, 2013.

[61] Matthew P. Juniper and Sebastien M. Candel. The stability of ducted compound flows and consequences for the geometry of coaxial injectors. *Journal of Fluid Mechanics*, 482:257–269, 2003.

[62] Cheolwoong Kang, Shinwoo Lee, and Kyubok Ahn. Combustion characteristics of shear coaxial injectors with different recess lengths under wide operating conditions. *International Journal of Aeronautical and Space Sciences*, 2024.

[63] Alex R. Keller, Joel Otomize, Anil P. Nair, Nicolas Q. Minesi, and R. Mitchell Spearrin. *High-diodicity impinging injector design for rocket propulsion enabled by additive manufacturing*. AIAA SCITECH 2022 Forum. AIAA Paper 2022-1265, 2022.

[64] Alex R. Keller, Vincent C. Phong, Fabio A. Bendana, and R. Mitchell Spearrin. Additively-manufactured shear tri-coaxial rocket injector mixing and combustion characteristics. *Aerospace Science and Technology*, 2024.

[65] Alex R. Keller, R. Mitchell Spearrin, and Fabio A. Bendana. Shear coaxial methane–oxygen injector mixing and combustion examined by laser absorption tomography. *Journal of Propulsion and Power*, 40(5):747–758, 2024.

[66] Alex R. Keller, Raymond M. Spearrin, Fabio A. Bendana, Dean Kaialau, Armando Perezselsky, and Andrew Cortopassi. *Coaxial rocket injector mixing and combustion via mid-infrared laser absorption tomography.* AIAA SCITECH 2024 Forum. AIAA Paper 2024-2420, 2024.

[67] D. Kendrick, G. Herding, P. Scouflaire, C. Rolon, and S. Candel. Effects of a recess on cryogenic flame stabilization. *Combustion and Flame*, 118(3):327–339, 1999.

[68] DN Kiaoulias, TA Travis, Jeffrey David Moore, and Grant Alexander Risha. Evaluation of orifice inlet geometries on single liquid injectors through cold-flow experiments. *Experimental Thermal and Fluid Science*, 103:78–88, 2019.

[69] Helene Knoll, Sörn Ocylok, Andreas Weisheit, Hauke Springer, Eric Jägle, and Dierk Raabe. Combinatorial Alloy Design by Laser Additive Manufacturing. *Steel Research International*, 88(8):1–11, 2017.

[70] N. Lamarque and T. Poinsot. Boundary conditions for acoustic eigenmode computations in gas turbine combustion chambers. *AIAA Journal*, 46:2282–2292, 2008.

[71] J. C. Lasheras, E. Villermaux, and E. J. Hopfinger. Break-up and atomization of a round water jet by a high-speed annular air jet. *Journal of Fluid Mechanics*, 357:351–379, 1998.

[72] Gaëtan Le Forester, Patrick Danous, Gilles Dantu, Axel Preuss, Frank Grauer, and Richard Strunz. First Firing Test Campaign of European Staged-combustion Demonstration. *45th AIAA/ASME/SAE/ASEE Joint Propulsion Conference and Exhibit*, pages 1–11, August 2009.

[73] Martin Leary, Mahyar Khorasani, Avik Sarker, Johnathan Tran, Kate Fox, David Downing, and Anton Du Plessis. *Fundamentals of Laser Powder Bed Fusion of Metals. (Ch.7 - Surface roughness).* Elsevier Inc., 2021.

[74] Daniel D. Lee, Fabio A. Bendana, and R. Mitchell Spearrin. Laser Absorption Spectroscopy of Carbon Monoxide near 4.97 μm for Temperature and Species Measurements in Hydrocarbon-Fueled Rockets. In *2018 AIAA Aerospace Sciences Meeting*, number 210059. American Institute of Aeronautics and Astronautics, 2018.

[75] Inchul Lee, Min Son, and Jaye Koo. Atomization and Combustion Characteristics of Ethanol/Nitrous Oxide at Various Momentum Flux Ratios. *Energy and Fuels*, 28(4):2770–2779, 2014.

[76] Aaron Lemcherfi, Rohan Gejji, Tristan Fuller, Ryan Strelau, William E. Anderson, and Carson D. Slabaugh. Investigation of combustion instabilities in a full flow staged combustion model rocket combustor. In *AIAA Propulsion and Energy Forum and Exposition, 2019*. American Institute of Aeronautics and Astronautics Inc, AIAA, 2019.

[77] Xinhai Li, Jian Guo, Bing Shen, and Peijie Zhang. Sensitivity analysis of injection mass flow to the inlet orifice radius of a gdi injector nozzle. *Processes*, 12(8):1740, 2024.

[78] Andrzej Lichtarowicz, Robert K Duggins, and Eric Markland. Discharge coefficients for incompressible non-cavitating flow through long orifices. *Journal of mechanical engineering science*, 7(2):210–219, 1965.

[79] Dasheng Lim and Stephen D. Heister. Transient response of a liquid injector to a transverse detonation wave at elevated initial pressure. *AIAA Aerospace Sciences Meeting, 2018*, (210059), 2018.

[80] Kevin William Linfield. *A study of the discharge coefficient of jets from angled slots and conical orifices*. Ph.D. thesis, University of Toronto, 2000.

[81] Yao Liu, Jianguo Tan, Minggang Wan, Lang Zhang, and Xiao Yao. Quantitative Measurement of OH and CH Chemiluminescence in Jet Diffusion Flames. *ACS Omega*, 5(26):15922–15930, 2020.

[82] Frank K. Lu and Eric M. Braun. Rotating Detonation Wave Propulsion: Experimental Challenges, Modeling, and Engine Concepts. *Journal of Propulsion and Power*, 30(5):1125–1142, 2014.

[83] Johannes Lux and Oskar Haidn. Effect of recess in high-pressure liquid oxygen/methane coaxial injection and combustion. *Journal of Propulsion and Power*, 25(1):24–32, 2009.

[84] Diego Manfredi and Róbert Bidulskỳ. Laser powder bed fusion of aluminum alloys. *Acta Metallurgica Slovaca*, 23(3):276–282, 2017.

[85] W. Mayer, A. Schik, M. Schäffler, and H. Tamura. Injection and mixing processes in high-pressure liquid oxygen/gaseous hydrogen rocket combustors. *Journal of Propulsion and Power*, 16:823–828, 2000.

[86] Lorenzo Mazzei, Riccardo Da Soghe, and Cosimo Bianchini. Cfd modelling strategies for the simulation of roughness effects on friction and heat transfer in additive manufactured components. *Turbo Expo: Power for Land, Sea, and Air*, 7C: Heat Transfer, 2021.

[87] F. R. Menter. Two-equation eddy-viscosity turbulence models for engineering applications. *AIAA Journal*, 32(8):1598–1605, 1994.

[88] Kevin Miller, James Sisco, Nicholas Nugent, and William Anderson. Combustion instability with a single-element swirl injector. *Journal of Propulsion and Power*, 23:1102–1112, 2007.

[89] Lewis F Moody. Friction factors for pipe flow. *Transactions of the American Society of mechanical engineers*, 66(8):671–678, 1944.

[90] C Joe Morgan and Daniel E Sokolowski. Longitudinal instability limits with a variable length hydrogen-oxygen combustor. Technical Report NASA-TN-D-6328, National Aeronautics and Space Administration, 1971.

[91] David Morrow. *Minimizing hydraulic losses in additively-manufactured swirl coaxial rocket injectors via analysis-driven design methods*. Master's thesis. University of California, Los Angeles, 2020.

[92] David Morrow, Anil Nair, and Raymond M. Spearrin. Minimizing hydraulic losses in additively manufactured swirl coaxial injectors. In *AIAA Propulsion and Energy 2019 Forum*, Indianapolis, Indiana, 2019. American Institute of Aeronautics and Astronautics.

[93] David S. Morrow, Anil P. Nair, and Raymond Mitchell Spearrin. Minimizing hydraulic losses in additively manufactured swirl coaxial injectors. *AIAA Propulsion and Energy Forum and Exposition, 2019*, (August):1–14, 2019.

[94] Mohammad Hossein Mosallanejad, Behzad Niroumand, Alberta Aversa, and Abdollah Saboori. In-situ alloying in laser-based additive manufacturing processes: A critical review. *Journal of Alloys and Compounds*, 872:159567, 2021.

[95] Ilja Muller, Markus Kuhn, Ivaylo Petkov, Sebastian Bletsch, Koen Huybrechts, and P Van Cauwenbergh. 3D-Printed Coaxial Injector for a LOX/Kerosene Rocket Engine. *Space Propulsion 2018*, 2018.

[96] Anil P. Nair, Alex R. Keller, David S. Morrow, Alexander B. Lima, R. Mitchell Spearrin, and Daniel I. Pineda. Hypergolic Continuous Detonation with Space-Storable Propellants and Additively Manufactured Injector Design. *Journal of Spacecraft and Rockets*, 59(4):1332–1341, 2022.

[97] Anil P. Nair, David Morrow, Alex R. Keller, Alexander Lima, Daniel I. Pineda, and R. Mitchell Spearrin. Rotating Detonation of Hypergolic Space-Storable Rocket Propellants with Additively-Manufactured Injector Design. In *AIAA Propulsion and Energy 2021 Forum*, Reston, Virginia, 2021. American Institute of Aeronautics and Astronautics.

[98] Joel C. Najmon, Sajjad Raeisi, and Andres Tovar. Ch. 2 - review of additive manufacturing technologies and applications in the aerospace industry. In Francis Froes and Rodney Boyer, editors, *Additive Manufacturing for the Aerospace Industry*, pages 7–31. Elsevier, 2019.

[99] Todd Neill, Donald Judd, Eric Veith, and Donald Rousar. Practical uses of liquid methane in rocket engine applications. *Acta Astronautica*, 65(5-6):696–705, 2009.

[100] Tesla Nikola. Valvular conduit, February 3 1920. US Patent 1,329,559.

[101] Yoshio Nunome, Hiroshi Tamura, Takuo Onodera, Hiroshi Sakamoto, Akinaga Kumakawa, and Takao Inamura. Effect of liquid disintegration on flow instability in a recessed region of a shear coaxial injector. *45th AIAA/ASME/SAE/ASEE Joint Propulsion Conference and Exhibit*, (August):1–10, 2009.

[102] V. C. Patel. Perspective: Flow at high reynolds number and over rough surfaces—achilles heel of cfd. *Journal of Fluids Engineering*, 120(3):434–444, 09 1998.

[103] James T. Peace, Dibesh D. Joshi, and Frank K. Lu. Experimental study of high-frequency fluidic valve injectors for detonation engine applications. *52nd Aerospace Sciences Meeting*, (March 2015):1–8, 2014.

[104] Steven D. Peery and Randy C. Parsley. Merits of full flow vs. conventional staged combustion cycles for reusable launch vehicle propulsion. In *AIP Conference Proceedings*, pages 605–610. AIP Publishing, 1996.

[105] Daniel I. Pineda, Laurel Paxton, Nikolaos Perakis, Chuyu Wei, Steven Luna, Hiba Kahouli, Matthias Ihme, Fokion N. Egolfopoulos, and R. Mitchell Spearrin. Carbon oxidation in turbulent premixed jet flames: A comparative experimental and numerical study of ethylene, n-heptane, and toluene. *Combustion and Flame*, 221:371–383, 2020.

[106] Arnau Pons, Tristan Fuller, Swanand V. Sardeshmukh, and William E. Anderson. Analysis of the interactions between acoustics and unsteady heat release in a self-excited single element combustor. In *2018 Joint Propulsion Conference*. American Institute of Aeronautics and Astronautics Inc, AIAA, 2018.

[107] K Ramamurthi and K Nandakumar. Characteristics of flow through small sharp-edged cylindrical orifices. *Flow measurement and Instrumentation*, 10(3):133–143, 1999.

[108] Michael Reader-Harris. *Orifice plates and venturi tubes*. Springer, 2015.

[109] H. Rehab, E. Villermaux, and E. J. Hopfinger. Flow regimes of large-velocity-ratio coaxial jets. *Journal of Fluid Mechanics*, 345:357–381, 1997.

[110] L.S. Rothman, I.E. Gordon, R.J. Barber, H. Dothe, R.R. Gamache, A. Goldman, V.I. Perevalov, S.A. Tashkun, and J. Tennyson. HITEMP, the High-Temperature Molecular Spectroscopic Database. *Journal of Quantitative Spectroscopy and Radiative Transfer*, 111(15):2139–2150, oct 2010.

[111] Hunter Rouse. *Elementary mechanics of fluids*. J. Wiley Sons, Inc., 1946.

[112] Enea Sacco and Seung Ki Moon. Additive manufacturing for space: status and promises. *International Journal of Advanced Manufacturing Technology*, 105(10):4123–4146, 2019.

[113] Isabelle C. Sanders, Fabio A. Bendana, China G. Hagström, and R. Mitchell Spearrin. Injector effects on hybrid polymethylmethacrylate combustion assessed by thermochemical tomography. *Journal of Propulsion and Power*, 37(6):928–943, nov 2021.

[114] Robert J Santoro and William E Anderson. Combustion instability phenomena of importance to liquid propellant engines. *Pennsylvania State Univ., Annual Rept. to US Air Force Office of Scientific Research*, pages 93–0667, 1994.

[115] S. Alexander Schumaker and James F. Driscoll. Coaxial turbulent jet flames: Scaling relations for measured stoichiometric mixing lengths. *Proceedings of the Combustion Institute*, 32 II(2):1655–1662, 2009.

[116] Stephen Alexander Schumaker. *An Experimental Investigation of Reacting and Nonreacting Coaxial Jet Mixing in a Laboratory Rocket Engine*. Ph.D. thesis, University of Michigan, 2009.

[117] Douglas Schwer, Andrew Corrigan, Brian Taylor, and Kailas Kailasanath. On Reducing Feedback Pressure in Rotating Detonation Engines. In *51st AIAA Aerospace Sciences Meeting including the New Horizons Forum and Aerospace Exposition*, Reston, Virigina, jan 2013. American Institute of Aeronautics and Astronautics.

[118] Myungbo Shim, Kwanyoung Noh, and Woongsup Yoon. Flame structure of methane/oxygen shear coaxial jet with velocity ratio using high-speed imaging and OH* CH* chemiluminescence. *Acta Astronautica*, 147(March):127–132, 2018.

[119] Masayasu Shimura, Takashi Ueda, Gyung Min Choi, Mamoru Tanahashi, and Toshio Miyauchi. Simultaneous dual-plane CH PLIF, single-plane OH PLIF and dual-plane stereoscopic PIV measurements in methane-air turbulent premixed flames. *Proceedings of the Combustion Institute*, 33(1):775–782, 2011.

[120] H. Shipley, D. McDonnell, M. Culleton, R. Coull, R. Lupoi, G. O'Donnell, and D. Trimble. Optimisation of process parameters to address fundamental challenges during selective laser melting of ti-6al-4v: A review. *International Journal of Machine Tools and Manufacture*, 128:1–20, 2018.

[121] Simona Silvestri, Maria P. Celano, Christoph Kirchberger, Gregor Schlieben, Oskar Haidn, and Oliver Knab. Investigation on Recess Variation of a Shear Coax Injector for a Single Element GOX-GCH4 Combustion Chamber. *Transactions of the Japan Society for Aeronautical and Space Sciences, Aerospace Technology Japan*, 14(ists30):13–20, 2016.

[122] S. L. Sing, S. Huang, G. D. Goh, G. L. Goh, C. F. Tey, J. H.K. Tan, and W. Y. Yeong. Emerging metallic systems for additive manufacturing: In-situ alloying and multi-metal processing in laser powder bed fusion. *Progress in Materials Science*, 119(March):100795, 2021.

[123] Timothy M. Smith, Christopher A. Kantzos, Nikolai A. Zarkevich, Bryan J. Harder, Milan Heczko, Paul R. Gradl, Aaron C. Thompson, Michael J. Mills, Timothy P. Gabb, and John W. Lawson. A 3D printable alloy designed for extreme environments. *Nature*, 617(7961):513–518, 2023.

[124] Jacob C. Snyder and Karen A. Thole. Understanding laser powder bed fusion surface roughness. *Journal of Manufacturing Science and Engineering*, 142(7):071003, 05 2020.

[125] Jiawen Song and Bing Sun. Coupled heat transfer analysis of thrust chambers with recessed shear coaxial injectors. *Acta Astronautica*, 132(December 2016):150–160, 2017.

[126] P.J. Spaur. *Investigation of Discharge Coefficients for Irregular Orifices*. Master's thesis. West Virginia University, 2011.

[127] Dheepa Srinivasan and Kiruthika Ananth. Recent Advances in Alloy Development for Metal Additive Manufacturing in Gas Turbine/Aerospace Applications: A Review. *Journal of the Indian Institute of Science*, 102(1):311–349, 2022.

[128] George P. Sutton and Oscar Biblarz. *Rocket Propulsion Elements*. John Wiley Sons, Inc., 8th edition, 2010.

[129] David T. and Reardon Frederick H. Harrje. *Liquid Propellant Rocket Combustion Instatbility*, volume NASA SP-194. National Aeronautics and Space Administration, 1972.

[130] K. M. Tacina and W. J.A. Dahm. Effects of heat release on turbulent shear flows. Part 1. A general equivalence principle for non-buoyant flows and its application to turbulent jet flames. *Journal of Fluid Mechanics*, 415:23–44, 2000.

[131] Thomas Teasley, Benjamin Williams, Andrew Larkey, Christopher Protz, and Paul Gradl. A Review Towards the Design Optimization of High-Performance Additively Manufactured Rotating Detonation Rocket Engine Injectors. *AIAA Propulsion and Energy Forum, 2021*, pages 1–39, 2021.

[132] Thomas W. Teasley, Christopher S. Protz, Andrew P. Larkey, Benjamin B. Williams, and Paul R. Gradl. A Review Towards the Design Optimization of High Performance Additively Manufactured Rotating Detonation Rocket Engine Injectors. In *AIAA Propulsion and Energy 2021 Forum*, Reston, Virginia, 8 2021. American Institute of Aeronautics and Astronautics.

[133] Baran Teoman, Andrei Potanin, and Piero M. Armenante. The discharge of complex fluids through an orifice: A review. *Chemical Engineering Research and Design*, 179:346–364, 2022.

[134] Sophonias Teshome, Ivett A Leyva, and Douglas Talley. Cryogenic High-Pressure Shear-Coaxial Jets Exposed to Transverse Acoustic Forcing. In *50th AIAA Aerospace Sciences Meeting including the New Horizons Forum and Aerospace Exposition*, number January, pages 1–22. AIAA Paper 2012-1265, 2012.

[135] Scott M. Thompson, Tausif Jamal, Basil J. Paudel, and D. Keith Walters. Transitional and turbulent flow modeling in a tesla valve. *ASME International Mechanical Engineering Congress and Exposition, Proceedings (IMECE)*, 7 B(April 2017), 2013.

[136] Zhihua Tian, Chaoqun Zhang, Dayong Wang, Wen Liu, Xiaoying Fang, Daniel Wellmann, Yongtao Zhao, and Yingtao Tian. A review on laser powder bed fusion of inconel 625 nickel-based alloy. *Applied Sciences*, 10(1):81, 2019.

[137] A. Townsend, N. Senin, L. Blunt, R.K. Leach, and J.S. Taylor. Surface texture metrology for metal additive manufacturing: a review. *Precision Engineering*, 46:34–47, 2016.

[138] John Tsohas and Stephen D. Heister. Numerical simulations of liquid rocket coaxial injector hydrodynamics. *Journal of Propulsion and Power*, 27:793–810, 2011.

[139] V. and W. Yang Anderson, editors. *Liquid Rocket Engine Combustion Instability*, volume 169. American Institute of Aeronautics and Astronautics, 1995.

[140] E. Villermaux, E. and Rehab. Mixing in coaxial jets. *Journal of Fluid Mechanics*, 425:161–185, 2000.

[141] Xavier Viot, A. Souchier, Gilles Dantu, and F. Lassoudière. High Thrust Engine Demonstrations. *45th AIAA/ASME/SAE/ASEE Joint Propulsion Conference and Exhibit*, pages 1–8, August 2009.

[142] John P Wanhainen, Harold C Parish, and E William Conrad. *Effect of Propellant Injection Velocity on Screech in 20,000-Pound Hydrogen-Oxygen Rocket Engine*, volume 3373. National Aeronautics and Space Administration, 1966.

[143] Chuyu Wei, Daniel I. Pineda, Christopher S. Goldenstein, and R. Mitchell Spearrin. Tomographic laser absorption imaging of combustion species and temperature in the mid-wave infrared. *Optics Express*, 26(16):20944, aug 2018.

[144] Chuyu Wei, Daniel I. Pineda, Laurel Paxton, Fokion N. Egolfopoulos, and R. Mitchell Spearrin. Mid-infrared laser absorption tomography for quantitative 2D thermochemistry measurements in premixed jet flames. *Applied Physics B*, 124(6):123, jun 2018.

[145] Peter Welch. The use of fast fourier transform for the estimation of power spectra: A method based on time averaging over short, modified periodograms. *IEEE Transactions on audio and electroacoustics*, 15(2):70–73, 1967.

[146] Leon M. Wenzel and John R. Szuch. *Analysis of Chugging in Liquid-Bipropellant Rocket Engines with Different Vaporization Rates*. National Aeronautics and Space Administration, 1965.

[147] Fernanda F. Winter, Nikolaos Perakis, and Oskar J. Haidn. Emission imaging and CFD simulation of a coaxial single-element GOX/GCH4 rocket combustor. *2018 Joint Propulsion Conference*, 2018.

[148] Roger D. Woodward, Sibtosh Pal, Shahram Farhangi, Gregory E. Jensen, and Robert J. Santoro. LOX/GH2 shear coaxial injector atomization studies: Effect of recess and non-concentricity. *Collection of Technical Papers - 45th AIAA Aerospace Sciences Meeting*, 10(January):6925–6946, 2007.

[149] Shuaijie Xue, Hongjun Liu, Lixin Zhou, Weidong Yang, Hongbo Hu, and Yu Yan. Experimental Research on Rotating Detonation with Liquid Hypergolic Propellants. *Chinese Journal of Aeronautics*, 31(12):2199–2205, 2018.

[150] Yen C. Yu, James C. Sisco, Stanford Rosen, Ajay Madhav, and William E. Anderson. Spontaneous longitudinal combustion instability in a continuously variable resonance combustor. *Journal of Propulsion and Power*, 28:876–887, 2012.

[151] Duyao Zhang, Shoujin Sun, Dong Qiu, Mark A. Gibson, Matthew S. Dargusch, Milan Brandt, Ma Qian, and Mark Easton. Metal Alloys for Fusion-Based Additive Manufacturing. *Advanced Engineering Materials*, 20(5):1–20, 2018.